



TECHNISCHE UNIVERSITÄT MÜNCHEN

DOCTORAL THESIS

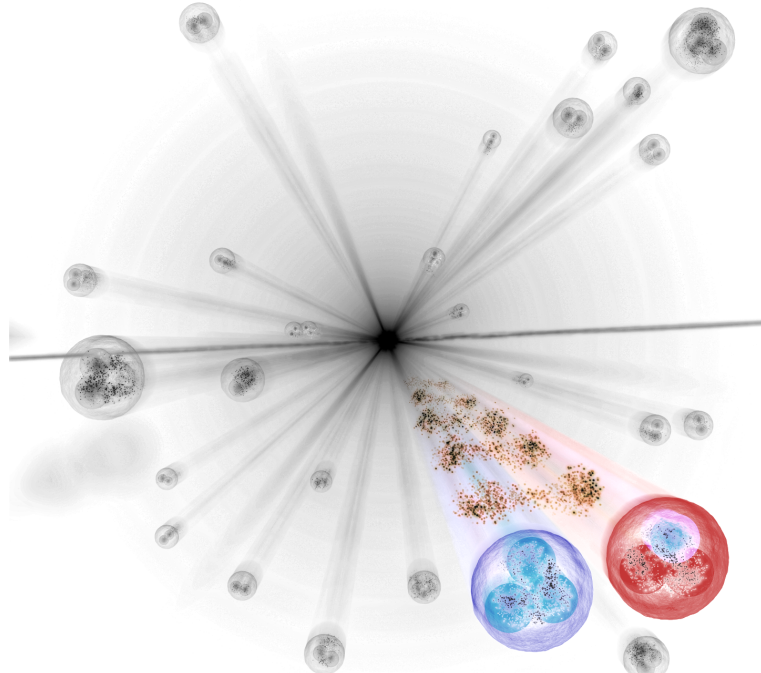
Analysis techniques for femtoscopy and correlation studies in small collision systems and their applications to the investigation of p- Λ and Λ - Λ interactions with ALICE

Author:

Dimitar Lubomirov Mihaylov

Supervisor:

Prof. Dr. Laura Fabbietti



*A thesis submitted in fulfillment of the requirements
for the degree of Doctor of Philosophy
in the
Physics Department*

February, 2021



Dense and Strange Hadronic Matter
Physik-Department
Technische Universität München

DOKTORARBEIT

**Analysemethoden für Femtoskopie und
Korrelationsstudien in kleinen Kollisionssystemen
und deren Anwendung zur Untersuchung von
p- Λ und Λ - Λ Wechselwirkungen mit ALICE**

Autor:

Dimitar Lubomirov Mihaylov

Betreuerin:

Prof. Dr. Laura Fabbietti

Vollständiger Abdruck der von der Fakultät für Physik der Technischen Universität München zur Erlangung des akademischen Grades eines Doktors der Naturwissenschaften (Dr. rer. nat.) genehmigten Dissertation.

Vorsitzender:

apl. Prof. Dr. Norbert Kaiser

Prüfer der Dissertation:

Prof. Dr. Laura Fabbietti

Prof. Dr. Elisa Resconi

Die Dissertation wurde am _____ bei der Technischen Universität München eingereicht und durch die Fakultät für Physik am _____ angenommen.

Declaration of Authorship

I, Dimitar Lubomirov Mihaylov, declare that this thesis titled, "Analysis techniques for femtoscopy and correlation studies in small collision systems and their applications to the investigation of p- Λ and Λ - Λ interactions with ALICE" and the work presented in it are my own. I confirm that:

- This work was done wholly or mainly while in candidature for a research degree at this University.
- I have not employed the services of an organization that provides dissertation supervisors in return for payment or that fulfills, in whole or in part, the obligations incumbent on me in connection with my dissertation.
- I have not submitted the dissertation, either in the present or a similar form, as part of another examination process.
- I have not yet been awarded the desired doctoral degree nor have I failed the last possible attempt to obtain the desired degree in a previous doctoral program.
- Where I have consulted the published work of others, this is always clearly attributed.
- Where I have quoted from the work of others, the source is always given. With the exception of such quotations, this thesis is entirely my own work.
- I have acknowledged all main sources of help.
- Where the thesis is based on work done by myself jointly with others, I have made clear exactly what was done by others and what I have contributed myself.

Signed:

Date:

TECHNISCHE UNIVERSITÄT MÜNCHEN

Abstract

Physics Department

Doctor of Philosophy

Analysis techniques for femtoscopy and correlation studies in small collision systems and their applications to the investigation of p- Λ and Λ - Λ interactions with ALICE

by Dimitar Lubomirov Mihaylov

Femtoscopy is a technique relating the correlations between pairs of particles to their emission source and interaction potential. Traditionally femtoscopy is used to study the properties of the emission source, mostly by using charged pion correlations, for which the correlation function is determined only by the Bose-Einstein statistics and Coulomb interaction.

The topic of this work is the non-traditional baryon-baryon femtoscopy, the goal of which is to study the interaction potential between different baryon pairs, assuming the emission source is fixed. Such an approach is quite challenging as it requires an exact treatment of the strong potential in order to compute the correlation function, as well as knowledge on the profile and size of the emission source. In the work presented here, a new "Correlation Analysis Tool using the Schrödinger equation" (CATS) has been developed to tackle the issue related to the modeling of the correlation function. In previous works it was proposed that in small collision systems the source is approximately the same for all baryon-baryon pairs and this feature leads to the opportunity of using the p-p correlations to fix the source, allowing to study the interaction of other pairs. However, the limits of validity of this method were never quantitatively studied. In particular, the decays of short-lived resonances are expected to influence the emission source differently based on the particle species involved. In this work a new model was developed to handle this effect, making possible to perform non-traditional femtoscopy with much higher precision.

This new analysis techniques and method developed were used by the ALICE collaboration to study a multitude of different baryon-baryon systems, including p- Λ , p- Σ^0 , p- Ξ^- , Λ - Λ , p- Ω^- and has even been applied to the meson sector to study the p- K^- interaction. Aside the development of CATS and the new source model, the author was the main analyzer of the p- Λ and Λ - Λ systems, therefore these results will be discussed in detail. In particular, the study of p- Λ has an important link to the equation of state of nuclear matter and the existence of massive neutron stars. In this work the chiral effective field theory computations are verified against the p- Λ data collected by the ALICE collaboration. The Λ - Λ system is of great theoretical interest, as some models predict the existence of a bound state, the so called H-dibaryon, which could be composed of two Λ s. The current work provides further experimental constraints on the Λ - Λ scattering parameters and binding energy of the hypothetical bound state.

Zusammenfassung

Femtoskopie ist eine Methode, die Korrelationen zwischen Teilchenpaaren mit ihrer Emissionsquelle und ihrem Wechselwirkungspotential in Beziehung setzt. Traditionell wird die Femtoskopie verwendet, um die Eigenschaften der Emissionsquelle zu untersuchen, hauptsächlich mittels Korrelationen zwischen geladenen Pionen, die durch die Bose-Einstein-Statistik und die Coulomb-Wechselwirkung entstehen. Das Thema dieser Arbeit ist die nicht-traditionelle Baryon–Baryon-Femtoskopie, deren Ziel es ist, das Wechselwirkungspotential zwischen verschiedenen Paaren zu untersuchen, unter der Annahme, dass die Emissionsquelle bestimmt ist. Dieses Verfahren ist herausfordernd, da es eine genaue Behandlung der starken Wechselwirkung erfordert, um die Korrelationsfunktion zu berechnen. Darüber hinaus sind Kenntnisse über die raum-zeitliche Ausdehnung der Emissionsquelle erforderlich. Im Rahmen dieser Arbeit ist ein neues Analyse-Framework (CATS) entwickelt worden, mit Hilfe dessen Korrelationsfunktionen modelliert werden können. Es wurde früher vorgeschlagen, dass in kleinen Kollisionssystemen die Quelle für alle Baryon–Baryon-Paare ungefähr gleich ist. Dies ermöglicht es Proton–Proton-Korrelationen zu verwenden, um die Quelle zu bestimmen und das Interaktionspotential anderer Paare zu untersuchen. Die Gültigkeitsgrenzen dieser Methode sind nicht bekannt, obwohl erwartet wird, dass der Zerfall kurzlebiger Resonanzen die Emissionsquelle je nach Partikelart unterschiedlich beeinflusst. In dieser Arbeit wurde ein neues Modell entwickelt, um diesen Effekt zu bestimmen und die nicht-traditionelle Femtoskopie mit viel höherer Präzision durchzuführen.

Diese neuen Analysemethoden wurden von der ALICE-Kollaboration verwendet, um viele verschiedene Baryon–Baryon-Systeme zu untersuchen, darunter $p-\Lambda$, $p-\Sigma^0$, $p-\Xi^-$, $\Lambda-\Lambda$, $p-\Omega^-$, sogar auch $p-K^-$ im mesonischen Sektor. Neben der Entwicklung von CATS und dem neuen Modell für die Quelle, war der Autor der Hauptanalysator der $p-\Lambda$ and $\Lambda-\Lambda$ Systeme, daher werden diese Ergebnisse detailliert diskutiert. Insbesondere steht die Untersuchung von $p-\Lambda$ in einem wichtigen Zusammenhang mit der Zustandsgleichung der Kernmaterie und der Existenz massereicher Neutronensterne. In dieser Arbeit wird die chirale effektive Feldtheorie anhand der von der ALICE-Kollaboration gesammelten $p-\Lambda$ Daten verifiziert. Das $\Lambda-\Lambda$ System ist von großem theoretischen Interesse, da einige Modelle die Existenz eines gebundenen Zustands vorhersagen, des sogenannten H-Dibaryon, das aus zwei Λ -Teilchen bestehen könnte. Diese Arbeit liefert weitere experimentelle Einschränkungen für die $\Lambda-\Lambda$ Streuparameter und für die Bindungsenergie dieses hypothetischen gebundenen Zustands.

Acknowledgements

The acknowledgments might seem as the easy part to write, but it is actually quite challenging, as it is difficult to single out anyone. The reason is that the group of Prof. Laura Fabbietti is more than just a team, it feels more like a big (Italian) family, where we laugh together, cry together, argue vigorously on the way to find solutions, but most importantly we always stay put and have each others backs. For that reason, perhaps the person deserving most credit is the Italian "mama" Laura, that managed to create this environment. The others that I simply have to give a very special thanks to are Oliver Arnold (Oli), which earned his name "Femto-daddy" as he set up the pioneering work in our group on the subject of femtoscopy and was my first real mentor in this field. Next came Valentina Mantovani Sarti (Vale), and she became the perfect Italian "grandma", fun when you need to be cheered up, wise when you need an advise, and knowledgeable when you need to learn. It is not an exaggeration to say that without her, I would have probably never gotten my PhD, hence a very big hug! This is the way! The other two people to single out were my German brothers (the Femtoboyz), Andreas Mathis (Andi) and Bernhard Hohlweiger (Bernie). The project presented in this thesis was essentially an undertaking shared between all three of us, and needless to say that without their huge contribution and fantastic team effort this work would have been of much lesser significance. Special thanks also go to Joana Wirth (JoJo), we might have not worked together on a single project, but we did together a bachelor, master and PhD in Laura's the group, something only few have achieved. To the special acknowledgments I also have to add Steffen Maurus, Tobias Kunz and Thomas Klemenz, as the best system admins make for great science. To Steffen: sorry for submitting a job that self-submits itself...

I will probably forget someone (apology), but here a list of many of the other members of our family at the office, that made me smile. Ante: the lord of Bash, with the wonderfully weird sense of humor and a true (honest) friend. And thanks for sharing the best cevapcici place in Munich with all of us! Oton: any grandpa needs no introduction, a bit grumpy but you always learn from him, even just by observing. Иван: С Вами, мой дорогой товарищ, мы укрепили болгаро-российскую дружбу!¹. Bhawani: as a theorist you bring new and interesting points of view, that would otherwise be hidden from us. Just make you sure to survive the nasty German food, as you are a great asset to our community. Marcel: the living proof that a big smile goes a long way, its about time that you join femto. And thanks for the Aspirin-Complex in Wuhan, it helped a lot with the unidentified² Chinese virus. Emma: how you do not freeze in winter is beyond me, I thought that long sleeves are what make us warm, I guess it is femtoscopy in your case. Cindy: without (free) coffee there is no physics, thanks for the nice little chats. (Baby) Laura: time for the Femtogirls to shine, and with you the future looks bright, keep it on sister! Berkin: the greatest secret Santa ever! Max: the padawan who had to do it all on his own. Diamonds are made under pressure, and you have all that it takes to make a great physicist! And last but not least: the rest of the LMEE gang (Torsten, Anisa and Alex) made the time together so much more fun! Oh, and Papa Gasik, who was just so fun to have around, and thanks to him I had the chance to (almost) touch an actual GEM foil as part of my service task.

Turning to my time in the group before my PhD, there are so many people that helped me through the years, but most of all it was my former supervisor Kirill

¹Ivan: With you, my dear comrade, we have strengthened the Bulgarian-Russian relationship!

²Let's not dig any further :)

Lapidus, who give me the needed self confidence for the long way leading to the PhD. Спасибо, и пора бы нам встретиться выпить в Москве!³

On the professional level, apart from the colleagues at the office, the people from the ALICE collaboration provided a lot of support, and I am grateful for their insightful input. In particular, the comments of Dariusz Miskowiec lead to a deeper understanding of the source, which would have been otherwise never achieved. Further, I have enjoyed and appreciated the work with Benjamin Dönigus and Harrald Appelshäuser on the $\Lambda\Lambda$ interaction. The work with people outside of the ALICE collaboration has also been very productive, in particular I would like to thank Johann Haidenbauer, Norbert Kaiser, Wolfram Weise, Akira Ohnishi, Yuki Kamiya and Tetsuo Hatsuda for the interesting discussions we had.

On the personal side, I would like to express my gratitude towards my parents, for sparking my interest in science in the first place. My mother in particular supported this endeavour in any possible way through the years. My grandparents were fantastic role models and helped me develop as a person, bringing in a never ending wisdom into my life. I was also blessed with great friends, which helped me remain sane during the very difficult challenges I have faced. Above all, Stanislav (Другаря) and Stanislava (Съни) were there for me through thick and thin, thanks guys! And most importantly, the greatest joy during the PhD was the birth of my son Julian. It is unbelievable how by the time I have finished, you little dude already knew what an atom is composed of! The future looks bright, perhaps you get a PhD before me :) Speaking about little guys, I have to thank the team at the AWO Kinderkrippe, that helped both me and Julian during the difficult COVID times.

³Thanks, and it is about time we meet in Moscow for a drink!

Contents

Declaration of Authorship	iii
Abstract	v
Zusammenfassung	vi
Acknowledgements	vii
1 Introduction	1
1.1 The goal of this work	1
1.2 The standard model of particle physics	1
1.3 Quantum chromodynamics	3
1.4 Baryon–baryon interaction and neutron stars	8
1.4.1 Overview	8
1.4.2 Baryon–baryon interaction	8
1.4.3 Neutron stars and the equation of state	11
1.5 Femtoscopy	15
1.5.1 A chronological overview	15
The way to non-traditional femtoscopy in small collision systems	15
The role of this work	18
1.5.2 The Koonin-Pratt relation	20
1.5.3 The source function	22
1.5.4 Lednický formalism	23
Identical particles	25
Coulomb force	26
1.5.5 Residual correlations	27
2 CATS framework	29
2.1 Overview	29
2.2 Evaluation of the wave function	30
2.3 Interaction channels	32
2.4 Evaluation of the correlation function	34
2.5 Understanding the strong interaction using CATS	34
2.6 Coupled channels	41
2.7 Corrections to the correlation function	44
2.7.1 Feed-down	44
2.7.2 Misidentifications and λ parameters	47
2.7.3 Momentum resolution	49
3 Experimental data	53
3.1 ALICE	54
3.1.1 Overview	54
Triggering system	55

Inner Tracking System	56
Time Projection Chamber	57
Time-Of-Flight detector	59
3.1.2 Basics of the ALICE data structure	60
Overview	60
AOD files	60
Monte-Carlo simulations	62
3.1.3 Collision systems and event cuts	62
3.1.4 Reconstruction of protons	63
Track reconstruction	63
Determination of the purity and primary fraction	63
3.1.5 Reconstruction of Λ s	65
V0 reconstruction	65
Determination of the purity and primary fraction	67
3.1.6 Raw Λ - Λ and p - Λ correlations	71
Pair cuts	71
Same and mixed events	73
3.2 Normalization of the correlation function	75
3.2.1 Overview	75
3.2.2 Addition of correlations	77
3.2.3 Practical applications	79
3.3 Handling the λ parameters	80
3.3.1 General overview	80
3.3.2 Correction for impurities	81
3.3.3 Sideband analysis	82
3.3.4 Momentum dependent decomposition analysis	83
3.4 Non-femtoscopic baseline	84
3.4.1 Origin	84
3.4.2 Effect on the correlation function	88
3.4.3 Future prospects	90
3.5 Modelling of the data	93
3.5.1 Data fitting	93
3.5.2 Systematic uncertainties	94
Overview	94
Uncertainties related to the data	95
Uncertainties of the fit	97
Confidence intervals	99
4 The emission source in small systems	101
4.1 Overview	101
4.2 Gaussian source	102
4.3 The resonance source model	104
4.3.1 Strategy and assumptions	104
4.3.2 Determining the kinematic of the primordial emission	106
4.3.3 The resonance source model	109
4.3.4 Results for p - p and p - Λ	110
4.4 Towards a universal source model	111

5 The Λ-Λ interaction	117
5.1 Introduction and physics motivation	117
5.2 Analysis techniques	121
5.3 Results and outlook	125
6 The p-Λ interaction	129
6.1 Introduction and physics motivation	129
6.2 Analysis techniques	131
6.2.1 Overview	131
6.2.2 Decomposition of the correlation signal	133
6.2.3 Sideband analysis	134
6.2.4 Unfolding	139
6.2.5 Data modelling	141
6.3 Results	142
7 Final remarks and outlook	149
7.1 Proton-Kaon	149
7.2 Proton- Ξ and proton- Ω	151
7.3 Proton- Σ	152
7.4 Outlook	153
A CATS tutorial	155
A.1 Overview	155
A.2 Simple source functions in π - π correlations	156
A.3 Inclusion of the strong interaction in potential form	159
A.4 The predefined interaction potentials	162
A.5 DLM_Ck: The correlation function as a histogram	165
A.6 Usage of the Lednický model and other custom correlation functions .	167
A.7 DLM_CkDecomp: Correcting the correlation function	169
B Details on the resonance source model	177

List of Figures

1.1	Standard Model of elementary particles	2
1.2	The basic QCD Feynman diagrams	3
1.3	The running coupling constant of QCD	4
1.4	The QCD phase diagram	5
1.5	Strangeness enhancement in HM pp collisions	7
1.6	Experimental and theoretical cross section of the $N\Sigma \leftrightarrow N\Lambda$ system	9
1.7	Nuclear equation of state in the presence of hyperons	12
1.8	Nuclear equation of state in the presence of hyperons from χ EFT	13
1.9	Hadronic wave functions in dense matter	14
1.10	Hybrid quark-hadron EoS (QHC19)	14
1.11	Femtoscopic principle	21
1.12	Residual correlations	28
2.1	Bessel functions	32
2.2	Typical meson exchange potential	35
2.3	Example potentials	36
2.4	Bessel functions	37
2.5	Example wave functions	39
2.6	Example phase shifts	40
2.7	Example correlation functions	42
2.8	Feed-down matrix ($p-\Lambda \rightarrow p-p$)	46
2.9	Projections of the feed-down matrix for $p-\Lambda \rightarrow p-p$	46
2.10	Residual correlation function for $p-\Lambda \rightarrow p-p$	47
2.11	Momentum smearing matrix for $p-p$	50
2.12	Projections of the momentum smearing matrix for $p-p$	51
2.13	Smeared correlation function for $p-p$	51
3.1	ALICE detector	55
3.2	Inner Tracking System	56
3.3	Time Projection Chamber	57
3.4	Energy loss in the TPC	58
3.5	Particle identification using the Time-Of-Flight	59
3.6	Workflow of the data reconstruction in ALICE	61
3.7	Template fits for the protons	66
3.8	Template fit for the protons in a single p_T bin	67
3.9	Fraction of protons based on the template fits	69
3.10	Experimental invariant mass distribution of $p\pi^-$	70
3.11	Invariant mass distribution of $p\pi^-$ as a function of p_T	70
3.12	Purity of the Λ and $\bar{\Lambda}$ candidates	71
3.13	CPA template fits for Λs	72
3.14	CPA template fit for Λs in a single p_T bin	72
3.15	The fractions of Λ as a function of p_T	73
3.16	Raw $\Lambda-\Lambda$ correlation	75

3.17	Raw p- Λ correlation	76
3.18	Two-particle angular distributions in pp collisions by ALICE	86
3.19	Two-particle angular ($\Delta\varphi$) distributions in pp collisions by ALICE	87
3.20	Two-particle angular ($\Delta\varphi$) distributions in pp collisions from AMPT	88
3.21	Long range baryon-baryon correlations in momentum space	91
3.22	Effect of quark-level Pauli suppression on $C(\Delta\varphi)$	92
4.1	Transverse mass dependence of a Gaussian source	103
4.2	Sketch of the resonance source model	106
4.3	Transverse mass dependence of a core Gaussian source	110
4.4	Resonance source model: probability density of the emission	111
4.5	Resonance source model: effect on the correlation function	112
4.6	Resonance source model compared to a Cauchy source	114
4.7	Resonance source model: effect of long lived resonances	114
4.8	Resonance source model: effect of ω meson onto π - π correlations	115
4.9	The r_{core} as a function of $\langle m_T \rangle$ for same charged pions	115
5.1	Results on $\Lambda\Lambda$ from KEK	118
5.2	Results on $\Lambda\Lambda$ from ALICE	119
5.3	The p-p correlation functions as measured in pp and p-Pb collisions	124
5.4	The Λ - Λ correlation functions	126
5.5	Theoretical $\Lambda\Lambda$ correlation functions	126
5.6	Updated Λ - Λ exclusion plot	127
5.7	Allowed $\Lambda\Lambda$ binding energy	127
6.1	The p- Λ cross section from experiment and χ EFT	130
6.2	The p- Λ theoretical correlation based on χ EFT	131
6.3	Experimental p- Λ correlation function	132
6.4	Invariant mass of Λ candidates with k^* below 24 MeV/ c	136
6.5	Purity of the Λ candidates as a function of k^*	137
6.6	Sideband correlations for p- Λ	138
6.7	Systematic variations of the sidebands	139
6.8	Corrected experimental p- Λ correlation function	140
6.9	Unfolding of the p- Λ correlation	141
6.10	Results on p- Λ (1)	143
6.11	Results on p- Λ (2)	143
7.1	Experimental p- K^- correlation function	150
7.2	Improved modelling of the p- K^- correlation function	151
7.3	Experimental p- Ξ^- correlation function	151
7.4	Experimental p- Ω^- correlation function	152
7.5	Experimental p- Σ^0 correlation function	153
A.1	Correlation of charged identical pions	159
A.2	Correlation of p- Λ (Usmani potential)	162
A.3	Repulsive core	163
A.4	Cutoff scale in <i>DLM_Ck</i>	167
A.5	Correlation of p- Λ (Lednicky model)	169
A.6	Decomposition of the p-p correlation	176

List of Tables

2.1	Toy potentials for different types of interaction	36
2.2	Scattering parameters of the toy potentials	38
3.1	Event selection criteria used for the pp 13 TeV and p–Pb at 5.02 TeV analyses	63
3.2	Track selection criteria used for proton reconstruction	63
3.3	Proton purities extracted from MC	64
3.4	Proton fractions extracted from the template fits	65
3.5	Systematic variations for Λ reconstruction	68
3.6	Λ purities extracted from the IM fits of the single particles	68
3.7	Λ fractions extracted from the template fits	71
3.8	Quantum statistics term for long-range correlations	91
3.9	Systematic variations for proton reconstruction	96
3.10	Systematic variations for Λ reconstruction	96
3.11	Confidence intervals for different number of fit parameters	99
5.1	Coupled channels for the $\Lambda\Lambda$ system	120
5.2	lambda parameters	122
5.3	The λ parameters used for the modelling of Λ – Λ	122
6.1	λ parameters for p– Λ	134
6.2	Weight parameters for the p– Λ sidebands	138
6.3	Summary of the theoretical description of p– Λ	144
A.1	Input for the predefined CATS potentials	164
B.1	List of resonances from the SHM feeding into protons	178
B.2	List of resonances from the SHM feeding into Λ particles	179

List of Abbreviations

ALICE	A Large Ion Collider Experiment
CATS	Correlation Analysis Tool using the Schrödinger equation
CPA	Cosine Pointing Angle
DCA	Distance of Closest Approach
EoS	Equation of State
FSI	Final State Interaction
HBT	Hanbury Brown and Twiss effect
HI	Heavy Ion
HM	High Multiplicity
ITS	Inner Tracking System
LHC	Large Hadron Collider
LO	Leading Order
MB	Minimum Bias
MC	Monte Carlo simulations
N	Nucleon
NLO	Next to Leading Order
NS	Neutron Star
PDG	Particle Data Group
PID	Particle Identification
PV	Primary Vertex
RHIC	Relativistic Heavy Ion Collider
RUN1	First period of LHC operation
RUN2	Second period of LHC operation
SM	Standard Model
SHM	Statistical Hadronization Model
SV	Secondary Vertex
TOF	Time of Flight detector
TPC	Time Projection Chamber
QCD	Quantum ChromoDynamics
QGP	Quark Gluon Plasma
χEFT	Chiral Effective Field Theory
Y	Hyperon

Chapter 1

Introduction

1.1 The goal of this work

The main topic of this thesis relates to the strong interaction between pair of baryons¹ in vacuum, in particular those containing strange quarks. The related fundamental theory is quantum chromodynamics (QCD), but due to its rich nature and non-perturbative character at low energies it is highly difficult to obtain solid theoretical predictions, nevertheless there are both numerical and effective approaches to gauge on the interaction. The numerical (lattice) calculations excel at providing predictions for the heavy particles, while the effective theories have a lot of free parameters to be determined by experimental data. The latter is of sufficient quality for the nucleons (protons and neutrons), however any particles containing a strange quark become very difficult to study by traditional methods, such as scattering experiments. Thus the domain of solid predictions by the lattice is not accessible experimentally, while the effective theories are only partially constrained. Further, these limitations lead to a lot of ambiguities in the theoretical predictions for interaction in dense medium, which is of significant importance in describing astrophysical objects, neutron stars in particular. Thus, it has been a long standing goal of nuclear physics to obtain a realistic equation of state (EoS) for the nuclear matter, and the main bottleneck has been the limited experimental data, both on the sub-atomic and astrophysical scale. The latter is likely to be addressed in the future by the increasing sensitivity of gravitational wave experiments, while the former can be improved by correlation techniques applied to particle produced at accelerator facilities. Recent measurements at the LHC proved that using the ALICE experiment to record high-multiplicity events² in pp collisions at 13 TeV provides sufficient statistics to study particle correlations between systems of baryon pairs, in which up to 3 of the total 6 quarks are strange. These results are seen as the beginning of a new era in the study of the strong nuclear force, as it can provide complementary constraints to the effective theories and the first direct experimental test of the lattice calculations. In this theses the related main advances in the analysis techniques will be presented, along with the physics results on the investigation of the Λ - Λ and p- Λ systems, where the Λ is a baryon consisting of an up, down and a strange quark.

1.2 The standard model of particle physics

In this chapter a brief introduction of the *standard model* (SM) of particle physics is given, only to introduce the terminology used in the present work. The standard

¹Objects build up of 3 quarks, such as protons and neutrons.

²Collisions in which the amount of produced particles is above the average for the corresponding system.

model postulates that the known matter and energy can be explained by classifying all particles into 4 different classes, quarks, leptons, gauge bosons and the higgs scalar boson, summarized in Fig. 1.1 [1]. The latter is responsible for the bare mass

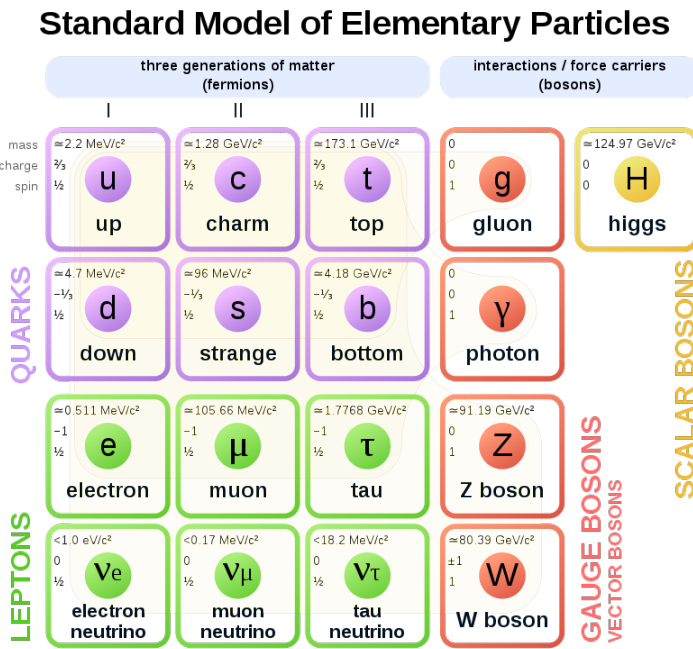


FIGURE 1.1: [2] The elementary particles within the Standard model.

of the rest of the particles. The gauge bosons are the force carriers mediating the strong (gluon g), weak (Z and W bosons) and electromagnetic (photon γ) forces. The gravitational force completes the picture of the four fundamental forces of nature, however it remains unexplained by the standard model. Thus, it is known to be incomplete, despite being so successful in describing the other three forces, causing a lot of effort to search for (particle) physics effects beyond the SM, so far without success. The building blocks of matter within the SM are the quarks and leptons, each coming in 6 different types (flavours). They are spin 1/2 fermions and grouped in three generations based on their mass. The leptons are either negatively charged or neutral, where the former are more heavy (electron, muon and tau) and the latter are the very light neutrinos (ν_e, ν_μ, ν_τ). The leptons can interact via the weak or, if charged, the electromagnetic force. The quarks are heavier than the leptons, carry electromagnetic charge and are the only known particles of non-integer (-1/3 and 2/3) elementary charge. Just as the leptons, they can interact via the electromagnetic and weak forces, however in addition they carry the so called color charge (red, green or blue), which is mediated by the gluons and responsible for the strong interaction. The underlying theory to describe the related effects is QCD, which will be further discussed in the next section. The three generation of quarks are consisting of the up-down (ud), strange-charm (sc) and bottom-top (bt) quarks, listed by an increasing order according to their mass. The lightest quarks, u and d , make the normal nuclear matter, i.e. protons uud and neutrons udd . Since both quarks and gluons contain the color charged, they are often grouped together as partons. Further, in the standard model each particle has a corresponding anti-particle, which has the same mass, spin and lifetime, but all its other quantum numbers are a subject to inversion based on the charge, parity, and time reversal (CPT) symmetry. Details on the CPT are available in standard physics textbooks, such as [1]. The main consequence is

that the electric and color charges of the anti-particles are always opposite to their particle counterpart. This implies there are three additional color types (anti-red, anti-green and anti-blue).

For reasons that will become clear in the next section, the quarks cannot be observed alone, but have to be contained within bound states of no net color charge, called hadrons. A color charge neutrality can be achieved either by combining a color with its anti-color, or by combining all three colors together. For that reason, the basic hadrons are either composed of an quark-antiquark ($q\bar{q}$) pair, or of three quarks or antiquarks (qqq or $\bar{q}\bar{q}\bar{q}$). The former are called mesons, the latter baryons. All mesons are unstable, the two lightest ones and most abundant in collider experiments, are the pions (π) and kaons (K), where the pions consist only of u and d quarks, while the kaons have one strange quark. Their corresponding masses³ are c.a. $140 \text{ MeV}/c^2$ and $495 \text{ MeV}/c^2$. The only hadron that is considered stable, at least compared to the age of the universe, is the proton (p) baryon, that has a mass of $938 \text{ MeV}/c^2$. The neutron (n) is only slightly heavier ($939 \text{ MeV}/c^2$) and becomes stable when bound inside an atomic nucleus. The protons and neutrons are the only two baryons present in the “everyday” matter, and commonly referred to as nucleons (N). The baryons containing one s quark, in addition to the u and d , could be present in astrophysical objects such as neutron stars, and are called *hyperons* (Y). The lightest hyperon is $\Lambda = (uds)$, it is neutral in charge and decays weakly into a $N\pi$ pair with a lifetime of 7.89 cm. The strong interaction of these particles is the main physics focus of this work.

1.3 Quantum chromodynamics

The *QCD* is the underlying theory of the *strong interaction*, that is based on color exchange by the force mediators, the gluons. The quarks are the only elementary particles subject to the strong force. There are two very unique features of QCD, that make it a much more complicated, but also more interesting, theory compared to the electroweak force. First, the gluons themselves carry the color charge, in permutations of color-anticolor. This implies that the gluon can couple to itself, giving rise to the 2nd and 3rd Feynman diagrams shown in Fig. 1.2. The higher order Feynman

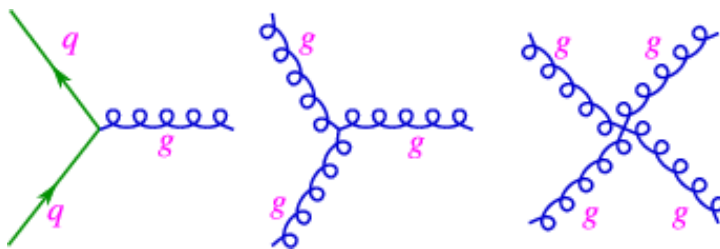


FIGURE 1.2: The basic QCD Feynman diagrams [3]. The rich nature of QCD is related to its unique feature of gluon self coupling (middle and right diagram).

diagrams involving multiple vertices and particle exchanges are typically irrelevant for the electroweak force, since they are suppressed by a factor of α^n , where α is the coupling constant and n is the order, i.e. number of vertices, of the interaction. The

³The units used in particle physics are called natural units, for which both the speed of light c and the Planck constant \hbar are considered dimensionless and equal to 1. To separate between energy, momentum and mass, it is common to add the corresponding factor of c or c^2 in the units.

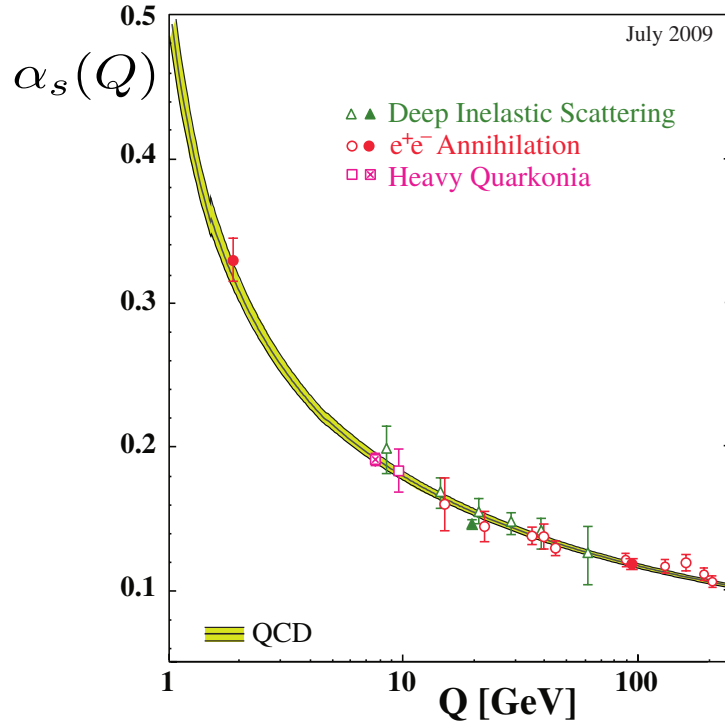


FIGURE 1.3: [4] The running coupling constant of QCD, compared to experimental constraints.

fine structure constant related to the electromagnetic interaction is $\approx 1/137$ and the corresponding α for the weak force is $\sim 10^{-17}$ to 10^{-16} , however for the strong interaction the corresponding “constant” has a very strong energy dependence, given by

$$\alpha_s(Q^2) = \frac{\alpha_s(\Lambda_{\text{QCD}}^2)}{1 + \beta_0 \alpha_s(\Lambda_{\text{QCD}}^2) \ln(Q^2/\Lambda_{\text{QCD}}^2)}, \quad (1.1)$$

with $\beta_0 = (11N_c - 2n_f)/(12\pi)$, where N_c is the number of colors and n_f the number of flavours (3 and 6 in the SM), Q is the momentum transfer (energy) of the interaction, and Λ_{QCD} is the QCD scale, which is around 200 MeV/c. The QCD coupling constant is plotted in Fig. 1.3. For low energy scatterings, or bound states such as hadrons, the coupling is close to 1, leading to an increased contribution of the higher-order vertices, making impossible the use perturbation theory to model the interaction. Moreover, in case two quarks start to separate spatially, the gluon self coupling leads to the creation of strong gluon fields between them, until it becomes energetically favorable to create a new $q\bar{q}$ pair. For that reason in the regime of large α_s (at low energies) the quarks cannot exist as single objects and have to be confined within hadrons. This feature of QCD is called *confinement*. Interestingly, quarks that are close together are almost non-interacting. This effect is called *asymptotic freedom*. At very large energies the coupling becomes weak, making possible to transition into a deconfined state of matter called *quark-gluon plasma* (QGP). Much is unknown about the QGP, although it is believed that it can be realized either at very high temperatures or net baryon densities. The corresponding QCD phase diagram is shown in the right panel of Fig. 1.4 and it postulates that the normal hadronic matter undergoes a phase transition to a deconfined state of quarks and gluons, which is supposedly a smooth crossover at low densities and high temperature, and of finite order at larger densities and smaller temperatures [5]. The former correspond to the conditions in the beginning of the Universe, and can be partially probed by high energy collider experiments, such as the Large Hadron Collider (LHC) and the Relativistic Heavy Ion Collider (RHIC). The large density and low temperature part

of the diagram corresponds to the matter in neutron stars, and low energy experiments, such as HADES, are able to test this axis of the phase diagram. Naturally, the conditions produced in the laboratory are still far from the related physics examples, but the qualitative direction on the energy-density axis is the same. At intermediate density and temperature a critical point separating the type of transition should exist and signs of it are actively searched experimentally, mostly by performing *beam energy scans* (BES) by making relatively short measurements and many different collision energies, e.g. at RHIC. In the future, the Compressed Baryonic Matter (CBM) experiment at the FAIR facility will perform similar measurements, but at lower energies and higher densities. The gray lines in Fig. 1.4 (right panel) correspond to

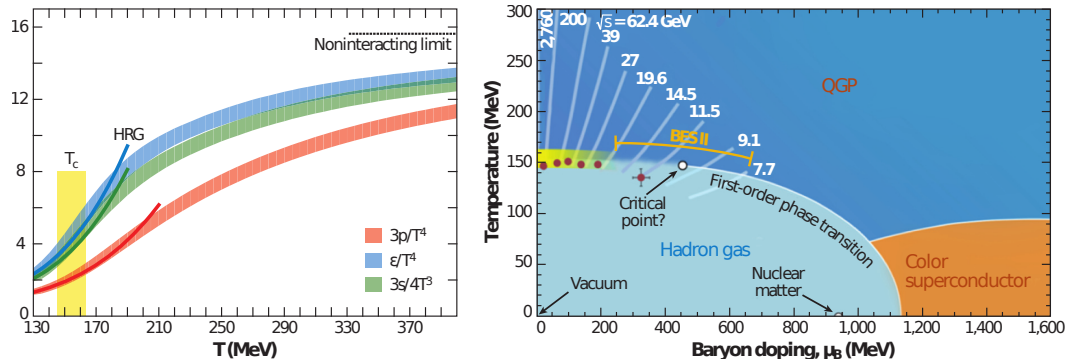


FIGURE 1.4: [5] The QCD phase diagram (right) and the lattice predictions on the energy density (ϵ) or entropy density (s) of hot QCD matter in thermal equilibrium at temperature T (left).

the different collision energies reached by the LHC and RHIC, the upper ends of the lines correspond to the maximum temperature that could be achieved, where the values marked as BES II are related to the second beam energy scan of RHIC, which is not yet finalized. Further, the left panel of Fig. 1.4 shows the predictions of numerical computations on the lattice of the energy density (or entropy, related to the number of degrees of freedom) as a function of the temperature at zero baryon potential, and there is a clearly predicted continuous crossover with critical temperature $T_c \sim 150$ MeV. The corresponding value of T_c is also present on the right panel as a yellow band and the red points are the existing fits of thermal models⁴ to the yields of produced particles in the collision at the time of the chemical freezeout⁵. While the two temperatures are not exactly the same, both are related to the point at which the matter is well described by the hadronic degrees of freedom. Hence the similarity of these values is considered as an evidence about the formation of a QGP in the earlier times of the evolution of the collision system (fireball). While a direct measurement confirming the creation of QGP at particle accelerators does not exist, there are further strong suggestions for this scenario. On the level of QCD, a strong hint is given by the jet-quenching effects. *Jets* are narrow cone-like structures of large transverse momentum consisting of multiple correlated hadrons, and their creation is explained by the confinement principle. In a simplistic picture, jets are the result of highly energetic $q\bar{q}$ pairs that start to separate until they split into two $q\bar{q}$ pairs, which behave in the same way causing an avalanche process until the energy

⁴Prediction on the amount of produced particles (yield) considering a thermal bath, where the system is defined by its temperature and chemical potential, while the abundance of each particle species depends on its mass.

⁵The point at which all inelastic scattering has stopped, hence the final composition of the produced particles is fixed.

of the individual quarks is low enough to form hadrons. However, if the process happens inside the QGP, the quarks loose a lot of energy through their interaction with the medium, which changes significantly the kinematic properties of the jets. This effect can be studied by means of the nuclear modification factor R_{AA} , which quantifies the change of the jet properties in heavy-ion (HI) compared to pp collisions, leading to observations compatible with theoretical predictions on the QGP. Further evidence in favour of the QGP creation in HI collisions is provided by the successful use of hydrodynamics to model the evolution of the fireball, as it predicts the collective expansion of the system and the resulting correlations (flow) of the produced particles.

For a long time the discussion of QGP and hydrodynamics concentrated only on heavy ion collisions, but in recent years there have been many measurements in smaller collisions systems, p-Pb and even pp, that had shown effects that can be modeled by hydrodynamics and thermal considerations, something that has been so far attributed to the QGP formation. This has stirred a lot of interest, as it could mean that either small droplets of QGP can be created even in pp collisions, or that there is another underlying mechanism that mimics, or causes, the effects seen in HI collisions. While these questions are not answered yet, there is one useful related feature that will be exploited in the present work. Generally, it is expected that the relative amount of produced baryons containing strange quarks is much lower in pp collisions compared to Pb-Pb, however a study at the LHC, performed by the ALICE collaboration, reviled that high-multiplicity (HM) pp collisions lead to a significant increase in the yields of the strange particles, which eventually smoothly transitions towards the values measured in Pb-Pb (Fig. 1.5). This property is essential for correlation studies, as it results in a big increase of the two particle pair statistics, if a dedicated trigger⁶ is used to select only HM events.

Ultimately, the goal of the present work is to study the hadron-hadron interaction and compare the results to theoretical predictions. The corresponding theories are based on the Lagrangian formalism, and exploit the symmetries of the interaction to reduce the amount of free parameters. The starting point is to use the quarks and gluons as degrees of freedom, using a non-Abelian SU(3) gauge theory that is extended to $SU(3) \times SU(2) \times U(1)$ in order to account for the weak and electromagnetic forces. The use of SU(3) implies that only 3 quarks are considered, namely u , d and s . The definition of the Lagrangian is

$$\mathcal{L} = \bar{\psi} (i\gamma^\mu - D_\mu - m) \psi - \frac{1}{4} G_{\mu\nu}^a G_a^{\mu\nu}, \quad (1.2)$$

where ψ represents the quark spinor field. The bare quarks masses, related to the Higgs mechanism, are included in the matrix m . The gauge derivative $D_\mu = \partial_\mu - ig\mathcal{A}_\mu^a \lambda_a$ is related to the quark propagation and the corresponding coupling to gluons, where λ_a are the Gell-Mann matrices responsible for the color charge upon interaction with a gluon, \mathcal{A}_μ^a are the 8 existing gluon fields with the color index a and $g = \sqrt{4\pi\alpha_s}$ is related to the QCD coupling constant. The second term in Eq. 1.2 is the unique QCD feature of gluon self-coupling, and given by $G_{\mu\nu}^a = \partial_\mu \mathcal{A}_\mu^a - \partial_\nu \mathcal{A}_\mu^a - g_s f^{abc} \mathcal{A}_\mu^b \mathcal{A}_\nu^c$, where f^{abc} are the structure constants of the

⁶The trigger is used during the data taking process, and it is the condition upon which the read-out of the detector activates to record the current collision. Since only a small fraction of all physical collisions can be saved, the trigger is used to bias the sample towards a desired physics case.

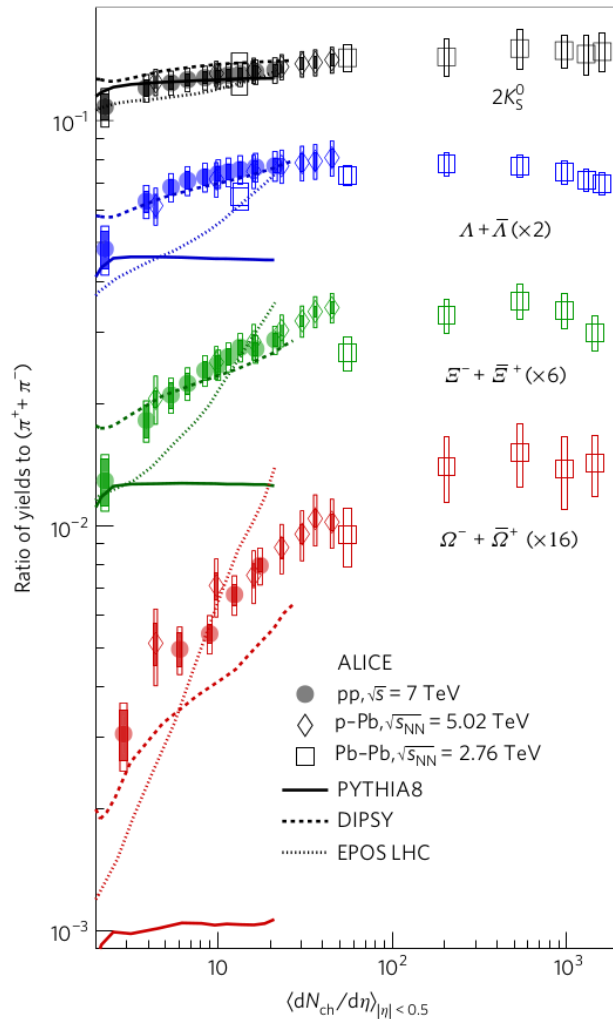


FIGURE 1.5: [6] Strangeness enhancement as a function of the multiplicity as measured by ALICE. It suggests that high-multiplicity triggered pp events can provide a lot of pair statistics for correlation studies involving strange baryons. The lines represent different models, none of which can reproduce the data.

SU(3) group. Due to the large coupling constant at low energies, the QCD Lagrangian cannot be solved analytically using perturbation theory. The approach to this issue is discussed in the next section.

1.4 Baryon–baryon interaction and neutron stars

1.4.1 Overview

The main topic of this thesis relates to the strong interaction between baryons, hyperons in particular. The fundamental theory is QCD, but applying it to study the interaction between hadrons is highly non-trivial, mostly due to the confinement principle governed by non-perturbative effects. The problem is approached by two main generic methods, first is the development of approximate effective perturbative theories, the second is the numerical solution to the non-perturbative problem. Both have their strengths and limitations, as at will become evident in the course of this section. However, let us for now put into context what is it that we would like to learn from these theories. The ultimate goal is to unravel the mysteries of QCD and the history of the Universe, but this is a rather ambitious and at present more of a philosophical problem. In practical terms, there are many intermediate milestones to reach before gaining enough knowledge to address the latter issue by physics, and perhaps one of the most important steps is to find the glue between the scales of sub-atomic and astrophysics. A good place to start is to study the *neutron stars* (NS), as they are the densest known type of stellar object in our Universe, typically having 1-2 solar masses (M_{\odot}) and measuring only ~ 20 km in diameter, which is often compared to having our Sun packed up in a Manhattan sized sphere. The corresponding mean density is larger than the one of the atomic nucleus ($3 \times 10^{17} \text{ kg/m}^{-3}$ or $\rho_0 = 0.17 \text{ fm}^{-3}$ in natural units), where the maximum density reached is still heavily disputed, but it could be as high as $5\rho_0$. Thus, the properties of NSs are driven by the multi-body hadronic interactions inside of their interior, and if the density of their core is high enough a phase-space transition and a deconfinement to quarks is not excluded (Fig. 1.4). For these reasons the study of neutron stars is related to hadron physics, QCD and astrophysics. In the present work, the main result related to neutron stars is the study of the p– Λ interaction, presented in chapter 6. In the next section the main aspects of the baryon–baryon interactions will be discussed, while in section 1.4.3 their application to the study of neutron stars will become evident.

1.4.2 Baryon–baryon interaction

The baryon–baryon interaction is quite well known for the nucleons, as they are the constituents of the stable matter and accessible for experiments. Traditionally, scattering data have been used to determine the properties of the interaction, e.g. by applying partial wave analysis on the available database of measured cross sections in different channels, leading to very accurate determination of the interaction. The results are often interpreted without going into the details of the QCD, by constructing effective potentials that use mesons as effective force mediators (e.g. the Yukawa potential) and/or additional phenomenological terms, such as a strong repulsive core at low distances. One of the advanced and commonly used potentials is the Argonne $v18$ [7], that contains 18 different operators related to the quantum numbers of the particles, such as spin and isospin, and their couplings. The large amount of operators is demanded by the high precision of the data, pushing the sensitivity

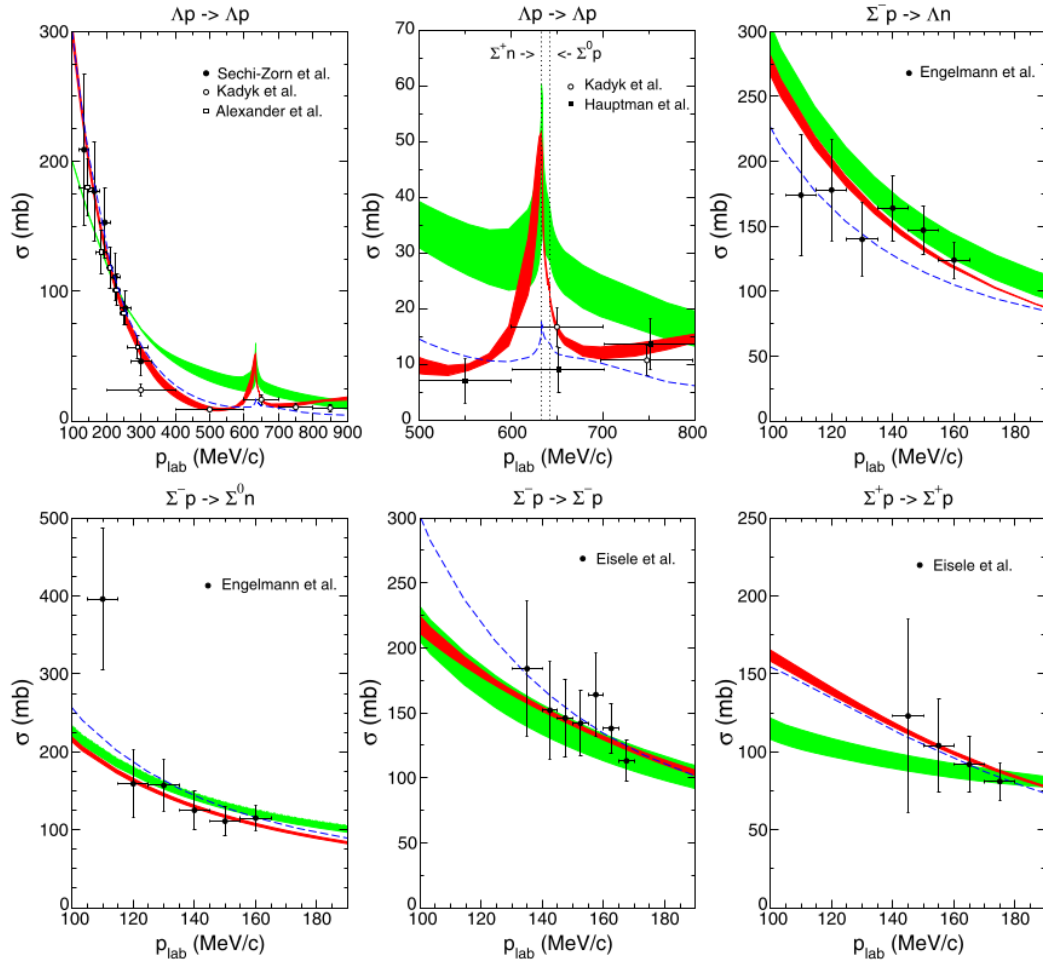


FIGURE 1.6: [8] Experimental and theoretical cross section of the $\text{N}\Sigma \leftrightarrow \text{N}\Lambda$ system. The different panels correspond to different channels of the coupled system. The genuine $p\Lambda$ interaction is shown in the first panel. The bands correspond to the chiral effective field theory calculations, performed at leading order (green) and next-to-leading order (NLO13).

down to very small effects. Further, the huge variety of stable elements and their associated isotops is reflected in advanced effective theories to model the multi body nucleon interaction, making possible to constrain the pure nucleonic equation of state not only in vacuum, but at ρ_0 as well.

Nevertheless, the situation is vastly different for any non-nucleonic baryons, as they are unstable, far more difficult to produce in large amounts, and for all practical purposes impossible to contain within an accelerator beam to perform scattering experiments. In fact, the only existing scattering data on hyperons is in the strangeness $S = 1$ sector, and the best constrained single system is the $p\Lambda$, for which a total of 36 data points exist. They provide a limited precision corresponding to momenta only above $p_{\text{lab}} = 130 \text{ MeV}/c$ (Fig. 1.6) [8]. The other available experimental constraints are based on the study of *hyperm nuclei*, in which one or two of the nucleons inside the nucleus are substituted by a hyperon [9–13]. These studies are strongly biased by the *three-body interaction*, hence they cannot be directly used to constrain the 2-body force, but are nevertheless the most valuable input for any theoretical models

that extend into the 3-body sector. Further, these experiments can discriminate between different spin states, which is fundamental for a deeper understanding of the interaction. The largest amount of hypernuclei data is for the Λ hyperon, and only a single double Λ hypernuclei exists, that allows to study the hyperon–hyperon interaction [14]. There is also just a single event for a Ξ hypernucleus [15]. For these reasons, the only hyperon system with a somewhat well understood interaction is $p\Lambda$ ⁷, while the experimental knowledge on any other nucleon–hyperon or hyperon–hyperon system was limited to qualitative hints.

The study of the strong interaction by the fundamental principles of QCD is possible by performing numerical simulations on a *lattice* [16]. The associated methods are still under development, and limited by the capabilities of the available hardware for super-computing. The main issue of this approach is that the computation becomes more expensive for low masses of the quarks, hence the simulations have been mostly performed for non-physical values of the quarks and correspondingly of all hadrons. This is less of an issue in the investigation of heavy particles, thus the lattice calculations have the interesting property of being accurate for systems of large mass, such as containing hadrons with strange quarks, and fail to perform in the light hadronic sector, most prominently for the basic nucleon–nucleon interaction. This is in complete contrast to the experimental situation, thus it is very difficult to validate the lattice approach. For that reason, it is important to push the experimental measurements into the multi-strangeness sector, where correlation techniques can play an important role, as they can be used to study any particle species produced and detected at an accelerator facility, as long as the production is abundant.

An alternative approach of studying the hadron–hadron interaction is the use of effective theories, such as *chiral effective field theory* (χ EFT) [8]. The main idea is to reduce the degrees of freedom by using the pions as force mediators between the hadrons, instead of quarks and gluons. Nevertheless, the known symmetries of the QCD Lagrangian are kept, thus all known particle species based on the quark model are still reproduced. The underlying symmetry of $SU(3)$ implies the consideration of the up, down and strange quarks only, ignoring their mass differences. This effect is referred to as an approximate flavour symmetry of the quarks. The χ EFT is perturbative, and it has been expanded to leading and next-to-leading order processes (LO and NLO) in the strangeness $S = -1$ sector, corresponding to the $p\Lambda$ interaction. The theory has been fitted to all available scattering data, with additional constraints based on the hypernuclei results.

Both the lattice and chiral calculations are performed by default for a 2-body interaction in vacuum, nevertheless the theories can be extrapolated to higher densities using an approach such as the iterative G-matrix procedure, in which the many body interaction is approximated with the superposition of multiple 2-body interactions [17]. This is important for drawing any conclusions on the neutron stars. Another property of the strong force at the hadrons level is the presence of *coupled channels*. This happens when two systems of identical quark content have differences in their quantum numbers, such as the isospin. In that case the wave functions, at the quark level, are symmetrized differently, leading to bound states of similar but non-identical masses and different decay modes. For example, both the

⁷In chapter 6 it will be shown, that using correlation techniques can improve our knowledge on that system and its related coupled channels.

Λ (isospin 0) and Σ^0 (isospin 1) are a configuration of uds quarks, but the Λ decays into a proton and a pion, while the Σ^0 decays into a Λ and a photon. The masses of the particles are $M_\Lambda = 1116 \text{ MeV}/c^2$ and $M_{\Sigma^0} = 1193 \text{ MeV}/c^2$. Consequently, a pair of $p\Lambda$ is coupled to $p\Sigma^0$, and in fact to $n\Sigma^+$, as all pairs have $uuudds$ quark content. The interaction between these pairs is strongly entangled and a precise description dictates the simultaneous correlated study of all systems. For the lightest pair, $p\Lambda$ in this example, the interaction below the threshold energy, at which the mass difference to $N\Sigma$ is compensated, is governed by a pure one channel dynamics. However, at the threshold there is a sudden change in the behaviour of the wave function and the corresponding phase shift, which is typically projected onto the cross section as a sharp cusp structure. While the direct observation has not been achieved by scattering data (Fig. 1.6), a high precision experimental study of the interaction will be able to resolve such structures (chapter 6), thus it is important that the theory includes coupling effects. For the χ EFT this is the case, as symmetry breaking effects are included in the formalism. For the lattice calculations they are often excluded in favour of gaining more statistics for the individual pure channels.

To gain deeper understanding of the behaviour of particles inside a dense medium, the genuine 3-body force has to be modeled in addition to the superposition of 2-body effects. This is still impossible to achieve on the lattice, nevertheless the χ EFT can approximate it by including a heavy excited baryonic state, such as the Δ resonance, as an effective mediator of the strong force. This allows for at least a qualitative understanding of the effects related to the Λ NN contact term [17].

1.4.3 Neutron stars and the equation of state

The stability of the neutron stars results from the counter-balance between the enormous gravitational pull and the inner fermion pressure exerted by the constituent hadrons, and/or quarks in case of deconfinement. The description is given by the Tolman-Oppenheimer-Volkoff (TOV) equation

$$\frac{dP}{dr} = -\frac{GM(r)}{r^2}\rho(P) \left[1 + \frac{P(r)}{\rho(P)c^2}\right] \left[1 + \frac{4\pi r^3 P(r)}{M(r)c^2}\right] \left[1 - \frac{2GM(r)}{rc^2}\right]^{-1}, \quad (1.3)$$

where r is a radial coordinate, $\rho(P)$ is the density relation to the pressure $P(r)$, $M(r)$ is the mass contained within a spherical volume of radius r , G is the gravitational constant and c is the speed of light. The TOV relation assumes that the object in question is spherical, and that the gravitational force is entirely counterbalanced by the internal pressure. This equation can be further corrected for objects with a large spinning frequency, which are deformed and subject to relativistic effects. Practically, the TOV formula can be used to obtain the mass–radius $m(R)$ relation for a neutron star. The only unknown is the connection between density and pressure $\rho(P)$, that is the nuclear Equation of State (EoS). The EoS is a prime subject of theoretical interest, as it is the ultimate macroscopic (effective) representation of nuclear matter. Naturally, the only way to obtain the fully accurate EoS is by understanding the microscopic properties of the strong interaction. On the other end of the scale, the astrophysical observations are mostly related to mass measurements of NSs and mergers observed by means of gravitational waves [18]. These provide further observables which are linked to the EoS and can be used to test its accuracy, nevertheless the results cannot be used as a direct input to infer the true solution. This is the main reason why the study of the interaction between the constituent particles is so crucial for a physics

motivated derivation of the EoS.

Concentrating on the hadron–hadron interaction, the starting point is the limit at $\rho \rightarrow 0$ (vacuum), which is microscopically governed by two particle interactions. As the density increases, the many body forces start to play a substantial role, leading to an effective in-medium potential $U(\rho)$ acting on the single particles. It is common to use the language of an effective mass of the particle inside the medium $m_{\text{eff}}(m, \rho)$, implying that it behaves as a free particle of a mass m_{eff} . This is relevant for the composition of the neutron star, as it influences the chemical potential μ for each present particle species X

$$\mu^{(X)}(\rho) = E_F^{(X)}(\rho) + m_{\text{eff}}^{(X)}(\rho), \quad (1.4)$$

where the Fermi energy $E_{F,X}$ is relevant for fermions (baryons). The particles formed inside the neutron stars are those of lowest chemical potential. The internal pressure of the NS is the sum of the Fermi energies of all constituents

$$P(\rho) = \sum_X E_{F,X}(\rho). \quad (1.5)$$

This is a very simple relation, however it has a property that makes its evaluation quite challenging. Namely, the individual terms $E_{F,X}(\rho)$ are *not* independent, as they are linked by the condition of creating the particle species of lowest $\mu^{(X)}(\rho)$. This implies that a stable configuration is obtained when all present species have equal chemical potentials. However, while the Fermi energy is trivial to evaluate, the effective mass inside Eq. 1.4 depends on the interaction between the particles, modeled by the effective in-medium potential $U(\rho)$. Hence, to obtain the mass–radius relation of a neutron star, the multi body nuclear forces acting between the individual particles have to be known in order to evaluate the corresponding chemical potentials and composition of the NS. Figure 1.7 shows an example of several different equations of state, based on quantum Monte-Carlo simulations, which consider either a pure neutron structure of the NS (green), or allow the inclusion of the Λ hyperon [19]. The red curve considers only the 2-body interaction, and the inlet of

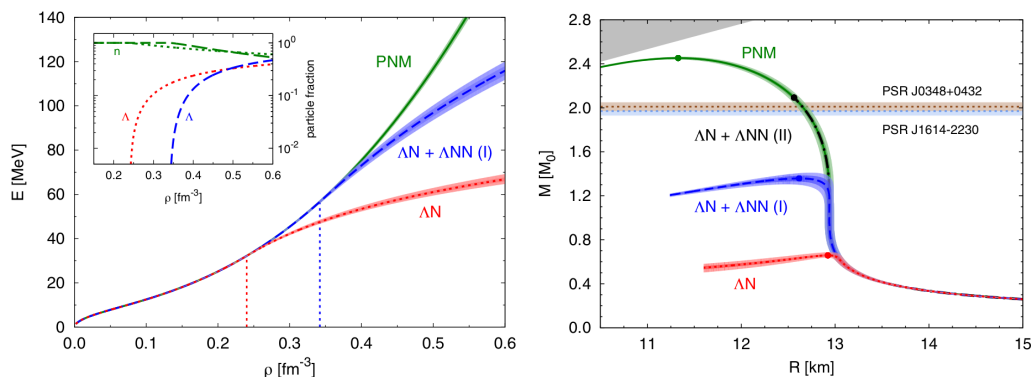


FIGURE 1.7: [19] Nuclear equation of state. The green line is a pure neutron matter case, the red line includes Λ s considering only the 2-body $N\Lambda$ interaction and the blue line accounts for the 3-body force in addition. The latter is constrained by hypernuclei data. The black dashed line extends the repulsiveness of the 3-body force to unphysical values. The left panel shows the EoS, the right panel the corresponding mass–radius relation for NSs.

the plot shows that the Λ s are expected to be present in significant amount already at

$\rho = 2\rho_0$, a density certainly expected to be reached within the NS. The corresponding energy–density relation shows that the presence of hyperons leads to a *softer* EoS, meaning that it is more easy to compress the matter as the internal pressure of the NS will be lower. If the TOV equation 1.3 is applied, the resulting mass–radius relation demonstrates that the soft EoS is incapable of explaining the existence of massive neutron stars ($M > 2M_\odot$), that are known to exist (right panel of Fig. 1.7). This paradox is known as the *hyperon puzzle*, i.e. the interaction of the hyperons suggests that it is attractive and thus these particles have to be present inside neutrons stars, nevertheless this is in conflict with the existing mass measurements. This puzzle is not yet answered, but there are multiple suggestions on the underlying physics involved. For example, Fig. 1.7 presents two additional EoS (blue and black lines), that include both the 2-body interaction and a repulsive genuine 3-body term. For the blue line the repulsion is fine tuned to be consistent with measurements of hypernuclei, and while the resulting EoS becomes slightly stiffer, it is still not capable of predicting a $2M_\odot$ neutron star. On the other hand, making the 3-body interaction unrealistically strong makes the presence of Λ hyperons energetically unfavorable, restoring the case of pure neutron matter. The message is that the 3-body interaction could be a piece of the puzzle, but according to this model it is not enough to explain it. Similar qualitative behaviour is confirmed by the χ EFT, as including the approximate genuine 3-body force predicts a stiffer equation of state compared to pure 2-body interaction [20]. The quantitative results are shown in Fig. 1.8, where the the chemical potential is plotted as a function of the density. The faded orange band

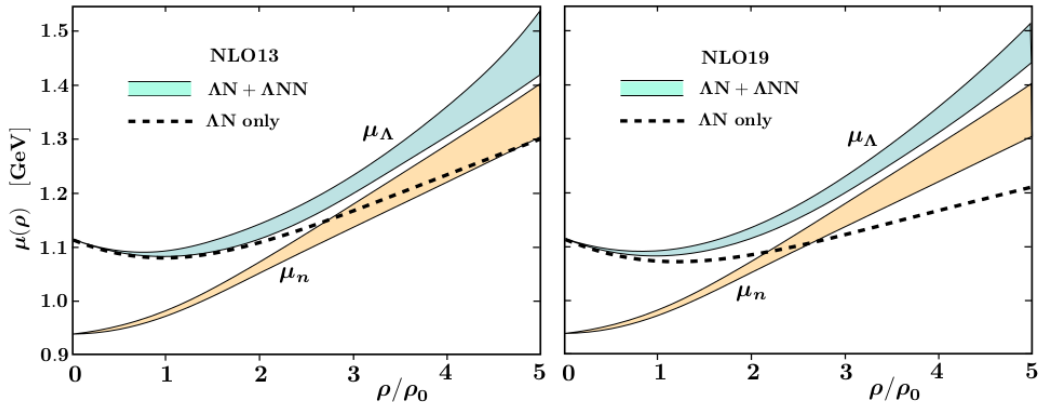


FIGURE 1.8: [20] Nuclear equation of state in the presence of hyperons from χ EFT. As long as the Λ chemical potential μ_Λ remains above the neutron one, the presence of Λ particles inside the NS is not possible.

corresponds to the chemical potential of the neutrons, the dashed line is the chemical potential for Λ s assuming only 2-body interaction and the cyan band includes both the 2 and 3-body effects. The left and right panels correspond to two slightly different parameterizations of the NLO calculation, where NLO13 is the original result from 2013 [8], and NLO19 has been obtained by weakening the coupling to the $N\Sigma$ channel [21]. The resulting differences in the interaction are rather subtle, where in vacuum and at low energies the 2-body attraction of NLO19 is slightly reduced, although in medium there is a stronger binding to the nucleons, leading to a softer EoS and a large overprediction of the binding energies of the hypernuclei measurements. Nevertheless, if the 3-body interaction is included, the related fit parameters are driven by the requirement of describing the hypernuclei and lead to a substantial repulsion in the 3-body sector, that results in a chemical potential consistently

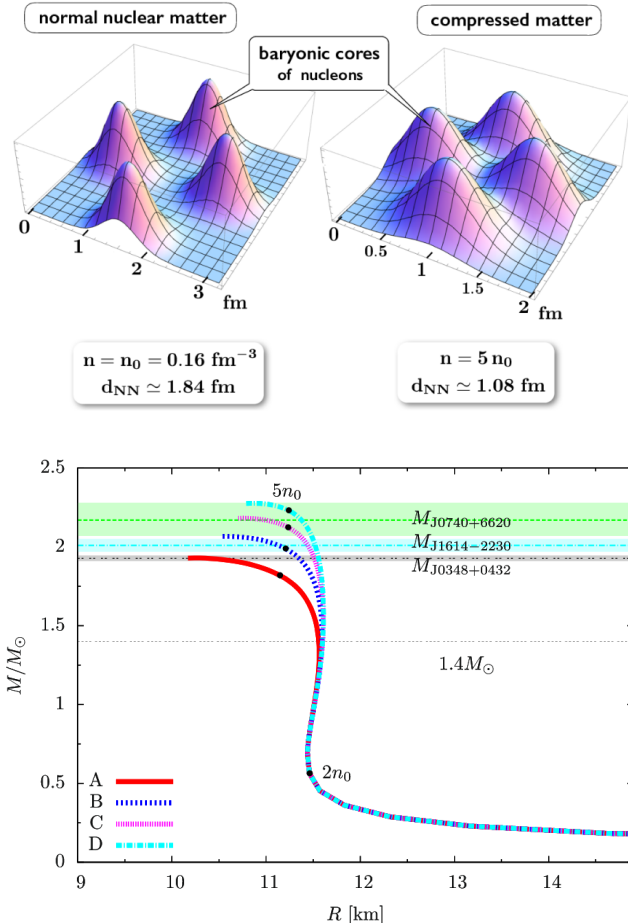


FIGURE 1.9: [22] Hadronic wave functions in dense matter. The left panel corresponds to normal nuclear matter density (ρ_0) and the right panel is at $5\rho_0$. In the case of the latter the wave functions overlap significantly and it is unclear of the hadronic degrees of freedom are still a valid assumption.

FIGURE 1.10: [23] Hybrid quark-hadron EoS (QHC19). The different lines correspond to different parameterizations, it is clearly possible to find a suitable set of parameters to describe all observed mass measurements of NSs.

larger for Λ s compared to neutrons. This is observed for both NLO13 and NLO19, although the latter produces a systematically stiffer EoS. This scenario prohibits the creation of hyperons inside the NS and answers the hyperon puzzle. An important caveat is that the accuracy of the approximate Δ contact term used to model the 3-body interaction has not yet been confirmed, hence the conclusions are highly model dependent and certainly not final. The issue could be addressed by more accurate experimental estimation of the genuine 3-body Λ NN force.

Another explanation to the hyperon puzzle is that the deconfinement phase (Fig. 1.4) is reached at densities lower than the threshold of hyperon production. This would imply that the hadronic wave functions significantly overlap and cannot exist as separate objects (Fig. 1.9). Consequently, the NS transforms into a quark star, that has a very different EoS, and the corresponding theoretical predictions have no problems of explaining NS masses of above $2M_\odot$. Further, there are theories attempting to implement a smooth crossover from hadronic to quark matter, such as the QHC19 model [23]. The corresponding EoS can explain the massive neutron stars (Fig. 1.10), however these types of calculations are highly speculative and need to be further refined.

In summary, obtaining a solid equation of state and the study of neutron stars are two entangled subjects, that can be approached from two perspectives. From astrophysical point of view, the mass measurements and neutron star mergers can be used to set empirical limits on the allowed properties of the EoS. However, the fundamental physics processes can only be understood by hadron physics and/or

QCD. The latter is certainly the more fundamental theory, but it is handicapped by the non-perturbative nature at low energies, while the numerical methods are very far from being capable of testing in-medium effects. Consequently, the practical approach is to concentrate on effective theories, where the χ EFT is the state of the art. However, at the moment it is capable of providing multiple parameter sets corresponding to different physical characteristics, that are all compatible with the measurements. The goal of this work is to address this issue by providing further constraints for the 2-body sector by means of correlation studies. In the next few years it is expected to extend these techniques to the 3-body problem, and further decrease the uncertainties related to 2-body interaction.

1.5 Femtoscopy

1.5.1 A chronological overview

The way to non-traditional femtoscopy in small collision systems

Femtoscopy is a technique, that relates momentum correlations between particles to the their emission region and final state interaction (FSI). The theoretical formalism for two particle correlations, which is the scope of this work, is well developed and will be summarized in this chapter. An extensive overview, with a focus on heavy-ion collisions, is provided by the work of M. Lisa, S. Pratt, R. Soltz and U. Wiedemann [24].

Historically, femtoscopy has its roots in astronomy, in particular the “*Hanbury Brown and Twiss effect*” (HBT) discovered in the late 1950’s [25, 26]. The original idea was to use the intensity fluctuations of stellar objects and relate those to the size of the light emitting source. This was made possible by splitting the light signal and directing it to two detectors, each performing an independent measurement of the intensity (I). Assuming a coherent time of emission, any correlations between the two measured intensities can be related to the spacial distribution of the emitting source. This method can be applied either to determine the size of a single star, or the spacial distribution of cluster of stars. In both cases the measured correlation function is

$$C(\vec{d}) = \frac{\langle I_1 I_2 \rangle}{\langle I_1 \rangle \langle I_2 \rangle} = 1 + \left| \int \rho(\vec{r}) e^{i(\vec{k}_1 - \vec{k}_2) \cdot \vec{r}} d^3 r \right|^2, \quad (1.6)$$

where I_i are the intensities measured by each detector, \vec{d} is the separation between the two detectors, \vec{k}_i are the wavevectors related to the incident photons in each detector and $\rho(\vec{r})$ the spacial distribution of the points of emission. A compact overview of the original HBT principle is provided in [27].

At the other end of the scale, the development of particle accelerators lead to an increasing complexity of the colliding systems in which many particles were produced, pions in particular due to their small mass. This posed many question about the description of the system on a femtometer scale, for example the spacial-temporal characteristics of the particle production. The mathematical formalism of the HBT effect could easily be adopted from the cosmological to the subatomic level, creating a whole new field called *femtoscopy*. In this formalism, an interference occurs due to the final state interaction (wave function) of the emitted particles, which depends on the energy (momentum). The intensity in the original HBT is replaced

by the measured yield of particles at a given momentum, while the spacial distribution $\rho(\vec{r})$ is represented by the location at which the final state interaction started to act, i.e. the spacial position of hadron formation (hadronization). This region is described as an effective *emission source* or a *source function* $S(\vec{r})$. The first experimental HBT analysis applied to hadrons dates as early as 1960, when Goldhaber et al. observed a deviation of the π - π correlations, measured in proton-antiproton annihilation processes, compared to the expectation based on the Fermi statistical model [28]. It was correctly suggested, that these effects are related to the Bose-Einstein statistics of identical bosons. The use of pion correlations to study the collision system became a standard technique in the 1970's, e.g. as can be judged by the title "Determination of the Fireball Dimensions from Second Order Interference Between Two-Pions" of a study performed at CERN [29], which spurred the development of the corresponding theoretical description [30, 31]. The theoreticians went a step further, and investigated how these type of correlation studies are influenced by the final state interaction, on one hand due to the Coulomb force, relevant for pions, but also by the strong force that becomes important for studying kaons and protons. The pioneers of the emerging theories were Richard Lednický, Vladimir Lyuboshitz and Mikhail Podgoretsky [32, 33]. Their work lead to the Lednický-Lyuboshitz model, which provides an effective description of the correlation function due to the strong interaction, using the effective range expansion as an approximate way to model the wave function. Further details are provided in section 1.5.4.

After the late 1970's and early 1980's, for a large period of time the experimental data could not reach the desired precision to challenge the theoretical advances done by Lednický, Lyuboshitz and Podgoretsky. The *renaissance* emerged in the early 2000's, when the Relativistic Heavy Ion Collider at the Brookhaven National Laboratory became operational. The main motivation of RHIC was to study the evolution of the dense system created in heavy-ion collisions, searching for signs of quark-gluon plasma formation. This was primarily achieved by studying collective flow effects, where the correlation studies are performed not on pairs, but on all charged particles detected in an event. The claimed discovery of the QGP was a great success, accompanied by the surprise that it can be theoretically treated as a "perfect liquid" and modeled by hydrodynamics [34, 35]. Nevertheless, it was suggested that two-particle correlation studies, which became trendy to be referred to as femtoscopy, provide a complementary way of testing model predictions by looking at parameters related to the emission source. The reason was that the presence of collective effects were expected to cause different modulation of the source depending on the relative orientation to the beam, providing further tests and constraints for the hydrodynamical picture. This topic has been summarized by Lisa, Pratt, Soltz and Wiedemann in [24]. The main observable has been the correlation function C related to the two-particle relative momentum ($q^* = 2k^*$) evaluated in the pair rest frame. Further details are available in section 1.5, nevertheless let us point out that the most important and commonly used relation in femtoscopy is

$$C(k^*) = \frac{\mathcal{P}(p_1^*, p_2^*)}{\mathcal{P}(p_1^*)\mathcal{P}(p_2^*)} = 1 + \int S(\vec{r}^*) \left[\left| \Psi(\vec{k}^*, \vec{r}^*) \right|^2 - 1 \right] d^3r^*, \quad (1.7)$$

where $\mathcal{P}(p_1^*, p_2^*)$ is the probability of the simultaneous detection of two particles with momenta p_1^* and p_2^* evaluated in their center of mass, leading to $p_1^* = p_2^* = k^*$, $\mathcal{P}(p_{1,2}^*)$ are the single particle emission probabilities and $S(\vec{r}^*)$ is the probability of

emitting two particles at a distance \vec{r}^* from one another. Note that Eq. 1.7 is essentially identical to Eq. 1.6, where both $\rho(\vec{r})$ and $S(\vec{r}^*)$ model the spacial distributions of the investigated source, and the other terms in the integral are related to a wave interference, which in the femtoscopic case is represented by the wave function of the relative motion of the particle pair $\Psi(\vec{k}^*, \vec{r}^*)$. The femtoscopy (HBT) method has been successfully applied to heavy-ion collisions, with many attempts to evolve the analysis techniques such that not only the spacial, but also the temporal properties of the emission are investigated, to obtain a more unique information compared to the standard flow techniques. The main subject of these studies were pion correlations, as the absence of strong interaction between them allows to model the interference term (wave function) in Eq. 1.7 by the simple rule of symmetrization of identical particles (given by an exponent) and correcting for Coulomb effects, leading to a very strong sensitivity on $S(\vec{r}^*)$. In addition, two particle correlation studies performed as a function of the opening angles between the particles can be used to understand the kinematics of the emission, which is strongly effected by the production of jets and the subsequent jet-quenching. The femtoscopic results confirmed the existing interpretations of the RHIC data, as the differential dependence of the source size on observables such as the transverse mass of the pairs could be described by hydrodynamics. However, in my personal opinion, given all available techniques to study the QGP formation, the femtoscopy technique provided the least amount of direct constraints to the theory, and mostly served as a consistency cross-check. Thus it can be claimed that femtoscopy worked too good both experimentally and theoretically, without providing any interesting “mystery to solve”, and perhaps for that very reason it slowly went out of favour.

The STAR collaboration attempted to revive femtoscopy by inverting the paradigm to study the final state interaction, governed by the wave function, as opposed to the emission source. This workflow is commonly referred to as *non-traditional femtoscopy*⁸. The most interesting related analysis by STAR was on Λ - Λ correlations [36], however there was no reliable way of constraining the source function or the residual correlations⁹ present in their measurement, leaving too many free parameters to be determined by a single fit to $C(k^*)$. This lead to an unexpected and controversial conclusion of a repulsive interaction, which was not predicted by any theory. The issue was resolved by a later re-analysis of the data, showing that a different assumption on the residual correlations leads to the complete opposite result of a mild attraction, which could be explained theoretically [37]. These instabilities of the method needed to be addressed, if any interesting physics conclusions were to be extracted by femtoscopy, requiring big improvements on the analysis side. Indeed the situation changed in the late 2010’s, with the *femtoscopy industrial revolution*. This happened as a result of the motivation of my supervisor, Prof. Laura Fabbietti, to search for alternative techniques to study the strong final state interaction between hadrons. This was required, due to the long standing issue in hadron physics of very poor experimental constraints for the 2-particle interaction of systems involving strange quarks. The vision of Laura was the usage of non-traditional

⁸Recently many major collaborations, including ALICE, labeled the non-traditional femtoscopy as “slang”, and advise the use of the term *study of the strong interaction via correlation techniques*. Personally, I have become attached to the original terminology and will be consistently using it in this work.

⁹An important source of contamination based on the decay of heavier particles into Λ s. Will be discussed in details later in the thesis.

femtoscopy at the LHC, applied to small collision systems in order to get better handle on the source function. The idea was that in these systems the emission of particles, baryons in particular, is mostly driven by high-energy (hard) scatterings of the constituent quarks and gluons of the colliding beams, and not influenced by in-medium effects within the speculated QGP present in heavy-ion reactions. The hard scatterings are subject to the rules of QCD, which has an approximate flavour symmetry implying similarity in the formation of hadrons independent on their quark content. In other words, the time and position of the hadron formation (emission) is expected to be alike for all species. If this is proven valid, a pair of particles with a known interaction, such as $p-p$, can be used to determine the properties of the emission source common for all baryon–baryon pairs. In term, this allows to study the final state interaction in systems with unknown or poorly constrained interaction potential, e.g. $p-\Lambda$ and $\Lambda-\Lambda$. Laura’s first PhD student to work on femtoscopy, Oliver Arnold, proved this concept in a pioneering analysis performed within the ALICE collaboration on data from the first period of LHC operation (RUN1) [38]. The analysed data sample was from pp collisions at 7 TeV, which had only limited statistics to perform baryon–baryon correlation studies and was insufficient to test the strong interaction to the desired precision. Nevertheless, the proof of concept was there, and in addition Oliver developed methods to fix the residual correlations in an independent data-driven way, paving the way for future precision studies. Indeed during the RUN2 of the LHC an enhanced statistical significance was achieved, and the purpose of this work is to continue the development of the ideas presented above, by studying the limits of their applicability, extending them in order to fit the requirements set by the increased precision and applying them to various baryon–baryon systems. This was a very broad project, thus it was distributed among 3 PhD students: myself, Andreas Mathis and Bernhard Hohlweger. Our work is very much entangled and it is impossible to present the global picture by discussing only my own contribution, nevertheless throughout the thesis I have attempted to emphasise clearly which part is my work, which was a team effort and which was the work of others.

The study of the strong interaction using correlation techniques turned into a story of great success, as it lead to 8 articles within 3 years, one of them in *Nature*, 2 in *PRL* and 3 in *PLB* [38–45], with another publication on $p-\Lambda$ interaction in the pipeline. In this thesis the main steps along the ladder of the recent reemergence of femtoscopy will be presented, alongside with their exciting future applications.

The role of this work

The present works aims at providing information on all achieved milestones, which ultimately allowed to perform data analyses on an “industrial scale”. Such a big project requires a unified analysis framework, capable of reconstructing the two-particle correlation functions experimentally, and provide the opportunity to test theoretical models. The former was the focus of Andreas and Bernhard, resulting in the FemtoDream package integrated into the global ALICE analysis framework, while the latter was my task, resulting in the creation of the “Correlation Analysis Tool using the Schrödinger equation” (CATS) [39]. The CATS framework will be introduced in chapter 2, in summary it is capable of combining the wave-function corresponding to the interaction with the emission source function. The tool is modular in nature, allowing the user large flexibility on the definition of the source function and interaction. The latter is either evaluated from a local real potential, by solving

the radial Schrödinger equation, or alternatively the (complex) wave-function can be imported externally, e.g. from a theoretical computation. Further, the CATS framework contains all necessary tools to apply typical experimental effects on top of the theoretical correlation, such as momentum resolution effects, residual correlations and misidentified particles. The software package was developed in C++, and also provides an interface to ROOT¹⁰ to reduce the complexity of data fitting.

After completing the software developments, the next step was to analyze the RUN2 ALICE data from pp collisions at 13 TeV, in particular continuing the RUN1 study of the p-p, p- Λ and Λ - Λ and extending it to p- Ξ^- . The investigation of p-p had the goal of constraining the emission region, while the initial use of p- Λ , which has a reasonably well known interaction, was to verify the assumption of a common source. We discovered that there are substantial discrepancies in the extracted source functions, which was attributed to the effect of short-lived resonances feeding into the particles of interest and extending the spacial position of their production away from the collision point. In a fast toy Monte-Carlo study, we confirmed that such a description can restore the common emission source, and proceeded with the analyses of Λ - Λ and p- Ξ^- by taking appropriate systematic uncertainties. Initially, the man power was distributed such that Andreas and Bernhard were responsible for the data reconstruction, I was responsible for the fitting. Eventually I concentrated only on the Λ - Λ analysis, Bernhard on p- Ξ^- , while Andreas started looking at the possibility of using events triggered for high-multiplicity (HM) to extend the statistics of all analyses, allowing to study further species of particle pairs. The Λ - Λ results were published in PLB [41] (chapter 5) and the p- Ξ^- in PRL [40]. Due to the success of these studies, further boosted by good news from Andreas that the high-multiplicity data is indeed a better environment for our investigations, the femto-team expanded significantly, with two post-docs joining our group (Dr. Valentina Mantovani Sarti and Dr. Otón Vázquez Doce). Valentina was given the burden of providing us with theoretical support, while Otón attempted to study the p- Ω^- interaction in the HM data set. In parallel Dr. Ramona Lea, a colleague from Trieste, performed a study of the p- K^- system with help from myself, Valentina and Otón, leading to a publication in PRL [43]. The analysis of the HM triggered pp collisions demanded an even deeper insight into the source function in order to reduce the systematic uncertainties, for that reason me and Bernhard performed a detailed investigation of the p-p and p- Λ systems and created a more accurate model for the emission process, that explicitly accounts for the effects of strongly decaying resonances. My involvement was the actual development of this model, while Bernhard performed all associated data reconstruction and analysis. Our work resulted in the development of a Monte-Carlo based source function, that resolves these issues and proves the existence of a common emission region for p-p and p- Λ . The results were published in PLB [44] and discussed in chapter 4. It is not an exaggeration to say that at this point a new epoch of studying the strong interaction began, as for the first time an experimental technique was capable of performing high-precision investigations involving hyperons, the most prominent examples being the p- Λ and p- Ξ^- systems. Moreover, for the first time p- Σ^0 and p- Ω^- pairs had become accessible, where the results on the latter, alongside with p- Ξ^- , were recently published in Nature [45]. The main highlight was the opportunity to test the lattice calculations, which do predict a bound state for the p- Ω^- system. Further, the high-precision

¹⁰A set of C++ libraries developed at CERN specifically for the purpose of data analysis in high-energy physics [46]. It excels, among other things, for the well organized histogram classes and the easy options to set up and perform data fitting.

data on $p\text{-}\Lambda$ could also be analyzed, a challenge taken by me and supported by Valentina. The results revealed that the new ALICE data set surpasses the precision of the existing measurements, and is sensitive not only to the genuine $p\Lambda$ interaction, but also to the coupling to $N\Sigma$ as well as the residual $p\text{-}\Sigma^0$ signal, providing a nice connection to the direct study of $p\text{-}\Sigma^0$ performed by Andreas [42] and allowing to test and constrain the χ EFT. The $p\text{-}\Lambda$ analysis is presented in chapter 6, while the associated publication is currently under collaboration review.

In summary, the structure of this work is the following:

- Chapter 1: The main physics aspects and experimental techniques related to this work, including the standard model, quantum chromodynamics, hadron–hadron interaction from effective theories and its link to astrophysics.
I was involved in the final stages of the first analysis within our group on non-traditional femtoscopy, published in PRC [38].
- Chapter 2: The theory behind the CATS framework related to non-traditional femtoscopy.
My work, supported by Valentina, published in EPJC [39].
- Chapter 3: Experimental data
 - Section 3.1: Overview of the methods for the experimental determination of the correlation function.
Work of Andreas and Bernhard.
 - Sections 3.2, 3.3, 3.4: Normalization and correction of the experimental correlation function.
Mostly my work.
 - Section 3.5: Modelling of the data.
My work.
- Chapter 4: The resonance source model.
Team effort with Bernhard, published in PLB [44].
- Chapter 5: The $\Lambda\text{-}\Lambda$ interaction.
My work, published in PLB [41].
- Chapter 6: The $p\text{-}\Lambda$ interaction.
My work, supported by Valentina, publication under collaboration review.
- Chapter 7: Completing the picture with an overview of the results from related analyses, performed by other analyzers.
I have contributed as a member of the paper committee to the $p\text{-}\Xi^-$ and $p\text{-}K^-$ analyses published in PRL [40, 43].

1.5.2 The Koonin-Pratt relation

Two particle correlations are studied by femtoscopy by relating their measurable correlation function $C(k^*)$ to the properties of their emission source $S(r^*)$ and wave function of the relative motion of the pair $\Psi(\vec{k}^*, \vec{r}^*)$ (Eq. 1.7). Figure 1.11 provides an illustrative description of the femtoscopic principle. In general, any correlation function is defined as the ratio between the probability density functions of a correlated *signal* (S) and uncorrelated *reference* (R) sample of the investigated observable.

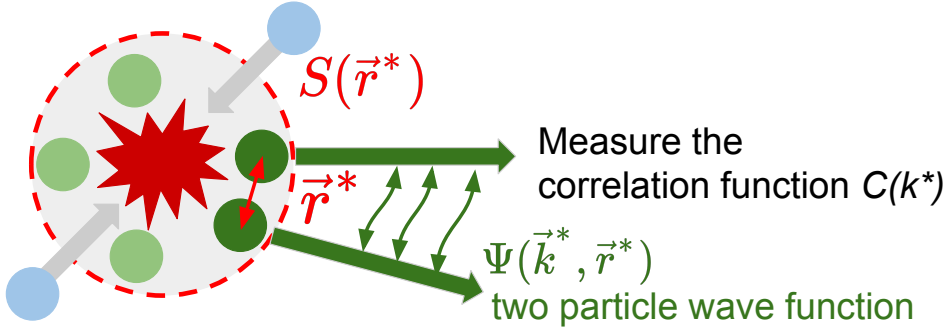


FIGURE 1.11: Femtoscopy principle. The two colliding beam particles (blue circles) result in the production of multiple particles (green circles) emitted from an effective surface called the emission source $S(\vec{r}^*)$. Particle close enough in momentum space (small k^*) will experience the final state interaction, leading to a modification of their measured k^* distribution.

For the purpose of femtoscopy, this is the yield of particle pairs measured as a function of their relative momentum q . The most common convention is to perform the analysis in the rest frame of the pair, denoted by a star (*), using the single particle momenta $k^* = q^*/2$, leading to the basic definition of the *experimental* correlation function

$$C_{\text{exp}}(k^*) = \frac{S(k^*)}{R(k^*)}. \quad (1.8)$$

The signal sample $S(k^*)$ is obtained by reconstructing all particles of interest and combining them in pairs for each recorded collision event (*same event sample*). The reference sample $R(k^*)$ is typically obtained by building pairs of particles each selected from a different event (*mixed event sample*). Alternatively $R(k^*)$ can be obtained directly from the single-particle emission distribution in the momentum space, obtaining the pairs by respecting the kinematic constraints introduced by the phase space of the underlying events. Nevertheless, there are a lot of caveats related to the mixed event sample, as it is prone to nonphysical correlations, further details are available in chapter 3.1.6. The corresponding statistical definition is

$$C_{\text{stat}}(k^*) = \frac{\langle \mathcal{P}_1(k^*) \mathcal{P}_2(k^*) \rangle}{\langle \mathcal{P}_1(k^*) \rangle \langle \mathcal{P}_2(k^*) \rangle}, \quad (1.9)$$

where $\mathcal{P}_{1,2}(k^*)$ is the normalized yield of emitting particles 1 and 2 with a specific momentum. This is already a bit simplified form, as in principle a directional dependence on the momentum could be present. Note, that both Eq. 1.8 and 1.9 will become equal to unity in the absence of any correlations. The Koonin-Pratt relation derives an equivalent definition of the correlation function, that relates it to the physical properties of the system, which will be referred to as *theoretical correlation function* [24]

$$C_{\text{th}}(k^*) = \int S(\vec{k}^*, \vec{r}^*) \left| \Psi(\vec{k}^*, \vec{r}^*) \right|^2 d^3 r^*. \quad (1.10)$$

The *emission source* function $S(\vec{k}^*, \vec{r}^*)$ represents the probability of creating (emitting) a particle pair of fixed $|\vec{k}^*|$ at a distance \vec{r}^* , where the vectors account only for

the relative orientation of \vec{k}^* and \vec{r}^* . This definition demands that

$$\int S(\vec{k}^*, \vec{r}^*) d^3 r^* = 1. \quad (1.11)$$

In practice, a fact discussed in chapter 3.4, any momentum dependence of the source is not included in the definition of the femtoscopic source function, leading to

Equation: Koonin-Pratt

$$C_{\text{th}}(k^*) = \int S(r^*) \left| \Psi(\vec{k}^*, \vec{r}^*) \right|^2 d^3 r^* \stackrel{k^* \rightarrow \infty}{=} 1, \quad (1.12)$$

which is the relation introduced by Eq. 1.7. The condition $\lim_{k^* \rightarrow \infty} C_{\text{th}}(k^*) = 1$ is enforced by the statistical interpretation given by 1.9, under the assumption that at very high relative momenta the particles separate fast enough to avoid the final state interaction. Other type of correlations may not have this property, e.g. particles produced back to back as a pair will be strongly correlated only at large k^* , thus the *normalization* condition here refers only to the pure femtoscopic signal. Further details on the correct normalization of the experimental correlation function are available in chapter 3.2. Nevertheless, the definition given by Eq. 1.12, combined with the fact that the source function is a probability density function (Eq. 1.11), implies that the correct convergence has to be guaranteed by the appropriate normalization of the wave function. Based on the Koonin-Pratt relation the correlation function is the value of the wave function averaged over the source distribution

$$C_{\text{th}}(k^*) = \left\langle \left| \Psi(\vec{k}^*, \vec{r}^*) \right|^2 \right\rangle, \quad (1.13)$$

and for the case of $k^* \rightarrow \infty$ the wave function is represented by a free wave. The standard quantum mechanical parameterization of a free wave is by an exponent of a complex phase shift, which has the required absolute value of 1. Further, as the source function is assumed to depend only on the radial component r^* , the angular integration ($4\pi r^{*2}$) within Eq. 1.12 can be absorbed by the source function

$$C_{\text{th}}(k^*) = \int_0^\infty S_{4\pi}(r^*) \left| \Psi(\vec{k}^*, \vec{r}^*) \right|^2 dr^* \stackrel{k^* \rightarrow \infty}{=} 1, \quad (1.14)$$

where $S_{4\pi}(r^*) = 4\pi r^{*2} S(r^*)$, and $\int_0^\infty S_{4\pi}(r^*) dr^* = 1$.

The Koonin-Pratt relation provides a link between a measurable quantity, the correlation function, to the integral of the source and wave functions. Clearly, a lot of differential information is lost by the integration over r^* , thus it is rather uncommon to attempt to study simultaneously both the emission and the interaction. The traditional femtoscopy assumes that the wave function is known, while the subject of investigation is the emission region, and vice versa for non-traditional femtoscopy.

1.5.3 The source function

In principle, the *source function* is a very complex object, as the particle emission is governed by the hadronization process, that is dominated by QCD effects. These are often difficult to model exactly, but can be effectively corrected for empirically directly onto the correlation function. For practical purposes, the source function is

simplified to suit the domain of femtoscopic studies at low k^* . The most common generic definition of the source function $S(\vec{r})$, is to treat it deferentially in each spatial direction in order to capture modifications due to collective effects. Further, it is assumed to be the convolution of two independent single particle emission functions $s_{1,2}(\vec{r}_{1,2})$. This requirement is not a necessity in order to use Eq. 1.10 and its derived relations, as long as $S(\vec{k}^*, \vec{r}^*)$ can be modeled by other means. Historically, the most practical coordinate system for heavy ion collisions is the out-side-long frame of reference, in which the longitudinal (long) direction is given by the beam axis, the outwards (out) by the direction of the total momentum of the pair perpendicular to the beam, while the sideways (side) axis is perpendicular to the other two. A detailed discussion of this choice of coordinate system and the physics motivation is available in [24]. In the case of non-strongly interacting particles, such as pions, the wave function can be decomposed along each axis, leading to the possibility of studying separately $C(k_{\text{out}})$, $C(k_{\text{side}})$ and $C(k_{\text{long}})$, inferring information on the 3 dimensional profile of the emission source. Nevertheless, for the study of strongly interacting particles such an analysis has never been performed, also not in the present work, as it would require a dedicated study on the decomposition of the wave function. With the increasing significance of the available data sets, it would perhaps be of future interest to perform such a study based on p-p pairs, for which the interaction is known, to compare the results to the pion source. Using a Gaussian profile along each axis of the emission has been very successful in the past, and while some modifications to it will be proposed in chapter 4, the core component of the source in this work is still a Gaussian, which is defined, for the single particles, as

$$s(r) \sim \exp\left(-\frac{r_o^2}{2R_o^2} - \frac{r_s^2}{2R_s^2} - \frac{r_l^2}{2R_l^2}\right), \quad (1.15)$$

where $r = \sqrt{r_o^2 + r_s^2 + r_l^2}$ and $R_{o,s,l}$ are the source dimensions along each axis (in the out-side-long system). The corresponding uncorrelated two-particle source function is

$$S(r) \sim \exp\left(-\frac{r_o^2}{4R_o^2} - \frac{r_s^2}{4R_s^2} - \frac{r_l^2}{4R_l^2}\right). \quad (1.16)$$

In the case of a symmetric source ($r_0 = R_o = R_s = R_l$), as used in this work, the above expression simplifies to

$$S(r) = \frac{1}{(4\pi r_0^2)^{3/2}} \exp\left(-\frac{r^2}{4r_0^2}\right). \quad (1.17)$$

Note that this definition is best suited for the out-side-long frame of reference, nevertheless for heavier particles, which are less influenced by the Lorentz boost, the profile remains similar in the pair rest frame. This convention is adopted in the present work, and further discussed in chapter 4.

1.5.4 Lednický formalism

The *Lednický model* has the goal of providing a simplified analytical treatment of the wave function within Eq. 1.12, that can relate the correlation function to the asymptotic solution of the interaction [33]. In scattering theory, the latter is approximated by the *effective range expansion*, that uses only two parameters, the *scattering length*

f_0 ¹¹ and the *effective range* d_0 , to describe the interaction, where f_0 is directly linked to the total cross section of the process [47, 48]. In this formalism, the wave function is expressed as the sum of a free wave and a scattered spherical wave modified by the scattering amplitude $f(\theta)$

$$\Psi(\vec{k}^*, \vec{r}^*) \approx e^{-i\vec{k}^*\vec{r}^*} + f(\theta) \frac{e^{ik^*r^*}}{r^*}, \quad (1.18)$$

where within the effective range expansion

$$f(k^*) \approx \left(f_0^{-1} + \frac{1}{2} d_0 k^{*2} - ik^* \right)^{-1}. \quad (1.19)$$

Substituting the wave function in Eq. 1.12 with the relations provided by Eq. 1.18 and 1.19, the resulting integral can be analytically solved in the case of a *Gaussian source* of width r_0 , and results in

Equation: Lednický-Lyuboshitz

$$C_{LL}(k^*) = 1 + \frac{1}{2} \left| \frac{f}{r_0} \right|^2 + \frac{2\mathcal{R}[f]F_1(2k^*r_0)}{\sqrt{\pi}r_0} - \frac{\mathcal{I}[f]F_2(2k^*r_0)}{r_0} \quad (1.20)$$

where

$$F_1(z) = \frac{e^{-z^2}}{z} \int_0^z e^{x^2} dx, \quad (1.21)$$

and

$$F_2(z) = \frac{1}{z} \left(1 - e^{-z^2} \right). \quad (1.22)$$

This derivation is done entirely within the asymptotic region of the wave function, implying that it only holds at distances far away from the scattering region. The typical range of the strong interaction is 2-3 fm, meaning that for a large emission source, c.a. above 4 fm, Eq. 1.20 should have no problem of describing the correlation function. However, such a large source value is only realized in heavy ion collisions at large energies, and experimentally a smaller emission source is often present. Further investigations of Prof. Lednický lead to the inclusion of a *small source correction term* that aims at providing an improved description.

Equation: Lednický-Lyuboshitz (small radius)

$$C_{LL}(k^*) = 1 + \frac{1}{2} \left| \frac{f}{r_0} \right|^2 \left[1 - \frac{d_0}{2\sqrt{\pi}r_0} \right] + \frac{2\mathcal{R}[f]F_1(2k^*r_0)}{\sqrt{\pi}r_0} - \frac{\mathcal{I}[f]F_2(2k^*r_0)}{r_0} \quad (1.23)$$

It is important to note, that this correction is represented by a negative term proportional to $\sim d_0/r_0$. This could lead to negative correlation function, an obvious artefact of reaching the limit of validity of the model. Thus, it is of utmost importance to validate the use of the Lednický model in small systems, in particular for repulsive potentials. Further discussion on the subject is provided in chapter 5, Fig. 5.6 in particular.

¹¹The standard sign convention in femtoscopy is assumed, where a positive f_0 corresponds to an attractive non-binding interaction.

By default, the Lednický relation works with a single set of scattering parameters, implying that the result is averaged over any spin or isospin dependence, and only the s scattering wave is considered. The total correlation function can be decomposed into the weighted sum of contributions associated to each spin or isospin channel (see chapter 2.3), as such it is trivial to include them in the analysis. Nevertheless, the higher order partial waves cannot be treated in a simple way, as there the modification is on the level of the wave function. Further, equations 1.20 and 1.23 are valid in the absence of Coulomb interaction and for non-identical particles, nevertheless both can be accounted for.

Identical particles

To handle the *identical particles*, one needs to respect the symmetrization of the wave function (Pauli principle) for each spin state. In general, the wave functions related to different spins, as well as the partial waves related to a specific angular momentum number l , are orthogonal to one another, as a result the square of the total wave function $|\Psi(r)|^2$ does not contain any interference terms and the correlation function can be written as a direct weighted sum of the individual spin states, where the weights are obtained based on the degeneracy (see chapter 2.3). The total wave function for each spin can be expressed as the sum of all partial waves

$$\Psi(r) = \sum_{l=0}^{\infty} \psi_l(r). \quad (1.24)$$

For identical particles, the symmetrization condition for the partial wave functions $\psi_l(r)$ is

$$\psi_l(r) = \frac{1}{\sqrt{2}} \left[\psi_l(r) + (-1)^{s+l} \psi_l(r) \right], \quad (1.25)$$

meaning that based on the oddness of $s + l$ half of the partial waves get canceled. The square of the total wave function becomes

$$|\Phi_s(r)|^2 = 2 \sum_l^{\text{odd/even}} |\psi_l(r)|^2, \quad (1.26)$$

where depending on the spin s only the odd or even l are considered. It can be proven, that in the absence of final state interaction (FSI), i.e. ψ_l are represented by the Bessel function corresponding to a free wave [47, 48], the correlation function for a Gaussian source is

$$C_s(k^*) = \int S(r^*) |\Phi_s(r^*)|^2 d^3 r^* = 1 + (-1)^s e^{-4r_0^2 k^{*2}}. \quad (1.27)$$

To investigate the FSI, let us define as $C_{\text{full}}(k^*)$ the resulting correlation for non-identical particles, and $C_{\text{FSI},s}(k^*)$ is modified for identical particles. The Lednický model can be used to obtain $C_{\text{full}}(k^*)$, thus for practical purposes we need to find its relation to $C_{\text{FSI},s}(k^*)$. From the above relations it follows that the full wave function

is expressed as $\Psi(r) = \frac{1}{2} [\Phi_s(r) + \Phi_{s+1}(r)]$, leading to

$$\begin{aligned} C_{\text{FSI},s}(k^*) &= \int S(r^*) |\Phi_s(r^*)|^2 d^3r^* = \\ &= \int S(r^*) \left[|2\Psi(r^*)|^2 - |\Phi_{s+1}(r^*)|^2 \right] d^3r^* = \\ &= 2C_{\text{full}}(k^*) - C_{s+1}(k^*). \end{aligned} \quad (1.28)$$

Note that the interaction is contained in $C_{\text{full}}(k^*)$, as the term $\Phi_{s+1}(r)$ is just added as a dummy to absorb the differences between $\Psi(r)$ and $\Phi(r)$. Next, Eq. 1.28 can be applied to the Lednický relation to adopt it to the case of identical particles

Equation: Lednický-Lyuboshitz (identical particles)

$$C_{\text{LL},s}(k^*) = 2C_{\text{LL}}(k^*) - 1 - (-1)^{s+1} e^{-4r_0^2 k^{*2}}. \quad (1.29)$$

There is one complication, related to the spin dependence of the quantum statistics term. The general Lednický formalism works in the spin averaged case, however this can no longer be done. Thus, to describe the correlation function by a single equation, one has to consider the individual spin states, evaluate their corresponding correlation functions, and sum them to obtain the final result. The most commonly studied case is of two spin 1/2 particles (total spin of 1), such as protons or Λ s, thus below a practical example of the evaluation of the Λ - Λ theoretical correlation function is presented. The two possible projections of the spin are 0 and 1, contributing with a ratio of 1:3 due to the degeneracy. It implies that the total correlation function is

$$C_{\text{LL},s=1}(k^*) = \frac{1}{4} C_{\text{LL},0}(k^*) + \frac{3}{4} C_{\text{LL},1}(k^*).$$

Since the interaction within the Lednický model contains only the s wave, which is present for $s = 0$ but not for $s = 1$ (Eq. 1.25), the term $C_{\text{LL},1}(k^*)$ becomes equal to the non-interacting case $C_1(k^*)$ (Eq. 1.27), resulting in

$$C_{\text{LL},s=1}(k^*) = \frac{1}{4} \left[2C_{\text{LL}}(k^*) - 1 + e^{-4r_0^2 k^{*2}} \right] + \frac{3}{4} \left[1 - e^{-4r_0^2 k^{*2}} \right].$$

Simplifying this expression leads to the final result

Equation: Lednický-Lyuboshitz (identical particles of total spin 1)

$$C_{\text{LL},s=1}(k^*) = \frac{1}{2} \left[C_{\text{LL}}(k^*) + 1 - e^{-4r_0^2 k^{*2}} \right]. \quad (1.30)$$

Coulomb force

The *Coulomb interaction* is far less trivial to handle, due to its long range nature. There are two possibilities to proceed, one is exact but non-analytical, and the other is approximate and analytical (Gamow approximation). The exact solution can be obtained from scattering theory, by using the related asymptotic solution of a Coulomb wave function as in Eq. 1.18, however the description becomes

$$\Psi(\vec{k}^*, \vec{r}^*) \approx e^{i\delta_c} \sqrt{A_c(\eta)} \left[e^{-i\vec{k}^* \cdot \vec{r}^*} F(-i\eta, 1, i\epsilon) + f_c(k^*) \frac{\tilde{G}(k^* r^*, \eta)}{r^*} \right], \quad (1.31)$$

where $\varepsilon = \vec{k}^* \vec{r}^* + k^* r^*$, $\eta = \alpha \mu q_1 q_2 / k^*$ and $\delta_c = \arg \Gamma(1 + i\eta)$. These relations assume input in natural units, α stands for the fine structure constant. Similarly to 1.18, the Coulomb relation 1.31 treats the wave function as an incoming and an outgoing wave, however both of their functional shapes are modulated, as well as the overall amplitude. The latter consists of the Coulomb phase shift δ_c and the Coulomb penetration factor

$$A_c(\eta) = \frac{2\pi\eta}{e^{2\pi\eta} - 1}. \quad (1.32)$$

The *Gamow approximation* stops at this point, ignoring the correction on the functional shape of the terms within the brackets. The Coulomb penetration factor $A_c(\eta)$, also referred to as the Gamow factor, can be factorized out within the Koonin-Pratt relation (Eq. 1.7) and the resulting correlation function is simply corrected by a multiplication with $A_c(\eta)$. This is a very crude simplification, that has poor accuracy and can only be used on data with large uncertainties, or as a tool to perform a quick qualitative estimation of the effect of the Coulomb interaction. The better way to proceed is to evaluate the full wave function, using the confluent hypergeometric function F and $\tilde{G} = \sqrt{A_c}(G_0 + iF_0)$, where F_0 and G_0 are the regular and singular s -wave Coulomb functions. Further, the Coulomb scattering amplitude $f_c(k^*)$ is modified as

$$f_c(k^*) = \frac{f(k^*)}{A_c(\eta)}. \quad (1.33)$$

Detailed definitions are available in [49] and [50]. The confluent hypergeometric functions cannot be analytically integrated out of the Koonin-Pratt equation, thus the Lednický model with an exact Coulomb correction can only be deployed by using a numerical integration. This is easy to perform using CATS, although at present the evaluation of the Lednický wave function is not explicitly included in the framework, hence it has to be computed separately.

1.5.5 Residual correlations

When unstable¹² particles are emitted they will decay and their daughters can be detected by the experimental set up. For that reason many of the measured stable or long lived ($c\tau \gtrsim \text{cm}$) particles, such as protons, pions, kaons, Λ etc., are often not produced in the primary collision, but through a decay process instead. Depending on the lifetime τ of the primordial particle, there are three possible scenarios: i) the decay length $c\tau$ is smaller than the scale of the source. Then the decay daughter is subject to the FSI and the standard femtoscopy formalism holds. ii) The decay length is similar to the source size ($\sim \text{fm}$), leading to a very short duration of the FSI, insufficient for a large modulation of the momenta of the primordial particles. Hence, the relevant interaction is only between the daughter particles, where the starting point of the interaction is shifted in space and time, leading to modifications of the source function. This effect is studied in detail in chapter 4. iii) The decay length is much larger than the size of the source. In that case, the FSI occurred between the primordial particles and by the time of the decay the daughter particles are too far away to be subject to further modulations of their momenta due to FSI. The last case is historically the most relevant, for this reason the terminology “*residual correlations*” or “*feed-down*” is used to describe it exclusively, as also done in the present work. A schematic representation is available in Fig. 1.12. The green arrows represent the

¹²In view of the experiment, any long lived particles that reach the detectors can be considered effectively “stable”. Hence unstable particles are those of mean free path $c\tau \ll 1 \text{ cm}$.

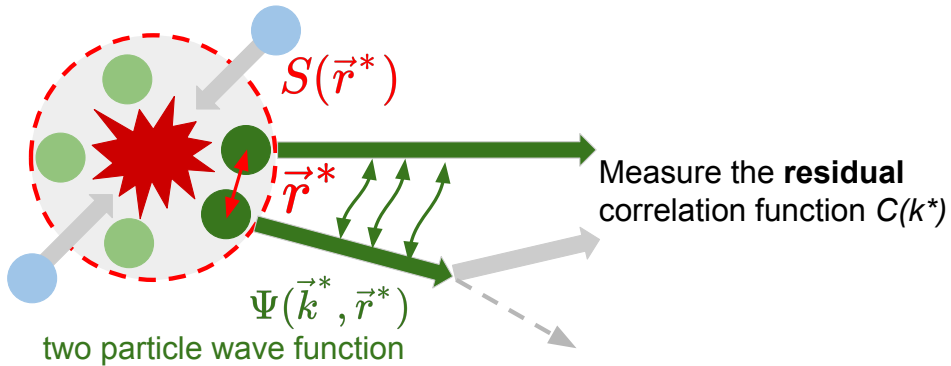


FIGURE 1.12: A schematic representation of the effect of residual correlations. The primordial (green) particle are the subject of the final state interaction, however if some of them decay far away from the collision point, but before they have reached the detector system, the measured pair corresponds to the daughter (secondary) particles. This leads to a contamination of the femtoscopy signal.

primordial particles, which experienced the FSI, but in this example one of them decayed into another particle (gray arrow). A practical example can be that initially a p- Λ pair was formed, and the Λ decayed into a proton, leading to a measured p-p pair. The correlation signal of the latter consists of the original p- Λ genuine correlation, convoluted with the modulation of the $\Lambda \rightarrow p$ momentum transfer. This process can be modeled purely by phase space and will be discussed in detail in chapter 2.7.3. The most important observation is that the strength of the residual signal is smaller compared to the underlying genuine signal. The measured $C(k^*)$, which is modified to

$$C(k^*) = \lambda_{\text{gen}} C_{\text{gen}} + \sum \lambda_{\text{res}} C_{\text{res}}, \quad (1.34)$$

where λ_{gen} corresponds to the fractional amount of genuine correlation signal, associated with primary particles, and λ_{res} are the amount of secondary signals feeding into the measured pair. The associated correlation functions C_{res} are either assumed flat, or modeled by transforming their signal of origin into the kinematics of the measured daughter particles. Since this transformation leads to a flattening of the correlation signal, the functional shape can be sometimes ignored and the correlation function simplifies to

$$C_{\text{res}}(k^*) - 1 = \lambda_{\text{gen}} [C(k^*) - 1], \quad (1.35)$$

letting λ_{gen} to be determined by the subsequent fit procedure to the experimental data. The such obtained value for the λ_{gen} parameter is not only associated to feed-down, but also to possible modifications of the Gaussian emission source, the width r_0 of which is fitted as well. The interpretation of the femtoscopy result has been reduced to the correct theoretical prediction of these two parameters, often studied differently, e.g. as a function of the pair transverse momentum. Nevertheless, in this work the goal is to perform precision studies of the strong interaction, requiring a much more robust fit and a significant reduction of the systematic uncertainties associated with the residual correlations and the emission source. Thus, the residual correlations, their amount in particular, has been explicitly studied, using the techniques introduced in by Oliver Arnold [38, 51]. The source function, specifically the effect of short-lived resonances, is investigated within the scope of this work and presented in chapter 4.

Chapter 2

CATS framework

2.1 Overview

In this chapter the “*Correlation Analysis Tool using the Schrödinger equation*” (CATS) will be introduced [39]. The starting point is the understanding of the requirements of femtoscopic analyses, which determines the design of the CATS framework. The most important relation in femtoscopy is given by Eq. 1.12 and connects the correlation function to the emission source and interaction potential. The typical methods used to study the correlation function, such as the Lednický model (Eq. 1.20), are limited to a Gaussian parameterization of the source function, and the interaction is modeled using the effective range expansion, which describes only the asymptotic solution of the wave function. This leads to inaccuracies when investigating small emission regions, which implies that these methods are mostly applicable to heavy-ion collisions. Moreover, the approximate treatment leads to difficulties when dealing with the Coulomb interaction 1.5.4. To overcome those limitations, the CATS framework was designed to compute the correlation function numerically based on Eq. 1.10 and the input for $S(\vec{k}^*, \vec{r}^*)$ and $\Psi(\vec{k}^*, \vec{r}^*)$ can be any analytical or non-analytical function. Note that here the source is allowed to have any 3 dimensional momentum and spacial dependence. The best option for the interaction is to use the theoretical wave function $\Psi(\vec{k}^*, \vec{r}^*)$ as a direct input, since this allows to probe theories, that include inelastic and coupled channel effects. Nevertheless, in some cases the interaction can be simplified to the form of a real local potential $V(r)$ and the wave function can be easily evaluated using the Schrödinger equation. For those reasons CATS includes a Schrödinger solver, and the input can be either provided in form of a potential $V(r)$, or directly as a wave function $\Psi(\vec{k}^*, \vec{r}^*)$.

The measured experimental correlation function (Eq. 1.8) differs from the genuine theoretical one (Eq. 1.10), due to several effects. On one hand the presence of *feed-down* into the measured particles (section 1.5.5) induces *residual correlations*, which are by default not included in the theoretical modelling, as it is a feature of the collision system. On the other hand, there are detector related effects, such as *momentum resolution*, acceptance and efficiency. For most practical purposes, femtoscopy allows to neglect the *acceptance and efficiency*, since they are only relevant for the description of particle spectra. However, the correlation function is a ratio between two yield distributions (Eq. 1.8), and as long as both have the same acceptance and efficiency the final result will be unbiased by those effects. Thus, those will be neglected, but one needs to be careful in setting up a reference sample that has equivalent detector effects as the correlated sample. A small caveat is that the source function depends on the properties of the detector. The simple explanation is that there is no reason to believe that the particle emission is completely symmetric in all spacial directions, meaning that the measured profile will be different depending

on the acceptance of the detector. If the emission source is to be studied and compared to theoretical predictions, the best approach is to include the acceptance and efficiency effects in the model that is tested.

In this chapter we will explore the simple theory behind CATS, and go into technical details only for the most relevant parts. Appendix A provides an extended tutorial of CATS, containing multiple practical examples. The CATS framework is implemented in C++ and consists of a core class, called “CATS”, as well as several supporting classes. The core class is used to compute the theoretical correlation function (Eq. 1.12), while the support (extension) classes were developed to provide additional utilities, such as correcting the theoretical curve for feed-down contributions, as well as containing several important predefined source functions and interaction potentials.

The femtoscopic analyses are often performed in the center of mass frame, which in the standard *notation* is denoted by a star (*) superscript over the momentum and radius. The quantum mechanics equations are applied to these observables, however in this work any relations are written *without the use of superscripts*. Any femtoscopic relations will include the superscripts, as long as they refer to the center of mass reference frame.

2.2 Evaluation of the wave function

In case the theory input for the interaction of two particles is provided by a real local potential $V(r)$, CATS uses the Schrödinger equation to evaluate the wave function $\Psi_k(\vec{r})$. At a fixed momentum k^1 it can be separated into a radial $R_k(r)$ and an angular part $Y(\theta)$

$$\Psi_k(\vec{r}) = R_k(r)Y(\theta), \quad (2.1)$$

where $Y(\theta)$ is described by the spherical harmonics. The wave function can have a φ dependence as well, but for a spherically symmetric potential the scattering process will not change the phase related to φ , thus, without loss of generality, only θ is considered. The radial wave function $R_k(r)$ is determined by the interaction potential. The *partial wave* decomposition is used to transform Eq. 2.1 into

$$\Psi_k(\vec{r}) = \sum_{l=0}^{\infty} R_{k,l}(r)Y_l(\theta) = \sum_{l=0}^{\infty} \underbrace{i^l(2l+1)\frac{u_{k,l}(r)}{r}}_{:=\Psi_{k,l}(r)} P_l(\cos\theta), \quad (2.2)$$

where l is the angular quantum number and $P_l(\cos\theta)$ are the Legendre polynomials, while $u_{k,l}(r) = rR_{k,l}(r)$ and satisfies the radial *Schrödinger equation*

$$\frac{d^2u_{k,l}}{dr^2} = \left[2mV_l(r) + \frac{l(l+1)}{r^2} - k^2 \right] u_{k,l}, \quad (2.3)$$

where m is the mass of the particle. For a pair of particles the problem is equivalent to evaluating Eq. 2.3 by substituting the momentum k with the single particle momentum k^* in the pair rest frame, the radius r with the relative distance between the particles r^* , and the mass m by the *reduced mass* $m = (m_1m_2)/(m_1 + m_2)$. The potential $V_l(r)$ can typically be provided by the theory. To compute the total wave

¹For simplicity the k dependence is denoted as a subscript.

function Eq. 2.3 has to be solved for all partial waves. For a low-energy scattering problem, only the lowest partial waves are relevant², while the rest of the partial waves follow approximately the free particle solution

$$\Psi_k(\vec{r}) = e^{ikz} = \sum_{l=0}^{\infty} i^l (2l+1) j_l(kr) P_l(\cos\theta), \quad (2.4)$$

where $j_l(kr)$ are the spherical Bessel functions. Note that equations 2.2 and 2.4 are identical, with the only difference that the radial wave function $u_{k,l}(r)/r$ is replaced with the Bessel function $j_l(kr)$. To compute the total correlation function, the CATS framework uses Eq. 2.2, and if the corresponding partial wave l has no additional interaction $u_{k,l}(r)/r$ is set to $j_l(kr)$, otherwise $u_{k,l}(r)/r$ is evaluated by solving Eq. 2.3. The sum requires a cutoff l_{\max} , which is dynamically set by imposing the condition

$$(2l_{\max} + 1) j_{l_{\max}}(kr) P_{l_{\max}}(\cos\theta) \rightarrow 0.$$

It is important to note, that those considerations are only valid for a short-ranged potential $V_l(r)$, that falls off faster than $1/r$. This condition is satisfied for the strong interaction, but not for the Coulomb potential. In case the *Coulomb interaction* is to be included in the calculation, the effective potential for solving Eq. 2.3 becomes

$$V_l(r) = V_{l,\text{strong}}(r) + V_{\text{Coulomb}}(r). \quad (2.5)$$

In this case one cannot use the Bessel functions to model the higher partial waves. Luckily the solutions of the radial Schrödinger equation for a Coulomb potential are known and can be evaluated using the confluent hypergeometric functions [cite](#). Moreover the GNU scientific libraries provide functions to evaluate them numerically [\[52\]](#).

For a pair of *identical particles* the proper symmetries of the wave functions have to be included in the formalism. Spin statistics tells us that

$$\Psi_k(r) = \frac{1}{\sqrt{2}} [\Psi_k(r) + (-1)^s \Psi_{-k}(r)], \quad (2.6)$$

where s is the total spin state of the system. Putting this into the context of the partial wave expansion (equations 2.2 and 2.4), one notices that if the individual partial wave functions are symmetric³ with respect to k , than for even s Eq. 2.6 leads to a complete cancellation of the partial waves, while for odd s it leads to doubling the amplitude of the partial wave. In case the partial waves are anti-symmetric, the opposite relations hold. An interesting property of the partial waves is that those with an even angular number l are symmetric, while odd l leads to an anti-symmetric behaviour. An illustrative example is shown in Fig. 2.1. Finally, the resulting condition for identical particles is

$$\Psi_k(r) = \frac{1}{\sqrt{2}} \sum_l \Psi_{k,l}(r) \left[1 + (-1)^{s+l} \right], \quad (2.7)$$

meaning that only the partial waves with even $s + l$ contribute to the total solution.

²Typically only the s-wave has a substantial contribution, although for pairs measured with higher statistics, such as p-p and p- Λ , one could be sensitive up to the d-waves

³for a symmetric function $f(x) = f(-x)$, for an anti-symmetric function $f(x) = -f(-x)$.

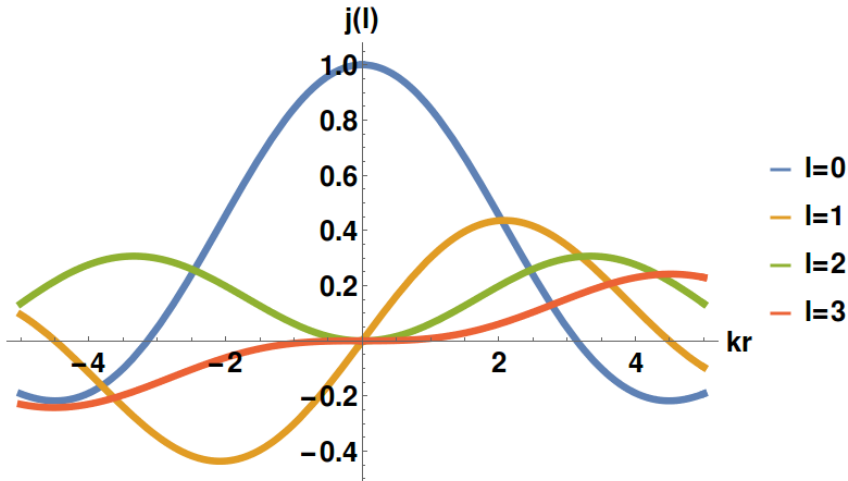


FIGURE 2.1: The spherical Bessel functions of the first kind, as an illustration for their symmetry properties. The even l result in symmetric function, the odd l in anti-symmetric.

So far we have only reviewed the theory behind the computation of the wave function. As the main focus of this work is related to the physics case, I would only like to outline the more important aspects related to the numerical implementation of this method into CATS. The normalization of the numerically evaluated wave function is matched to the asymptotic solution (at large r), which also leads to the determination of the phase shifts. The differential equation is solved by an Euler method including an adaptive step size, to boost the performance. A higher order Runge-Kutta method was initially considered, however implementing an adaptive grid becomes non-trivial, while the existent adaptive Euler method was already performing sufficiently well, with no more than 40 ms⁴ needed for the evaluation of a single partial wave. In fact, this method was outperforming the Runge-Kutta method with a fixed grid size.

2.3 Interaction channels

The interaction between a pair of particles typically depends on the exact spin and isospin configuration. Thus the methods presented in chapter 2.2 can only be applied to a specific spin/isospin channel. In a realistic experimental environment, all configurations occur with a certain probability and contribute to the total correlation function. A simple example, that will be generalized later, is the p-p interaction in the s -wave. The proton is a spin 1/2 particle, meaning that a system of two protons can occupy either a state of total spin 0 or 1. The spin projection for a spin 0 system can only be zero (singlet state), while the projection of the spin 1 can be -1,0,1 (triplet state). If there is no spin polarization, each of these four states is equally probable, inferring a total probability for the spin 0 (1) states of 1/4 (3/4). If the potentials corresponding to the singlet and triplet state are both known, the individual wave functions $\Psi_{S=0}$ and $\Psi_{S=1}$ can be computed using the prescription from the previous section, while the corresponding correlation functions $C_{S=0}(k^*)$ and $C_{S=1}(k^*)$ can be evaluated from Eq. 1.12. Given the probability for each spin state to occur, the total

⁴The speed was tested on my personal laptop, on a single-core clocked at 2.6 GHz.

correlation function is given⁵ by $C(k^*) = 1/4 \cdot C_{S=0}(k^*) + 3/4 \cdot C_{S=1}(k^*)$. This simple example can easily be generalized to handle all types of *degeneracies* present for the interaction at hand. In case of spin, the weights with which each state contributes to the correlation function is

$$w_{(s)} = \frac{(2s+1)}{(2s_1+1)(2s_2+1)}, \quad (2.8)$$

where s is the total spin of two particles with spin s_1 and s_2 . The same relation holds in the case of isospin (I) degeneracy

$$w_{(I)} = \frac{(2I+1)}{(2I_1+1)(2I_2+1)}. \quad (2.9)$$

The situation is a bit more complicated, if one considers the total angular momentum (j) of a specific partial wave (l). This is due to the fact, that each partial wave has an independent degeneracy. The total wave function is than a combination of all possible configurations of the partial waves, weighted by the corresponding degeneracy factors. Since j is a good quantum number, the resulting states are orthogonal to one another and for this reason the same weights can be applied to the total correlation function. The weights corresponding to a particular j state are

$$w_{(s,l,j)} = \frac{(2j+1)}{(2l+1)(2s+1)}. \quad (2.10)$$

The sum of the weights over all available I , s and j states should be 1, i.e. $\sum_I w_{(I)} = \sum_s w_{(s)} = \sum_j w_{(s,l,j)} = 1$. The resulting generalized representation of the wave function is

$$|\Psi_k(r)|^2 = \sum_{I,s} w_{(I)} w_{(s)} \sum_{l,j} w_{(s,l,j)} |\Psi_{k,l,j}(r)|^2, \quad (2.11)$$

where the sum over j obeys the rule $j \in [|l-1|, l+1]$. Inserting Eq. 2.11 into 1.12 allows to compute the total correlation function.

The practical implementation of Eq. 2.11 in CATS introduces the notion of *interaction channels*. The definition in CATS is even more generic, and a single channel represents one unique configuration of the wave function, which is manually configured. This implies that there is no explicit notion of I , s and j , and the total wave function is

$$|\Psi_k(r)|^2 = \sum_{\text{channel}} w_{\text{channel}} \sum_l |\Psi_{k,l}(r)|^2. \quad (2.12)$$

For each channel separate interaction potentials $V_l(r)$ are used to evaluate the corresponding correlation function. Alternatively, if the wave functions of the individual channels are known, they can be directly set in CATS, allowing the use of complex values, a feature crucial when dealing with more advance models, e.g. involving inelastic and coupled channels. Further details and example on the input to CATS can be found in appendix A.

⁵Strictly speaking one has to add the wave functions, which could lead to non-trivial mixed terms for $|\Psi|^2$. This is resolved by the orthogonality of the different states.

2.4 Evaluation of the correlation function

So far the focus was on the computation of the wave function, but the ultimate goal of CATS is to compute the correlation function. The missing component is the source function $S(r^*)$, which is defined as the probability to emit a pair of particles at a relative distance r^* . A typical simplification is to assume a Gaussian emission profile. However, this is often insufficient to explain experimental measurements, e.g. in π - π correlation studies [53–57]. Thus the CATS framework provides an interface to include any source function into the computation, where the allowed variables of the source are r^* , k^* and $\theta_{rk}^* = \triangle(\vec{r}^*, \vec{k}^*)$. This set of variables provides a full description of the kinematics of the emission in the center of mass of the pair, as long as a spherically symmetric potential is used. An example of the technical implementation in CATS is provided in appendix A. A detailed explanation of the source function and the inclusion of the effect of particle production through intermediate short lived strongly decaying resonances can be found in chapter 4. Once the source function is set up in CATS, Eq. 1.12 is used to evaluate the correlation function. The integration is performed numerically, where for the purpose of optimizing the speed of the integration, the source is pre-evaluated and stored in a dynamically allocated grid.

At this stage all of the information regarding the strong interaction and the source function is included. Still, this is not yet sufficient to compute the correlation function, as the total wave function will be further modified if the two pairs are identical or charged (Equations 2.5 and 2.6). The inclusion of the Coulomb interaction can be done in two different ways. One is to include a Gamow correction factor on top of the wave function (see chapter 1.5.4), which is an approximate method that typically works only for lighter particles. This option is mostly to be used as an estimate. In case the interaction is defined with a potential function, CATS can include the Coulomb interaction at the level of the Schrödinger equation, which leads to an exact solution. This is done by setting the product of the charges (q_1 and q_2) of the two particles $q_{12} = q_1 q_2$. Further, if the Schrödinger solver is used, it requires information about the reduced mass of the particles. With all these parameters set, the CATS framework is in a position to evaluate the corresponding correlation function.

2.5 Understanding the strong interaction using CATS

To illustrate the influence of different potentials on the wave- and correlation functions, let us consider few exemplary toy potentials. A convenient parameterization is presented in the work by Kenji Morita [37], in which the focus is on studying the Λ - Λ interaction and the investigated potentials $V(r)$ have the functional form

$$V(r) = V_1 \exp(-r^2/\mu_1^2) + V_2 \exp(-r^2/\mu_2^2). \quad (2.13)$$

The typical baryon-baryon potentials have a range only up to few femtometers (fermi). In the case of meson exchange models the tail is dominated by a slightly attractive one-pion exchange, the intermediate range tends to be attractive due to two-pion exchange, and at very short distances (below 1 fm) most of the baryon-baryon pairs exhibit a repulsive core, which could be described either by the exchange of vector mesons (e.g. ω) or some phenomenological function. A schematic representation of the interaction potential is shown in Fig. 2.2 [58]. The features of such potentials can be captured in a good approximation with Eq. 2.13. The inter-

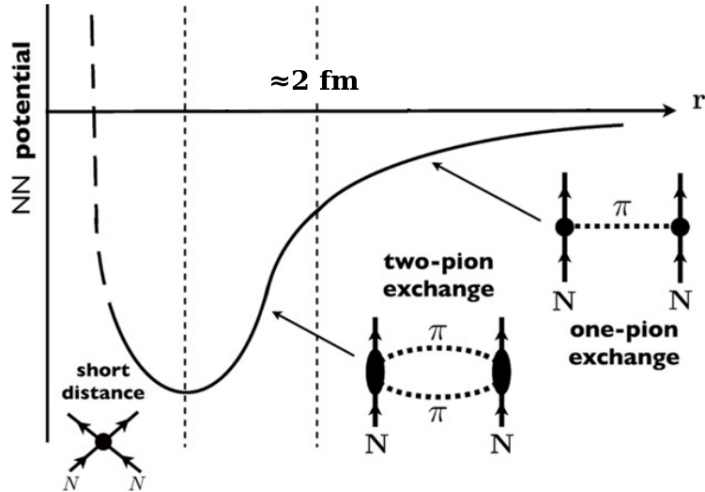


FIGURE 2.2: A typical meson exchange potential, describing the short-ranged strong interaction potential between baryon-baryon pairs. The plot is based on [58].

play between the attractive well and the repulsive core can lead to three classes of potentials: non-binding attractive, binding attractive and a repulsive potential. Depending on the potential type, the solution of the wave function $u(r)$ is modulated differently. At small distances the shape of $u(r)$ is completely deformed, while at large distances it converges towards $a(r)$ with a constant shift in the phase. The general solution $u(r)$ of the Schrödinger equation is computed using the dimensionless variable $\rho = rk$ and satisfies the relation

$$u(\rho) = a(\rho + \delta), \quad (2.14)$$

where $\delta(k)$ is called the *phase shift* and is determined by the interaction potential. We will look at few useful relations provided by the *effective range expansion*, which provides a prescription to expand $\delta(k)$ and describe the low momentum region with two effective parameters: the *scattering length* f_0 and the *effective range* d_0

$$k \cot(\delta(k)) \xrightarrow{k \rightarrow 0} \frac{1}{f_0} + \frac{1}{2} d_0 k^2 + \mathcal{O}(k^4). \quad (2.15)$$

Note, that there are two sign conventions for f_0 , the one used by Eq. 2.15 assumes that a positive f_0 corresponds to an attractive interaction, while a negative f_0 can represent either a repulsive or a binding potential. Eq. 2.15 relates the wave function and the corresponding potential $V(r)$ to just two *scattering parameters* (f_0 and d_0). These provide a very simple and intuitive way of characterizing the interaction. In case of a *bound state*, the effective range expansion relates the parameters

$$E_B = \frac{1}{md_0^2} \left(1 - \sqrt{1 + 2d_0 f_0^{-1}} \right)^2, \quad (2.16)$$

where m is the reduced mass of the two particles. The binding energy E_B has to be a real number, thus the expression under the square root sign has to be positive, inferring that for a bound state

$$|f_0| \geq 2d_0. \quad (2.17)$$

If this condition is not fulfilled, the interaction has to be repulsive in nature. The absolute value is needed to take into account that for a bound state or a repulsive interaction f_0 is negative.

The above expressions are shown as a result without proof, however to get a deeper understanding of the connection between the interaction potential, the resulting wave- and correlation functions and the scattering parameters, we will look at the results from CATS, investigating three different scenarios for the potential (Eq. 2.13). Let us define a repulsive (V_-), an attractive (V_+) and a binding (V_B) potential, the parametrizations of which are summarized in Table 2.1. The attractive part of these

Potential	Rep. strength V_1 (MeV)	Rep. range μ_1 (1/fm)	Attr. strength V_2 (MeV)	Attr. range μ_2 (1/fm)
V_-	2000	0.7	-150	1.0
V_+	1000	0.5	-150	1.0
V_B	125	0.5	-150	1.0

TABLE 2.1: The parameterizations of the potentials, based on Eq. 2.13. The strength and range of the attraction is the same for all potentials, but the repulsion is very different. An example for the technical implementation in CATS is available in the appendix A.4.

potentials is set to be similar to the meson exchange models describing the Λ - Λ interaction, but the repulsive core is chosen arbitrarily to illustrate the properties of the interaction. As such these potentials are *not* physical. In the following discussion the CATS computation will be performed with a reduced mass of 1116 MeV, assuming that the two particles are non-identical. Further, it is assumed that the interaction has a single channel, and the potentials V_- , V_+ and V_B refer to the s -wave only. The resulting potentials are plotted in Fig. 2.3. In the parametrization of the potentials

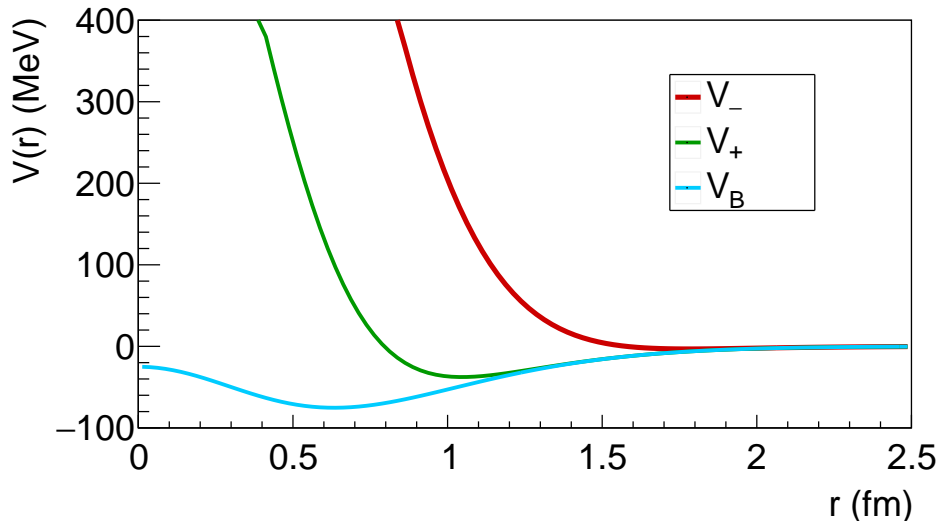


FIGURE 2.3: The example potentials V_- (repulsive), V_+ (attractive) and V_B (binding). They all share the same attractive part, but the repulsive core differs in strength and range.

(Eq. 2.13) one of the Gaussians is representing a repulsive core, which differs among the potentials both in strength V and range μ . The repulsive potential (V_-) has a long

ranged repulsive core ($\mu = 0.7$ fm) of large strength ($V = 2000$ MeV), while for both of the attractive potentials the range of the repulsion is smaller ($\mu = 0.5$ fm) and the strength weaker. For the binding potential the strength of the repulsive core is only 125 MeV, which is 8 times weaker compared to V_- , and 4 times weaker compared to V_+ . In the absence of any interaction the solution to the Schrödinger equation corresponds to a free wave, which is decomposed in partial waves by the Bessel functions (Eq. 2.4). Consequently the amplitude of the total wave function $|\Psi_k(r)|^2$ is equal to unity and the resulting correlation function (Eq. 1.12) is exactly $C(k) = 1$, independently of the source. This is only true for non-identical particles, which do not experience the Coulomb interaction. In case this condition is not satisfied, the resulting solution to the wave function is still analytically known, however it is not a constant anymore, resulting in a source-dependent solution to the correlation function⁶. However, to study the effect of the strong interaction the principle is the same regardless of the wave function symmetrization or the Coulomb potential, namely, the correlation signal related to the final state interaction is resulting from the difference of the baseline solution and the solution including the strong potential. In the current example the baseline solution is given by the free wave, described by the Bessel functions. The s -free wave is plotted in Fig. 2.4 for different momenta k . The solution depends on the dimensionless quantity $\rho = kr$, thus at large momenta the wave function oscillates much more rapidly with r . In the presence of a short ranged

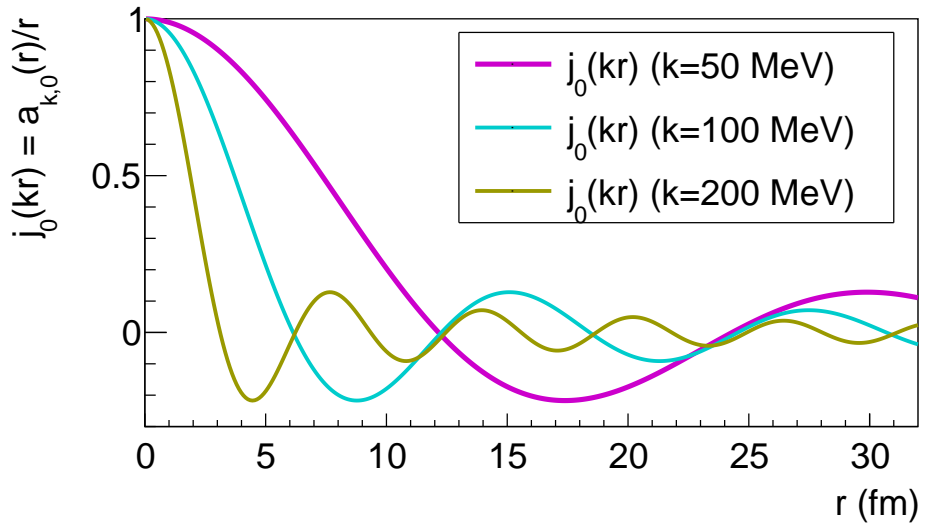


FIGURE 2.4: The Bessel function $j_0(kr) = \sin(kr)/(kr)$ corresponding to the s -wave ($l = 0$) at three different momenta. The functional shape depends on $\rho = kr$, thus at higher energy these functions, which represent the asymptotic solution $a_{k,l}(r)/r$ to a free wave, oscillate faster.

potential, the convergence scale towards the asymptotic solution of the Schrödinger equation depends on ρ , implying that at large k or large r the true solution is in its asymptotic regime. According to the femtoscopic equation 1.12, the correlation function is the average value of the wave function, given the probability density of the source $S(r)$

$$C_{\text{th}}(k) = \langle |\Psi|^2 \rangle = \int S(r) \left| \Psi(\vec{k}, \vec{r}) \right|^2 d^3r. \quad (2.18)$$

⁶This is the principle of the traditional HBT analysis of identical pions, which uses the symmetrization of the wave function to gain sensitivity to the source.

This implies that any depletion or enhancement of the wave function will be transferred to the correlation function, and the distribution of the source determines which region of r is being probed. For example, a small emission source will test mostly the inner part of the wave function, while a larger source will be mostly sensitive to the asymptotic solution. This is an important point, to which we will be returning on multiple occasions when discussing the choice of the experimental collisions system. In Fig. 2.5 we can see the wave functions corresponding to the three potentials. The upper panel shows the s -wave radial functions at $k = 50$ MeV, where the gray dashed-dotted line represents the free wave solution $a(\rho)/r$, the colored solid lines are the true solutions $u(r)/r$ and the colored dotted lines correspond to the shifted free wave $a(\rho + \delta)/r$, where δ is computed from the condition

$$u(r)/r \stackrel{k \rightarrow \infty}{=} a(\rho + \delta)/r = a(kr + \delta)/r. \quad (2.19)$$

The middle panel in Fig. 2.5 shows the corresponding amplitude of the total wave function $|\Psi_k(r)|^2$, assuming that all other partial waves follow the free wave solutions. In the lower panel of the plot there are three exemplary source functions, representing Gaussian emission profiles corresponding to typical pp, p–Pb or heavy-ion collisions. An immediate observation is that the shifted asymptotic solution (dotted lines) overlaps with the true solution for distances above just 1-2 fm. These solutions are determined directly by the phase shifts, which at low relative momenta are effectively described by the the scattering parameters f_0 and d_0 (Eq. 2.15). This feature is the main idea behind the *Lednický model*, which relates the correlation function to f_0 and d_0 . This model contains an additional correction term, aiming at reducing the discrepancy between the true and asymptotic solution at very low distances (see chapter 1.5.4). This correction is approximate and works better for attractive potentials (see chapter 5). For this reason the Lednický model is best suited to study larger emission systems, in which the correlation function looses sensitivity to the low distance region due to the very broad emission source (lower panel in Fig. 2.5). At large distances, the partial waves converge to the asymptotic solution, but are shifted on the r -axis. The corresponding phase shifts are computed by CATS and plotted in Fig. 2.6. For V_- the phase shift δ is small and negative, and at large r the true solution of the wave function is pulled away from zero. The V_+ potential behaves in a similar manner at large distances, only that the phase shift is positive, resulting in a solution that is pulled in towards smaller distances. For the binding potential V_B the situation is similar to V_+ , i.e. positive δ , however the effect of the shift is much more pronounced, since $u(r)$ is shifted by almost half a period. The phase shifts can be used to compute the scattering parameters corresponding to the three potentials, which is achieved by fitting the left hand side of Eq. 2.15, using the parameterization of the right hand side. The extracted scattering parameters are listed in Table 2.2. The obtained scattering length has the expected

Potential	f_0 (fm)	d_0 (fm)
V_-	-0.8	0.6
V_+	1.1	5.0
V_B	-4.7	1.3

TABLE 2.2: The scattering parameters corresponding to the example potentials, evaluated from the phase shifts.

sign, as the attractive potential yields a positive f_0 , while the repulsive and binding

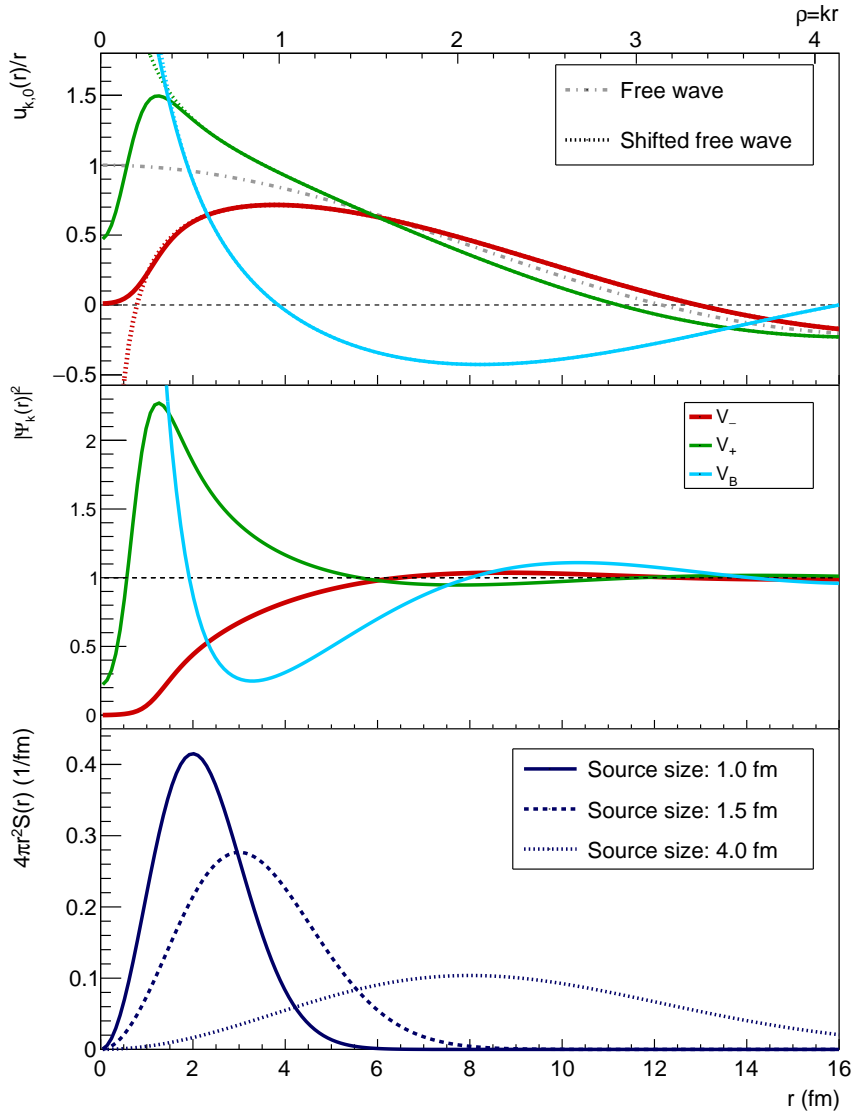


FIGURE 2.5: Example wave functions at $k = 50$ MeV, corresponding to the three toy potentials. The upper panel contains the s -waves, the middle panel contains $|\Psi_k(r)|^2$. The solid lines correspond to the solution with the strong potential ($u(r)/r$), the gray dashed dotted line to the free wave solution ($a(\rho)/r$) and the colored dotted lines show the asymptotic solution including the phase shift ($a(\rho + \delta)/r$). The correlation function is produced by the combination of the *source function* (lower panel) and deviation of $|\Psi_k(r)|^2$ from unity.

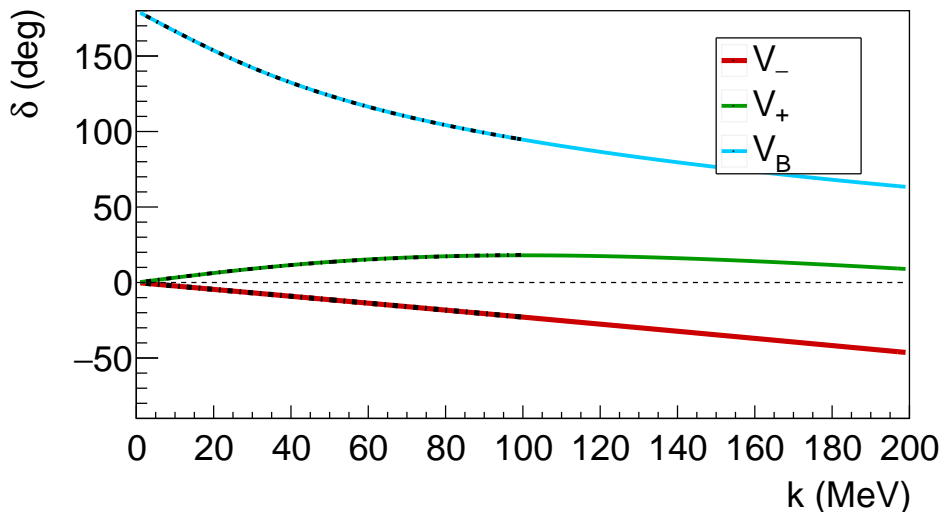


FIGURE 2.6: Example *phase shifts*, corresponding to the three toy potentials. These can be fitted at low k , in this case below 100 MeV, to extract the scattering parameters based on Eq. 2.15. The fit to each curve is represented by a dashed-dotted black line.

potentials have a negative f_0 . The absolute value of the scattering length reflects the strength of the potential⁷, while the effective range d_0 corresponds roughly to the range of the interaction. Eq. 2.17 allows to discriminate between the repulsive and binding interaction, stating that $d_0 > |f_0|/2$ corresponds to a repulsive interaction. Unsurprisingly, this condition is fulfilled by V_- but not by V_B . While the scattering parameters provide an effective characterization of the interaction potential, the main modulation of the wave function due to the strong interaction is in the range of up to few fermi. Thus the exact shape of the wave function is needed to provide an accurate description of the correlation function, in particular in the case of small emission sources. Intuitively, the repulsive potential should result in a depletion of the wave function at small relative distances, implying that the two particles have a reduced probability to be close to one another. This is indeed seen in Fig. 2.5. Due to the conservation of probability, one would expect that this is reflected in a higher expectation that the particles are located at larger relative distance. This is confirmed by Fig. 2.5, as there is a slight enhancement of the V_- solution compared to the free wave for $r > 4$ fm. By contrast, for both of the attractive potentials the wave functions are modulated in the opposite direction, meaning that the two particles are more likely to be found at small relative distances, while a certain depletion at intermediate ranges is observed. For the binding potential V_B the effect is much stronger, as the wave function is very sharply peaked at low r (below 2 fm), and strongly depleted at intermediate radii of around 2-8 fm. The correlation function is determined by $\langle |\Psi_k|^2 \rangle$, thus it is interesting to see how these differences are translated onto it (Fig. 2.7). At large distances r , the solution of the wave function oscillates mildly around unity, which would result in an approximately flat correlation. However, at low distances the deviations from unity are significant for all potentials. The correlation signal is typically enhanced with decreasing source size, as the most significant effect on the wave function is at small relative distances. This is indeed observed for the V_- and V_+ potentials in Fig. 2.7. The situation is much

⁷Large $|f_0|$ corresponds to a strong interaction.

more interesting in the presence of a *bound state* (V_B). The wave function (Fig. 2.5) is sharply peaked at $\rho < 1$, but at the expense of a significant depletion at $\rho \sim 1$. For this reason, a small emission source results in a correlation function that has a large enhancement at low k , and a dip structure at $k \gtrsim 100$ MeV. By contrast, if the same interaction is studied with a larger emission source, the very low ρ region is not captured any more, and the dominant contribution to the correlation signal is the depletion at intermediate ρ , resulting in a correlation consistently below unity (the bottom panel in Fig. 2.7). This is an important property of femtoscopy, as it tells us that a unique signature of a bound state is a flip around unity in the measured correlation signal as a function of the source size. Different source sizes can be accessed by changing the collision system, or studying the data as a function of centrality, thus enabling the experimental verification of bound states. An exclusive summary of the above discussion is given in the two summary boxes below.

Summary: Effect of different potentials on the wave function

At large relative distances ($\rho = rk \gg 1$), the effect of the strong interaction is not felt and the partial waves are simply shifted by a phase. The amplitude of the total wave function oscillates around the default solution^a.

At small distances ($\rho < 1$) an attractive potential leads to an enhancement of the wave function, corresponding to a larger probability to find the two particles close to one another, while a repulsive interaction will lower this probability and produce a depletion in the wave function. This region is the dominant factor for the strength of the correlation signal for non-binding potentials.

At intermediate ranges ($\rho \sim 1$) the conservation of probability inverts the previous effect, i.e. an attractive interaction will cause a slight depletion, while a repulsive potential will result in a small enhancement of the wave function. The strength of this effect is significantly enhanced for binding potentials.

^aThe default solution equals unity for the case of non-identical particles in the absence of Coulomb interaction. The other cases pose no computational problem, since they can be evaluated analytically, nevertheless the solution is not a constant.

Summary: The effect of different sources on the correlation function

The features of the wave function are translated to the correlation function by the source function $S(r)$ and are imprinted as a function of the relative momentum $k = \rho/r$.

Small emission sources (such as in pp collisions) are mostly sensitive to the $\rho < 1$ region, which exhibits strong sensitivity to the interaction.

Large emission sources (such as in heavy-ion collisions) reduce the sensitivity to $\rho < 1$, thus the correlation signal weakens. Binding potentials produce a large depletion signal at $\rho \sim 1$, which dominates the correlation signal.

2.6 Coupled channels

The interaction between particle pairs is often influenced by the presence of *coupled channels*. This happens when two systems share the same quantum numbers,

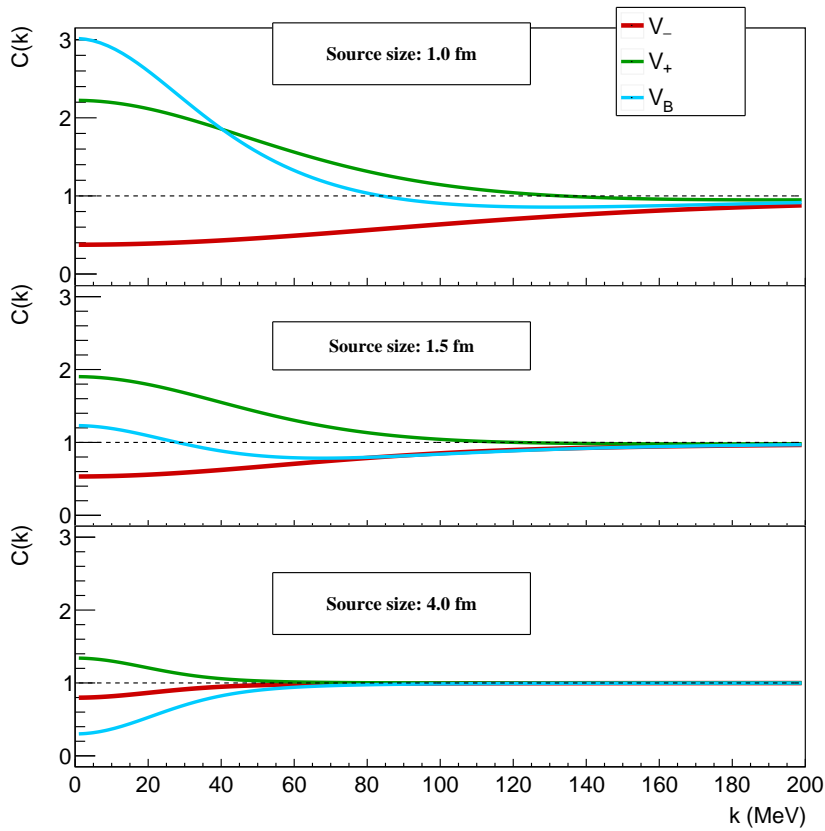


FIGURE 2.7: Example correlation functions corresponding to the three toy potentials, evaluated assuming different source sizes. The change of the latter is reflected in a modulation of the amplitude of the signal. A characteristic behaviour of a bound state is the sensitivity of the correlation profile to the source size.

e.g. p-K⁻ and n- \bar{K}^0 . In that case the wave functions of the individual states are no longer independent solution to the Schrödinger equation, which in the language of the Hamiltonian H is written as

$$H\Psi = E\Psi. \quad (2.20)$$

For a non-coupled problem the Hamiltonian is a operator defined by a single potential, and the problem is reduced to solving a single equation (2.3). However, for a coupled-channel problem H becomes a matrix, which links together the wave functions of all N coupled states:

$$\begin{pmatrix} H_{11} & \dots & H_{1N} \\ \vdots & \ddots & \vdots \\ H_{N1} & \dots & H_{NN} \end{pmatrix} \begin{pmatrix} \Psi_1 \\ \vdots \\ \Psi_N \end{pmatrix} = E \begin{pmatrix} \Psi_1 \\ \vdots \\ \Psi_N \end{pmatrix}. \quad (2.21)$$

The off-diagonal terms are those related to the coupled channel, and $H_{ij} = H_{ji}$. Note that the coupling can occur both in the angular and radial part of the wave function. The former is related to coupling of different partial waves, that share the same s and j quantum numbers. These couplings are often weak enough to be neglected. For the radial part of the wave function, a coupling could occur for particle pairs which share the same quark contents. Solving a coupled-channel equation is challenging both numerically and theoretically, since it requires the knowledge of the full

Hamiltonian. Any advanced theoretical prediction should be able to provide these Hamiltonians, and the wave functions are usually computed as well. Since such coupled channels are not implemented in CATS yet, the wave functions are directly employed as an input for the interactions where the coupled channels drive the interaction. A small caveat is that advance calculations can result in complex wave functions, and while those can be included in CATS, an issue arises in the matching to the asymptotic solution. The latter, and the corresponding phase shift, are always assumed to be real, thus for complex wave functions the matching to the asymptotic region fails. This is not a problem, as long as the complex solution is known for all distances r^* at which $S(r^*) \not\approx 0$. This condition is not automatically monitored by CATS, hence it is the responsibility of the user to verify the accuracy of the result. If the source extends into the asymptotic region, the resulting correlation function could be present obvious numerical artefacts, such as steps or oscillations within the correlation function.

The work of Yuki Kamiya et al. [59] provides a thorough explanation on how to build the correlation function in the presence of coupled channels. In the following paragraph the most important aspects have been summarized.

Each of the wave functions Ψ_j (Eq. 2.21) represents a single final state. The typical textbook treatment of scattering problems, evaluates the total wave function by imposing the boundary condition of a fixed initial state (the beam and the target have a known composition), while the outgoing solution is a superposition of all coupled states. The link between the incoming and outgoing states is given by the scattering amplitude f or the S -matrix. For the radial part of the wave function this implies

$$\psi_j^{(+)}(k, r) \rightarrow \frac{1}{2ik} \left[\delta_{ij} \frac{u_j^{(-)}(kr)}{r} + f_{ij}(k) \frac{u_j^{(+)}(kr)}{r} \right], \quad (2.22)$$

where $(-)$ and $(+)$ represent the incoming and outgoing waves respectively and i corresponds to the initial state. By contrast, in femtoscopy the boundary condition is posed by the outgoing wave, as the measured correlation function corresponds to a specific measured final state, which is produced from an initial state composed of the superposition of all coupled channels. This results into

$$\psi_j^{(-)}(k, r) \rightarrow \frac{1}{2ik} \left[\delta_{ij} \frac{u_j^{(+)}(kr)}{r} + A_{ij}(k) \frac{u_j^{(-)}(kr)}{r} \right], \quad (2.23)$$

where $A(k)$ plays a similar role as the scattering amplitude, while i is specified by the measured state. The total wave function is the weighted sum of all individual channels

$$\Psi(k, r) = \sum_j \omega_j^{1/2} \Psi_j(k, r), \quad (2.24)$$

where ω_j represents the probability of producing a specific initial state. This probability is not related to the hadron-hadron interaction, but rather to the hadronization process. Thus, in a good approximation, the values of these parameters can be based on the thermal model of hadron production. Usually ω_j is considered constant, which is certainly true in first order, but it could depend on k^* or r^* . When relating the wave function to the correlation function (Eq. 1.10 and 2.24) one has to consider the fact, that the total source function could be different for each initial

state, resulting in the relation:

$$C_{\text{th}}(k^*) = \sum_j \int \omega_j S_j(\vec{k}^*, \vec{r}^*) \left| \Psi_j(\vec{k}^*, \vec{r}^*) \right|^2 d^3 r^*. \quad (2.25)$$

It is important to note, that the functions Ψ_j have different asymptotic behaviour. The asymptotic region is defined by the kr values at which the influence of the strong interaction potential is negligible, thus resulting in $A_{ij}(k) \approx 0$. Consulting Eq. 2.23, the asymptotic solution is given by

$$\psi_j^{(-)}(k, r) \rightarrow \delta_{ij} \frac{u_j^{(+)}(kr)}{2ikr}. \quad (2.26)$$

This term is zero for $i \neq j$, while for $i = j$ it has the standard asymptotic solution of a single-channel Schrödiger equation. This implies that the inclusion of the coupled channels has no contribution at large $\rho = kr$ values, thus for large emission sources the coupling can often be neglected.

A very interesting observation can be made from Eq. 2.23 and 2.25. The correlation function depends only on k^* , and the interaction part of the wave function $\Psi_j(\vec{k}^*, \vec{r}^*)$ is determined only by $A_{ij}(k)$. The radial dependence of the wave function is embedded in $u_j^{(+/-)}(k, r)$, both of which can be analytically expressed without any knowledge on the interaction [59]. In scattering theory, the transition between an initial and a final state can be modeled by the S -matrix operator, that requires N independent variables to be uniquely defined⁸. This implies, that the amplitudes $A_{ij}(k)$ can be related to the S -matrix, linking the latter directly to the correlation function. Consequently, the measurement of the correlation functions associated to all N channels of a coupled system are sufficient to fully model the interaction. To this end only a selection of all contributing channels can be studied in the final state.

2.7 Corrections to the correlation function

In an experimental environment the measured correlation function is not only composed of the primary correlation signal, but carries the residual signal of **feed-down** contributions and of **misidentified particles**. In addition, the measured spectra are influenced by **detector resolution** effects. In this section we will focus our attention on how to take these effects into account, when modelling the data.

2.7.1 Feed-down

Let the particles X and Y be a subject for a study of correlation function $C_{X-Y}(k^*)$. For the moment a perfect measurement with 100% purity and no resolution effects is assumed. Nevertheless, not all particles stem from the collision region, as some of them are produced via intermediate decays (see chapter 1.5.5 and Fig. 1.12). The

⁸For an effective description averaged over the different partial waves and spin configurations.

total yield of particle X (and correspondingly for Y) is

$$X = \sum_{i=0}^{N_{X,F}} f_{X_i} X_i, \quad (2.27)$$

where $N_{X,F}$ is the number of possible production mechanisms of X , X_i is the absolute yield of particles produced by a specific channel, and f_{X_i} is the fractional amount of each production mechanism. The fractions f_{X_i} are normalized to unity

$$\sum_{i=0}^{N_{X,F}} f_{X_i} = 1. \quad (2.28)$$

In the notation used in this work, X_0 are the primordial particles that are emitted from the emission source and experience final state interaction, while $X_{i \neq 0}$ are the particles stemming from feed-down. In the latter case, there is a primary particle Z_{X_i} decaying into X in a time frame larger than the typical interaction scale of femtometers, which is typical for all weak and electromagnetic decays. *Throughout this work the term feed-down will only refer to non-strong decays. The effect of the strongly decaying resonances requires dedicated treatment and is discussed in chapter 4.* The final state interaction occurs between the primary particles Z_{X_i} and Z_{Y_j} ⁹ and the measured particle pair $X_i - Y_j$ will carry the residual correlation signal of $Z_{X_i} - Z_{Y_j}$. The residual correlation signal is

$$C_{X_i - Y_j}(k^*) = \int \mathcal{T}_{k^*, k'}(X_i Y_j \rightarrow XY) C_{Z_{X_i} - Z_{Y_j}}(k') dk', \quad (2.29)$$

where k' is the single particle momentum in the pair rest frame of the mother particles, $C_{Z_{X_i} - Z_{Y_j}}(k')$ is their correlation function and $\mathcal{T}_{k^*, k'}$ is a matrix describing the relation between the single particle momenta of the mother (k') and the daughter (k^*) particles, evaluated in the corresponding center of mass frames. In the special case of two primary particles ($i = j = 0$) $\mathcal{T}_{k^*, k'} = 1$. The resulting total correlation function is

$$C_{X - Y}(k^*) = \sum_{i=0}^{N_{X,F}} \sum_{j=0}^{N_{Y,F}} f_{X_i} f_{Y_j} C_{X_i - Y_j}(k^*). \quad (2.30)$$

This equation is based on solid theoretical basis, and is detector independent. Nevertheless, it depends on the experimental environment, as the fractions f_{X_i} are determined by the collision energy and geometry. This dependence is non-trivial and the best approach is to determine f_{X_i} using a data-driven method, that will be introduced in chapters 3.1.4 and 3.1.5. The matrix $\mathcal{T}_{k^*, k'}$ is a simple kinematics term, which for high collision energies is only determined by the decay kinematics of the studied channel. Let us examine one simple case, namely the $p - \Lambda \rightarrow p - p$. The needed transformation is the conversion from k' of the primary particles (a proton and a Λ) into the k^* of the two measured particles (two protons, one primary and one stemming from the Λ decay). The easiest way to produce the transformation matrix is to use numerical Monte-Carlo procedure, simulating the decay. In this work we have adopted the phase-space generator integrated in ROOT called “TGenPhaseSpace” [46]. The principle is to generate protons and Λ s with random momenta, let

⁹This is just an example, all possible permutations are $X - Y$, $Z_{X_i} - Y$, $X - Z_{Y_j}$, $Z_{X_i} - Z_{Y_j}$

the Λ decay into a proton and a pion and correlate the initial $k'(\text{p}-\Lambda)$ to the final relative momenta between the protons $k^*(\text{p}-\text{p})$. It can be demonstrated that the probability for the transition $k^*(\text{p}-\Lambda) \rightarrow k^*(\text{p}-\text{p})$ is independent on the single particle momenta. Indeed, in the absence of any polarization, the decay of the Λ does not have a preferred direction, as such there cannot be any correlation of the decay kinematics between the different k^* bins, apart from trivial phase space constraints that are only depending on the masses of the particles involved. Thus $\mathcal{T}_{k^*, k'}(\text{p}-\Lambda \rightarrow \text{p}-\text{p})$ can be generated with any choice of initial momenta. The matrix generated in the present example, and used in all presented analyses containing this feed-down channel, is shown in Fig. 2.8. To perform the transformation from a specific k' to k^* , the integral

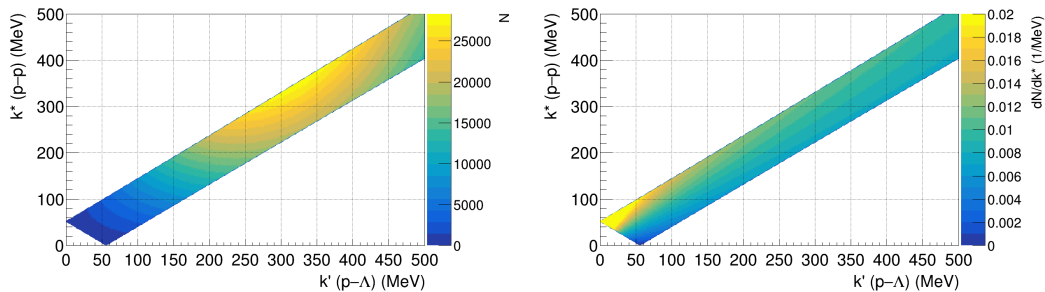


FIGURE 2.8: The feed-down matrix, converting the initial $\text{p}-\Lambda$ k' to the measured k^* of the $\text{p}-\text{p}$ pair. The left panel shows the raw generated matrix, for which the x, y, z components of the initial single particle momenta were generated from a Gaussian distribution of mean 0 and standard deviation of 350 MeV. The right panel represents the same matrix, normalized such to represent the probability to transform $k' \rightarrow k^*$.

of the corresponding projection onto k^* has to be normalized to unity. The resulting matrix is shown in the right panel of Fig. 2.8, while the individual projections evaluated at several k' values are shown in Fig. 2.9. A low initial k' is transformed to a higher k^* , leading to a redistribution of the original correlation signal onto a large k^* range, ultimately producing a residual correlation function much flatter than the original signal, as seen in Fig. 2.9. Throughout the analyses presented in this work

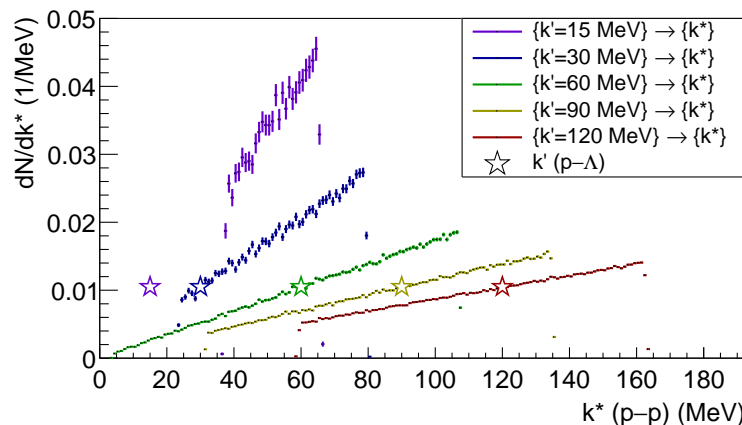


FIGURE 2.9: The projections of the normalized feed-down matrix (right panel in Fig. 2.8) onto k^* for different initial k' . The value of the latter is represented by the stars.

there are multiple feed-down channels investigated, for which the evaluation of the

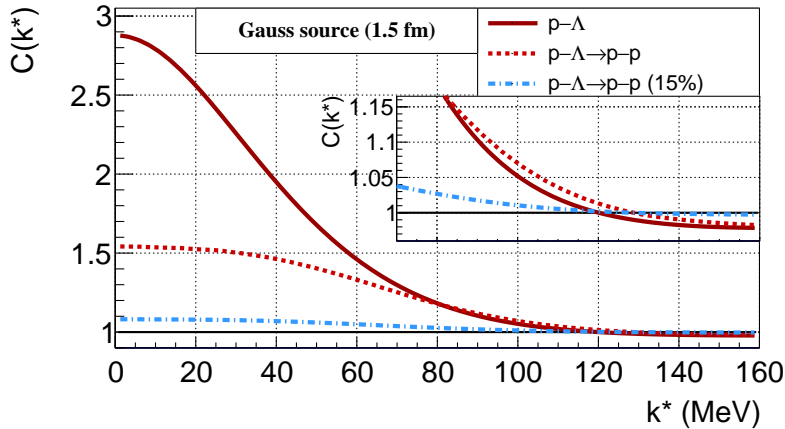


FIGURE 2.10: Comparison between the genuine $p-\Lambda$ and residual $p-\Lambda \rightarrow p-p$ correlation functions (red lines). The dashed-dotted blue line is the residual correlation scaled down by 8%. The emission source is a Gaussian of size 1.5 fm, and the interaction is modeled using the Usmani potential [60].

transformation matrices is done with the same prescription.

To compute the full correlation function the needed ingredients are all feed-down contributions to the particle pair, the corresponding fractions and the original correlation functions between X_i and Y_j (Eq. 2.30). In practice this is not feasible, since one cannot have experimental access to all feed-down correlations, neither a reliable theoretical modelling. In many practical cases this is not an issue as the transformation matrix tends to flatten the correlation signal by a significant amount. Moreover if the fractions are low, the contribution to the total correlation signal becomes insignificant. Fig. 2.10 demonstrate this feature, by showing the residual correlation function related to $p-\Lambda \rightarrow p-p$, before (red dotted line) and after (blue dashed-dotted line) re-scaling by the corresponding fractions, which are chosen realistically, based on the subsequent analysis of ALICE data from minimum bias pp collisions at 13 TeV. The amount of primary protons is assumed to be 87%, while the amount of protons stemming from Λ s is 8.8%. In addition, it is assumed that only 1/2 of the Λ s are primary, while the rest stem from (flat) feed-down. The resulting modulation (8%) of the correlation function computed using Eq. 2.30, taking both the combinations $f_{X_i} = 0.87, f_{Y_i} = 0.088 \cdot 0.5$ and $f_{Y_i} = 0.87, f_{X_i} = 0.088 \cdot 0.5$.

An important remark, is the presence of *non-direct feed-down*, such as $p-\Xi \rightarrow p-\Lambda \rightarrow p-p$. This is reflected in the fact, that the functions $C_{Z_{X_i}-Z_{Y_j}}(k^*)$ in Eq. 2.29 should not be considered as genuine correlations between the particles Z_{X_i} and Z_{Y_j} , but should themselves be corrected for the effect of feed-down. This recursive relation is implemented in the CATS framework, an example of which is provided in appendix A.7. The feed-down into heavier particle is much smaller or not present, allowing to choose a suitable cut-off scale beyond which any higher order residual correlations are neglected.

2.7.2 Misidentifications and λ parameters

Up to this point, our discussion neglected the misidentified or falsely reconstructed particles. These can be treated similarly as the feed-down contributions, with the notable difference that there is no kinematic smearing involved (Eq. 2.29), i.e. $\mathcal{T}_{k^*,k'} =$

1 and $C_{X_i-Y_j}(k^*) = C_{Z_{X_i}-Z_{Y_j}}(k^*)$. This could lead to a significantly non-flat shape of $C_{X_i-Y_j}(k^*)$ (Eq. 2.30) associated with the misidentifications. The quantification of these contributions is done by following the prescription in [38]. In this notation, depending on the sub-index of i associated with the yield of X_i is

$$X_i = \begin{cases} \text{primary} & \text{for } i = 0, \\ \text{feed-down} & \text{for } 1 \leq i \leq N_{X,F}, \\ \text{misidentified} & \text{for } N_{X,F} \leq i \leq N_{X,F} + N_{X,M}, \end{cases} \quad (2.31)$$

where $N_{X,F}$ ($N_{X,M}$) correspond to the number of feed-down (misidentified) sources associated with the production (measurement) of particle X . The total number of primary, feed-down and misidentified particle is X_0 , X_F and X_M respectively, where

$$X_F = \sum_{i=1}^{N_{X,F}} X_i, \quad (2.32)$$

and

$$X_M = \sum_{i=1+N_{X,F}}^{N_{X,F}+N_{X,M}} X_i, \quad (2.33)$$

If $X = X_0 + X_F + X_M$ corresponds to the total number of particles, the probability for the origin of the particle is

$$P(X_i) = X_i / X. \quad (2.34)$$

For a particle pair $X-Y$ the contribution to the correlation function related to the origin of the particles is defined as

$$\lambda_{i,j} = P(X_i)P(Y_j), \quad (2.35)$$

where $\lambda_{0,0}$ corresponds to the amount of genuine signal in the correlation function. Based on the definition of $P(X_i)$ and $P(Y_j)$

$$\sum_{i,j} \lambda_{i,j} = 1. \quad (2.36)$$

These λ *parameters* are an essential component in the decomposition of the correlation function, and carry the full information about the feed-down and misidentifications. With the inclusion of the latter, Eq. 2.30 is modified to

$$C(k^*) = \sum_{i=0}^{N_{X,F}+N_{X,M}} \sum_{j=0}^{N_{Y,F}+N_{Y,M}} \lambda_{i,j} C_{X_i-Y_j}(k^*), \quad (2.37)$$

where the sum over i,j is now running both over the feed-down and misidentification channels related to the particles X and Y . The λ parameters are often determined by the fit of the correlation signal, however this could lead to significant systematic uncertainties. To avoid this bottleneck, an independent data-driven approach was developed to evaluate the λ parameters [38]. The observables to be determined are the single particle purities, the fractional amount of feed-down contribution to each of the particle species, as well as the fractional amount of misidentifications. Using the above notation, the *purity* (impurity) is defined as

$\mathcal{P}(X) = (X_0 + X_F)/X$ ($\bar{\mathcal{P}}(X) = X_M/X$). It is beneficial to combine the two definitions as

$$\mathcal{P}(X_i) = \begin{cases} \mathcal{P}(X) = (X_0 + X_F)/X & \text{for } i \leq N_{X,F}, \\ \bar{\mathcal{P}}(X) = X_M/X & \text{else.} \end{cases} \quad (2.38)$$

The fractions are defined as

$$f(X_i) = \begin{cases} X_i/(X_0 + X_F) & \text{for } i \leq N_{X,F}, \\ X_i/X_M & \text{else,} \end{cases} \quad (2.39)$$

leading to

$$P(X_i) = \mathcal{P}(X_i)f(X_i) = \frac{X_i}{X}. \quad (2.40)$$

The λ parameters can now be expressed based on measurable single particle quantities (Eq. 2.35 \oplus 2.40)

$$\lambda_{i,j} = \mathcal{P}(X_i)f(X_i)\mathcal{P}(Y_j)f(Y_j), \quad (2.41)$$

where the purities \mathcal{P} and fractions f can be fixed from the data. More details on their experimental determination are presented in chapters 3.1 and 3.3. If the purity in the analyzed sample is high enough, any non-flat contribution to the correlation signal will be masked by the statistical uncertainties of the data. However, if the purity is lower, the correct shape of the background signal should be obtained. If the source of the impurities is known and can be modeled theoretically, they can be trivially accounted for by using Eq. 2.37. If the background is not known, as often the case for particles reconstructed via the invariant mass technique, a very powerful approach to measure the correlation related to the background is performing a *sideband* analysis. The methodology is to select particle candidates outside of the expected invariant mass region, which results in a highly impure sample. The correlation function of the resulting particle pairs will be approximately equal to the pure background signal $C_{X_i-Y_j}(k^*)$ in the studied system. Further details on this procedure can be found in the theses of my colleagues Andreas Mathis and Bernhard Hohlweger [61, 62], as well as in chapter 3.3.3.

2.7.3 Momentum resolution

In this subsection we will discuss the effect of the finite **momentum resolution** on the correlation function. The momentum smearing depends only on the final particle species, and is thus independent of the feed-down effects. Similarly to the modeling of feed-down (Eq. 2.29), the momentum smearing is applied via a matrix of the form $\mathcal{M}_{k^*,k'}(X_i Y_j \rightarrow XY)$. To obtain the total correlation function one would still use Eq. 2.37, with the functions $C_{X_i-Y_j}(k^*)$ (Eq. 2.29) defined as

$$C_{X_i-Y_j}(k^*) = \int \mathcal{M}_{k^*,k'}(X_i Y_j \rightarrow XY) \mathcal{T}_{k^*,k'}(X_i Y_j \rightarrow XY) C_{Z_{X_i}-Z_{Y_j}}(k') dk', \quad (2.42)$$

where

$$\mathcal{M}_{k^*,k'} = \begin{cases} \mathcal{M}_{k^*,k'}(X_0 Y_0 \rightarrow XY) & \text{for } i \leq N_{X,F} \text{ and } j \leq N_{Y,F}, \\ \mathcal{M}_{k^*,k'}(X_i Y_j \rightarrow XY) & \text{else} \end{cases} \quad (2.43)$$

and

$$\mathcal{T}_{k^*,k'} = \begin{cases} \mathcal{T}_{k^*,k'}(X_i Y_j \rightarrow XY) & \text{for } i \leq N_{X,F} \text{ and } j \leq N_{Y,F}, \\ 1 & \text{else.} \end{cases} \quad (2.44)$$

Note, that Eq. 2.43 implies the smearing matrix is independent of the feed-down, nevertheless it can differ among the different types of misidentifications. The momentum smearing matrix is extracted from full scale Monte-Carlo simulations of the detector response. An example of such a matrix for the p-p correlation is shown in Fig. 2.11. This matrix is normalized to represent the probability to reconstruct a specific initial k' onto k^* . Fig. 2.12 shows several projections of this matrix. The resolution effect is approximately Gaussian, which can be used to model the resolution analytically. The effect of the smearing on the theoretical p-p correlation function is shown in Fig. 2.13. The effect is rather pronounced at low k^* , due to the highly non-linear functional shape of the correlation function. The effect of the smearing is much smaller for smooth functions, such as the p- Λ correlation. Examples of the technical implementation in CATS is available in appendix A.7.

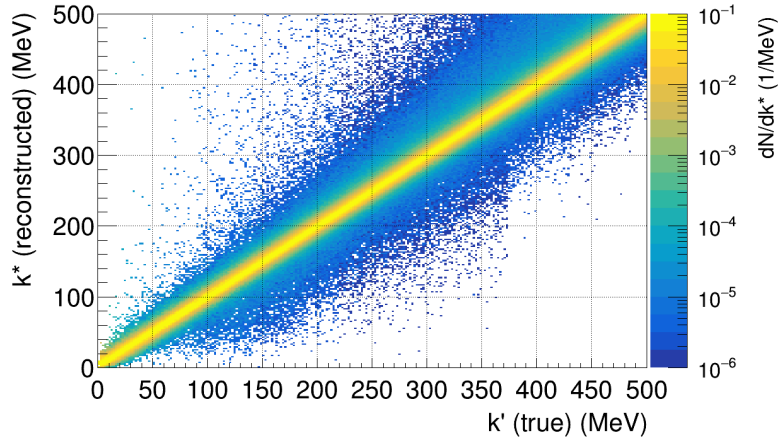


FIGURE 2.11: The momentum smearing matrix for p-p, extracted from MC simulations. The projections onto k^* are normalized for each k' .

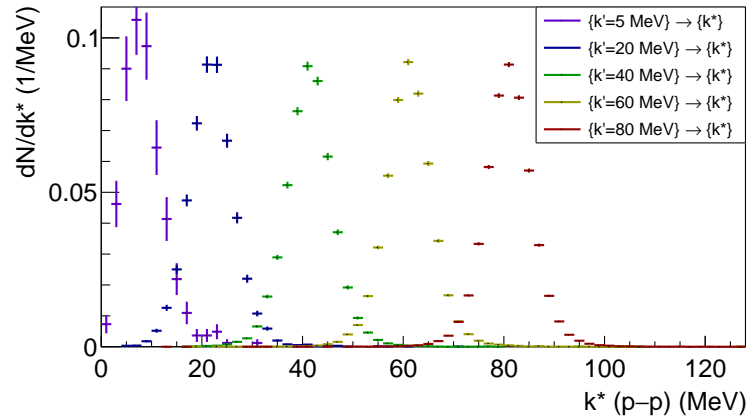


FIGURE 2.12: The projections of the momentum smearing matrix for p-p (Fig. 2.11) onto k^* for different initial k' . The shape is approximately Gaussian, although at low momenta it is affected by edge effects, resulting in longer tails.

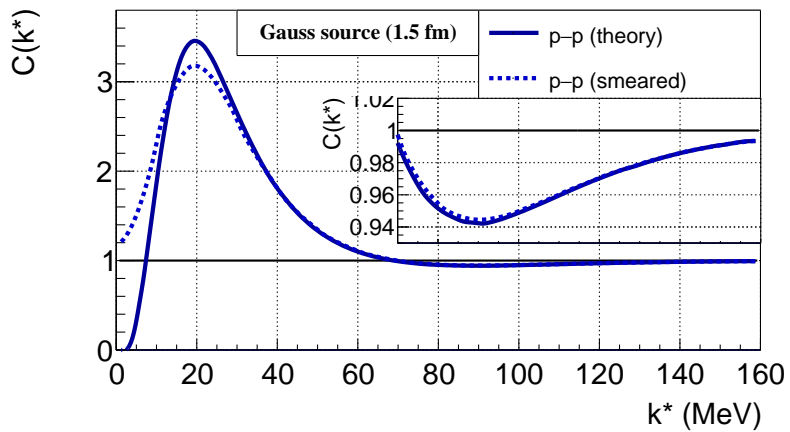


FIGURE 2.13: Comparison between the theoretical p-p (solid line) and smeared (dotted line) correlation functions. The emission source is a Gaussian of size 1.5 fm, and the interaction is modeled using the Argonne v_{18} potential [7].

Chapter 3

Experimental data

In this chapter the attention is on the experimental aspects of this thesis. The first section serves as an overview of the general physics opportunities at the LHC, focusing on the opportunities to perform correlation studies. Section 3.1 will focus on the ALICE¹ experiment, which was used to obtain the data used in the present work. The reconstruction of the correlation function, and the methods associated with it, are embedded in the “FemtoDream” framework². The remaining section in this chapter will discuss the details related to this particular work, which need to be considered in the analyses of Λ - Λ and p- Λ correlations presented in chapters 5 and 6.

The CERN complex is situated near Geneva, Switzerland, and hosts the largest accelerator complex existing on the planet as of 2020. The largest machine is the *Large Hadron Collider (LHC)*, designed to collide protons and/or heavy ions at total collision energies of up to 14 TeV. The main motivation for building the LHC was the study of open fundamental questions in particle physics, in particular related to the *standard model* and theories beyond. The standard model of particle physics is a gauge quantum field theory, used to describe the electroweak and strong interactions. The mathematical representation is given by the unitary product group $SU(3) \times SU(2) \times U(1)$, where the $SU(3)$ component relates to the strong interaction. The “picture” of the standard model is plotted in Fig. 1.1 (chapter 1.2).

The discovery of the *Higgs boson* has been viewed as a big success both for the LHC and standard model [63]. Nevertheless, the known shortcomings of this model lead to expectations of finding experimental clues supporting theories beyond the standard model, such as supersymmetry, extra dimensions etc [64]. For this reason, the absence of evidence from the LHC supporting these theories has been disappointing for many physicists, however the experiments operating at these high energies have very rich physics programs, that are not limited to the above topics. The unprecedented amount of collected data compared to any previous collider experiment allow to study in details the kinematic distributions of the produced particles, which can be linked to the properties of the initial energy density of the colliding matter, the subsequent evolution of the produced quark gluon plasma (QGP) and the hadronization process. To achieve this, it is highly beneficial to study the separate types of particles deferentially, which requires a detector with good particle identification (PID) capabilities. As it will become evident in the next section, the best experiment for this purpose is ALICE. Further, the femtoscopy technique can be applied

¹A Large Ion Collider Experiment

²Disclaimer: “FemtoDream” was developed by my colleagues Andreas Mathis and Bernhard Hohlweger [61, 62]. The reconstruction of the proton and Λ particles is based on their default recommendation for data sets, selection criteria etc.

to study the interaction and/or emission source of any particle pairs among the produced species, which also requires good PID. For this reason the ALICE experiment provides the perfect environment to study both the QGP formation, as well the final state interaction between the particles. Regarding the latter, the ALICE collaboration described itself as “A new laboratory to study hadron-hadron interactions” [45], while I would add that a good alternative abbreviation for the experiment would be *A new Laboratory to Investigate and Constrain Exotic hadron-hadron interactions*.

3.1 ALICE

This section highlights the main features of the ALICE detector, and the methods used for particle reconstruction, including creating the same- and mixed-event pairs to be used for femtoscopic analysis. The latter is mostly related to the work of my colleagues Andreas Mathis and Bernhard Hohlweger, which developed the “FemtoDream” section within the analysis framework of ALICE, called *AliPhysics*, and discussed in details in their theses [61, 62]. The present work provides an exclusive summary of the most important aspects of the data reconstruction, which is typically divided into 3 stages: i) direct detection of charged particles (such as pions, kaons and protons); ii) reconstruction of ‘V0’ particles decaying into two charged daughters (e.g. $\Lambda \rightarrow p\pi^-$); iii) reconstruction of ‘cascade’ particles, decaying into a V0 and a charged daughter (e.g. $\Xi^- \rightarrow \Lambda\pi^-$). This work concentrates on p- Λ and Λ - Λ correlations, thus only the reconstruction of protons and Λ will be discussed, although the methods can be generalized to any directly detected charged particle or V0. The reconstruction of the cascades has many similarities to the treatment of the V0 candidates, however it is omitted from the discussion as it is irrelevant for the scope of the presented analyses.

3.1.1 Overview

ALICE (A Large Ion Collider Experiment) is one of the four major experiments installed at the LHC. It is the only dedicated heavy-ion experiment, with the main physics motivation of studying the state of matter at extreme temperatures, at which QGP is expected to be produced. The experiment has 19 sub-detector systems, from which the most unique one, compared to the rest of the LHC experiments, is the large Time Projection Chamber (TPC) allowing for very precise tracking, good particle identification capabilities and sensitivity to very low momentum particles (down to *transverse momentum*³ of c.a. $p_T = 0.2$ GeV/c) due to the lower magnetic field (0.5 T) inside the detector. The limiting factor for ALICE is the low interaction and data read-out rates, the latter being limited to only ~ 1 kHz, which is 100 times lower compared to the ATLAS experiment. This is due to the ~ 1 μ s time span of reading out a single event, during which the detector is not recording any further collisions. The ALICE detector and its performance is described in details in [65–68], in the following a brief summary of the detectors relevant for the femtoscopy studies will be presented, in particular the triggering system, the tracking and particle identification detectors. The central detectors, mainly responsible for tracking and PID, are designed in a cylindrical shape oriented parallel to the beam pipe providing full azimuthal coverage (Fig. 3.1). The polar acceptance is typically measured in units of *pseudorapidity* $\eta(\theta) = -\ln[\tan(\theta/2)]$. This observable is anti-symmetric around the direction perpendicular to the beam pipe, i.e.

³The transverse momentum p_T is momentum in the direction perpendicular to the beam axis.

$\eta(\pi/2 + \theta') = -\eta(\pi/2 - \theta')$, and is very convenient to describe the geometry of the detector. A pseudorapidity of η close or equal to zero represents particle emitted in the transverse beam direction ($\theta \approx \pi/2$), and is described as *mid-rapidity*. Particles emitted flying in the beam direction ($|\eta| \gtrsim 1$)⁴ are described as forward ($\eta > 0$) and backward ($\eta < 0$) rapidity. The central detectors of ALICE are designed to measure the particles emitted at mid-rapidity ($|\eta| \lesssim 1$). A schematic representation of the ALICE detector is shown in Fig. 3.1.

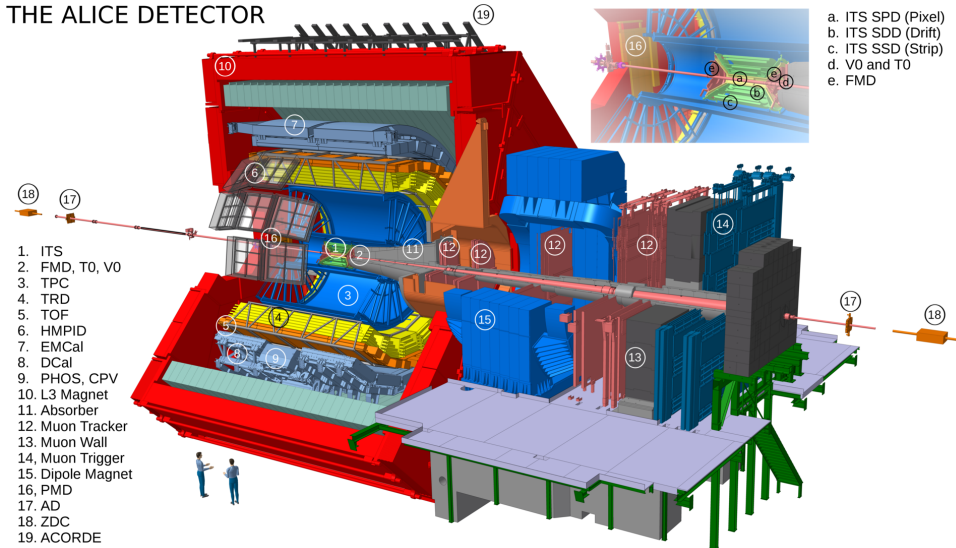


FIGURE 3.1: Schematic representation of the ALICE detector during the Run-2 data taking period (2015-2018) [69].

Triggering system

The *triggering system* is responsible for activating the read-out sequence in case an interesting event occurs. There are multiple triggering conditions, depending on the desired physics case [68]. The most basic condition is the *minimum-bias trigger* (MB), which ideally should not introduce any physics bias towards the event, and activate at the presence of any collision between the beams. The other trigger types are collectively called 'rare', and they have a more specific physics driven condition. To enhance the statistics of certain type of events during the data taking the MB trigger can be switched off in favour of the rare triggers. As the amount of recorded events is limited by the long read-out time, and not by the interaction rate of the colliding beams, the rare triggers can exploit the 1 kHz read-out rate, allowing to obtain large amount of statistics for studying special physics cases. In particular, for non-traditional femtoscopy the *high-multiplicity trigger* (HM) in pp collisions is extremely useful to boost the amount of reconstructed particle pairs. The HM events are triggered, on average, at the presence of 30-40 charged particles per unit of rapidity, leading to more combinatorial possibilities to build the particle pairs of interest. Moreover, at large multiplicities in pp reactions the relative amount of particles containing strange quarks is significantly increased [6], which benefits studies of particle pairs such as p- Λ , Λ - Λ , p- Ξ^- , p- Ω^- etc.

The main sub-system of ALICE responsible for the triggering are the V0 detectors,

⁴A good "pocket number" to remember is $\eta(\pi/4) \approx 0.9$

which are two plastic scintillator arrays placed on both sides of the interaction point. The V0A detector is located at 3.4 m from the interaction point, covering the pseudorapidity range of $2.8 < \eta < 5.1$, while the V0C detector is located at -0.9 m, covering $-3.7 < \eta < -1.7$. The V0 system provides only information about traversing charged particles and are used as counters. They provide the information required by the MB condition, and the commonly used 'V0AND' trigger is activated if coincident hits produced by charged particles are present in both of the V0A and V0C scintillators. The HM trigger is also activated by the V0 system, however a higher amount of minimal hits is required. In the present analysis the HM trigger condition used is called 'kHighMultV0', and the V0 threshold is tuned such that 0.17% of the highest multiplicity events with at least one measured charged particle within $|\eta| < 1$ are selected.

Inner Tracking System

The *Inner Tracking System* (ITS) is the most inner central detector, located at radii between 3.9 and 43.0 cm from the beam interaction point. It consists of 3 lightweight silicon based sub-systems, called Silicon Pixel Detector (SPD), Silicon Strip Detector (SSD) and Silicon Drift Detector (SDD). The total coverage in pseudorapidity is $|\eta| < 0.9$, however the SPD can detect particles up to $|\eta| = 1.95$. Fig. 3.2 shows the basic layout of the ITS. The primary strength of this detector is its ability to re-

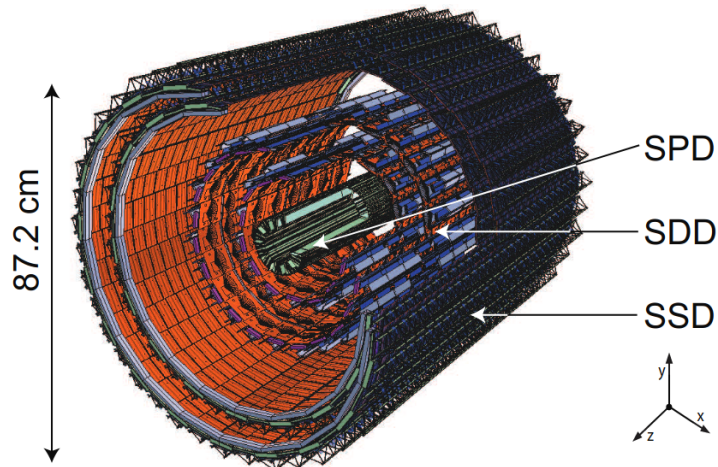


FIGURE 3.2: The Inner Tracking System of ALICE.

construct the trajectories of the emitted particles with high precision, which allows to locate the interaction point of the colliding beam particles (**Primary Vertex (PV)**) with a precision of less than $100 \mu\text{m}$ and constrain the direction of the momentum of the emitted charged particles. Moreover, the reconstruction and localization of secondary vertices, such as from decays of hyperons, benefits from matching the information about the daughter tracks measured by the other detectors to the ITS, leading to improved momentum reconstruction, higher purity and rejection of possible *pile-up* events⁵. Compared to the other central detectors in ALICE, the ITS has the unique ability to measure very low momenta particles, with p_T down to $0.1 \text{ GeV}/c$.

⁵A pile-up event consists of tracks that stem from different physical collisions, that were wrongly reconstructed in the same event. The fast read-out of the ITS helps to reject such events.

Time Projection Chamber

The *Time Projection Chamber* (TPC) is the main detector system of the ALICE experiment. It is located in the central barrel after the ITS, cylindrical in shape extending from 85 to 247 cm from the interaction point. It covers the pseudorapidity range of $|\eta| < 0.9$. The schematic layout of the TPC is shown in Fig. 3.3. It has a volume of

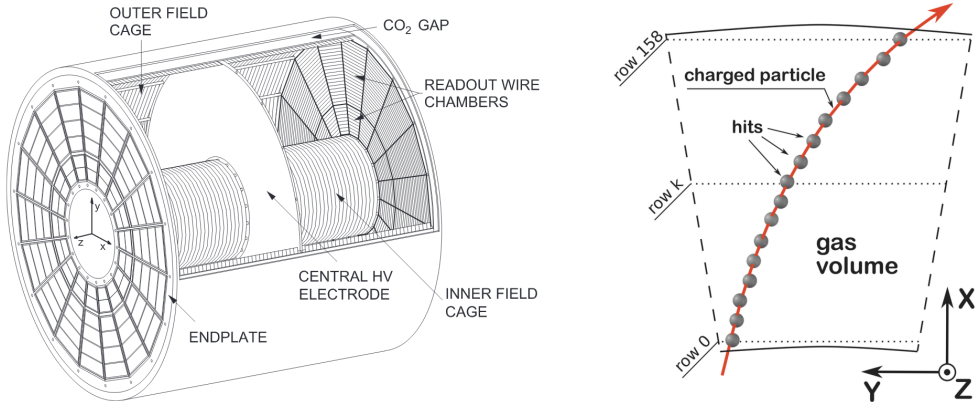


FIGURE 3.3: The ALICE Time Projection Chamber. The left panel represents a schematic layout of the device [70], while the right panel shows an exemplary sketch of a reconstructed track [71].

90 m³ filled with gas and is divided into two drift regions characterized by an electric field of 400 V/cm. Charge particles traversing the detector ionize the gas and the resulting electrons drift towards the two endplates of the detector, where the signal is amplified and readout. The amplitude of the detected signal can be used to infer the energy loss of the traversing particle, which will be used for the PID. A single particle can result in up to 159 charge clusters, which are interpreted as individual spatial points (hits) of the trajectory of the particle (track). The xy position of each hit is determined by the location of the collected charge cluster in the endplate, while the z position is determined from the time offset between the initial event collision time and the time at which the electrons reached the endplate. The drift velocity of the electrons is 2.7 cm/ μ s, resulting in a maximum drift time of 92 μ s. To reconstruct an event, the readout chambers are activated for the first 100 μ s after the collision, while for the following 200 μ s a gating grid is used to electrically separate the amplification from the drift region, allowing to neutralize all ions created during the amplification stage. In total, this leads to a maximum readout time per event of 300 μ s, resulting in a maximum readout rate of 3-4 kHz. This is the main factor limiting the data collection rate of ALICE, nevertheless it is a necessary compromise as the TPC represents the best technological device capable of providing robust tracking and *PID performance*, capable of coping with the simultaneous reconstruction of up to 10000 charged particles per event, as occurring in the most central Pb–Pb collisions. Recent advances in the research and development of the TPC technologies, mostly related to a GEM based read-out, have led to the possibility to upgrade the device to record the data at a rate of 50 kHz, which will significantly increase the performance of the detector for the data taking periods starting in 2021 [61].

The full reconstruction of a track requires knowledge on the spatial coordinates of the hits (right panel in Fig. 3.3) and on the energy loss based on the amount of charge collected during the readout. The momentum reconstruction is done by measuring the bending radius of the track, which is related to the applied magnetic field and

the momentum over charge ratio of the particle, while the particle identification is performed by using the Bethe-Bloch equation, which is given by the relation

$$\left\langle \frac{dE}{dx} \right\rangle = A_1 \cdot \frac{z^2}{\beta^2} \left[\ln \left(A_2 \cdot \frac{\beta^2}{1 - \beta^2} \right) - \beta^2 \right], \quad (3.1)$$

where $A_{1,2}$ are constants depending on the properties of the material (gas), while z and β are the charge number and velocity of the particle. Relating the velocity to the momentum p and mass m of the particle ($p = m\beta / \sqrt{1 - \beta^2}$) Eq. 3.1 becomes

$$\left\langle \frac{dE}{dx} \right\rangle = A_1 \cdot z^2 \cdot \frac{m^2 + p^2}{p^2} \left[\ln \left(A_2 \cdot \frac{p^2}{m^2} \right) - \frac{p^2}{m^2 + p^2} \right]. \quad (3.2)$$

Equation 3.2 implies that the average measured energy loss, as a function of the mo-

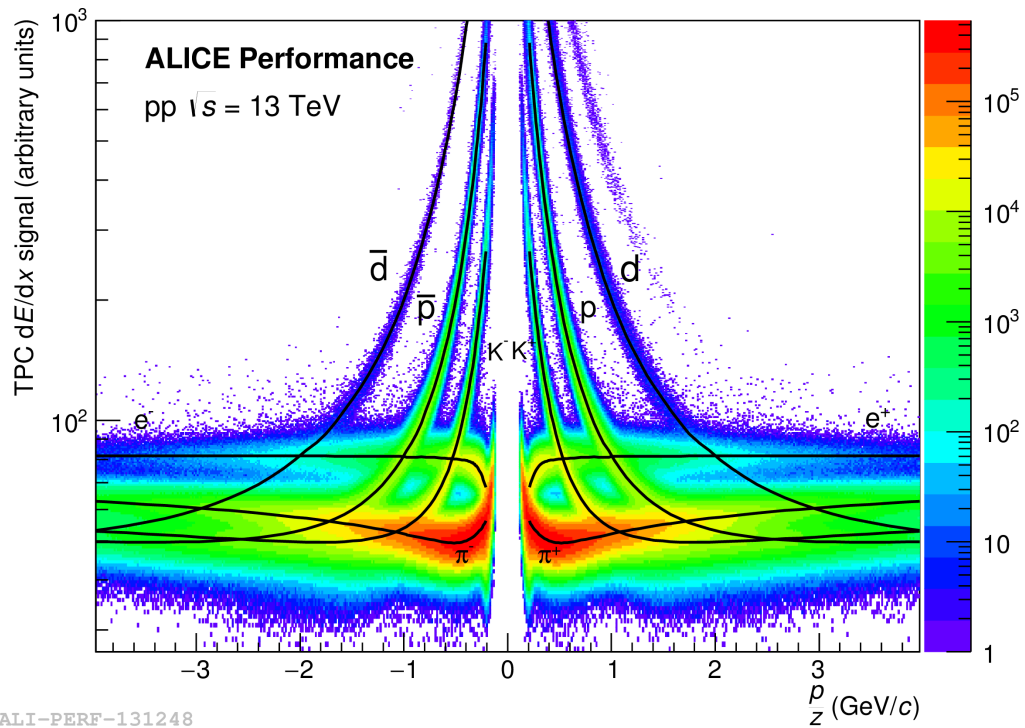


FIGURE 3.4: The energy loss as a function of momentum over charge, as measured by the ALICE TPC for pp collisions at 13 TeV.

mentum, has different functional shape depending on the mass of the particle. This property is used to determine the mass, and consequently species, of the particle based on its measured momentum and energy loss. Fig. 3.4 shows the corresponding ALICE performance plot for the TPC, where the black lines are the theoretical predictions for $\langle dE/dx \rangle (p)$ evaluated assuming the masses of the electrons, pions, kaons, protons and deuterons. The colors on the plot represent the measured amount of tracks (increasing from blue to red) with a specific $\langle dE/dx \rangle (p)$. As expected, the measured yield is clustered in several bands, each following the theoretical prediction of a specific mass hypothesis, allowing the particle identification. The width (σ) of each band is related to the resolution of the TPC. At small momenta (below c.a. 1 GeV/c) the individual particles (bands) are separated quite well, however at larger momenta the resolution becomes insufficient to perform the PID. This issue can be addressed by using complementary information from other detectors, such as the Time-Of-Flight, to obtain better resolution at large momenta, at the expense of

reduced tracking efficiency and acceptance. To determine the best mass hypothesis in this work each particle is assigned a n_σ parameter measuring the discrepancy in number of σ (resolution) between the theoretical expectation to measure $\langle dE/dx \rangle (p)$ for a given particle species and the measured value.

Time-Of-Flight detector

In the analyses presented in this work the outer most central barrel detector used is the *Time-Of-Flight* (TOF). It is located at a radial distance of 370 to 399 cm from the interaction point and has the same coverage in pseudorapidity as the TPC ($|\eta| < 0.9$). The TOF measures the arrival time of the particles, allowing to determine the time of flight from the interaction point to the detector and consequently the velocity of the particle. By combining this information with the momentum measurement from the other detectors the mass can be evaluated

$$m = p \sqrt{\beta^{-2} - 1}. \quad (3.3)$$

Eq. 3.3 implies a unique functional relation between the velocity and momentum of the particle for different masses. Similarly as to the particle identification using the energy loss in the TPC, the TOF detector can be used to perform PID by plotting $\beta(p)$ and the associated measured bands (Fig. 3.5) corresponding to the different particle species. In contrast to the TPC, the separation power for the different mass hypothe-

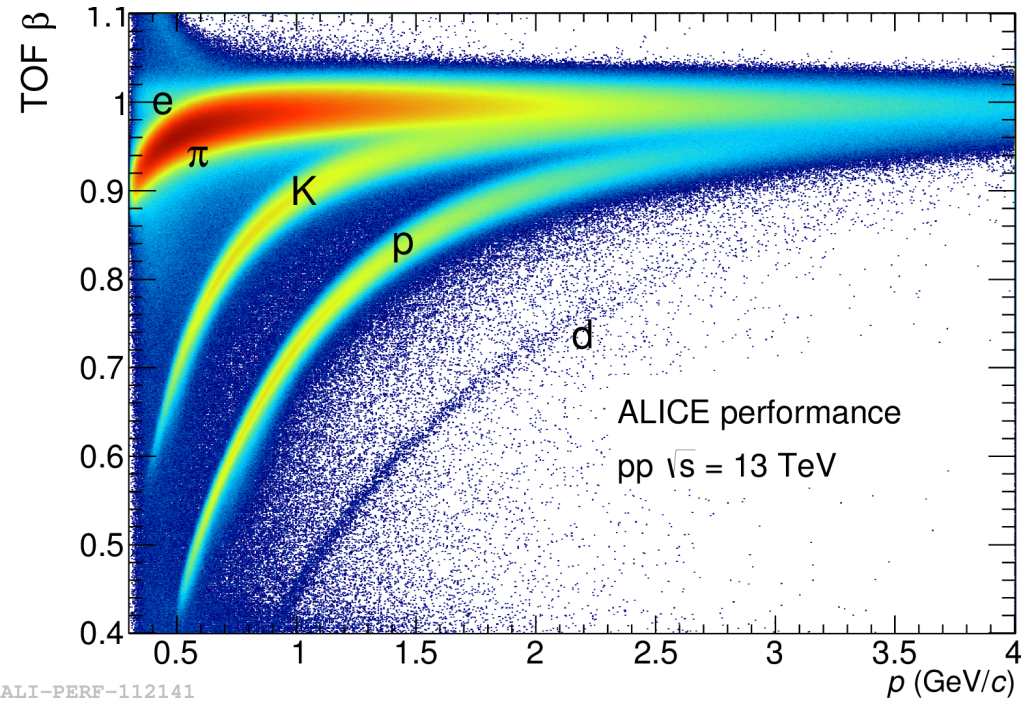


FIGURE 3.5: Particle identification using the Time-Of-Flight detector.

ses extends to higher momenta, allowing to separate protons from pions even up to $4 \text{ GeV}/c$. However, as the Time-Of-Flight detector is located further away from the interaction point, it has lower reconstruction efficiency due to the increased probability of particle absorption before it reaches the detector and a reduced acceptance for low momentum particles, as they can be curled back into the TPC by the magnetic field. Moreover, to reconstruct a particle using both the TPC and the TOF, the track hits in both detectors need to be matched, leading to further reconstruction

inefficiencies. Hence a significant amount of tracks, in particular at low momenta, are lost if the combined TPC and TOF information is used to perform the PID. Thus the analyses in this work require the TOF information only for particles with higher momenta, while the low momentum particles are identified only by using the TPC. Depending on the usage of the TOF, the n_σ related to a specific mass hypothesis is defined as

$$n_\sigma = \begin{cases} n_{\sigma, \text{TPC}} & \text{using TPC only,} \\ \sqrt{n_{\sigma, \text{TPC}}^2 + n_{\sigma, \text{TOF}}^2} & \text{using TPC and TOF.} \end{cases} \quad (3.4)$$

Further details on the usage of the n_σ parameter will be provided in section 3.1.4.

3.1.2 Basics of the ALICE data structure

Overview

The software framework used to handle all reconstruction procedures is based on ROOT, and called *AliRoot*. The first stage of the particle reconstruction begins with the actual data taking, which is the acquisition of raw data during the LHC beam times. The data taking is divided into individual *runs*, each typically lasting from several minutes to few hours, during which the configuration of all ALICE sub-detectors is fixed. The operators in the ALICE control room are monitoring the sub-systems and perform basic quality assurance tests, which dictates the decision making on starting or stopping a run and changing the configuration of the detector systems. The information of the run conditions is stored, as it is vital for the following calibration of the data. The following data reconstruction consists of multiple steps, which are the initial analysis for cluster finding (track hits), estimation of the primary vertex location using the SPD information, track reconstruction of the charged particles⁶ using a Kalman filter, re-evaluation of the location of the primary vertex based on the reconstructed tracks, search for tracks that could stem from a secondary (decay) vertex and combine them into potential particle candidates (V0s, representing K^0 s and Λ s) and finally search for possible cascade decays into a V0 and a charged particle (Ξ^- and Ω^-). In addition, all steps before and including the tracking need to undergo a calibration process, in which the data is corrected for detector effects. The first two stages of the calibration (*CPass0* and *CPass1*) are done automatically promptly after the data taking. If required, follow-up re-calibrations can be performed manually at any given later stage, although these are done only if an essential problem is found, as they will bias existing results based on *CPass0* or *CPass1*. Finally, the information used for the reconstruction is saved in *ESD* files and saved on the CERN computing grid⁷. This workflow is schematically summarized in Fig. 3.6.

AOD files

The *ESD* files are large and resource intensive, for this reason they are further filtered into *AOD* files, which are the main source for physics analysis. In simple terms, the

⁶Only long lived particles can be reconstructed, the prime examples are electrons, muons, pions, kaons and protons.

⁷The network of all computing resources available to the institutes participating to experiments at CERN.

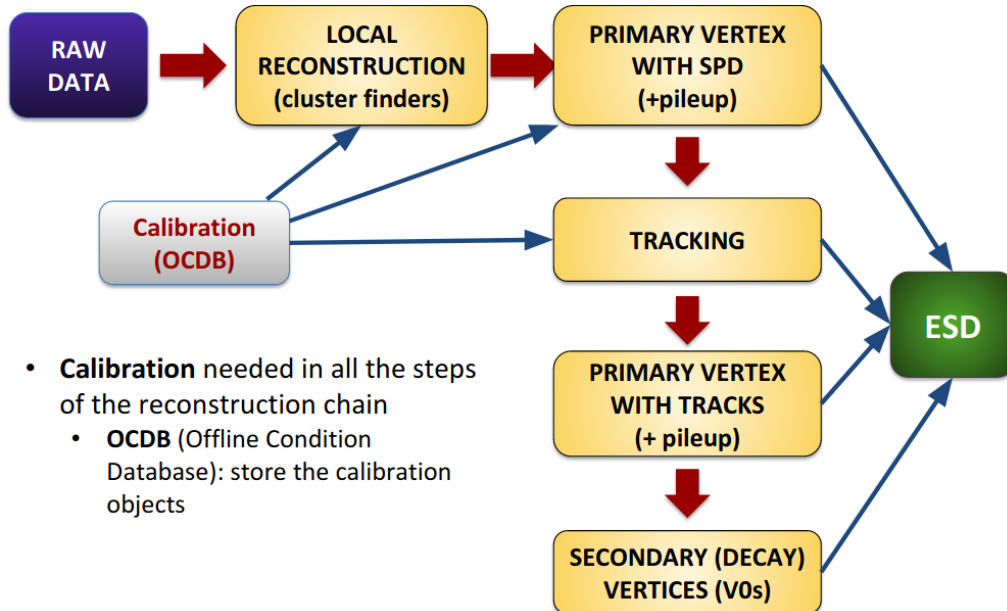


FIGURE 3.6: Workflow of the data reconstruction in ALICE.

information in the AOD is reduced to the observables relevant for physics (momentum, charge, etc.), the topological properties of the tracks (e.g. closest distance to the primary vertex) and only the most relevant observables used to estimate the quality of the track reconstruction (e.g. number of hits in the TPC, shared hits between the tracks, etc.) is saved. In addition to the tracks, the basic characteristics of the underlying event is also stored, such as the multiplicity estimation. Notably, the track in each event can be reconstructed using different criteria, resulting in slightly different tracks in the final event. Depending on the requirements of the specific analysis a specific track reconstruction could be favoured, for this reason the AOD files introduce a filter-bit (FB) mask for each track, storing the information whether the track satisfies a certain set of quality criteria. The most commonly used filter-bits are 96 and 128, where the former represents the *global tracks* and the latter the *TPC-only tracks*. The global tracks are build by using the combined information between the ITS and the TPC, where the first hit in the ITS has to be within SPD or SDD. The TPC-only tracks are constrained to the SPD vertex, however the tracking and momentum determination is based only on the information from the TPC. These filter-bits are not exclusive and cannot be used together. In femtoscopy analyses the default choice is to use the TPC-only tracks, as in Pb-Pb collisions there is a known issue of global tracks sharing clusters in the ITS as well inhomogeneous performance of the detector due to dead sectors. This leads to poorer reconstruction of particle pairs located at close momenta, which are the only physics wise relevant particles for femtoscopy. In the pp data collected at 13 TeV these effects are reduced, nevertheless to remain conservative all analyses presented in this work will use the momentum information of the particles reconstructed with TPC only. The main issue of using the TPC-only tracks is the reduced spatial resolution of the track, which leads to a poorer determination on the distances between the tracks and/or vertices. In the present work, this is resolved by adopting a “hybrid” approach, in which the selected TPC-only tracks are required to have a matching global track used to extract the corresponding topological information.

For some data taking periods even the AOD files are too heavy for the available

computing resources, requiring further filtering of the data in order to optimize the analysis. Such filtering is analysis specific and the resulting output files are called *nanoAODs*.

Monte-Carlo simulations

Several steps of the femtoscopy analysis require the availability of full-scale Monte-Carlo (MC) simulations, meaning a simulation of the collision system (event by event), the subsequent transport through the detector material, response of the read-out electronics, calibration and data-filtering leading to the final AOD files. These simulations provide the full information about the initially generated event and the corresponding reconstructed tracks, allowing to understand the response of the detector. In particular, these MC results are used to study the resolution effects of the detector (sec. 2.7.3), to determine the fraction of secondary feed-down particles (sec. 3.1.4 and 3.1.5) and the purity of the detected charged particles, all of which are essential to perform a comparison between theoretical predictions and the experimentally measured correlation function. The ALICE collaboration provides multiple sets of general purpose MC simulations, each anchored to the experimental conditions of the different data taking periods. In the present analysis the collision system is simulated using Pythia 8 [72], while the transport through the detector is modeled with Geant 3 [73]. The detector response is simulated using the AliRoot package.

3.1.3 Collision systems and event cuts

In the following analyses, the two investigated particle pairs are p- Λ and Λ - Λ , which require the reconstruction of both proton and Λ particles. As previously discussed, non-traditional femtoscopy benefits from using small collision system, and if a bound state is present the shape of the correlation function varies strongly with the system size. Moreover, in small collision systems it is reasonable to assume that the emission source is similar for all emitted particles, making possible to extract the emission source from the p-p correlation function, thus reducing the uncertainties in the Λ - Λ and p- Λ analyses. The best data set to perform such studies is the statistics rich high-multiplicity data sample collected in pp collisions at 13 TeV, which became available in 2019. As the analysis of Λ - Λ started earlier, to minimize the uncertainties and enhance the sensitivity to the possible existence of a bound state multiple data sets at different source sizes were used to analyze this system, namely the MB pp collisions at 7 and 13 TeV, alongside with the p-Pb collisions at 5.02 TeV. In the present work the Λ - Λ correlation function in pp collisions at 7 TeV is used from a previous ALICE analysis [38, 51]. To analyze a specific data set, one needs to select the required trigger⁸, analyze only those data runs and recorded events that passed certain basic quality assessment criteria⁹ determined by the ALICE collaboration. Further detail can be found in chapter 3.1 of [74]. Moreover, events for which the SPD reconstructed multiple primary vertices are tagged as pile-up and rejected from the sample¹⁰. The rest of the event cuts are considered to be standard quality cuts by ALICE and listed in table 3.1.

⁸AliRoot flags: *kINT7* for the minimum biased events and *kHighMultV0* for the HM sample.

⁹AliRoot flags: *default* physics selection and *check* for an incomplete data acquisition (DAQ).

¹⁰AliRoot flags: *AliEvent::IsPileUpFromSPD()* and *AliEventUtils::IsSPDClusterVsTrackletBG()*.

Selection criterion	Value
z vertex offset	$ vtx_z < 10 \text{ cm}$
Contributors to track vertex	$N_{\text{contrib,track}} > 1$
Contributors to SPD vertex	$N_{\text{contrib,SPD}} > 0$
Distance between track and SPD vertex	$d_{\text{vtx,track-SPD}} < 0.5 \text{ cm}$
SPD vertex z resolution	$\sigma_{\text{SPD},z} < 0.25 \text{ cm}$

TABLE 3.1: Event selection criteria for the pp 13 TeV and p-Pb 5.02 TeV analyses

Selection criterion	Value
Pseudorapidity	$ \eta < 0.8$
Transverse momentum	$0.5 < p_T < 4.05 \text{ GeV}/c$
TPC cluster	$n_{\text{TPC}} > 80$
Crossed TPC pad rows	$n_{\text{crossed}} > 70$ (out of 159)
Findable TPC clusters	$n_{\text{crossed}}/n_{\text{findable}} > 0.83$
Tracks with shared TPC clusters	rejected
DCA to PV in xy	$ d_{\text{PV},xy} < 0.1 \text{ cm}$
DCA to PV in z	$ d_{\text{PV},z} < 0.2 \text{ cm}$
Particle identification	$ n_\sigma < 3$

TABLE 3.2: Track selection criteria used for proton reconstruction. The systematic variations are given in Table 3.9 of section 3.5.2.

3.1.4 Reconstruction of protons

Track reconstruction

The reconstruction of protons is required in order to study the p- Λ interaction. As they are charged and stable, the protons are measured directly by ALICE by using the reconstructed tracks. As discussed in section 3.1.2 the tracks used to evaluate the momenta of the particles are TPC-only, however all topological cuts are applied to the corresponding global tracks. The particle identification is performed by using only the energy loss information from the TPC for particles with a momentum p below 0.75 GeV/c , while for higher momentum tracks the TOF information is required to evaluate the n_σ related to the PID hypothesis (see section 3.1.1, Figures 3.3, 3.5 and Eq. 3.4). To ensure a high purity sample of protons strict cuts are imposed to the tracks, summarized in table 3.2. There are two topological cuts on the *distance of closest approach* (DCA) to the PV (d_{PV}) to ensure the predominant selection of primary protons and suppress the contribution of protons stemming from feed-down.

Determination of the purity and primary fraction

Evaluating the *purity* and the *primary fraction* of protons is required for the determination of the λ parameters (section 2.7.2). The employed strategy is identical to the analysis of pp data at 7 TeV [38, 51], using the MC output to evaluate the purity, and a MC based data-driven template fit to extract the fractions of primary and secondary protons. The determination of the purity is performed by reconstructing proton candidates from the full scale simulation and checking their original species

Data set (Trigger)	Proton purity
pp at 13 TeV (MB)	99.00%
pp at 13 TeV (HM)	99.43%
p-Pb at 5.02 TeV (MB)	98.43%

TABLE 3.3: Proton purities extracted from MC.

using the generator level (Pythia) information. The ratio between the correctly identified protons and the total amount of reconstructed proton candidates is defined as the purity. All of the analyzed data samples have very high purity (above 99%) and the exact values are listed in table 3.3. Apart from the impurities, there is an additional source of contamination in the proton sample related to the experimental environment, namely protons stemming from the material of the detector itself, e.g. if it has been knocked out or produced in a reaction between the detector material and some traversing particle. This scenario is typically negligible, with a possible effect only for low momentum protons. The MC simulations provide the opportunity to select only protons with a specific origin, separating the real from the misidentified and material protons, as well as primary¹¹ from feed-down protons. This allows to study deferentially each source of protons, in particular their topological properties reconstructed by the detector, such as the distance of closest approach to the primary vertex. The DCA is a very powerful observable to separate between the different types of protons, as the weak decays happen on the scale of several centimeters, which can be resolved by the detector, leading to a broadening of the DCA distribution of the secondary protons. Moreover, the protons stemming from the material of the detector originate from a randomized location which has only a weak correlation to the position of the primary vertex, leading to a flatter DCA distribution. The weighted sum of all these distributions results in the total experimentally measured DCA

$$d_{\text{PV},xy}(r) = \sum_i \omega_i d_{\text{PV},xy}^{(i)}(r), \quad (3.5)$$

where i is indexing all known sources of protons, in this case primaries, feed-downs from Λ and Σ^+ , materials and misidentifications. The weights ω_i are known in the MC simulations, and it is possible to use them directly to study the experimental correlation function. Nevertheless, no event generator can model the ratios of all particles precisely and deviations from the data are expected, biasing the analysis significantly. To reduce the model dependence of ω_i , they can be extracted by assuming that the MC simulations reproduce the functional shape of $d_{\text{PV},xy}^{(i)}(r)$ (right side of Eq. 3.5) and fit ω_i to the experimentally measured $d_{\text{PV},xy}(r)$ (left side of Eq. 3.5). This procedure is called *template fitting* and it works best when the individual DCA templates have a significant statistical differences compared to the experimental data. In the present case of studying protons, the differences between the primary, secondary and material protons are significant, however it is difficult to separate between the two sources of secondary feed-down ($\Lambda \rightarrow p\pi^-$ and $\Sigma^+ \rightarrow p\pi^0$) or misidentified protons. Hence, the template fit is performed with 3 templates (primary, secondary, material), while fake protons are ignored due to their very low (<1%) contribution. The result for MB pp collisions at 13 TeV, presented deferentially in bins of p_T , is

¹¹Within the MC simulations a primary particle is considered as produced in the pp collision or is the product of a strong or electromagnetic decay.

Data set (Trigger)	Primary protons	Secondaries from Λ	Secondaries from Σ^+
pp at 13 TeV (MB)	87.4%	8.8%	3.8%
pp at 13 TeV (HM)	82.3%	12.5%	5.2%
p–Pb at 5.02 TeV (MB)	86.3%	9.6%	4.1%

TABLE 3.4: Proton fractions extracted from the template fits.

shown in Fig. 3.7 and 3.8. These figures demonstrate how the experimentally measured $d_{PV,xy}(r)$ distribution can be described as a superposition of the individual templates obtained from simulations. The plotted range corresponds to the full fit range, however the fractions are evaluated only in the DCA range corresponding to the reconstruction condition ($|d_{PV,xy}| < 0.1$ cm). The resulting fractions, as a function of p_T , are shown in the right panel of Fig. 3.9. The uncertainties of the fit procedure are generally very small, and for practical purposes excluded from the analysis. As expected, the amount of material contribution is negligible, apart for very low p_T protons. Most of the protons (80-90%) are primaries, while the feed-down protons are around 10-20%, where this fraction increases at low p_T . The amount of feed-down from Λ with respect to the contribution from Σ^+ is assumed to be 70:30, based on the yields provided by Pythia. Further details about obtaining this ratio is given in the [next section](#). The fraction averaged over the underlying p_T distribution, shown in the upper-left panel of Fig. 3.9, is marked with dashed lines on the right panel of the same figure. Due to the very small amount of material protons, to obtain the fractions used in the analysis the latter is assumed to be 0% and the average amount of primaries and secondaries scaled accordingly. These values are used to compute the λ parameters. However, for precision studies it is important to consider as part of the systematic uncertainties the bias due to the above assumptions, namely the p_T dependence¹² and exclusion of the material protons from the analysis. For the p– Λ analysis presented in chapter 6 this has been taken into account. Table 3.4 summarizes all proton fractions and purities used in the present work.

3.1.5 Reconstruction of Λ s

V0 reconstruction

The reconstruction of Λ particles uses the V0 objects saved in the standard ALICE output (AOD files, see section 3.1.2). Relatively standard topological cuts tuned for the selection Λ particles are applied to those V0s. Each V0 is build from two opposite charged tracks, where in the case of Λ s the mass hypothesis of a proton and a pion is used for the two daughter tracks. The cuts applied to the V0s are summarized in Table 3.5. The last two cuts are applied on the invariant mass, where the last one is to select the range of the expected Λ peak. The second to last cut is used to reject contamination from V0s corresponding to neutral kaons, done by assuming the two daughter tracks of the V0 have the pion mass. This is relevant, as there is some amount of misidentified daughter protons, which were in fact pions stemming from the decay of a K^0 . The *cosine pointing angle* (CPA) observable listed in table 3.5 is defined as the cosine of the angle between the momentum of the V0, obtained from the sum of the momenta of the two daughters, and the straight line

¹²The p_T dependence is correlated with a k^* dependence, as particles with low relative momenta tend to have a slightly lower p_T than the average.

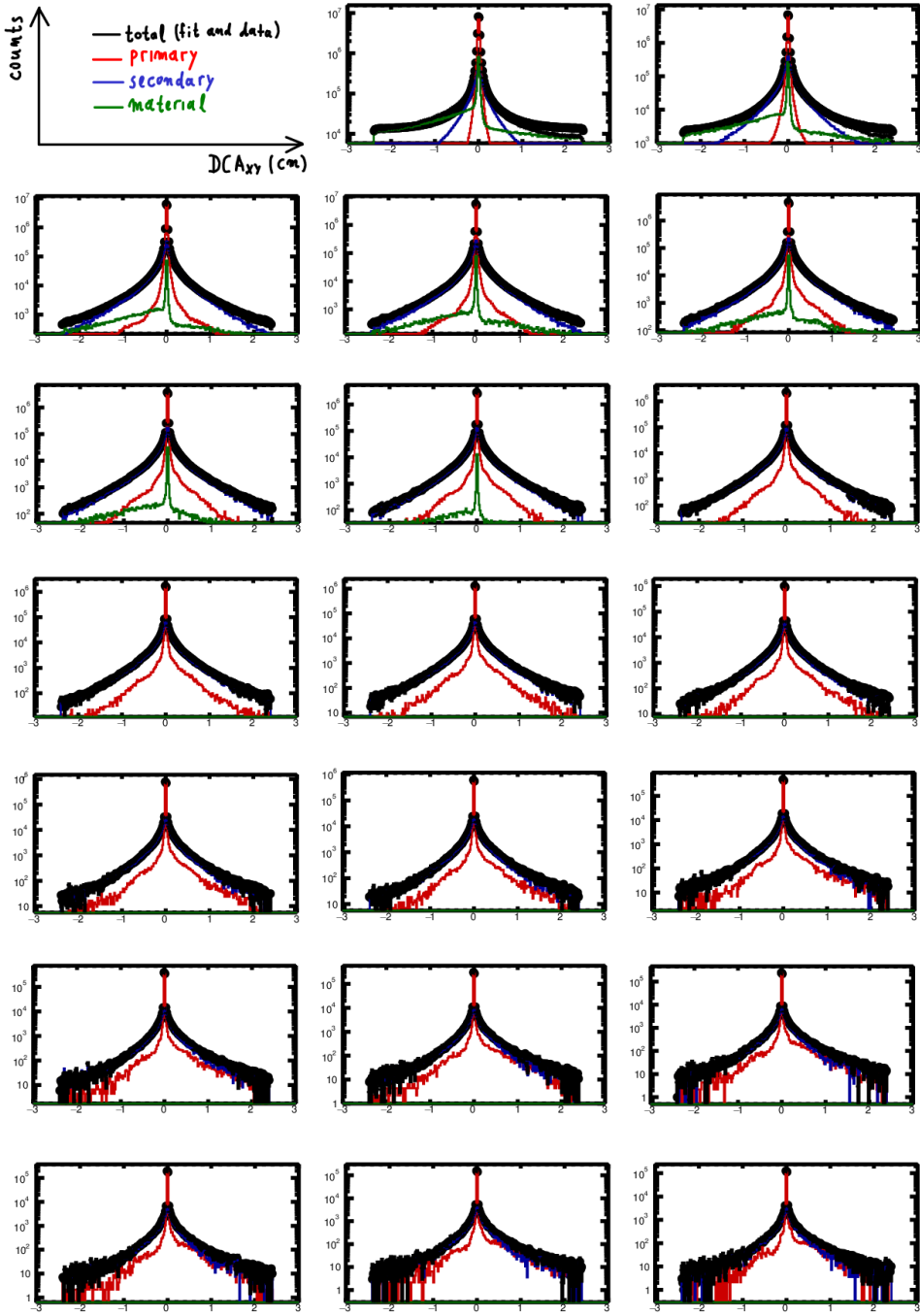


FIGURE 3.7: The template fits to the DCA of the protons for the MB pp collisions at 13 TeV. The black points represent the data, which are described rather well by the weighted sum of the individual templates (colored areas). The full p_T of $(0.5, 4.05)$ GeV/c range is split in 20 intervals of equal length, each fitted individually and represented as a separate panel. The lowest p_T is shown in the first (top left) panel, and each next (in the order right and down) panel corresponds to the adjacent interval. The results are similar for all collision systems.

connecting the PV to the *secondary (decay) vertex* (SV) of the V0. For a Λ decay in a perfect experiment this angle should be 0, and the corresponding cosine equal to 1. In reality the CPA is only close to unity, and has a characteristic shape depending

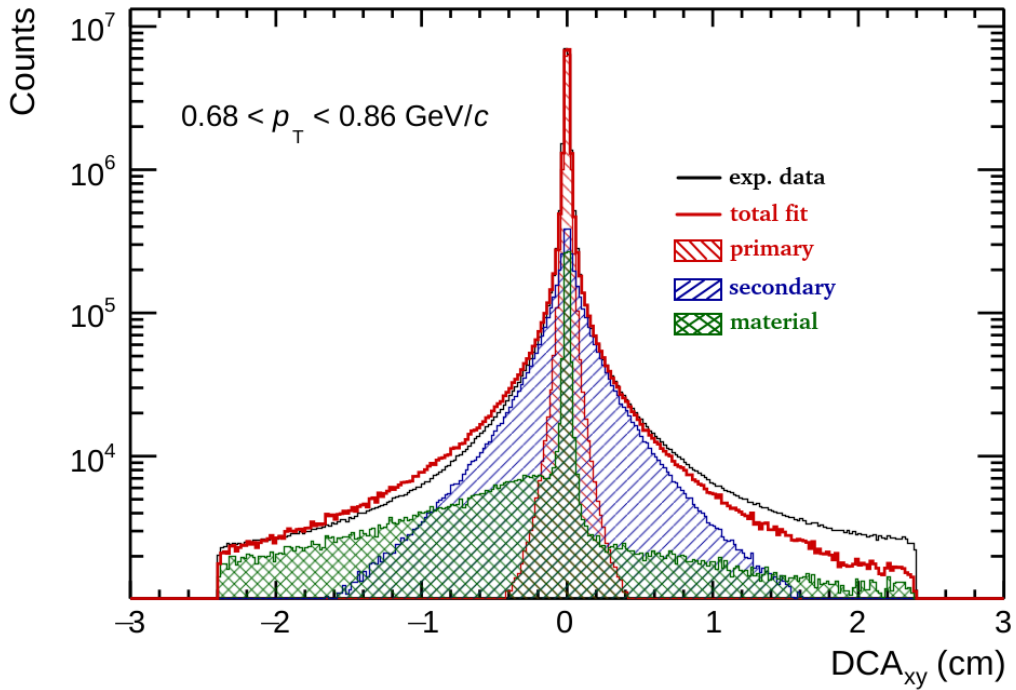


FIGURE 3.8: A single template fit to the DCA of the protons for the MB pp collisions at 13 TeV for $p_T \in [0.68, 0.86]$. The black points represent the data, the thick red line is the final fit result composed of the weighted sum of the individual templates (colored areas). While the tails of the distribution are not that well reproduced, the range below 0.2 cm, as used in the analysis, is very well described.

on the physical source of the V0, a feature that can be used to evaluate the amount of primary Λ s, as described in the next section.

Determination of the purity and primary fraction

The purity determination of the Λ is done directly from the experimental data, by fitting the *invariant mass spectrum* (IMS) of the selected Λ candidates with a function that contains separate terms to model the background and the signal (Λ peak). Typically the peak in the spectrum is Gaussian in shape, which is driven by the detector resolution. Nevertheless, it is often observed that in a real experimental environment there could be several competing factors determining the resolution, leading to a slightly more complex structure of the peak and a better description is provided with the sum of two or even three Gaussian functions. The results from the IM fits in different p_T ranges, as well as the corresponding purities of the Λ and $\bar{\Lambda}$ particles, are shown in figures 3.10, 3.11 and 3.12. These fits have been performed by assuming a polynomial of second order for background function, and the sum of two Gaussians for the signal. The p_T integrated result for the purity in the different collision systems is shown in table 3.6. These purities correspond to the single particles, and could deviate slightly for the Λ candidates used to build pairs at low relative momenta. Typically this discrepancy is neglected, however for the high precision study performed in the p- Λ system a more detailed evaluation of the purity based on the Λ candidates in the mixed event sample will be proposed in chapter 6.2. For the Λ - Λ system it is sufficient to use directly the results in table 3.6 to evaluate the λ parameters. The fraction of primary Λ particles is evaluated in a similar template

Selection criterion	Value
<i>Daughter track selection criteria</i>	
Pseudorapidity	$ \eta < 0.8$
Number of TPC clusters	$n_{\text{TPC}} > 70$
DCA to the PV	$d_{\text{PV}} > 0.05 \text{ cm}$
Particle identification	$ n_{\sigma, \text{TPC}} < 5$
Out-of-bunch pile-up removal	Hit in ITS SPD or SSD or TOF timing
<i>V_0 selection criteria</i>	
Transverse momentum	$p_T > 0.3 \text{ GeV}/c$
Secondary (Λ decay) vertex (SV) position	$ i_{\text{SV}} < 100 \text{ cm}, i=x,y,z$
Transverse radius of the decay vertex r_{xy}	$0.2 < r_{xy} < 100 \text{ cm}$
DCA between the daughter tracks at the SV	$\text{DCA}(p, \pi) < 1.5 \text{ cm}$
Cosine of the Pointing Angle α (CPA)	$\cos \alpha > 0.99$
K^0 rejection (IM)	$0.48 < M_{\pi^+\pi^-} < 0.515 \text{ GeV}/c^2$
Λ selection (IM)	$ M_{p\pi} - M_{\Lambda, \text{PDG}} < 4 \text{ MeV}/c^2$

TABLE 3.5: Selection criteria used for Λ reconstruction. The systematic variations are given in Table 3.10 of section 3.5.2.

Data set (Trigger)	Λ purity
pp at 13 TeV (MB)	96.8%
pp at 13 TeV (HM)	96.0%
p–Pb at 5.02 TeV (MB)	93.8%

TABLE 3.6: Λ purities extracted from the IM fits of the single particles.

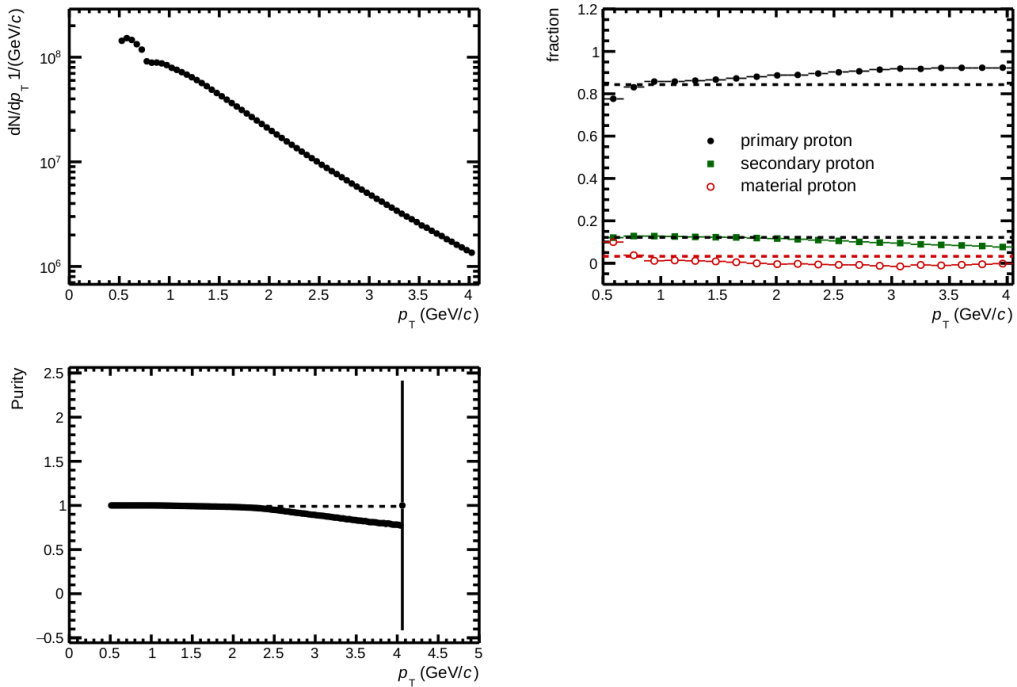


FIGURE 3.9: The fractions of protons based on the template fit as a function of p_T (top right panel), the p_T distribution of the protons (top left panel) used to obtain the averaged amount of fractions. The bottom panel represents the purity of the protons, extracted directly from the MC.

fitting procedure as for the protons (see section 3.1.4), however instead of the DCA to the PV the fitted observable is the CPA. Unlike in the case of protons, the misidentification represent a significant fraction in the template fit and cannot be dropped out. Due to its model independence, the purity obtained from fitting the invariant mass spectrum is more reliable. For this reason after the CPA templates have been fitted to the data, the resulting amount of fakes is subtracted and not considered in the computation of the relative fractions of the other contributions. Further, as in the case of the proton template fits, the amount of the material contribution will be ignored. The feed-down to the secondary Λ particles is physically composed of $\Sigma^0 \rightarrow \Lambda\gamma$, $\Xi^- \rightarrow \Lambda\pi^-$ and $\Xi^0 \rightarrow \Lambda\pi^0$, however due to the electromagnetic decay of the Σ^0 its lifetime is quite short ($22 \cdot 10^3$ fm) making impossible to separate experimentally a primary Λ from a secondary Λ stemming from Σ^0 . Moreover, in Pythia the Λ particles stemming from a Σ^0 are tagged as primary, thus in the template fits presented below this convention is adopted. Nevertheless, the decay length of $22 \cdot 10^3$ fm is large enough to ensure that the final state interaction occurs before the decay, hence the measured Λ has to be considered as a secondary particle in the femtoscopy formalism. To determine the amount of these particles, the primary Pythia template is used to determine the amount of Λ particles that are either primary or stemming from Σ^0 , while the exact ratio between the two is considered to be 1:3 (secondary:primary). This is a reasonable assumption based on isospin symmetry, which assumes that the particle production is thermally driven and the similar masses of the Λ and Σ lead to the expectation of producing them in the same amount. In terms of isospin, Λ is $I = 0$ and Σ is $I = 1$ state, implying that the projection of the third component $I_3 = 0$ for Λ and $I_3 \in \{-1, 0, 1\}$ for Σ , where in the latter case $I_3 = 0$ corresponds to Σ^0 and represents 1/3 of the available states. This is reasonably well

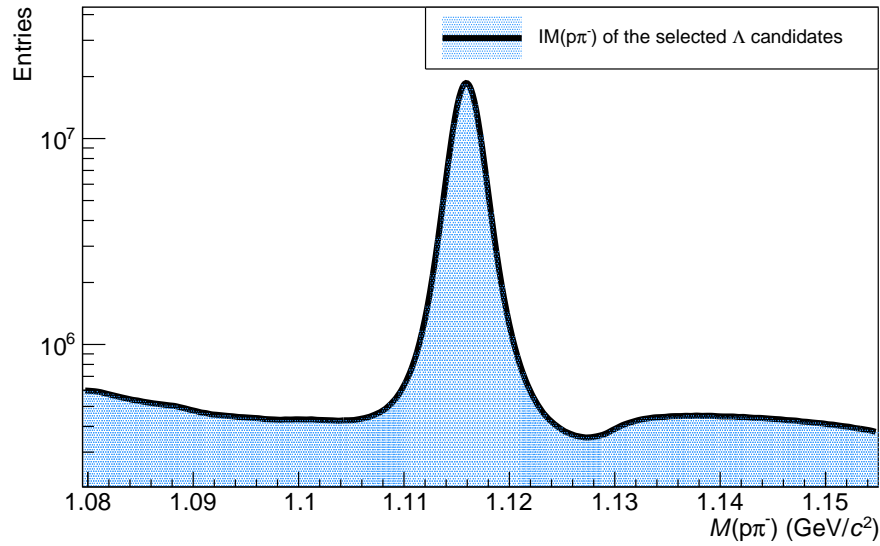


FIGURE 3.10: Experimental Λ invariant mass distribution of $p\pi^-$, after applying all selection criteria, for the HM pp 13 TeV data set. The logarithmic y -axis visualizes the underlying background contamination, which will be studied in detail for the p - Λ correlations function (sections 3.3.3 and 6.2).

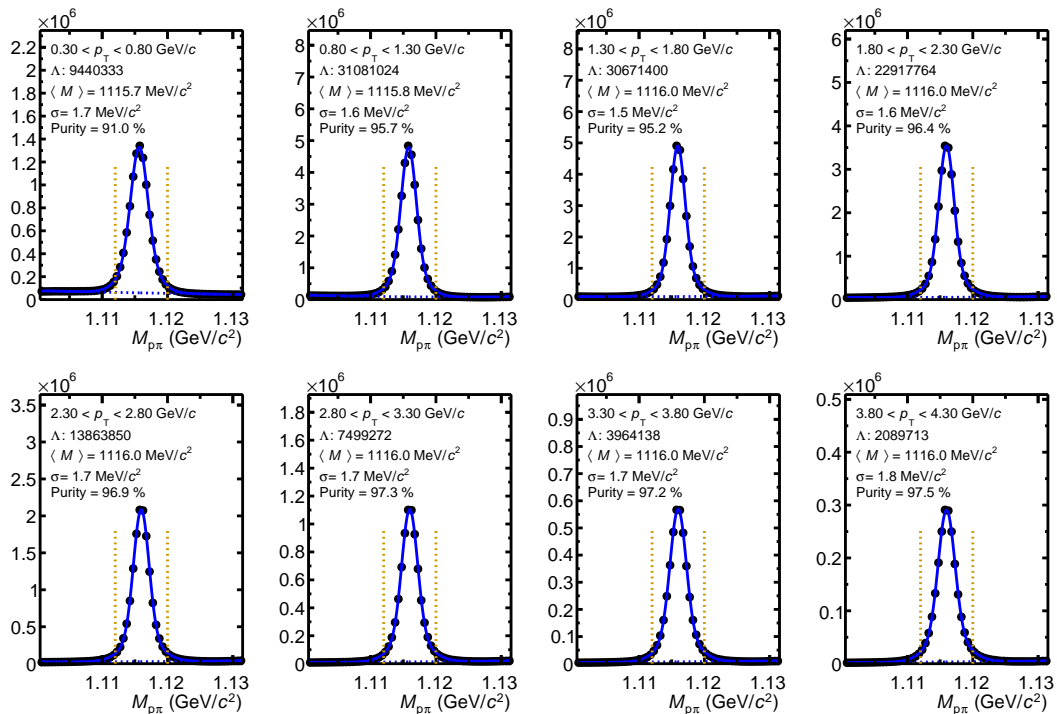


FIGURE 3.11: Experimental Λ invariant mass distribution of $p\pi^-$ for different p_T bins, after applying all selection criteria, for the HM pp 13 TeV data set.

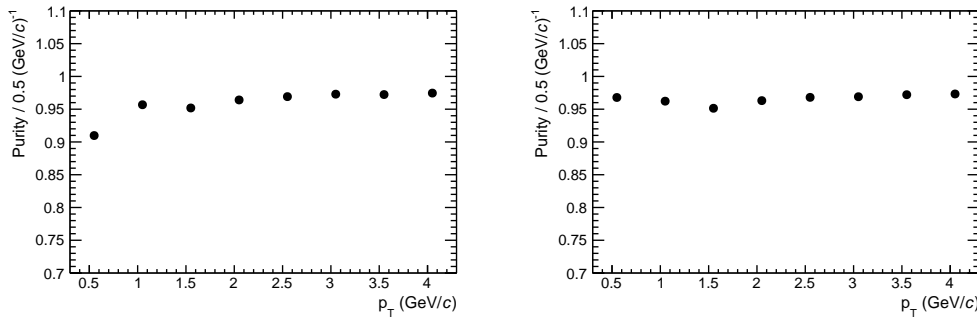


FIGURE 3.12: Purity of the Λ (left) and $\bar{\Lambda}$ (right) candidates as a function of their transverse momentum.

Data set (Trigger)	Primary Λ	Secondaries from Σ^0	Secondaries from Ξ
pp at 13 TeV (MB)	60.1%	20.0%	19.9%
pp at 13 TeV (HM)	57.6%	19.2%	23.2%
p–Pb at 5.02 TeV (MB)	52.1%	17.4%	30.5%

TABLE 3.7: Λ fractions extracted from the template fits. The Ξ secondaries are composed both of Ξ^- and Ξ^0 , typically assumed to contribute in equal amount.

reproduced by thermal models, such as Thermal Fist [75], and Pythia itself, both predicting a $\Sigma^0:\Lambda$ ratio of 0.4. This ratio seems to be quite stable at various energies, starting from 3.18 GeV [76] up to the TeV scale, for which preliminary ALICE results from pp collisions at 7 TeV have experimental constraints of 0.38 ± 0.10 [77], leading to agreement with the expectations. While all of these results are similar, they have a spread of c.a. 20%, for that reason in all presented analysis the ratio between $\Sigma^0:\Lambda$ is assumed to be 0.33 ± 0.07 and represents the largest source of uncertainty related to the λ parameters. This result is compatible with the assumed ratio between Σ^+ and Λ used in the determination of the fraction of secondary protons discussed in the [previous section](#). The final results on the fractions of the different Λ source is summarized in table 3.7, while the corresponding results from the template fits for the HM pp collisions at 13 TeV are shown in figures 3.13, 3.14 and 3.15. The plotted range corresponds to the full fit range, however the fractions are evaluated only in the CPA range corresponding to the reconstruction condition (smaller than 0.99).

3.1.6 Raw Λ – Λ and p– Λ correlations

Pair cuts

The final set of selection criteria is directed to the reconstructed particle pairs used in the same- and mixed-event samples. If in a single event multiple Λ candidates share a daughter track, to avoid auto-correlations only the candidate with the larger CPA is kept. Moreover, all daughter protons of the Λ s are required to *not* satisfy the conditions for a primary particle (table 3.2) and the Λ candidates must not have been used to reconstruct a cascade (Ξ) particle.

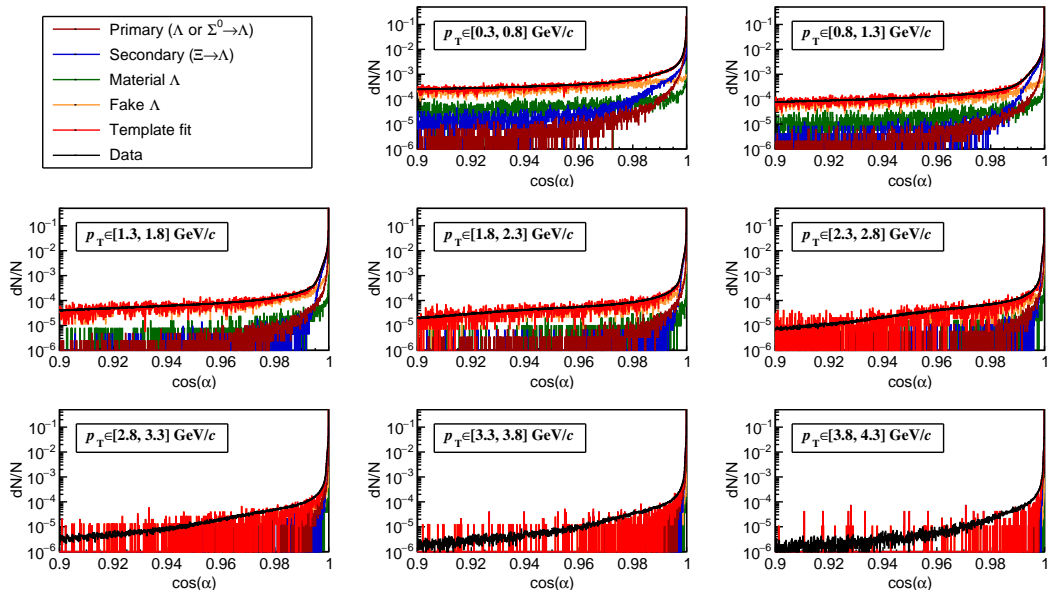


FIGURE 3.13: Adjusted Monte Carlo templates from Pythia to the experimental data for HM pp collisions at 13 TeV. Due to the shape of the templates one has a good discrimination of the origin of the Λ s.

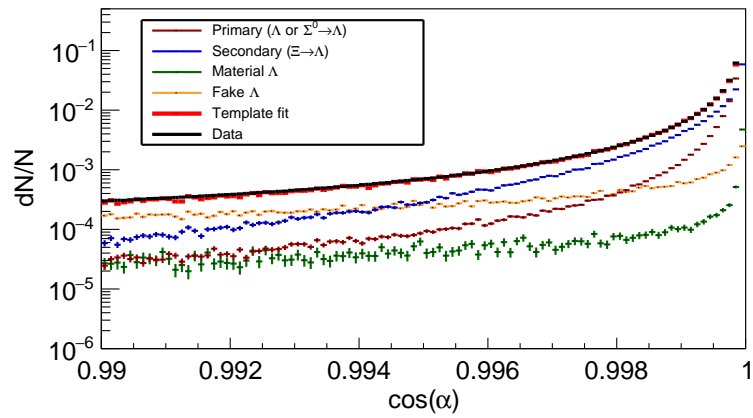


FIGURE 3.14: Adjusted Monte Carlo Templates from Pythia to the experimental data in the full p_T range for HM pp collisions at 13 TeV.

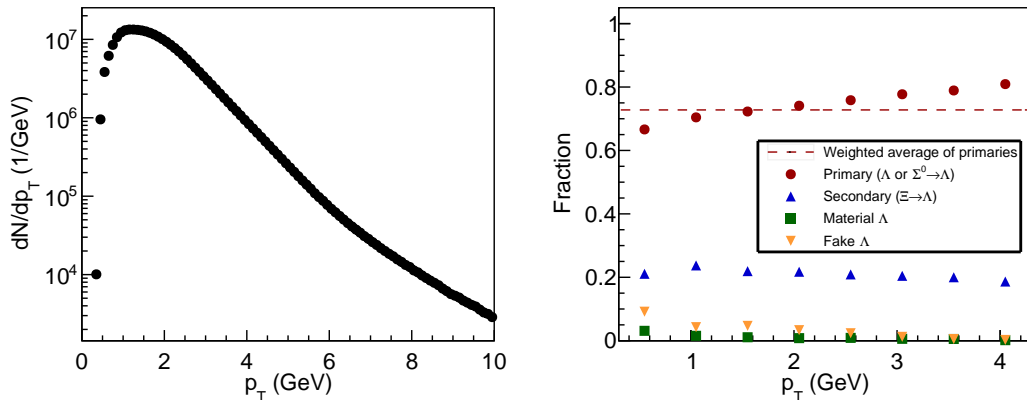


FIGURE 3.15: *Right panel:* The fractions of Λ as a function of p_T obtained from a template fitting method for HM pp collisions at 13 TeV. The averages of the quantities are obtained by employing (*left panel*) the production probability dN/dp_T of Λ .

Same and mixed events

The final stage of the data reconstruction is the evaluation of the correlation function. As introduced in chapter 1.5.2, experimentally the definition is

$$C_{\text{raw}}(k^*) = \frac{N_S(k^*)}{N_R(k^*)}, \quad (3.6)$$

where $N_S(k^*)$ is the measured yield of the correlated *signal* sample of pairs and $N_R(k^*)$ is a *reference* sample of uncorrelated pairs. This definition corresponds to a unnormalized raw correlation function, where the normalization methods are discussed in section 3.2. The signal sample is trivially obtained by building all possible combinations of particle pairs available in each recorded event, using the protons and Λ s satisfying the required single particle selection criteria (sections 3.1.4 and 3.1.5). The most commonly used technique to build an uncorrelated reference sample is called *event mixing*, in which non-physical events are build using the selected single particles, by enforcing that these (mixed) events do not contain any two particles that were detected in the same physical event. This ensures that the individual particles in the mixed events have the correct kinematic properties, but are free of direct final state correlations with respect to all other particles in the particular mixed event. Finally, $N_R(k^*)$ is build by using all possible permutations of particle pairs from the mixed events and computing their k^* distribution. In theory, the pool of particles available for the mixed events is composed of all measured particles during the data taking, which is in the order of 10^7 up to 10^8 particles, where very rarely more than 2 of them stem from the same event. This results in a practically infinite amount of permutations available to build the mixed events. This allows to design a mixed event sample with a statistics far greater than the same event sample, eliminating the factor of an additional uncertainty for $C_{\text{raw}}(k^*)$.

There are multiple effects to be considered in order to minimize the artificial correlations related to the event mixing. To leading order, such correlations occur due to the difficulty of ensuring the exact same single particle kinematics within the reconstructed pairs in the same- and mixed-event samples, which is mostly affected

by the multiplicity of the event. Moreover, depending on the position of the PV the reconstruction efficiency and acceptance of the particles change, introducing further bias in the measured k^* between two particles stemming from different events. On the level of the correlation function, this is accounted for by allowing for a *non-femtoscopic baseline*¹³ interfering with the femtoscopic signal (discussed further in section 3.4). The modelling of this baseline assumes a smooth minor modification to the femtoscopic signal, thus it is of utmost importance to decrease the bias in the mixed events as much as possible. In the analyses presented in this work this is achieved by creating discrete classes of mixed events, based on the event multiplicity and PV position on the beam (z) axis, which are later summed together to obtain the total yield $N_R(k^*)$. While the kinematics in each event is now more realistic, the relative contribution of each event class is not automatically accounted for. If the mixed events are summed up directly, the resulting multiplicity distribution will be different compared to the same events, requiring to re-weight the multiplicity classes (m) of the mixed events by

$$N'_R(k^*) = \sum_m \omega_m N_{R,m}(k^*), \quad (3.7)$$

where $N_{R,m}(k^*)$ is the yield of the mixed event sample for a particular multiplicity class m and ω_m are weights obtained from the condition

$$\int_0^\infty N_{S,m}(k^*) dk^* = \omega_m \int_0^\infty N_{R,m}(k^*) dk^*, \quad (3.8)$$

where $N_{S,m}(k^*)$ is the yield of the same event sample for a particular multiplicity class m . The integration over k^* ensures equal amount of particle pairs in each specific multiplicity class both for the same- and mixed-events. At this point it is important to mention that equations 3.7 and 3.8 will not only change the relative amount of contribution of each multiplicity bin, but will lead to an overall re-normalization¹⁴ of the correlation function due to the enforced condition 3.8. In traditional femtosecopy studies the normalization is chosen such to fulfil the condition $C(k^* \rightarrow \infty) \rightarrow 1$. In the recent non-traditional femtosecopy studies in small collisions systems ([38]) the normalization is determined directly by the fit, due to the absence of a large flat region in $C_{\text{raw}}(k^*)$ due to the non-femtoscopic contributions. Thus any initial *normalization* will loose its physics interpretation, but unfortunately this was not realized up until the normalization was studied in detail during the p- Λ analysis (section 3.2). For this reason all previous studies, including of Λ - Λ , attempted to perform the re-weighting without biasing the enforced initial normalization. We will omit the unnecessary technical details, but please note that the consequence for the Λ - Λ analysis is that the weights ω_m are obtained by changing the integration limits of Eq. 3.8 to $k^* \in [200, 900]$ MeV/ c . This leads to an approximately correct re-weighting, and the systematic checks related to the variation of these limits did not show any significant deviations. Moreover, in the course of the present work it was verified that using Eq. 3.8 with the proper limits leads to a difference in the correlation function in the femtoscopic region of $< 0.1\%$, which is smaller than the experimental uncertainties. In the future operation of the LHC the statistical uncertainty will become smaller than 0.1%, requiring the use of Eq. 3.8 in order to avoid an unnecessary systematic bias.

¹³The bias from the mixed events is *not* the only effect included in this effective baseline.

¹⁴In chapter 3.2 it will be shown not only that this is not an issue, but such a normalization has to be used to avoid any bias.

The raw correlation functions for Λ - Λ and p- Λ are shown in figures 3.16 and 3.17 respectively.

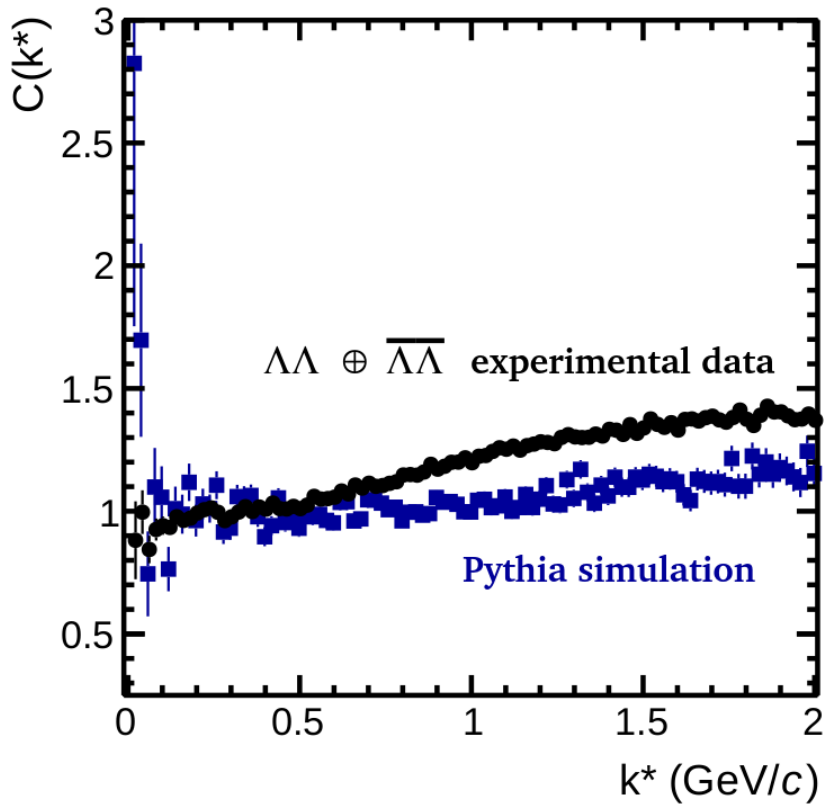


FIGURE 3.16: Raw Λ - Λ correlation, the black points representing the data and the blue points the corresponding Monte-Carlo simulation.

3.2 Normalization of the correlation function

3.2.1 Overview

The *normalization* of the correlation function is important in order to compare to theoretical predictions or when additive corrections to the correlation functions are applied. In heavy ion collisions, the correlation function typically flattens above the femtoscopic region, usually for k^* above 200-300 MeV. In small collisions systems, such as pp, the situation is complicated by the presence of a stronger femtoscopic signal, often leading to a complete absence of convergence towards a flat correlation, making impossible to normalize the raw correlation function at large k^* . This is clearly seen in figures 3.16 and 3.17, which also demonstrate that the long-range¹⁵ correlations are not reproduced by MC, thus they cannot be corrected for. Hence, in small collisions systems a normalization term is included in the fit procedure

$$C_{\text{raw}}(k^*) = \mathcal{N}C_{\text{fit}}(k^*), \quad (3.9)$$

where \mathcal{N} is an overall normalization factor, accounting for the unknown true value, and $C_{\text{fit}}(k^*)$ is the function used to model the correlation function theoretically. This

¹⁵The physics origin of the long-range correlations are not yet understood, but a dedicated discussion is presented in section 3.4.

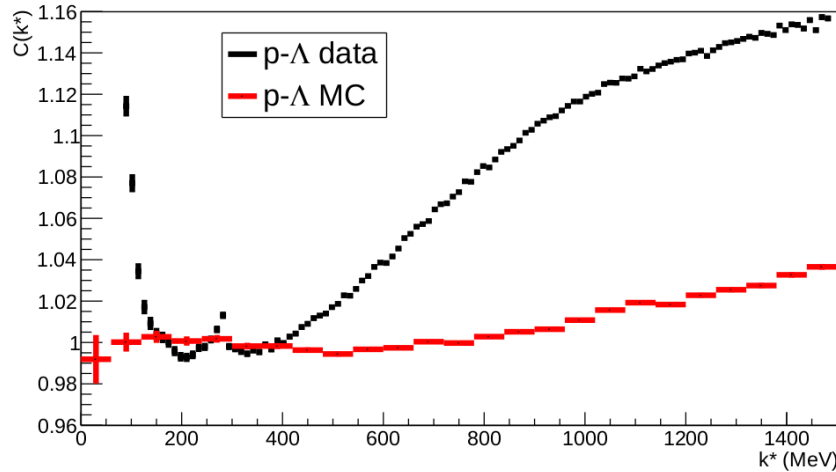


FIGURE 3.17: Raw p- Λ correlation, the black points representing the data and the red points the corresponding Monte-Carlo simulation.

includes both the femtoscopic signal and the expected non-femtoscopic corrections. Both systems analyzed in this work (Λ - Λ and p- Λ) have been fitted using this type of parameterization, (chapters 5 and 6). Naturally, all of the fit parameters will be correlated, implying that \mathcal{N} will depend on the choice of source function, the interaction model and the non-femtoscopic background, all of which determine the functional shape of $C_{\text{fit}}(k^*)$. If the modelling is correct, than it can be assumed that $C_{\text{exp}}(k^*) \approx C_{\text{fit}}(k^*)$, leading to

$$C_{\text{exp}}(k^*) = \frac{C_{\text{raw}}(k^*)}{\mathcal{N}}. \quad (3.10)$$

This implies that the normalization constant can be determined by the fit, and than applied to correct the raw correlation function. However, it is very misleading to present the experimental data in this way, as the normalization is model dependent, potentially leading to an uncontrolled systematic bias. Presenting $C_{\text{raw}}(k^*)$ is not practical either, as the normalization is completely off and it makes the plot unintuitive to interpret. For these reasons, the general decision was made to always normalize the raw correlation function at an intermediate k^* range¹⁶

$$C_{\text{exp}}(k^*) = \mathcal{N}_{\text{exp}} C_{\text{raw}}(k^*), \quad (3.11)$$

where \mathcal{N}_{exp} is determined such as to result in the same amount of yield in the same- and mixed-event distributions in the chosen range of k^* . As long as Eq. 3.9 is used to perform the fit, with \mathcal{N} as a free fit parameter, replacing $C_{\text{raw}}(k^*)$ by $C_{\text{exp}}(k^*)$ will only modify the resulting value for \mathcal{N} , without an effect on the physics interpretation. For this reason it is safe to re-normalize $C_{\text{raw}}(k^*)$ in any desired way, as done for the plots in figures 3.16 and 3.17.

¹⁶Anywhere between 200 and 500 MeV depending on the shape of the correlation.

3.2.2 Addition of correlations

The method of re-normalizing the correlation function in an arbitrary k^* region has one major disadvantage, which only becomes relevant when *adding together multiple correlation functions*. The practical cases are the addition of the correlation functions coming from two particles (X – X) and the corresponding anti-particles (\bar{X} – \bar{X})¹⁷, or if some of the decomposition terms in the correlation, related to the λ parameters introduced in section 2.7.2, are known and need to be corrected for by subtraction. For example, the latter is relevant when correcting for impurities using the sideband technique, which will be discussed in section 3.3.3.

Let us understand the generic problem, by starting from the fact that the correlation function is composed of a same-event sample $S(k^*)$ and a reference correlation free sample $R(k^*)$ ¹⁸, assuming that each of them contains two distinct types of particle pairs (X and Y). The total correlation is given by

$$C(k^*) = \frac{S(k^*)}{R(k^*)} = \frac{S_X(k^*) + S_Y(k^*)}{R_X(k^*) + R_Y(k^*)}, \quad (3.12)$$

where $S(k^*) = S_X(k^*) + S_Y(k^*)$ and $R(k^*) = R_X(k^*) + R_Y(k^*)$. A fair treatment of the *reference sample* imposes the condition of having the same fraction of pairs X and Y as in the same-event sample

$$\frac{\int_0^\infty S_X(k^*) dk^*}{\int_0^\infty S_Y(k^*) dk^*} = \frac{\int_0^\infty R_X(k^*) dk^*}{\int_0^\infty R_Y(k^*) dk^*}. \quad (3.13)$$

Let us define the weights $w_{X/Y}^{S/R}$ such that

$$\begin{aligned} S_X(k^*) &= w_X^S(k^*) S(k^*) \\ S_Y(k^*) &= w_Y^S(k^*) S(k^*) = [1 - w_X^S(k^*)] S(k^*) \\ R_X(k^*) &= w_X^R(k^*) R(k^*) \\ R_Y(k^*) &= w_Y^R(k^*) R(k^*) = [1 - w_X^R(k^*)] R(k^*). \end{aligned} \quad (3.14)$$

With these definitions, the w weights relate the probability density functions of the samples $S(k^*)$ and $R(k^*)$ to the decomposed distributions $S_{X/Y}(k^*)$ and $R_{X/Y}(k^*)$. Consequently, Eq. 3.12 becomes

$$C(k^*) = \frac{S(k^*)}{R(k^*)} = \frac{w_X^S(k^*) S(k^*) + w_Y^S(k^*) S(k^*)}{w_X^R(k^*) R(k^*) + w_Y^R(k^*) R(k^*)}. \quad (3.15)$$

To understand the meaning of this reformulation, let us consider the following practical example: assume Y are pairs of misidentified X . The purity of X will correspond to the weight $w_X^S(k^*)$, which in general has a k^* dependence. This dependence can be different in the reference sample, however if both $S(k^*)$ and $R(k^*)$ are based on the same pool of single particles, the average purity should be identical, which is equivalent to the statement that the total fractional amount of impurities should be the same in $S(k^*)$ and $R(k^*)$ (Eq. 3.13).

¹⁷Physics-wise the expected correlation function due to the final state interaction has to be identical. For this reason, experimentally the X – X and \bar{X} – \bar{X} correlation functions are always added together, unless there is some major difference in the experimental detection of particles and anti-particles.

¹⁸Typically this is the mixed-event sample, although in general it could be any other distribution serving the same purpose.

Our goal is to study the addition of correlations, as such we need to find a relation between $C(k^*)$ and the correlation functions $C_X(k^*)$ and $C_Y(k^*)$. By definition, the samples $S_{X/Y}(k^*)$ and $R_{X/Y}(k^*)$ contain the correlated and uncorrelated pairs of X and Y , hence the following definitions hold true

$$\begin{aligned} C_X(k^*) &= \frac{S_X(k^*)}{R_X(k^*)}, \\ C_Y(k^*) &= \frac{S_Y(k^*)}{R_Y(k^*)}. \end{aligned} \quad (3.16)$$

To proceed, let us transform Eq. 3.15

$$\begin{aligned} C(k^*) &= \frac{w_X^S(k^*)S(k^*) + w_Y^S(k^*)S(k^*)}{R(k^*)} = \frac{w_X^S(k^*)S(k^*)}{R(k^*)} + \frac{w_Y^S(k^*)S(k^*)}{R(k^*)} = \\ &= \frac{w_X^R(k^*)}{w_X^R(k^*)} \frac{w_X^S(k^*)S(k^*)}{R(k^*)} + \frac{w_Y^R(k^*)}{w_Y^R(k^*)} \frac{w_Y^S(k^*)S(k^*)}{R(k^*)} = \\ &= \frac{w_X^R(k^*)S_X(k^*)}{w_X^R(k^*)R(k^*)} + \frac{w_Y^R(k^*)S_Y(k^*)}{w_Y^R(k^*)R(k^*)} = \\ &= \frac{w_X^R(k^*)S_X(k^*)}{R_X(k^*)} + \frac{w_Y^R(k^*)S_Y(k^*)}{R_Y(k^*)} = \\ &= w_X^R(k^*)C_X(k^*) + w_Y^R(k^*)C_Y(k^*). \end{aligned} \quad (3.17)$$

The above equation implies, that to add the two correlation functions, we need to scale each of them with the amount of X and Y fractions present in the original sample, where the weights are taken from the uncorrelated reference sample¹⁹. All of the above calculations had a single restriction, given by Eq. 3.13, which demands that ratio of the total yield in the same-event and the reference sample has to be identical for the pairs of type X and Y . The normalization presented in the previous section implies that Eq. 3.13 corresponds to

$$\frac{\int_{a_X}^{b_X} S_X(k^*) dk^*}{\int_{a_Y}^{b_Y} S_Y(k^*) dk^*} = \frac{\int_{a_X}^{b_X} R_X(k^*) dk^*}{\int_{a_Y}^{b_Y} R_Y(k^*) dk^*}, \quad (3.18)$$

where the pairs X are normalized for $k^* \in [a_X, b_X]$ and Y for $k^* \in [a_Y, b_Y]$. Due to the complex k^* dependence of all variables there is no guarantee that the relation 3.13 is compatible with 3.18, unless the integration limits are chosen specifically to satisfy 3.13. The only way to fulfil 3.13 independently of the underlying distributions, is to normalize the same-event and reference samples to their total yield ($k^* \in [0, \infty)$). This procedure will be referred as *natural normalization*, as it implies that both $S(k^*)$ and $R(k^*)$ are treated as probability density functions, which goes back to the fundamental definition of the correlation function (Eq. 1.7).

The above relations were obtained assuming only two contributions to the correlation function (X and Y), however the relations are very easy to generalize to the manipulation of any number of contributions

$$C(k^*) = \frac{S(k^*)}{R(k^*)} = \frac{\sum_i S_i(k^*)}{\sum_i R_i(k^*)}, \quad (3.19)$$

¹⁹This is quite logical, as these weight should be compatible with the λ parameters from section 2.7.2, which are based on uncorrelated single particle properties.

$$\begin{aligned} S_i(k^*) &= w_i^S(k^*)S(k^*) \\ R_i(k^*) &= w_i^R(k^*)R(k^*), \end{aligned} \quad (3.20)$$

$$\sum_i w_i^S(k^*) = \sum_i w_i^R(k^*) = 1 \quad (3.21)$$

$$C(k^*) = \frac{S(k^*)}{R(k^*)} = \frac{\sum_i w_i^S(k^*)S(k^*)}{\sum_i w_i^R(k^*)R(k^*)}, \quad (3.22)$$

$$C_i(k^*) = \frac{S_i(k^*)}{R_i(k^*)}, \quad (3.23)$$

$$C(k^*) = \sum_i w_i^R(k^*)C_i(k^*), \quad (3.24)$$

where i is indexing the different contributions, and a consistent normalization requirement is best achieved through natural normalization, in which S , S_i , R and R_i are treated as probability density functions, having their integral over the full k^* normalized to unity.

3.2.3 Practical applications

Practically, the following statements are mathematically equivalent to the considerations in section 3.2.2:

- **Direct addition of the same-event or the reference samples:**

According to the numerator (denominator) of Eq. 3.12, the total same-event (reference) sample $S(k^*)$ ($R(k^*)$) is simply the direct sum of the individual distributions $S_X(k^*)$ and $S_Y(k^*)$ ($R_X(k^*)$ and $R_Y(k^*)$). Thus, if all of $S_X(k^*)$, $S_Y(k^*)$, $R_X(k^*)$ and $R_Y(k^*)$ are known, the total correlation function can be obtain by adding them according to Eq. 3.12.

- **Weighted arithmetic mean for the same-event or reference sample:**

If the distributions $S'_X(k^*)$, $S'_Y(k^*)$, $R'_X(k^*)$ and $R'_Y(k^*)$ are treated as probability density functions²⁰, Eq. 3.12 can be rewritten as

$$C(k^*) = \frac{w_X S'_X(k^*) + w_Y S'_Y(k^*)}{w_X R'_X(k^*) + w_Y R'_Y(k^*)} \quad (3.25)$$

where the weights w are the total yields of their corresponding distributions ($w_X = \int S_X(k^*)dk^*$ etc.). These weights have to be identical for the same-event and the reference sample, in order to respect the condition 3.13. The numerator and denominator in 3.25 are the mathematical definition of an arithmetic mean. Thus, if all the individual distributions $S'_X(k^*)$, $S'_Y(k^*)$, $R'_X(k^*)$ and $R'_Y(k^*)$ are know, and the fractional contributions of X and Y to the total correlation, $C(k^*)$ can be evaluated. This was the default method used to add the particle-particle and antiparticle-antiparticle correlation functions in this work.

- **Weighted arithmetic for the correlation functions:**

Equations 3.12, 3.25 and 3.17 are all equivalent and in Eq. 3.17 $C(k^*)$ corresponds to the weighted mean of $C_X(k^*)$ and $C_Y(k^*)$. However, in contrast to the derivation of 3.25, the weights are evaluated at each k^* value. In the practical case of saving correlation functions in histograms, the addition of two

²⁰i.e. normalized to the total yield, such as $S'_X(k^*) = S_X(k^*) / \int S_X(k^*)dk^*$ etc.

correlation functions is reduced to adding the corresponding histograms using (bin by bin) the arithmetic mean, without requiring any prior knowledge on the same-event or reference samples. An important caveat is that Eq. 3.17 is obtained under the assumption that 3.13 is fulfilled. As discussed, this is true independently of the same-event or reference samples only if they are treated as probability density functions, implying a normalization over their total yields.

In conclusion, the *natural* normalization of the correlation function is to evaluate it based on the probability density functions of the same-event and reference samples. The pure femtoscopic signal converges to unity at larger k^* , thus it is more intuitive to present the data with a normalization resulting in $C(k^*) \approx 1$ just above the femtoscopic region. To avoid any issues with the addition of the individual correlation functions, it is highly recommended to always work with the *natural* normalization of the correlation functions, and re-normalize the final result (for purely visual purposes) only after all analytical manipulations have been carried out. This strategy has been employed in the analyses presented in this work.

3.3 Handling the λ parameters

3.3.1 General overview

The decomposition of the correlation function was introduced from a theoretical standpoint in section 2.7. The main result is contained in Eq. 2.37

$$C(k^*) = \sum_{i=0}^{N_{X,F}+N_{X,M}} \sum_{j=0}^{N_{Y,F}+N_{Y,M}} \lambda_{i,j} C_{X_i-Y_j}(k^*), \quad (2.37)$$

which states that all contributions (i, j) to the correlation function can be accounted for if their corresponding fractions $\lambda_{i,j}$ and functional shapes $C_{X_i-Y_j}(k^*)$ are known. Here X and Y represent the investigated particles species, while N_F and N_M are the number of distinct correlation signals present in the experiment, with F and M corresponding to feed-down and misidentifications respectively. In practice, there are multiple complications in the determination of each $\lambda_{i,j}$ and $C_{X_i-Y_j}(k^*)$, instead alternative methods for correcting for these contributions is needed. In this section we will discuss some data-driven approaches to treating the contamination from the misidentified particles. In the scope of the correlation function, the fractions and purities used in the determination of the λ parameters should be associated with the particles used to build the pairs. To first order, these coincide with the single particles selected for the analysis, as done for the Monte-Carlo template fits to the data presented in sections 3.1.4 and 3.1.5. Nevertheless, depending on the number of selected particles in an event, a single particle can be used to build multiple pairs. Moreover, the kinematic and topological properties, including the purity, of the particles depend on the properties of the underlying event, such as the multiplicity. This leads to a difference in the *purities and fractions* evaluated from all selected single particles and from the particles used to build a pair. In addition, a k^* dependence of λ is expected to occur. As discussed in section 3.1.6, a perfect reference sample should exhibit the exact same properties as the same-event sample, apart from correlations due to the final state interaction. Thus the mixed-event sample should be used to obtain λ parameters that are not biased by the final state interaction. In fact, in very statistics rich data sets the bias that is present in the same-event sample could be used to disentangle the different contributions to the correlation function, which

will be discussed in section 3.3.4.

Within this work, the Λ - Λ analysis has been performed by ignoring the k^* dependence of the λ parameters, where the purity and fractions of the Λ particles are evaluated directly from the single particles. This is an approximate approach to the λ parameters, but it works well up to a precision of c.a. 1%, which is not achieved for Λ - Λ . The p- Λ analysis performed in HM p-p collisions has a much larger precision, making the correlation function sensitive to second-order effects. It was found that the contribution related to misidentified Λ particles is the most relevant of these effects, thus the p- Λ purity evaluation is performed based on the invariant mass spectra of the mixed-events at low k^* , while the fraction of secondaries to the Λ s is attributed a larger uncertainty, consistent with the expected k^* dependence. The details are discussed in the following sub-sections and in the [p- \$\Lambda\$ chapter](#).

3.3.2 Correction for impurities

The impurities related to *misidentified particles* could produce a non-flat correlation signal, that will contaminate the measured correlation function. The strength of the contamination is determined from the purities of the measured particles, and the corresponding λ parameters (see section 2.7.2). Simplified, the contribution to the total $C(k^*)$ is

$$\begin{aligned} C(k^*) &= \lambda_{\text{pure}} C_{\text{pure}}(k^*) + \lambda_{\text{misid}} C_{\text{misid}}(k^*), \\ C(k^*) - 1 &= \lambda_{\text{pure}} [C_{\text{pure}}(k^*) - 1] + \lambda_{\text{misid}} [C_{\text{misid}}(k^*) - 1], \end{aligned} \quad (3.26)$$

where λ_{pure} is the amount of pure signal, $\lambda_{\text{misid}} = 1 - \lambda_{\text{pure}}$ is the amount of impurities and $C_{\text{pure}}(k^*)$, $C_{\text{misid}}(k^*)$ are the corresponding correlation functions. It is commonly assumed that $C_{\text{misid}}(k^*) \approx 1$, and the modeling of the impurities is reduced to a simple re-scaling stemming directly from the λ_{pure} parameter. In principle, the $C_{\text{misid}}(k^*)$ can deviate significantly from unity, as seen in the p- Λ correlation (chapter 6, Fig. 6.6). Nevertheless, the effect is reduced by λ_{misid} , thus one can neglect its contribution if the modification of the correlation function $C(k^*)$ is smaller than the uncertainty $\Delta C(k^*)$, resulting in the condition

$$\begin{aligned} \Delta[C(k^*) - 1] &> \max[\lambda_{\text{misid}} C_{\text{misid}}(k^*) - 1] \\ \Delta[C(k^*)] &> \lambda_{\text{misid}} \cdot \max[C_{\text{misid}}(k^*) - 1]. \end{aligned} \quad (3.27)$$

This expression “measures” how much $C_{\text{misid}}(k^*)$ deviates from the assumed flat solution, with respect to the uncertainties of $C(k^*)$, and will be used later on to gauge the possibility of approximating the misidentifications.

Next, let us examine the different sources of misidentifications and the strategies of accounting for their effect. The simplest case is a *direct misidentification*, in which a particle is assigned the wrong species, e.g. a kaon labeled as a proton. If the studied correlation is p- Λ , this would result in a certain amount of $K^+ - \Lambda$ signal present in the measurement. Assuming the corresponding $\lambda_{K^+ - \Lambda}$ is known, this contribution can be modeled by either using existing theoretical predictions to evaluate $C_{K^+ - \Lambda}(k^*)$, or perform an associated experimental measurement of the $K^+ - \Lambda$ correlation function. Both of these methods are often inefficient, as the associated theoretical and experimental uncertainties tend to be very large. Thus it is advisable to reduce λ_{misid} as much as possible, until the contamination can be neglected following Eq. 3.27. This is feasible for the direct detection of particles, such as protons,

kaons and pions, in all ALICE measurements up to date, as the achieved purity is very high ($> 99\%$). Indeed for $K^+ - \Lambda \rightarrow p - \Lambda$ the high proton purity allows to disregard this particular contribution. However, there is a second type of misidentifications, which occurs as a *combinatorial background* when reconstructing V0 or cascade particles (Λ , Ξ , etc.) based on the invariant mass of their decay products. In that case most of the falsely reconstructed candidates stem from the combination of two particles, which are *not* produced in the same decay process. The associated signal $C_{\text{misid}}(k^*)$ is non-trivial, as it mainly consists of one real and one fake particle, where the latter carries the kinematical properties of two different particles, which are still produced in the same event and could be correlated, femtoscopically or otherwise, to the correctly reconstructed candidate inside the pair. For example, in the $p - \Lambda$ correlation function a misidentified Λ is built from a proton and a pion which are part of the background of the invariant mass spectrum of $p\pi^-$. The resulting correlation is created from a true proton and a fake Λ , where the signal will consist of $p-p$, $p-\pi^-$ and perhaps even 3-body $pp\pi^-$ signals, all of which will be shifted or smeared along the k^* axis due to the different kinematics compared to the Λ candidate, making impossible to model $C_{\text{misid}}(k^*)$ theoretically. Nevertheless, there are data-driven alternatives, such as using a *sideband analysis* or a *momentum dependent decomposition analysis*.

3.3.3 Sideband analysis

The sideband analysis is a data-driven approach, which relies on estimating $C_{\text{misid}}(k^*)$ by intentionally pairing background particle candidates to build up the correlation function. For a pair $X-Y$, we could have 3 distinct types of background correlations, stemming from $X-\tilde{Y}$, $\tilde{X}-Y$ or $\tilde{X}-\tilde{Y}$ ²¹. For the purpose of simplicity, we would only concentrate on studying a single contribution. The $p-\Lambda$ correlation function will be used as an example, as this method will be applied to it in section 6.2.3. Due to the very high proton purity in ALICE, we can assume that the only relevant background stems from misidentified Λ particles ($\tilde{\Lambda}$), forming $C_{\text{misid}}(k^*)$ out of $p-\tilde{\Lambda}$ pairs. Based on the invariant mass spectrum of the Λ candidates (Fig. 3.10), it is evident that outside of the peak region all the candidates are background (misidentified) particles and can be used to select $\tilde{\Lambda}$. To reconstruct $C_{\text{misid}}(k^*)$ the exact same procedure is followed as to obtain the $p-\Lambda$ correlation (section 3.1.6), with the only difference being the modified invariant mass range of selection of $\tilde{\Lambda}$ instead of Λ . An important check to perform is, if the range of the IM spectrum matters to the resulting sideband correlation function, in particular when selecting $\tilde{\Lambda}$ from the *left* or the *right* sideband, corresponding, respectively, to IM values smaller or larger than the Λ mass. Identical $C_{\text{misid},\text{left}}(k^*)$ and $C_{\text{misid},\text{right}}(k^*)$ point to equivalent kinematical and topological conditions for all background track around the peak region, in which case it is safe to assume that the background underneath the peak has the same properties. This allows to obtain $C_{\text{misid}}(k^*)$ from the weighted average sum of the two sideband correlations. On the contrary, if $C_{\text{misid},\text{left}}(k^*) \neq C_{\text{misid},\text{right}}(k^*)$ the precise determination of $C_{\text{misid}}(k^*)$ becomes impossible, nevertheless a reasonable assumption is that the true background is composed of a superposition between the two sidebands

$$C_{\text{misid}}(k^*) \approx \omega_{\text{left}} C_{\text{misid},\text{left}}(k^*) + \omega_{\text{right}} C_{\text{misid},\text{right}}(k^*), \quad (3.28)$$

²¹In this notation, X is a correctly identified particle, while \tilde{X} is a misidentified particle, i.e. wrongly reconstructed and identified as X .

where the weights ω_{left} and ω_{right} need to be determined separately, as well as study their systematic uncertainty.

Given $C_{\text{misid}}(k^*)$, based on Eq. 3.26 the *pure (corrected)* correlation function is

$$C_{\text{pure}}(k^*) = \frac{C(k^*) - \lambda_{\text{misid}} C_{\text{misid}}(k^*)}{\lambda_{\text{pure}}} = \frac{C(k^*) - (1 - \lambda_{\text{pure}}) C_{\text{misid}}(k^*)}{\lambda_{\text{pure}}}. \quad (3.29)$$

In the specific case of p- Λ , the misidentifications are only related to Λ , thus λ_{pure} corresponds to the purity of the Λ particles. Further details and the results on the p- Λ analysis are presented in the dedicated section 6.2.3.

3.3.4 Momentum dependent decomposition analysis

In this section we will discuss an elegant method to separate all individual contributions to the correlation function in a data-driven approach, which is unfortunately very demanding on statistics and not applicable to any of the RUN2 results. Nevertheless, it is an alternative option to the methodology adopted in the analyses up to date, and it might become feasible to use on RUN3 data (beyond 2021).

The idea is to study the purity and the fractions of primaries and secondaries, separately for the particles used to build the same- and mixed-event pairs, deferentially as a function of k^* . In principle, there is little difference to the current strategy of performing invariant mass or template fits in several bins of p_T (sections 3.1.4 and 3.1.5), however the input data will stem from the same- and mixed-events and the differential analysis has to be performed over k^* with a similar binning as the correlation function. The latter is the bottleneck leading to the requirement of a very large data sample. Based on equations 3.19 to 3.24 the total correlation function is given as the weighted sum of all individual states into which it is decomposed. In the standard formalism of the λ parameters equations 2.37 and 3.24 become equivalent, with the weights w_i^R being replaced by λ_{ij} and the correlation $C_i(k^*)$ with $C_{X_i-Y_j}(k^*)$, corresponding, respectively, to the weight and functional shape of each contribution X_i-Y_j , further notated as ij , to the correlation function. From equations 2.37, 3.19, 3.20 and 3.23 it follows that

$$C(k^*) = \sum_{ij} \lambda_{ij}^R(k^*) C_{ij}(k^*), \quad (3.30)$$

$$C_{ij}(k^*) = \frac{S_{ij}(k^*)}{R_{ij}(k^*)} = \frac{\lambda_{ij}^S(k^*) S(k^*)}{\lambda_{ij}^R(k^*) R(k^*)} = \frac{\lambda_{ij}^S(k^*)}{\lambda_{ij}^R(k^*)} C(k^*), \quad (3.31)$$

where the weights $\lambda_{ij}^S(k^*)$ and $\lambda_{ij}^R(k^*)$ are the λ parameters obtained from the same-event and reference (mixed-event) samples respectively. The formalism requires that the evaluation of these parameters is performed deferentially in k^* .

The physics significance and interpretation of Eq. 3.31 is that given a measured correlation function $C(k^*)$ and a *precise* determination of the $\lambda(k^*)$ parameters in the

same- and mixed-event samples, it is possible to disentangle all individual contributions²² to the correlation signal in a data-driven²³ approach. This is made possible by the fact that the yield of the correlated sample, as a function of k^* , is modified for correlated particles, leading to a re-distribution of the yield over k^* , that is unique for each contribution to the correlation. It is important to note, that here we use the assumption of a *perfect* reference sample, for which the average properties of the single particles are identical for the same- and mixed-event samples. This implies that the λ_{ij} parameters averaged over k^* satisfy

$$\lambda_{ij} = \int_0^\infty S_{ij}(k^*) \lambda_{ij}^S(k^*) dk^* = \int_0^\infty R_{ij}(k^*) \lambda_{ij}^R(k^*) dk^*. \quad (3.32)$$

The above condition should be utilized as a cross-check to validate the usage of Eq. 3.31. If Eq. 3.32 is not fulfilled, the evaluation of the *reference (mixed-event) sample* has to be revised.

The method of *momentum dependent decomposition* has been developed in the scope of this PhD thesis and used to investigate the statistics rich data sample for the p- Λ analysis, using the HM pp collisions at 13 TeV. Nevertheless, it has been found that $\lambda_{ij}^S(k^*)$ cannot be determined with the required precision.

3.4 Non-femtoscopic baseline

3.4.1 Origin

The two-particle correlation function is not exclusive to the effects of the final state interaction, but it contains *any* source of correlations. Their origin might be artificial or physics related. The former is linked to the reference sample, which is often not fully satisfying the properties of the same-event sample (see e.g. section 3.1.6 or Eq. 3.32). The focus of this section is on the physics effects associated to a correlated emission included in the *source function* $S(\vec{r}^*, \vec{k}^*)$. The cause of these non-femtoscopic correlations can be very diverse in nature, as they can originate from the multiple stages of the evolution of the collision system. These effects are best studied either with *angular two-particle correlations*, in which the effect of the final state interaction is significantly reduced, or by studying the collective (flow) effects present in the system [78–80].

From a modelling perspective, the evolution of the collision system begins with a defined set of initial conditions. In HI reactions these are related to the *QGP* formation, typically determined by the temperature and energy density of the medium, used as an input for an effective hydrodynamical evolution of the system. After the medium reaches certain energy density, a particalization happens, which is the transformation of the hydrodynamical fluid to particles²⁴, that can be either partons or hadrons. The former are an intermediate step in advance modellings. The produced hadrons can experience further re-scattering among themselves, typically modeled by transport models. For pp collisions the situation is considered different, due to the smaller

²²Those are the genuine correlation, feed-down contributions and contamination due to misidentifications.

²³The determination of the λ parameters is typically data-driven, although the usage of MC simulations is often required, e.g. for the template fits or determination of the proton purity.

²⁴This is purely an *effective* theoretical approach, in reality the full description of the system is governed by QCD, nevertheless it is difficult to simulate large systems based on first principles.

size of the collision system, which makes the bare use of hydrodynamics no longer applicable. Instead, the initial stage of the evolution has to be described by the hard QCD scattering processes²⁵ between the colliding particles, causing the creation of high-energetic partons glued together by the gluon self-interaction into *color strings*. This is the basis of the fragmentation models, which are commonly used in MC generators such as Pythia. A single sting can be modeled by a quark–antiquark ($q\bar{q}$) pair with large energy, which due to the color confinement splits, depending on the so called *string tension*, into two $q\bar{q}$ pairs of lower energy. The process of splitting continues recursively, until the energy is low enough for the quarks and antiquarks to hadronize into mesons and anti-mesons (qq or $\bar{q}\bar{q}$) or baryons and anti-baryons (qqq and $\bar{q}\bar{q}\bar{q}$). The hadrons produced by a single string are strongly collimated, leading to a cone-like emission structures. These are called *mini-jets*, and are observed experimentally in pp collisions. Based on existing measurements, it is known that the correlations due to mini-jets are very strong for meson pairs as well as for baryon–antibaryon pairs, but are not contributing significantly to baryon–baryon correlations. This fact has been backed up by Monte-Carlo simulations and at present the interpretation is that the baryon number conservation acts locally on the partons undergoing fragmentation to hadrons, which makes the production of a baryon–baryon pair inside a mini-jet energetically unfavorable, as it requires the coincident production of an antibaryon–antibaryon pair. Studies performed on two-particle angular correlations are compatible with this picture, as shown in Fig. 3.18 and 3.19, although they reveal significant deviations between the predicted correlation from Monte-Carlo simulations, Pythia in particular. This discrepancy is also seen in the long-range correlations in momentum space (see Fig. 3.16 and 3.17). In fact, in recent years Pythia has struggled to describe many of the results in small collision, in particular at high-multiplicities, such as the enhanced production of strange particles or the angular distributions reminiscent to the flow-like structures observed in HI collisions [6, 79–82]. The authors of Pythia addressed many of these issues during the *Quark matter conference 2018* [83], concluding that the Lund model of hadronization, as used in Pythia, has reached its limit and new developments are needed in order to progress. One prominent approach is the use of the *core-corona model*, which attempts to combine the fragmentation of partons (corona) with a hydrodynamical fluid (core). It has been suggested that for large energy densities, such as for low p_T (soft) particles in high-multiplicity collisions, the partons can form a medium that behaves collectively as a fluid and hydrodynamics can be employed. On the other hand, high p_T fragments will escape from this medium and will form the corona, which is modeled by traditional fragmentation models. Nevertheless, a major criticism towards the core-corona model is the mixing of an effective approach (hydrodynamics) with a physics motivated modelling (Lund model) and the current lack of a physical interpretation to do so. To address this, it has been speculated that an onset of QGP (droplets) in pp collisions is present, in particular at higher multiplicities, or that the partonic interactions at large energy density can lead to similar effects [81, 82]. There is still no solid theoretical conclusion about either of these statements. In practice, the EPOS transport model has adopted the core-corona approach [84, 85]. It can provide better description of certain kinematic observables, including collective effects in small systems, nevertheless it still fails to reproduce the other above discussed observables. Recent developments in theory lead to the idea of using a dynamical initialization of the core and corona, enabling to describe the strangeness enhancement in HM pp collisions [86], but it is yet not clear if such

²⁵Hard scattering processes are characterized by a large momentum transfer.

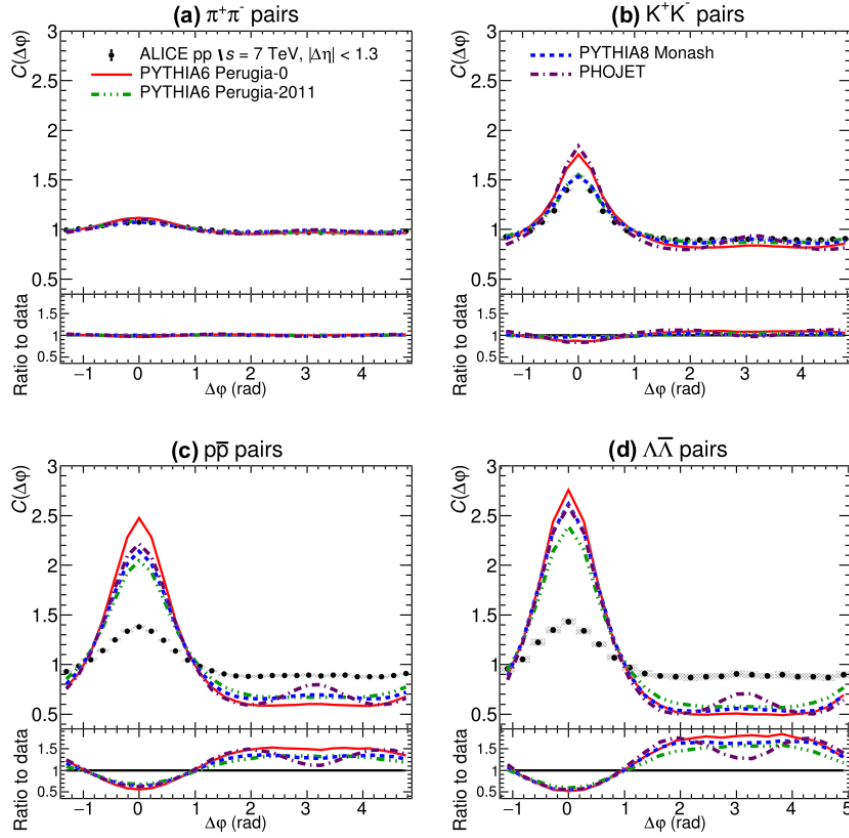


FIGURE 3.18: Two-particle angular ($\Delta\varphi$) distributions in 7 TeV pp collisions measured by ALICE [80]. The upper panels represent meson-antimeson pairs, while the lower panel shows baryon-antibaryon pairs. Both the data points and MC predictions (colored lines) predict a mini-jet contribution at $\Delta\varphi = 0$ and a flat behaviour at large $\Delta\varphi$, however the strength of the signal is overpredicted in the MC.

an approach can lead to a better description of the angular correlations between the emitted particles.

An alternative approach to solve the puzzle of hadronization in small systems is to use a *quark coalescence model*. The coalescence is characterized by a quantum mechanical modeling of the quarks, and the hadron formation is described by the overlapping wave functions of the individual quarks. Originally, quark coalescence models were applied to heavy ion data at the Relativistic Heavy Ion Collider (RHIC) for gold–gold collisions at 130 GeV [87], with the goal of gaining deeper understanding of the strong elliptic flow observed in this system. This was embedded in the AMPT model [88], which employs a multiphase evolution of the collision system, modelling each step with a physics driven model. The first phase is based on string fragmentation, where the Pythia-based HIJING model²⁶ is used [89], followed by an explicit treatment of the scattering between partons with Zhang’s parton cascade (ZPC). The next phase is the hadronization, which traditionally is modeled using the Lund fragmentation, or alternatively by quark coalescence. Finally, the scatterings among the hadrons are described by the relativistic transport model ART [90]. The AMPT model aims at providing a more solid physics understanding of the collision system without using hydrodynamics. The focus of the model has been mostly

²⁶HIJING has a special emphasis on describing the role of the mini-jets in any collision system.

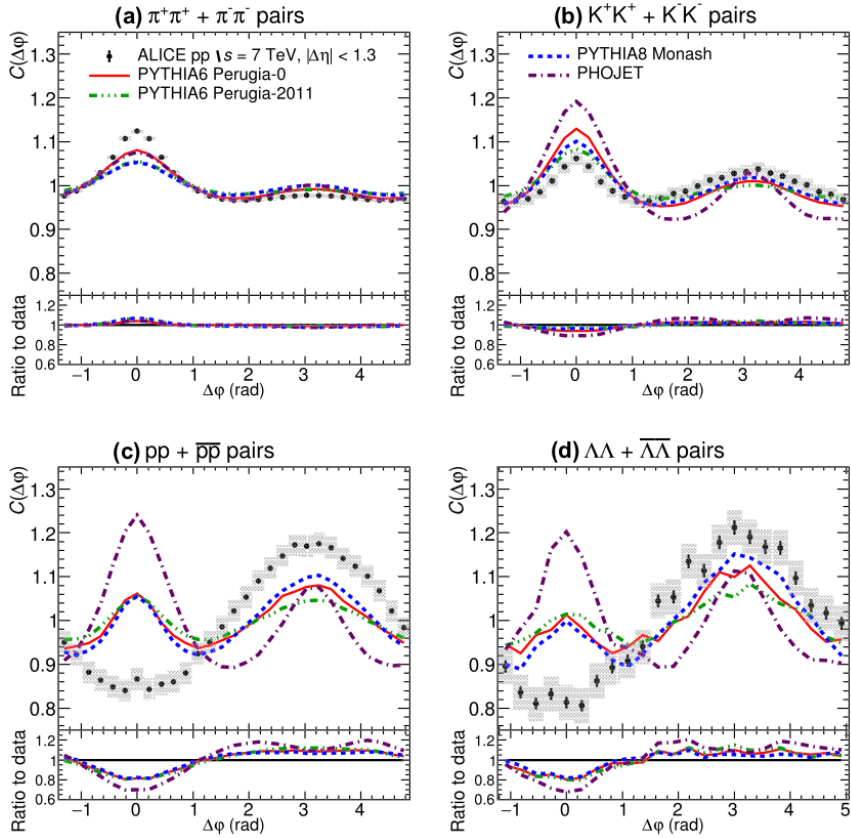


FIGURE 3.19: Two-particle angular ($\Delta\varphi$) distributions in 7 TeV pp collisions measured by ALICE [80]. The upper panels represent meson-meson pairs, while the lower panel shows baryon-baryon pairs. The data points and MC predictions (colored lines) show a qualitative agreement and quantitative disagreement for meson-meson pairs, however for baryon-baryon pairs they are in complete disagreement at $\Delta\varphi = 0$.

on heavy-ion collisions, however the interesting discoveries in small collision systems lead to a lot of effort in improving the AMPT model, in particular the quark coalescence [91]. Figure 3.20 shows the recent results published by the AMPT authors, demonstrating a qualitative agreement to the ALICE data for the two-particle angular distributions [92]. Further, an independent study by the same team claims that the improved AMPT model predicts accurately the strangeness enhancement in high-multiplicity pp collisions [93]. Both of these studies relied on changing certain parameters within the AMPT model, thus this is not yet a proof for an exact and simultaneous description of these effects. Nevertheless, in my personal view this is a major step in the field, even more supported by the fact that AMPT can be successfully applied to heavy-ion collisions as well [94]. In section 3.4.3 I will suggest possible further studies in order to examine the validity of quark coalescence models, relating to the two particle correlations in momentum state and the observed long-range baryon-baryon correlations in the ALICE results in pp collisions (Fig. 3.16 and 3.17).

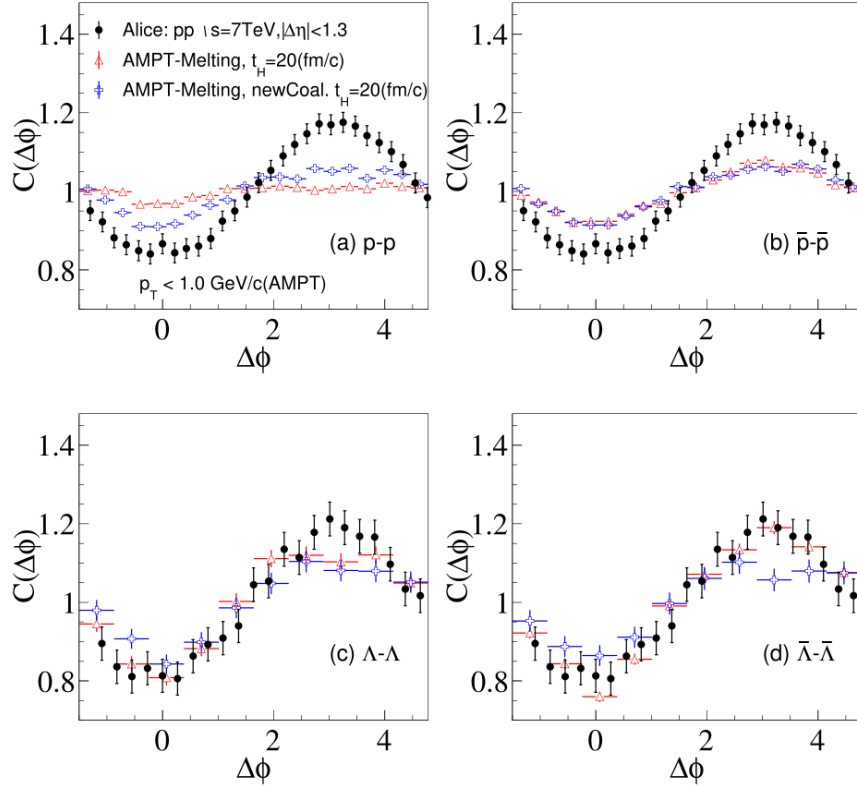


FIGURE 3.20: Two-particle angular ($\Delta\phi$) distributions in 7 TeV pp collisions simulated with the improved coalescence model in AMPT (blue points) [92]. The simulations are separated for baryon–baryon and antibaryon–antibaryon correlations in the left and right panels correspondingly, while the experimental data (black) shows the combined result.

3.4.2 Effect on the correlation function

Section 3.4.1 discussed the complexity related to the origin of the non-femtoscopic correlations. Due to the lack of deeper understanding of the issue, for practical purposes there are approximate ways of modeling these correlations. The general idea is to perform a separation of variables on the source function $S(\vec{r}^*, \vec{k}^*)$

$$S(\vec{r}^*, \vec{k}^*) = C_{\text{non-femto}}(k^*) S(r^*), \quad (3.33)$$

where $C_{\text{non-femto}}(k^*)$ is referred to as a *non-femtoscopic baseline correction* and $S(r^*)$ is the source function including only the radial dependence, which is the commonly used convention in the field. The angular dependence is assumed to be a trivial (flat), thus excluded from Eq. 3.33. Following the Koonin-Pratt relation (Eq. 1.12) the experimental correlation is expressed as

$$C_{\text{exp}}(k^*) \approx C_{\text{non-femto}}(k^*) \cdot C_{\text{femto}}(k^*), \quad (3.34)$$

where $C_{\text{femto}}(k^*)$ is the pure femtoscopic correlation function, using a source function with a radial dependence only. Typically the final state interaction is not included in Monte-Carlo simulations, implying $C_{\text{femto}}(k^*) = 1$. Thus the reconstruction of the correlation function from an ideal full scale simulation will result in

$C_{\text{MC}}(k^*) = C_{\text{non-femto}}(k^*)$. As demonstrated in section 3.4.1, MC simulations often struggle to reproduce the data quantitatively, however as long as a qualitative description is available, one can assume $C_{\text{MC}}(k^*)$ deviates only slightly from $C_{\text{non-femto}}(k^*)$ and is expressed as

$$C_{\text{non-femto}}(k^*) \approx b(k^*) \cdot C_{\text{MC}}(k^*), \quad (3.35)$$

where $b(k^*)$ is a smooth function inducing a small correction to the MC data. An alternative parameterization is

$$C_{\text{non-femto}}(k^*) \approx \mathcal{N} [\omega_{\text{MC}} C_{\text{MC}}(k^*) + b_a(k^*)], \quad (3.36)$$

where $b_a(k^*)$ is an additive correction to the MC data, \mathcal{N} is a re-normalization factor and ω_{MC} is the weight with which the original MC signal enters the correlation. The latter plays a similar role as a λ parameter, although it is not limited to be smaller than unity, due to the possibility that MC simulations under-predict the strength of the signal. The terms $b_m(k^*)$ and $b_a(k^*)$ have to be smooth by construction, thus they are often parameterized with a low degree polynomial.

Depending on the collision system and the investigated particle species the strategies of accounting for the non-femtoscopic contributions are different. In *heavy ion collisions* the dominating effect is the collective expansion of the fireball, leading to flow-like effects. These are typically modelled by hydrodynamics, e.g. using the THERMINATOR Monte-Carlo event generator [95]. The resulting $C_{\text{MC}}(k^*) \approx C_{\text{non-femto}}(k^*)$, avoiding the need to use an additional correction. Moreover, these systems tend to have a very broad flat region in both $C_{\text{exp}}(k^*)$ and $C_{\text{MC}}(k^*)$, allowing to normalize the data directly to the femtoscopics convention. This reduces significantly the systematic uncertainties related to the modelling of the data, which is an advantage over small collision systems. In *small collision systems*, Monte-Carlo (Pythia) simulations tend to work qualitatively for meson-meson correlations (Figs. 3.18 and 3.19), which are dominated by the pure mini-jet contribution, allowing the use of Eq. 3.35 or 3.36 to account for the non-femtoscopic correlations. This situation is similar for baryon-antibaryon correlations (Fig. 3.18). For baryon-baryon correlations Pythia fails completely in the reproduction of the experimental observations in $\Delta\varphi$ (Fig. 3.19). However, there is one particularity that can be exploited to adapt Eq. 3.35 to the baryon-baryon case. Figures 3.16 and 3.17 show that the Pythia predicted correlation signal at low k^* is rather small, leading to a minor non-flat behaviour regardless of the studied particle species. Apart from the expected femtoscopic signal, the data shows a similar trend for $k^* < 400 \text{ MeV}/c$ attributed to the suppression of mini-jets, which are the main contributor to the non-flat signal present in $C_{\text{MC}}(k^*)$. This observation warrants the assumption $C_{\text{MC}}(k^*) \approx 1$, despite of the discrepancies between data and MC in the angular space. This leads to $C_{\text{non-femto}}(k^*) \approx b(k^*)$ and

$$C_{\text{exp}}(k^*) \approx C_{\text{non-femto}}(k^*) \cdot C_{\text{femto}}(k^*) = b(k^*) \cdot C_{\text{femto}}. \quad (3.37)$$

This relation will be used to model the data in the analyses presented in this work, and is the recommended approach to any *baryon-baryon* correlations, until more accurate theoretical predictions become available.

To choose the *functional shape* of $b(k^*)$, one should consider the fact that for baryon-baryon correlations in small collision systems $b(k^*) = C_{\text{non-femto}}(k^*)$ represents all

non-femtoscopic correlations. In the absence of final state interaction, these are still expressed as the ratio of a same-event $S(k^*)$ and a reference $R(k^*)$ sample, both of which correspond to an yield of particle pairs distributed in the k^* space. There is no physics reason for a sharp cut-off in the distributions, thus both should converge smoothly towards zero at $k^* \rightarrow 0$, i.e. at very small k^* $S(k^*) \propto R(k^*) \propto \text{constant}$, leading to $S(0)/R(0) = C_{\text{non-femto}}(0) = \text{constant}$. Assuming that $C_{\text{non-femto}}(k^*)$ is expressed as a polynomial, the easiest way to guarantee the condition of a flat functional shape at zero is to remove the linear term

$$C_{\text{non-femto}}(k^*) = \mathcal{N} \left(1 + \sum_{i=2}^{N_p} p_i k^{*i} \right), \quad (3.38)$$

where \mathcal{N} is a normalization constant, compatible with the definitions in section 3.2, p_i is the parameter related to the polynomial order i and N_p is the degree of the polynomial used. Such a simple modelling of the baseline will work only over a limited k^* range, in particular due to the non-flat long-range correlations, which can be related not only the hadronization process, but to biases in the phase-space of the reference sample. Thus it is advisable to extend the studied k^* range only a bit beyond the expected femtoscopic region. In practical terms, this is reflected in a typical upper limit for the k^* between 300 and 500 MeV/ c .

3.4.3 Future prospects

This section presents a possible explanation of the *long-range correlations* observed in the momentum space of the experimental data, as well as ideas for future studies.

For small collision systems, the non-femtoscopic signal is dominated by the hadronization process and contains some kinematic constraints, e.g. due to the limited phase space and problems with the reference sample. Following the idea of hadrons produced from the *coalescence of quarks*, it is reasonable to assume that the wave functions of the quarks obey the quantum statistic rules and symmetrize accordingly. Consequently, the hadronization of identical string fragments (quarks) close in position and momentum space will be suppressed. Naively, this would restrict the emission of adjacent baryon–baryon pairs with multiple identical quarks, which can be modeled with the typical femtoscopic expression related to quantum statistics for a Gaussian source of size r_0

$$C(k^*) = 1 - \mathcal{A} \exp(-k^{*2} r_0^2), \quad (3.39)$$

where \mathcal{A} is the strength of the signal. It is expected to decrease for baryon–baryon pairs of more diverse quark content. The hadronization time (τ_{had}) in pp collisions at 7 TeV has been reported to be between 0.3 and 0.5 fm [96], imposing similar values for the special separation between the quarks r_{had} . Figure 3.21 shows the long range part of the correlation functions for p–p, p– Λ , Λ – Λ and p– Ξ pairs in HM pp collisions at 13 TeV. Most of these correlation functions are unpublished, but have been obtained using the standard analysis techniques introduced in this chapter. To check if the long-range correlations are compatible with the picture of Pauli-blocking on the quark level all these correlations have been fitted in the range $k^* \in [600, 1600]$ MeV/ c using

$$C_{\text{exp}}(k^*) = \mathcal{N} [1 + p_1 k^*] [1 - \mathcal{A} \exp(-k^{*2} r_{\text{had}}^2)], \quad (3.40)$$

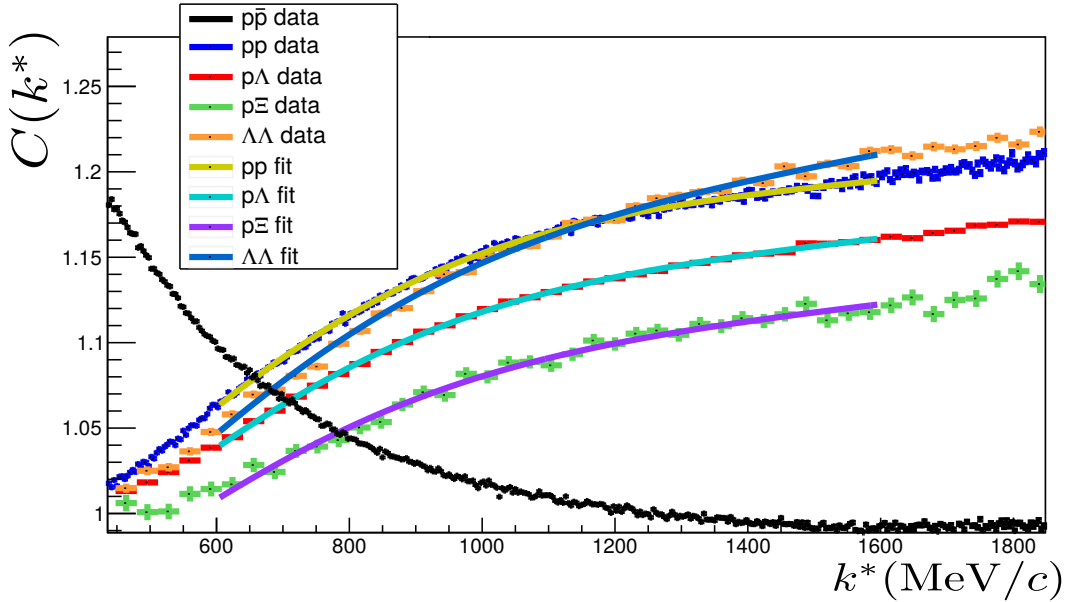


FIGURE 3.21: Long range baryon-baryon correlations in momentum space. The colored crosses represent the data points, while the lines the corresponding fits. The black data points are for baryon-antibaryon, demonstrating the big contribution of mini-jets for the latter, as well the absence of long-range suppression.

which accounts for a quantum statistics term of variable strength and width, multiplied by a linear baseline. The latter is included to absorb any long-range kinematics and is inspired by the linear shape of $C_{MC}(k^*)$ in this region (Figs. 3.16 and 3.17). No femtoscopic signal is expected due to the large k^* values. The hadronization scale should be similar for all particles, thus we can treat r_{had} as a common parameter for the 4 different systems, and perform a scan over the expected values to determine the best global χ^2 . The resulting fits are the lines in Fig. 3.21, and the corresponding fit parameters are summarized in Table 3.8. The fit does provide a very good descrip-

Pair	\mathcal{A}	$\mathcal{A}/\text{purity}$
p-p	0.197 ± 0.002	0.199 ± 0.002
$\Lambda-\Lambda$	0.189 ± 0.007	0.205 ± 0.008
p-Lambda	0.169 ± 0.002	0.177 ± 0.003
p-E ⁻	0.152 ± 0.014	0.159 ± 0.015

TABLE 3.8: The strength of the quantum statistics term needed to describe the long correlations of the different baryon-baryon systems.

tion of the long-range correlations in all systems, and the preferred value for r_{had} is 0.3 fm, which is compatible with expectations. The strength parameter \mathcal{A} follows a descending order for p-p, $\Lambda-\Lambda$, p-Lambda and p-E. Based on our ansatz, this is indeed the expected ordering, apart for p-p and $\Lambda-\Lambda$ which should be similar as in both cases the baryons are identical. However, the parameter \mathcal{A} is not only related to the hadronization, but depends on the amount of impurities and feed-downs. The latter could carry some Pauli signal, as the feeding particles have similar quark composition as their daughters, with up to 1 quark difference in the composition. There is no straight forward way of accounting for these effects, nevertheless the misidentified particles related to Λ and E stem from a combinatorial background, for which there

is no reason to assume coherent emission. For this reason it is sensible to correct \mathcal{A} by dividing it by the purity of the pair. The results in Table 3.8 demonstrate that the observed ordering is preserved, but now the p–p and Λ – Λ correlations have slightly more similar values. These observations, combined with the fact that there is no such long-range step-like structure observed in baryon–antibaryon correlations (e.g. p– \bar{p} is shown in Fig. 3.21), are strongly suggestive of a link to the quark coalescence. It is interesting to study if the long-range structure observed in the k^* space can describe the measured $\Delta\varphi$ relations for baryon–baryon correlations (Fig. 3.19). A very fast cross check is to make a small toy model, in which the kinematics of single particle emission is taken from a transport model, EPOS on the generator level in this example, and build the corresponding same- and mixed-event samples. Only an acceptance cuts on the momenta and η of the particles is applied to match the typical ALICE analyses. In the same-event sample the pairs are accepted only with a certain probability, which is based on Eq. 3.39 with the extracted results for $r_{\text{had}} = r_0$ and \mathcal{A} in the p–p system. This introduces the desired correlation in k^* , while building the $C(\Delta\varphi)$ is trivial, as the angular properties of the particles are known in the simulation. The result is shown in Fig. 3.22, where the measured ALICE data is compared to the prediction from EPOS with and without the inclusion of Pauli suppression. The default EPOS settings result in a correlation similar to the one observed in Pythia, and it fails completely in the description of the data. However, the inclusion of a quantum statistics suppression terms leads to a reduction of the peak at $\Delta\varphi = 0$ and an enhancement at $\Delta\varphi = \pi$, just as the data. The default strength of the Pauli signal of $\mathcal{A} = 0.2$ is not enough to explain the discrepancy, while $\mathcal{A} = 0.4$ provides a better description. Given the extremely crude toy model employed, it is not a surprise that a quantitative description of the experimental data cannot be obtained simultaneously in k^* and $\Delta\varphi$. Nevertheless, it is rather interesting to see that Pauli suppression term resembles the correlation shapes observed in both variables, suggestive that a deeper investigation is worthwhile.

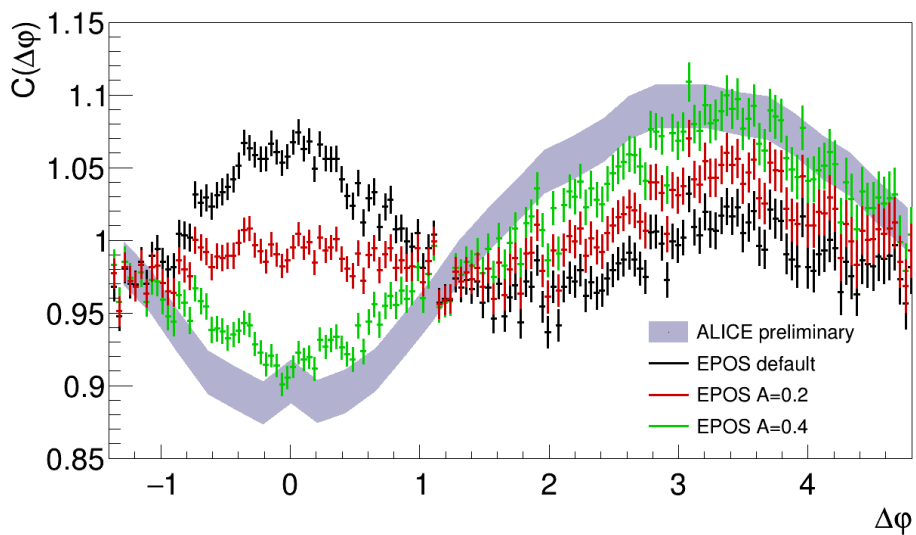


FIGURE 3.22: Comparison between the ALICE preliminary results [97] (gray band) for the p–p correlation in $\Delta\varphi$ and the results from the toy model using EPOS and a Pauli suppression term (see the text). The inclusion of the latter leads to a better description of the data.

In conclusion, the long range correlations in the momentum space are surely related to the overall shape of the $\Delta\varphi$ variations, and the observed shapes seem compatible with a picture of Pauli-suppressed hadronization of the quarks on the spatial-temporal scale of 0.3 fm. The development of models, such as AMPT, incorporating these effects is vital for the deeper understanding of underlying physics. At present there are no full scale AMPT simulations applied to the ALICE data, but for the future studies this is going to be an essential step that has to be executed in close collaboration with the AMPT development team. The long-range correlations are practically not limited by statistics in the collected data during LHC RUN2 period, making possible to perform these type of studies immediately. Using baryons is favorable due to the lack of contamination from resonances, making more easy to deliver quantitative predictions. The main goal would be to understand the differences between baryon–baryon and baryon–antibaryon systems and see if they can be traced back to their quark content. For practical purposes, understanding the long-range correlations will increase the constraining power of MC simulations to the non-femtoscopic contaminations at low k^* , reducing the associated uncertainty of the correlation function. At present the statistical uncertainties of the data are comparable to the systematic uncertainties of the non-femtoscopic baseline. It is expected that during the RUN3 of the LHC the collected raw data by ALICE will increase up to a factor of 100, leading to 10 times smaller statistical uncertainties. Moreover, dedicated online triggers for the benefit of femtoscopic studies are being considered, which could increase the statistics even more. This would imply that the systematic uncertainties will be dominant in any future femtoscopic study at ALICE, which are currently driven by the uncertainty of the baseline and the λ parameters. The former can be addressed with the above suggestions, while the latter could benefit from the suggestions presented in section 3.3.4.

3.5 Modelling of the data

3.5.1 Data fitting

In the present work the femtoscopic fit to the data is performed by

$$\begin{aligned} C_{\text{fit}}(k^*) &= C_{\text{non-femto}}(k^*) \cdot C_{\text{femto}}(k^*) = \\ &= \mathcal{N} (1 + p_1 k^* + p_2 k^{*2} + p_3 k^{*3}) C_{\text{femto}}(k^*). \end{aligned} \quad (3.41)$$

The signal $C_{\text{femto}}(k^*)$ is evaluated using the CATS framework, where the functional shape is determined by the emission source and the final state interaction. The main goal of the current analyses is to constrain and test existing theoretical predictions for the Λ – Λ and p – Λ interaction, thus all parameters related to $C_{\text{femto}}(k^*)$ have been fixed. The modelling of the source function is based on the assumption of a *common emission source* for all baryons and fixed from the p – p correlations (see chapter 4 and [44]). Since a solid description of the baseline is not available (see section 3.4) the fit parameters related to $C_{\text{non-femto}}(k^*)$ are left free. The downside of this approach is the fact that any bias in the modelling of the source or the interaction will be reflected in the non-femtoscopic parameters, making impossible to extract the functional shape of $C_{\text{non-femto}}(k^*)$ in a model independent way. Hence, the choice of ALICE was *not* to correct the baryon–baryon experimental data for $C_{\text{non-femto}}(k^*)$, allowing further investigations of the related effects outside of the collaboration. Still, assuming an accurate determination of the source function, the best fit provides a lower limit for the χ^2 describing the discrepancy between the interaction

theory and the data, independent of the baseline. The corresponding confidence intervals allow to quantify the accuracy of the different theoretical models, and exclude those providing the worst χ^2 (section 3.5.2).

The non-femtoscopic contribution $C_{\text{non-femto}}(k^*)$ is assumed to be a polynomial of up to third degree. As discussed in section 3.2, the experimental data cannot be reliably normalized to the femtoscopic correlations due to the presence of strong long-range effects, for this reason the constant term of the polynomial \mathcal{N} is not fixed. For the Λ - Λ correlation the default fit is performed by ignoring all other orders of the polynomial, since the large uncertainties of the data make it compatible with an approximately flat baseline and the inclusion of too many additional degrees of freedom would make the fit unstable. Nevertheless, there is a large amount of residual correlations feeding into Λ - Λ , which are assumed to be flat. To account for the possibility of a small non-flat feed-down correlations convoluted with a certain amount of non-femtoscopic correlations, the fit for Λ - Λ allows for a non-zero linear term p_1 of the baseline as part of the systematic variations. On the other hand, the p- Λ correlation is measured to much better precision, and the feed-down contributions are modeled in greater depth. This implies that the baseline is used exclusively to consider non-femtoscopic correlations, that can be described by Eq. 3.38. For that reason the baseline polynomial was chosen to be of third degree, with a zero linear order term ($p_1 = 0$).

3.5.2 Systematic uncertainties

Overview

The *systematic uncertainties* are defined as any non-statistical bias introduced by the experimental apparatus, data reconstruction or the subsequent theoretical modelling and fitting. There is no perfect recipe to account for these types of uncertainties, since from a philosophical perspective they can be extended to infinity, e.g. a good systematic check is to build multiple accelerator complexes of similar size to the LHC and redo all analyses with new experiments. Such a treatment of the systematics has obvious practical limitations, thus it is essential to find a simplified workflow that allows to get a realistic estimate on the systematic biases. A generally accepted practice is to assume that any observable \mathcal{X} is subject to *statistical and systematic fluctuations*, both following a *Gaussian distribution* around some true value $\mathcal{X}_{\text{true}}$. These two sources of uncertainties are ideally *independent*, thus the total uncertainty σ_{tot} is given as

$$\sigma_{\text{tot}}^2 = \sigma_{\text{stat}}^2 + \sigma_{\text{syst}}^2, \quad (3.42)$$

where σ_{stat} and σ_{syst} correspond to the pure statistical and systematical uncertainty. The relevant question becomes how to determine the individual components in Eq. 3.42. The statistical uncertainties are trivial to handle, as they are related to the number of counts recorded in the experimental distributions. To gauge the systematic uncertainties slightly different settings in the particle reconstruction and fit procedures are selected, leading to a modification of the originally measured value \mathcal{X}_0 to \mathcal{X}_i , where i is indexing the different modifications. Performing a large number of random variations will reveal the probability distribution of the observable \mathcal{X} related to the systematic uncertainty. There is one practical problem, namely that the resulting distribution could contain fluctuations of statistical nature, as each systematic variation selects a slightly different subset of the data. There could be other effects, mostly detector specific, leading to further correlations between the different

types of uncertainties. For example, in ALICE each modification of the selection criteria requires a numerical iteration on the grid over the full data set, and due to the slightly unstable behaviour of the computing resources some of the analyzed files will result in an error state²⁷. The errors on the grid tend to be random, as such the exact reproducibility of the final results is impossible, leading to yet another statistical fluctuation. For these reasons, the distribution of \mathcal{X}_i cannot be used to obtain σ_{syst} . Fortunately, this issue has one elegant solution, that involves the *bootstrap method*. It uses a random re-sampling of the data to create purely statistical fluctuations in any data set. Imagine we have discrete data sampled in a histogram \mathcal{D} , \mathcal{D}_i corresponds to the measured value in the i -th bin and \mathcal{E}_i is the statistical uncertainty. The bootstrap method will create a new histogram \mathcal{D}' , in which the value of each bin is selected from a Gaussian distribution of mean \mathcal{D}_i and standard deviation \mathcal{E}_i , leading to a spectrum identical to the original one, up to the artificially created fluctuations. Let the observable \mathcal{X}_i be the result of analysing the spectrum \mathcal{D}_i , clearly applying the same analysis procedure to \mathcal{D}'_i will lead to a modified value \mathcal{X}'_i . The probability distribution of \mathcal{X}' will contain *all* sources of uncertainties, including the statistical fluctuations, systematics related to the variations of the reconstruction criteria, grid fluctuations and any correlations among them. In simple terms, the standard deviation of this distribution corresponds to σ_{tot} . As long as it is approximately Gaussian, the effective systematic uncertainty that is independent²⁸ on the statistical fluctuations is

$$\sigma_{\text{syst}} = \sqrt{\sigma_{\text{tot}}^2 - \sigma_{\text{stat}}^2} \quad (3.43)$$

The power of the bootstrap method is twofold. Firstly, it can propagate and project the uncertainties from a measured spectrum \mathcal{D} to any observable \mathcal{X} . Secondly, it can be used to separate the statistical from the systematic uncertainties, as the bootstrap method can either be applied to the default measured spectrum \mathcal{D}_0 or to all variations \mathcal{D}_i , obtaining σ_{stat} and σ_{tot} respectively. In this work the bootstrap method is employed for both the Λ - Λ and p - Λ analyses, the details are presented in chapters 5 and 6.

Uncertainties related to the data

The measured correlation function is biased by the experimental conditions. The acceptance and efficiency of the ALICE detector do not play a significant role for femtoscopy, due to the fact that the effect of the efficiency is canceled out by the division of the same- and mixed-events samples. The acceptance influences both the source function and the non-femtoscopic baseline, however for the purpose of this work the observables of interest are related to the final state interaction, and those are independent of detector effects. Nevertheless, the source function is assumed to be common for all baryons, thus it is important to perform the reconstruction of the baryons with cuts that ensure similar acceptance for all species. Further, the influence of small changes in the selection criteria (section 3.1) onto the extracted correlation function need to be quantified and included in the systematic uncertainties. The most accurate treatment involves a variation of the selection criteria, a re-evaluation of all analysis parameters that depend on the acceptance, the λ parameters and source size in particular, and perform an independent fit to each variation. This is challenging to perform from a technical and computational point of view,

²⁷The success rate of the analysis on the grid varies between 95 – 99%.

²⁸Note that here *no* assumption is made, the observable σ_{syst} is defined as independent on the statistical fluctuations.

Condition	Default	Variations		
		p-Pb MB	pp MB	pp HM
$ \eta < X$	0.8	0.7, 0.9	0.77, 0.85	
$p_T > X \text{ GeV}/c$	0.5		0.4, 0.6	
$n_{\text{TPC}} > X$	80	70	70, 90	
$ n_\sigma < X$	3	2, 5	2.5, 3.5	

TABLE 3.9: Systematic variations for proton reconstruction (all default cuts are in Table 3.2). All 3 data sets are analyzed with the same default cuts, but the systematic uncertainties are slightly different.

Condition	Default	Variations		
		p-Pb MB	pp MB	pp HM
<i>Daughter track selection criteria</i>				
$ \eta < X$	0.8	0.7, 0.9	0.77, 0.83	
$n_{\text{TPC}} > X$	80	70	70, 90	
$d_{\text{PV}} > X \text{ cm}$	0.05		0.06	
$ n_{\sigma, \text{TPC}} < X$	5		4	
<i>V₀ selection criteria</i>				
$\text{DCA}(p, \pi) < X \text{ cm}$	1.5		1.2	
$\cos \alpha > X$	0.99	0.998	0.995	

TABLE 3.10: Systematic variations for Λ reconstruction (all default cuts are in Table 3.5). All 3 data sets are analyzed with the same default cuts, but the systematic uncertainties are slightly different.

thus, in case the uncertainty is dominated by the statistical component, the initial variation of the systematic selection criteria is sufficient. For the ALICE studies up to RUN2 the statistical uncertainties are larger or comparable to the systematics, for this reason the simplified approach is adopted. The resulting uncertainties will be conservatively overestimated, as the deviations related to the different λ parameters will be absorbed into them.

The systematic variations of the reconstruction criteria performed on the proton and Λ candidates are summarized in Tables 3.9 and 3.10. These variations are chosen such that any combination leads to a maximum change in the yield of selected pairs in the same-event sample of 25%, minimizing the bias discussed above. The systematic reconstruction of $C_{\text{exp}}(k^*)$ is performed for the default cuts and 44 variations based on randomly chosen values for the parameters listed in Tables 3.9 and 3.10. In the case of p- Λ , the correlation function is additionally corrected for misidentified Λ s using the sideband method, as described in section 3.3.3 and chapter 6. This procedure leads to 4 additional systematic variations applied to all of the 45 extracted experimental correlation functions, leading to a total of 180 variations of $C_{\text{exp}}(k^*)$.

Within the ALICE collaboration, the femtoscopic results are usually represented by plotting the data points of $C_{\text{exp}}(k^*)$ corresponding to the default cut variations and

the associated statistical error bars. The systematic uncertainties are plotted in addition as a gray box sitting on top of the data points, and its size on the y -axis corresponds to σ_{syst} evaluated separately for each bin of the histogram using Eq. 3.43. The total uncertainty in each bin is obtained by applying the bootstrap method on randomly chosen cut variations, just as described in the previous sub-section.

Uncertainties of the fit

The last step of the analysis is the fit procedure, invoked to study theoretical models. The generic strategy of handling the uncertainties follows the logic described in this section so far, where the parameters susceptible to the systematics are identified and varied within some limits. The fit is performed multiple times, each by choosing a random variation of the fit parameters and a correlation function corresponding to a random cut variation²⁹. In case the fit function has some free parameters, their total and statistical uncertainties are obtained by switching the bootstrap method on and off.

The characterization of the final result is based on the *goodness of the fit*. The *frequentist statistical approach* is more traditional and easy to use, as opposed to performing a bayesian analysis. In the present work we only discuss the former, in particular the use of χ^2 as an observable to judge on the quality of the fit. In the following discussion we will only outline the properties relevant for the conclusions in the presented analyses. The χ^2 is defined as

$$\chi^2 = \sum_i^{\text{data pts}} \left[\frac{\text{data}_i - \text{theory}_i}{\text{uncertainty}_i} \right]^2, \quad (3.44)$$

which is a positive number accumulative for the discrepancy between the data and the theory. Clearly the value of χ^2 will grow for a high number of data points, thus a more practical observable is

$$\chi^2_{\text{ndf}} = \frac{\chi^2}{N_{\text{dof}}} = \frac{\chi^2}{N_{\text{pts}} - N_{\text{par}}}, \quad (3.45)$$

where N_{dof} are the number of degrees of freedom, defined as the difference between the number of data points N_{pts} and number of free fit parameters N_{par} . Typically $N_{\text{pts}} > N_{\text{par}}$, allowing to approximate $\chi^2_{\text{ndf}} = \chi^2 / N_{\text{pts}}$, which allows to determine not only a global χ^2_{ndf} , but also a local value in a sub-range of the fit region. This convention is used in this work.

The statistical interpretation of χ^2 is rooted in the assumption that the data points are a statistical fluctuations from their true value. An infinite amount of trials will result in a probability density function describing the likelihood of obtaining a certain χ^2 . The mean of this distribution is located at $\chi^2_{\text{ndf}} = 1$. This likelihood is characterized by the p -value (p_{val}), which is defined as the probability of obtaining a statistical fluctuation resulting in a larger χ^2 compared to the current one, i.e. it equals the integral of the χ^2 distribution in the range (χ^2, ∞) . Commonly, the deviations between the theory and data are given in terms of n_{σ} , which is the number of standard deviations of a Gaussian distribution, that lead to a fraction p_{val} of entries that lie

²⁹E.g. for $p\text{-}\Lambda$ this corresponds to choosing 1 random correlation function out of the 180 available.

outside the central interval spanned by n_σ . This is the root of the so called 68-95-99.7 rule, stating that the 1-2-3 σ deviation corresponds to $1 - p_{\text{val}} = \{68, 95, 99.7\}\%$ ($p_{\text{val}} = \{0.32, 0.05, 0.003\}$). The expected frequency of obtaining such $n\sigma$ is one in 3-22-370 trials. The convention in particle physics dictates that a discrepancy between the theory and the data larger than 3σ is a hint that the model does not describe the data, 4σ is an evidence ($1:16 \cdot 10^3$ chance of fluctuation), while 5σ ($1:1.7 \cdot 10^6$ chance of fluctuation) is a discovery. Note that this is a hand-waving description that many statisticians and physicists dislike, nevertheless it provides an easy guide for interpreting the experimental results.

Imagine that the theoretical model at hand is perfect, and the experimental data set contains only statistical fluctuations. A large amount of independent measurements should lead to an average $\langle \chi^2_{\text{ndf}} \rangle = 1$. On the other hand, if the theoretical model has some systematic bias, the mean of the χ^2_{ndf} will be shifted towards higher values. The third possible scenario is that the model is over-defined, which will lead to $\langle \chi^2_{\text{ndf}} \rangle < 1$. In all cases a *true* value for $\langle \chi^2 \rangle$ exists, but unfortunately there is no practical way of determining it, as such the measured χ^2 merely represents the probability of a statistical fluctuation under the assumption of an ideal model. However, a χ^2 can be assigned to each systematic variation (χ_i^2) and the width of the χ_i^2 distribution represents the systematic uncertainty associated with its determination, while the corresponding average $\langle \chi^2 \rangle$ can be interpreted as the most likely χ^2 . It is illogical to assign uncertainty to a probability, as the interpretation becomes rather difficult³⁰, thus typically $\langle \chi^2 \rangle$ is used to provide the final χ^2 value. By now it has become evident that the usage of a single number, such as the χ^2 or n_σ , is underestimating the complexity of the statistics involved, which is the reason why in exclusive studies it is preferable to use an alternative approach, such as Bayesian analysis. Nevertheless, regarding the final state interaction there are typically many measurements available, stemming from different collision systems, experiments, different analysis techniques, and the data base is constantly expanding. This implies that each new analysis, or a PhD thesis, eventually becomes a single point to populate the world-averaged *true* χ^2 distribution related to the particular observable at hand. As such, the usage of the frequentist statistical approach (χ^2 in particular) is well motivated.

In the above discussion the bootstrap method was purposefully not mentioned, as there is an important subtlety that prohibits its use in the evaluation of the χ^2 . This is related to the fact, that the additional random re-sampling of the measured data has the effect of creating a data set that contains the uncertainty related to the true value twice! Ones because of the statistical nature of the original data, and twice because of applying the bootstrap on top of it. For large amount of iterations the latter will result in an increase of $\langle \chi^2 \rangle$ of each bin by 1. If the bootstrap is applied to all bins, than $\langle \chi^2_{\text{ndf}} \rangle$ will be increased by unity as well. This holds if the data is compared to a fixed model, in case of a fit with certain degrees of freedom the fluctuations of the bootstrapped samples provide enough phase-space for the fit to converge better, leading to a reduced increase of $\langle \chi^2 \rangle$. Nevertheless, a bias in the χ^2 is always present, for this reason the evaluation of the χ^2 must be done by applying only the systematic variations, without the bootstrap.

³⁰A sentence like “The probability of the probability of obtaining the measurement” sound extremely confounding.

As a final remark, let us discuss few potential pitfall of using $\langle \chi^2 \rangle$ from the systematic variations to quantify the fit procedure. One is the human factor, which involves the selection of reasonable limits on the selection criteria, i.e. making sure that the analysis is performed such that the physics result remains unbiased by the modification of the parameters. E.g. changing the cosine pointing angle of the Λ candidates will bias the λ parameters, thus the related variation should be rather small, unless the λ parameters are re-evaluated on each re-iteration. Another problem arises if some variations are not purely systematical, but related to the uncertainties, often statistical, of the physics parameters within the theoretical model. An example would be the source size, which is only known to a certain precision, and thus has to be varied in the fit procedure. In that case the different values of the parameter are not systematic variations, instead they represent unique *hypotheses* ν , each delivering a $\langle \chi^2_\nu \rangle$ ³¹ value to judge on the agreement to the data. The *best* hypothesis $\langle \chi^2_{\text{best}} \rangle$ is the one of lowest χ^2 . Averaging over all hypotheses is not good practice, as it disregards the potential sensitivity of the experimental measurement to the physics parameter in question, leading to an overall higher (less conservative) $\langle \chi^2 \rangle > \langle \chi^2_{\text{best}} \rangle$ value. The correct goodness of the fit is represented by $\langle \chi^2_{\text{best}} \rangle$.

Confidence intervals

There is an alternative way of making theoretical comparisons to the data, by computing the related *confidence intervals*. Let the theoretical description of the data depends on certain set of parameters ν , and each parameter set can be used to model the experimental data, representing a different hypothesis. One can define

$$\Delta\chi^2_\nu = \langle \chi^2_\nu \rangle - \langle \chi^2_{\text{best}} \rangle. \quad (3.46)$$

It can be shown, that $\Delta\chi^2_\nu$ is distributed according to a χ^2 distribution with the number of degrees of freedom corresponding to the number of free parameters in the theory. A confidence interval contains the p_{val} fraction of most probable parameter sets. Table 3.11 provides some numerical values relating $\Delta\chi^2_\nu$, p_{val} , n_σ and ν . The

n_σ	p_{val}	ν				
		1	2	3	4	5
1	68.27%	1.00	2.30	3.53	4.74	5.89
2	95.45%	4.00	6.18	8.02	9.72	11.3
3	99.73%	9.00	11.8	14.2	16.3	18.2

TABLE 3.11: Confidence intervals for different number of fit parameters ν and their corresponding $\Delta\chi^2_\nu$ values.

usage of $\nu = 1$ is common whenever the required uncertainties are for a single parameter, while $\nu > 1$ includes the correlation between the multiple parameters. The analytical calculations of the values in Table 3.11 are done by

$$p_{\text{val}} = 1 - \int_0^{\Delta\chi^2_\nu} \mathcal{X}_{\text{pdf}}(\chi^2, \nu) d\chi^2, \quad (3.47)$$

³¹The value $\langle \chi^2_\nu \rangle$ implies that the χ^2 of each hypothesis is still averaged over the purely systematic variations, but *without* including variations of any parameters that represent a physics hypothesis.

where $\mathcal{X}_{\text{pdf}}(\chi^2, \nu)$ is the probability density function of χ^2 with ν degrees of freedom, and the corresponding confidence level is

$$n_\sigma = \sqrt{2} \cdot \text{erfc}^{-1}(p_{\text{val}}). \quad (3.48)$$

The confidence intervals allow for relative comparison of multiple parameterizations of a given theoretical model. The estimation of the confidence interval can be used together with the bootstrap method, as the bias in the χ^2 value will be canceled out in Eq. 3.46. To estimate the confidence interval from a bootstrapped MC procedure, the desired amount of best p_{val} iterations are kept, and the minimum/-maximum values for the parameters ν determine the corresponding most probable range. Notably, the confidence interval contains *no* information about the goodness $\langle \chi^2_{\text{best}} \rangle$ of the best fit, thus this method is *exclusively* used to make relative comparisons between different theoretical parameterizations, with the assumption that the underlying model provides accurate description of the physical system.

Chapter 4

The emission source in small systems

4.1 Overview

The Koonin-Pratt relation (Eq. 1.12) states that the correlation function is defined by two components, the two-particle wave function $\Psi(\vec{r}^*, \vec{k}^*)$ of the pair relative motion and the two-particle source function $S(r^*)$. As discussed in the introduction section 1.5, the traditional approach has been to use π - π correlations in order to describe the emission source, while this work concentrates on non-traditional femtoscopy. The idea is to constrain the source function, in order to obtain a clear signal related to the interaction. To achieve that the pp collision system has been considered a suitable environment, as the production of hadrons is driven by the hard QCD scattering of the quarks constituting the beam particles and the approximate flavour symmetry leads to an expected similar behaviour regardless of the flavours involved. Translated into the language of femtoscopy, all hadrons will be formed on a by the same underlying physical process, resulting in identical effective emission source. If true, this would allow to determine $S(r^*)$ from the pp correlation function, as the pp interaction is known to a high precision. Further, the same emission source can be assumed for other particle pairs, such as Λ - Λ , p - Λ , p - Ξ , p - Ω^- , p - K etc., allowing to use the corresponding correlations only for the study of the FSI.

The *source function* is a very complicated object, as in principle it depends on the time of emission of the two particles, on their kinematics, on the underlying event etc. For practical purposes all femtoscopic analyses attempt to simplify the problem to some effective parameterization of the source, which provides a reasonable description and interpretation of the data. As discussed in chapter 1.5.3, the most common assumption is to convolute two time-independent single particle emission sources of Gaussian profile, into a two-particle source. The resulting analytical relation is

$$S(r) = \frac{1}{(4\pi r_0^2)^{3/2}} \exp\left(-\frac{r^2}{4r_0^2}\right), \quad (1.17)$$

where r_0 is the source size (width). This is the generic expression for the 3 dimensional Gaussian source, as used in the Koonin-Pratt equation. Since the relation 1.17 is radial symmetric the relevant 1 dimensional probability density function of r^* is obtained with a trivial angular phase space factor

$$S_{4\pi}(r^*) = 4\pi r^{*2} S(r) = \frac{4\pi r^{*2}}{(4\pi r_0^2)^{3/2}} \exp\left(-\frac{r^{*2}}{4r_0^2}\right). \quad (4.1)$$

The Gaussian profile of the source has been hugely successful in its description of heavy-ion collisions, and has been further shown to be applicable in pp collisions as well [38], in particular for baryon–baryon correlations. However, for π – π correlations in small collision systems, the situation has been different, as a Cauchy emission profile has been by far favoured by the experimental data [53, 54]. This has been largely attributed to the production of pions via strong decays of resonances, but has not been explicitly proven for pp collisions, although studies for HI collisions showed that an effective increase of the π – π source size of c.a. 1 fm can be directly linked to resonance decays [98]. In smaller systems this could also lead to a modification of the profile. Further, in HI collisions re-scattering effects between the produced hadrons could lead to further modifications, that can be eventually used to study the in-medium behaviour of the particles [99, 100]. The latter is not relevant for pp collisions.

This chapter presents the first detailed related quantitative study on the effect of *resonance decays* in pp collisions, attempting to keep the simplistic picture of a time-independent Gaussian source function and the ansatz of an identical size for *all* produced hadrons. This was achieved by developing a dedicated Monte-Carlo procedure to model the emission source and the results were recently published in PLB [44]. The investigation is performed on the baryon sector, however Maximilian Korwieser is currently extending this study to π – π correlations as part of his master thesis and his results will be outlined as an outlook. The focus of this work is the development of the MC procedure and its integration into CATS, while details on the data reconstruction are available in [44, 62]. Summarizing, the cuts used for the track reconstruction are identical to the ones described in Tables 3.2 and 3.5, with certain additional pair cuts for p–p (so called close-pair-rejection) and slight differences in the systematic variations. The p– Λ correlation is investigated in a smaller k^* range, only up to 224 MeV, in order to reduce the influence of the non-proven theoretical predictions for the coupling $N\Sigma$ –p Λ ¹. The smaller fit range allows to assume that the non-femtoscopic baseline is a constant.

4.2 Gaussian source

The analysis of ALICE data for pp collisions at 7 TeV showed that both the p–p and p– Λ correlation functions are well described by a Gaussian emission source of similar size (1.13 fm). Nevertheless, it was rather unclear to which precision this assumption works, thus when the pp 13 TeV high-multiplicity data set became available a detailed study on that topic was started. Due to the larger statistics, the analysis was performed differentially as a function of the *transverse mass* of the pairs, defined as

$$m_T = \sqrt{k_T^2 + m^2}, \quad (4.2)$$

where m is the average mass of the particle pair and k_T is the average transverse momentum (in the laboratory frame) of the two particles. This is needed, as a rather strong m_T scaling is known to exist in heavy ion collisions [100, 101], and it has also been observed in small systems [53, 54]. It is typically associated with the collective expansion of the system. A multiplicity dependent analysis would further increase the precision of extrapolating the results between different species of pairs, nevertheless the associated effects are smaller compared to the m_T dependence and

¹A dedicated study regarding the coupling is presented in chapter 6.

disregarded in the present analysis. The baryon–baryon pairs with the best known interactions from theory are p–p and p– Λ , where the former can be modeled using the Argonne v_{18} potential [7] and the latter using NLO χ EFT [8]. The experimental constraints on p– Λ are scarcer, thus as a cross-check the LO version of χ EFT was adopted in addition. This is very conservative, as the LO results are known to fail to predict even the p– Λ scattering parameters. The correlation function in each m_T for both p–p and p– Λ is fitted using the CATS framework, where the free fit parameters are the Gaussian source size r_0 and $C_{\text{non-femto}}(k^*)$, the latter being a simple constant by default, with a systematic variation allowing for a linear term. The resulting $r_0(m_T)$ are plotted in Fig. 4.1. Both the p–p and p– Λ exhibit a strong m_T scaling,

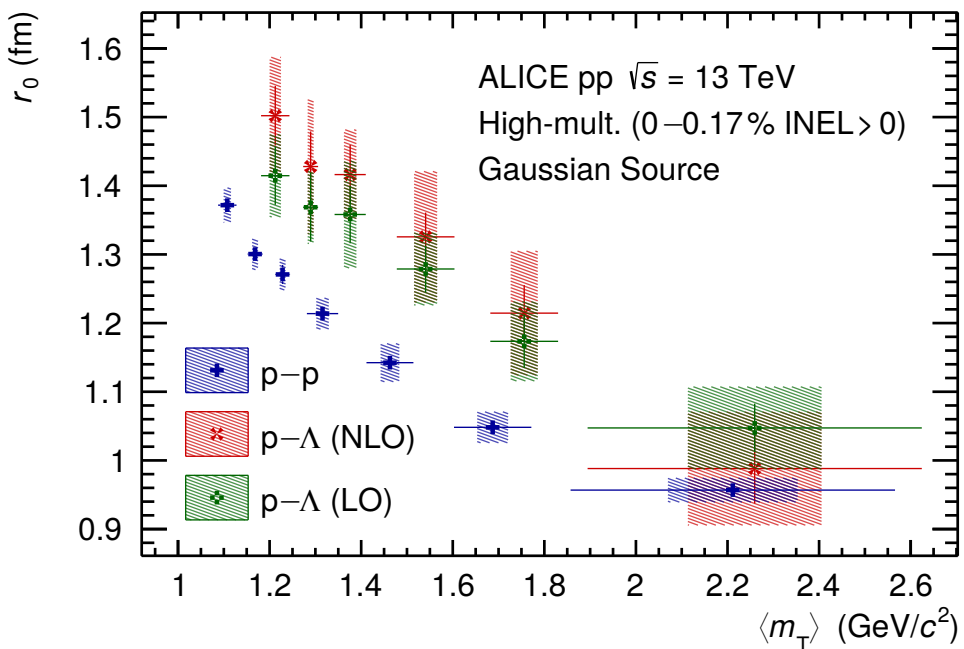


FIGURE 4.1: [44] Source radius r_0 as a function of $\langle m_T \rangle$ for the assumption of a purely Gaussian source. The blue crosses result from fitting the p–p correlation function with the strong Argonne v_{18} [7] potential. The green (red) crosses result from fitting the p– Λ correlation functions with the strong χ EFT LO [102] (NLO [8]) potential. Statistical (lines) and systematic (boxes) uncertainties are shown separately.

however the absolute value for r_0 is systematically larger for the p– Λ correlation function. The results for the latter seem to be only mildly dependent on the different parameterization for the interaction, giving confidence on the obtained result for the source size. The observed difference in r_0 between p–p and p– Λ is worrying, as it questions the ansatz for a common parameterization of the source function in all baryon–baryon pairs. Nevertheless, it was expected that this oversimplified treatment of the emission has limits on its applicability, and Fig. 4.1 merely demonstrates that these are already reached at the LHC. It is now extremely interesting to see if addressing some of the known shortcomings could restore the common scaling of the radius for p–p and p– Λ .

4.3 The resonance source model

4.3.1 Strategy and assumptions

The most straight forward consideration, is to check if a different source profile can be applied to describe the experimental data. In particular, it is known the the Gaussian distribution is a limiting case of the more generic *Lévy stable distribution*. The distinctive feature of all stable distributions is that the convolution of two of them is still of the same type, albeit with modified parameters. While there are multiple parameters that can define the most generic type of Lévy stable distributions, the typical approach in femtoscopy is to consider two parameters, one is the width (source size) and the other is the stability parameter α . The general probability density function of a Lévy stable distribution is non-analytical, nevertheless the characteristic function is

$$\varphi(x) = \exp [ix\mu - |xc|^\alpha] \quad (4.3)$$

where μ is the location parameter, corresponding to the mean in case $\alpha \neq 1$, while c is scale parameter related to the width² of the distribution. The stability parameter α has numerical values between 1 and 2³, where the former represents a Cauchy⁴ and the latter a Gaussian distribution. A non-Gaussian Lévy distribution can occur for a random emission that has a heavy tail. Physically, a large tail can either be related to the exponential decay of resonances, or it can be a genuine effect of the hadronization process. The latter is possible due to the large spread in the distribution of the momentum transfer related to the QCD hard scatterings, that could lead to string fragments of very different energies and an uneven distribution of the spacial components of hadron formation. In the study of pion correlations the use of a Lévy stable distribution had become more common [54], as it provides a better description to the measured data. Nevertheless, a solid physics interpretation is yet not present. In the scope of this work, it was verified that the p-p correlation function does not allow for a variation of $\alpha < 1.5$, with an estimated best agreement to the data for $\alpha > 1.7$. On the other hand, the p- Λ correlation can be better described using a pure Cauchy distribution ($\alpha = 1.0$). This implies that the tails of $S(r^*)$ are different for p-p and p- Λ , where a possible physics reason is the production of proton and Λ particles through intermediate short lived strongly decaying resonances. In this case there will be an offset to the formation of the hadrons following an exponential law, that would be different depending on the particle species. In a private communication with Prof. Francesco Becattini expressed his support for the idea of investigating this effect, and has provided us with the results of his computation of the fraction of resonances in pp collisions at 7 TeV⁵, based on the *Statistical Hadronization Model* (SHM). In essence, this model assumes a thermal (Boltzmann) production of all particles and resonances, depending only on the mass of the particles and the available energy. The small system dictates the use of the canonical

²There are different conventions, in femtoscopy the radius is often defined as $r_0 = 2^{1/\alpha}c$ (Nolan notation) [103], which leads for a Gaussian distribution ($\alpha = 2$) to $r_0 = \sqrt{2}c$.

³Actually α can go down to 0, however the distributions with $\alpha < 1$ have shapes that have never been seen experimentally, and theoretically they are related to a production at a critical point, hence they could only be relevant in Pb-Pb collisions for QCD studies [104].

⁴The computation of the correlation function using the symmetrized free wave of two identical particles is effectively the Fourier transform of the source function. Given a Cauchy source, this leads to an exponential correlation function. For this reason the Cauchy source is often referred to (slightly inaccurately) as an exponential source.

⁵The results for 13 TeV are expected to be similar, regardless if for MB or HM events.

ensemble within SHM. The result of this computation is that the final yield of protons (Λ s) is composed of only $\omega_{\text{prim}} = 35.78\%$ (35.62%) primordial particles, while the rest stems from the decay of resonances. These numbers are suggestive that the effect of these decays is a dominant factor in the production (emission) of the baryons. The full lists for resonances feeding into proton and Λ particles included in the SHM are given in appendix B (Tables B.1 and B.2).

To create a model treating the effect of short lived resonances explicitly, several assumption have been made and listed below.

Assumption 1: Equal time of emission

All primordial particles and resonances are emitted at the same time.

Assumption 2: Independent Gaussian emission

All primordial particles and resonances are emitted independently from a *core Gaussian source*.

Assumption 3: Free-streaming resonances

The strongly decaying resonances do *not* experience any sort of interaction. They propagate freely between their spacial positions of production and decay.

Assumptions 1 and 2 are a reflection of the common femtoscopic conventions, while assumption 3 is motivated by the time-scale of the decays, typically on the order of few fm/ c , which is too short for a significant modification of the momentum due to the final state interaction, that requires tens or even hundreds of fermi to become dominant. The source function of the final state particles is represented by a *core Gaussian emission profile*, and a halo related to the spacial offset of the emission introduced by the resonances. The question at hand is how to compute the resulting distribution $S(r^*)$, and the sketch in Fig. 4.2 visualizes the problem. There or two points of primordial emission (mothers 1 and 2) separated by \vec{r}_{core}^* and two points of the final state particles (daughters 1 and 2) separated by \vec{r}^* . Note, that the coordinate system is, as always, determined by the pair rest frame of the final state particles and the source function of interest is $S(|\vec{r}^*|) = S(r^*)$. The final separation r^* is expressed as

$$\vec{r}^* = \vec{r}_{\text{core}}^* - \vec{s}_{\text{res},1}^* + \vec{s}_{\text{res},2}^*, \quad (4.4)$$

where $\vec{s}_{\text{res},1(2)}^*$ is the distance traveled by the first (second) resonance. This is related to the flight time t_{res} and linked to the momentum and mass of the corresponding resonance by

$$\vec{s}_{\text{res}}^* = \vec{\beta}_{\text{res}}^* \gamma_{\text{res}}^* t_{\text{res}} = \frac{\vec{p}_{\text{res}}^*}{M_{\text{res}}} t_{\text{res}}. \quad (4.5)$$

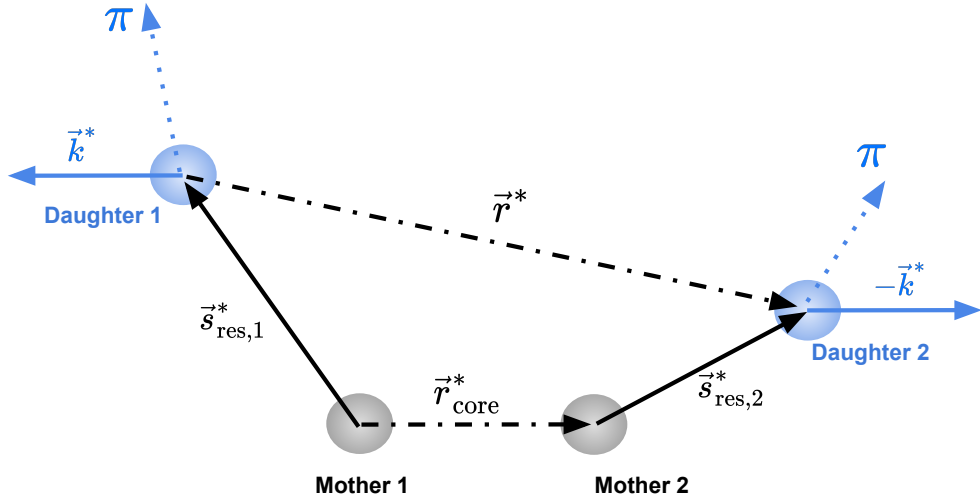


FIGURE 4.2: [44] A sketch illustrating the modification of \vec{r}_{core}^* into \vec{r}^* . The initial (final) state particles are represented by gray (blue) disks. If the initial state particles are the primordial particle species of interest, the corresponding \vec{s}_{res} becomes zero.

To evaluate the absolute value of r^* one can transform Eq. 4.4 to

$$\begin{aligned}
 r^{*2} = & r_{\text{core}}^{*2} + \frac{p_{\text{res},1}^{*2}}{M_{\text{res},1}^2} t_{\text{res},1}^2 + \frac{p_{\text{res},2}^{*2}}{M_{\text{res},2}^2} t_{\text{res},2}^2 - 2r_{\text{core}}^* \frac{p_{\text{res},1}^*}{M_{\text{res},1}} t_{\text{res},1} \cos \angle(\vec{r}_{\text{core}}^*, \vec{p}_{\text{res},1}^*) + \\
 & 2r_{\text{core}}^* \frac{p_{\text{res},2}^*}{M_{\text{res},2}} t_{\text{res},2} \cos \angle(\vec{r}_{\text{core}}^*, \vec{p}_{\text{res},2}^*) - 2 \frac{p_{\text{res},1}^* p_{\text{res},2}^*}{M_{\text{res},1} M_{\text{res},2}} t_{\text{res},1} t_{\text{res},2} \cos \angle(\vec{p}_{\text{res},1}^*, \vec{p}_{\text{res},2}^*).
 \end{aligned} \tag{4.6}$$

The idea behind a Monte-Carlo determination of the source function is to sample r^* iterative using Eq. 4.6, where the masses of the resonances are known and all other parameters are of statistical nature and can be random sampled if their probability density functions are known. Following assumption 2, $|\vec{r}_{\text{core}}^*| = r_{\text{core}}^*$ can be random sampled from a typical Gaussian source (Eq. 4.1). The flight time of the resonance t_{res} follows an exponential distribution with mean lifetime τ_{res} . The widths $\Gamma_{\text{res}} = 1/\tau_{\text{res}}$ of resonances are assumed to be known from the available data in the PDG [105]. The remaining parameters are related to the kinematic properties of the emission, i.e. the magnitude and direction of the momenta of the emitted resonances, that can be described in the pair rest frame with 5 independent parameters. These are the magnitudes of the momenta of the two resonances, their angles of emission with respect to \vec{r}_{core}^* and their relative angle. These parameters are next to impossible to obtain experimentally, thus they need to be extracted from a theoretical model.

4.3.2 Determining the kinematic of the primordial emission

The most practical approach is to obtain the 5 kinematic parameters of Eq. 4.6 is to use a transport model, such as Pythia or EPOS [72, 84, 85]. The latter has been shortly introduced in section 3.4 and described as an improvement over Pythia in terms of the treatment of the hadronization process. The EPOS model provides the

opportunity to study the particles at the different level of the evolution of the collisions systems, thus there is the the primordial resonances can be selected before they have decayed into the final state particles. Moreover, EPOS provides the spatial coordinates of the emission, a factor relevant for the determination of the angles $\angle(\vec{r}_{\text{core}}^*, \vec{p}_{\text{res}}^*)$. For those reasons the EPOS 3.117 transport model was selected in the present study. The simulations were performed⁶ at the generator level, i.e. no full scale simulation of the ALICE detector and 4π acceptance, for HM pp collisions at 13 TeV. Nevertheless, it was verified that applying the standard acceptance cut on the final state particles ($|\eta| < 0.8$ and $p > 0.4$ GeV/c) do not change the results within the statistical uncertainties, thus to boost the statistics of the 20 million available events the presented analysis is performed using the 4π acceptance.

The EPOS model is based on the core-corona approach, for which a fraction of the particles are produced from string fragmentation (corona) and the rest are produced from a hydrodynamics simulation (core). The resonances included in the hydrodynamic simulation are based on a grand canonical ensemble, predicting similar yields as the SHM. Nevertheless, the resonances produced in the corona follow an oversimplified rule of creating the heavy resonances first, as long as there is enough energy available. Moreover, the list of resonances used in the corona is different than the one used in the core, leading to large internal inconsistencies. These reasons motivate the use of the SHM for the determination of the amount of resonances. Still, EPOS allows to determine the kinematic properties of these resonances, which depend mainly on their mass. Due to the differences in the lists of resonances used by EPOS and SHM it is not possible to obtain from EPOS all required species, however, using the results presented in Tables B.1 and B.2, the average particle mass and lifetime of the resonances feeding into a proton or a Λ are equal to $\langle M_{\text{res},p} \rangle = 1.36$ GeV/c², $\langle \tau_{\text{res},p} \rangle = 1.65$ fm/c, $\langle M_{\text{res},\Lambda} \rangle = 1.46$ GeV/c², $\langle \tau_{\text{res},\Lambda} \rangle = 4.69$ fm/c.

Digression: On the right track

Already here it is interesting to observe, that there is a substantial difference in the average lifetime of the resonances feeding into protons and Λ s. In the case of the latter the larger $\langle \tau_{\text{res},\Lambda} \rangle$ will lead to a more pronounced increase in the effective \vec{r}^* compared to \vec{r}_{core}^* (Eq. 4.4), resulting in a larger effective source size for p- Λ pairs in comparison with p-p, just as seen in Fig. 4.1.

These average masses can be forced to be the same for the list of resonances in EPOS, by applying a re-weighting to the resonance yields. Details are available in appendix B. It than becomes possible to create an effective list of resonances for EPOS, that satisfy the requirements of the SHM. Further, the decays of the resonances have to be simulated in order to obtain the momenta of the daughter particles, which represent the final state protons and Λ s that determine the coordinate system. Thus the same-event daughters are paired, and all spacial and momentum components are boosted into their rest frame. This creates the required (discrete) probability density function for the kinematic properties of the pairs stemming from resonances and allows to perform random sampling from it to populate the distribution $S(r^*)$ (Eq. 4.6). Moreover, by sampling directly from the pairs, all correlations between the parameters are automatically included. Note, that while EPOS provides the vector \vec{r}_{core}^* , only its direction is being used, while the absolute value is random sampled according to a Gaussian source. This is required by the ansatz of this model, in which

⁶Special thanks to colleague Ante Bilandzic, who set up the simulations.

the core Gaussian⁷ source size r_{core} is an independent variable.

The sketch in Fig. 4.2 is the generic representation when both of particles in the final state pair stem from a resonances. Naturally, it is possible that one or both of the final state particles are primordial, in which case the terms inside Eq. 4.6 containing the momentum p_{res} become zero. In case only the first particle stems from a resonance, the relation becomes

$$r^{*2} = r_{\text{core}}^{*2} + \frac{p_{\text{res},1}^{*2}}{M_{\text{res},1}^2} t_{\text{res},1}^2 - 2r_{\text{core}}^* \frac{p_{\text{res},1}^*}{M_{\text{res},1}} t_{\text{res},1} \cos \angle(\vec{r}_{\text{core}}, \vec{p}_{\text{res},1}^*), \quad (4.7)$$

if only the second particles stems from a resonance

$$r^{*2} = r_{\text{core}}^{*2} + \frac{p_{\text{res},2}^{*2}}{M_{\text{res},2}^2} t_{\text{res},2}^2 + 2r_{\text{core}}^* \frac{p_{\text{res},2}^*}{M_{\text{res},2}} t_{\text{res},2} \cos \angle(\vec{r}_{\text{core}}, \vec{p}_{\text{res},2}^*), \quad (4.8)$$

and if both particles are primordial

$$r^* = r_{\text{core}}^*. \quad (4.9)$$

The 4 different scenarios corresponding to Eq. 4.6-4.9 occur with different probability, that is determined by the amount of primordial particles $\omega_{\text{prim},1}$ and $\omega_{\text{prim},2}$. The source function is given by

$$S(r^*) = \omega_{\text{prim},1} \omega_{\text{prim},2} S_{\text{core}}(r^*) + \quad (4.10)$$

$$\omega_{\text{prim},1} (1 - \omega_{\text{prim},2}) S_{\text{res},2}(r^*) + \quad (4.11)$$

$$(1 - \omega_{\text{prim},1}) \omega_{\text{prim},2} S_{\text{res},1}(r^*) + \quad (4.12)$$

$$(1 - \omega_{\text{prim},1}) (1 - \omega_{\text{prim},2}) S_{\text{res},1,2}(r^*), \quad (4.13)$$

where the source function $S_{\text{core}}(r^*)$ is the Gaussian core (Eq. 4.9), $S_{\text{res},1}$ and $S_{\text{res},2}$ are the sources resulting from including the contribution of the short lived resonances related to particles 1 and 2 to the core (Eq. 4.7, 4.8), and $S_{\text{res},1,2}$ contains all resonances (Eq. 4.6). In practice the individual source functions described above do not need to be computed explicitly, but it is sufficient to sample r^* from Eq. 4.6-4.9 with the corresponding weight factors occurring in Eq. 4.10.

With the above prescription, the total source function $S(r^*)$ can be evaluated numerically. One pitfall is that the sampling is unconstrained in the momentum space, thus the source is averaged over k^* . Indeed the standard femtosopic assumption is of a k^* independent source, however in practice this approximation is limited in the range of k^* , thus the Monte-Carlo procedure should be applied only to final state particle pairs of low relative momentum. This introduces a cut-off scale k_{source}^* in the present analyses set to 200 MeV/c. Another detail is that one has to sample from EPOS not only the resonances, but the primordial proton and Λ baryons as well, since they are needed to evaluate the angles in case one of the final state particles is primordial. A step-by-step summary of the **resonance source model**, as well the implantation in CATS, is provided in the next subsection.

⁷The profile of the EPOS core source is not Gaussian and known to fail in the description of experimental data, as it is to narrow and overpredicts the strength of the measured femtosopic signal. Details are available in [39].

4.3.3 The resonance source model

Resonance source model 1: The use of a thermal model

- Define the desired final state particle species as X_1 and X_2 .
- Evaluate the relative amount of primordial particles ω_{prim} , and secondary particles stemming from strongly decaying resonances.
- Compute the average mass $\langle M_{\text{res}} \rangle$ and average lifetime $\langle \tau_{\text{res}} \rangle$ of the resonances feeding into each species.

Resonance source model 2: The use of a transport model

- Simulate the desired collision system with a transport model containing both the spacial and momentum coordinates of the particles.
- Select the initial state particles, i.e. the primordial X_1 and X_2 as well as the resonances decaying into them, and group them into pairs.
- Simulate the decay of the resonances, following simple phase-space rules, to obtain the momenta of their corresponding daughter (final state) particles.
- Boost the coordinates into the pair rest frame formed by the final state particles.
- Keep the following information about the initial state pairs:
 - Momentum value p_{res}^* of each initial state resonance.
 - Angle between the momentum vector of each resonance, with respect to the vector of the initial spacial separation \vec{r}_{core}^* .
 - Angle between the two (if present) resonances in the initial state.

Resonance source model 3: Implementation in CATS

- The required input is the source size of the core Gaussian r_{core} , as well as the relevant output of the thermal model and the transport model (see above).
- The initial separation r_{core}^* is sampled randomly.
- One of the four scenarios for the initial pair, primordial–primordial, primordial–resonance, resonance–primordial or resonance–resonance, is chosen at random based on the probability factors ω_{prim} (see Eq. 4.10).
- Pick a random pair from the transport model, with $k^* < k_{\text{source}}^*$, corresponding to the selected scenario.
- Depending on the scenario, Eq. 4.6–4.9 are employed to evaluate the final state separation r^* .
- Iterative repetition to create the probability density function of $S(r^*)$.

4.3.4 Results for p-p and p- Λ

The result of fitting the p-p and p- Λ correlations with a pure Gaussian source resulted in an offset of the obtained source size (section 4.2, Fig. 4.1). The same data can be refitted by using the resonance source model, using r_{core} as a free fit parameter instead of r_0 . The resulting m_T scaling is shown in Fig. 4.3. The striking observation

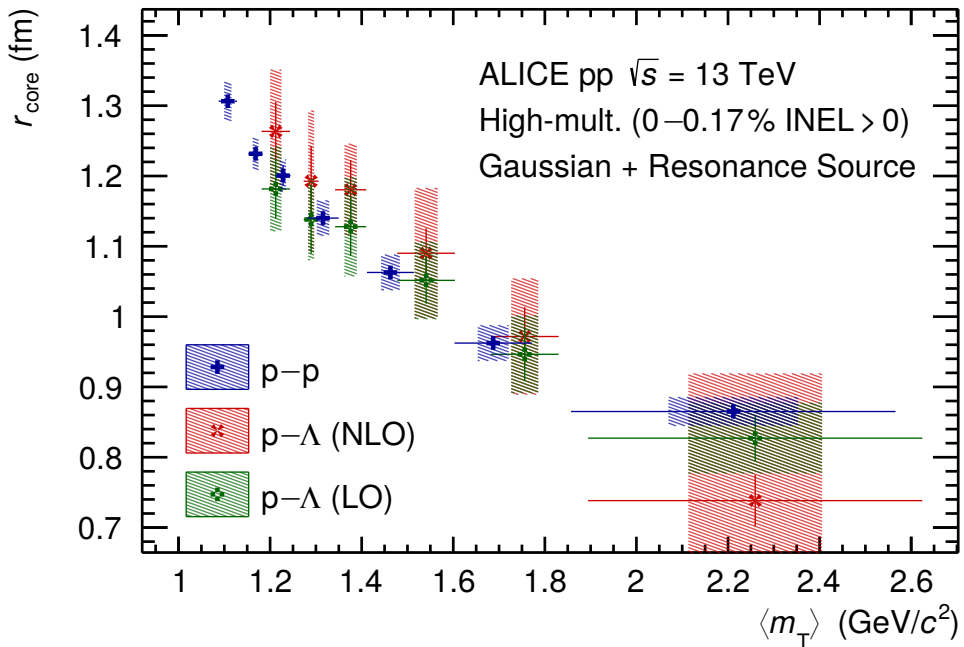


FIGURE 4.3: [44] Source radius r_{core} as a function of $\langle m_T \rangle$ for the assumption of a Gaussian core with added resonances. The blue crosses result from fitting the p-p correlation function with the strong Argonne v_{18} [7] potential. The green (red) crosses result from fitting the p- Λ correlation functions with the strong χ EFT LO [102] (NLO [21]) potential. Statistical (lines) and systematic (boxes) uncertainties are shown separately.

is that now the p-p and p- Λ m_T dependent *core* source size is, within the uncertainties, exactly the same. The absolute value of r_{core} is quite small, ranging between 1.3 and 0.8 fm for m_T between 1 and 2.2 GeV, and it represents the scale of emission of the primordial particles at the time of hadronization. To gain a deeper understanding, let us examine the actual source distributions presented in Fig. 4.4, where the third m_T bin of Fig. 4.1 and Fig. 4.3 is examined. The black dashed line corresponds to the Gaussian core source $S_{\text{core}}(r^*)$, while the blue (red) circles represent the total source function $S(r^*)$ after the inclusion of all resonances (Eq. 4.10). An immediate observation is the presence of a tail in the total source, that is more pronounced for p- Λ . This is expected, due to the exponential nature of the propagation length of the resonances \bar{s}_{res}^* and because of the larger average lifetime of the resonances decaying into Λ . This is very reasonable, but how is it reflected onto the correlation function? Figure 4.5 shows the corresponding theoretical correlation functions, evaluated for $r_0 = 1.28$ fm and $r_{\text{core}} = 1.20$ fm. They look almost identical, which is related to the fact that the profiles of the source functions look identical up to c.a. 5 fm for both a pure Gaussian and a core Gaussian with included resonances. The differences are only in the tail region, which is sampled with much lower probability, thus introducing only mild changes in the correlation function. As a result, it can be claimed

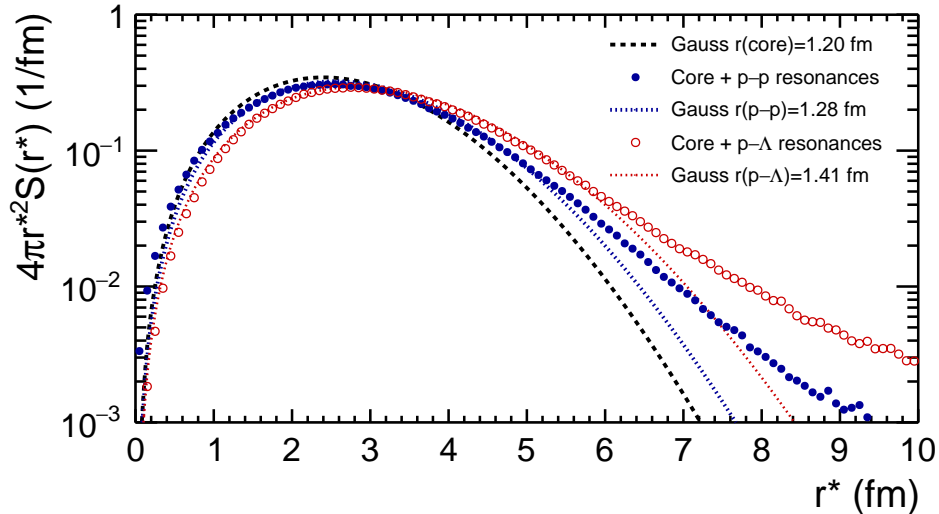


FIGURE 4.4: The source functions for p–p (blue circles) and p– Λ (red open circles), generated by folding the exponential expansion due to the decay of the respective parent resonances with a common Gaussian core with $r_{\text{core}} = 1.2$ fm (dashed black line). The dotted lines represent the corresponding effective Gaussian distributions, fitted to the total source.

that the emission source has approximately a Gaussian shape, even after the inclusion of resonances. The size r_0 is an *effective Gaussian source size* that is different than r_{core} and does not remain constant for all particle species. Nevertheless, this property allows to convert the parameterization of the source function from r_{core} to r_0 , allowing for a simplified analytical parameterization of $S(r^*)$, e.g. to perform the computation faster or use the Lednický model.

In summary, to describe the correlation function the usage of Gaussian source is sufficient in most practical cases, however the size parameter r_0 has no relevant physical interpretation and, more importantly, it is specific for the different particle species. By contrast, using the parameterization of the resonance source model allows the use of a single parameter to describe different correlation systems, defined as a core Gaussian source size r_{core} . Based on the agreement between p–p and p– Λ it is claimed that any baryon–baryon pair with an average m_T within the investigated limits will have the same core source size, while the full source function can be obtained by applying the resonance source model. This method has been successfully applied to describe the p– Λ , p– Ξ and p– Ω^- pairs [40, 45]. The study of the p– Λ interaction is presented in section 6.

4.4 Towards a universal source model

The resonance source model already provides a better understanding of the emission process, but it is merely a single step in an uncharted territory. It is likely that it will undergo refinements in the future, as more accurate data are collected. But the first and very necessary improvement is to relate it to the study of any hadron–hadron pairs, regardless of their mesonic or baryonic nature. The most commonly studied meson–meson pair is the π – π , due to the high precision of the measurements and absence of the strong interaction, making the modelling of the femtoscopic correlation

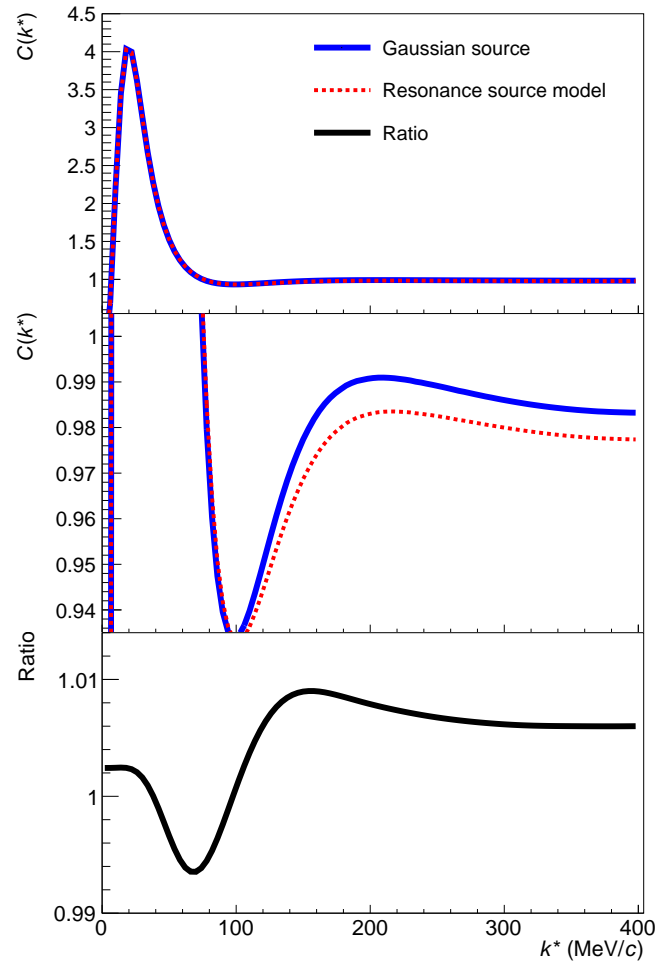


FIGURE 4.5: The correlation functions evaluated using a pure Gaussian (blue solid line) or the resonance source model (red dashed line). The top panel is the full correlation function, the middle panel is zoomed on the y -axis to highlight the differences in the long-range part of the femtoscopic signal. The bottom panel shows the ratio between the two, which is very minor (<1%) and are unlikely to be resolved within the uncertainties of the fitting procedure, unless the underlying non-femtoscopic background is fixed to a better precision.

function much easier. However, there are many other complications of studying π - π in small collision system, the most prominent being the presence of a large, and yet not fully understood, mini-jet background (see section 3.4). Further, there are many more resonance species with a much larger spread in their mass, compared to the baryons, making the effective modelling presented in this chapter increasingly difficult. Still, a master student in our group, Maximilian Korwieser (Max), was given the task of testing the applicability of the resonance source model to describe same charged π - π correlation in minimum bias pp collisions at 13 TeV. The description of the correlation functions is still far from perfect, but Max already found very interesting evidence suggesting that the modelling of pions, with the new approach, is feasible and could explain some measured but not yet understood properties of the π - π correlation functions. One interesting observation is the preferred Cauchy profile of the source function. If all resonances are included into the modelling of the source, contributing to 73% of the pion yield, the modification of the core Gaussian is extremely strong, resulting in a distribution that can be effectively modeled by a Cauchy source (Fig. 4.6), scaled down by a factor $\lambda = 0.9$. The other interesting point, is that this scaling can be explained (4.7) by the large tail introduced by very long lived resonances ($c\tau > 25$ fm), which contribute with 5.5% to the total yield and on the level of pairs introduce a c.a. 10% non-interacting⁸ particle pairs. Further, the ω meson has a 7.5% contribution to the pion yield and $c\tau \approx 23$ fm, which is within the limits of what can still be considered as a distance relevant for the final state interaction. Both scenarios, including the ω explicitly in the source or as a flat contribution with an additional scaling of $\lambda_\omega = 0.86$, were compared (Fig. 4.8) and apparently there are very minor deviations, pointing out that even the pion yield related to ω results in a flat signal. Previous π - π analysis did indeed use λ as a free fit parameter, and the obtained values are consistent with the current observations. The π - π correlations were studied double differentially as a function of the multiplicity and transverse mass, revealing a slight m_T scaling in all multiplicity bins, as revealed by the official ALICE preliminary results shown in Fig. 4.9. Within the present uncertainties, the highest multiplicity bin seems to connect the value of r_{core} to the measurement of the p-p correlation (Figures 4.9 and 4.3). It should be stressed, that the multiplicity correspondence here is not exact, and moreover there are still quite large systematic uncertainty inside the π - π analysis, thus any final conclusions are premature. Nevertheless, these results give indicate that the model can be adapted to describe all hadron-hadron systems, although it will take even more dedicated effort, e.g. by performing a 3D spacial analysis for the pions, correcting for effects of the Lorentz boost on the source, better description of the non-femtoscopic background etc. Further, studying the p- K^+ correlation, where the interaction is rather well known, can provide an intermediate step in the connection of the source functions for meson-meson and baryon-baryon. Another open question is if the resonance source model is suitable for p-A collisions, such as p-Pb. The final goal (hope) is to address all of these issues successfully, and find “the one universal source to rule them all”.

⁸The long tail is located almost entirely outside the domain relevant for femtoscopy, i.e. their spacial separation is so large that the final state interaction is negligible and the corresponding correlation function is flat.

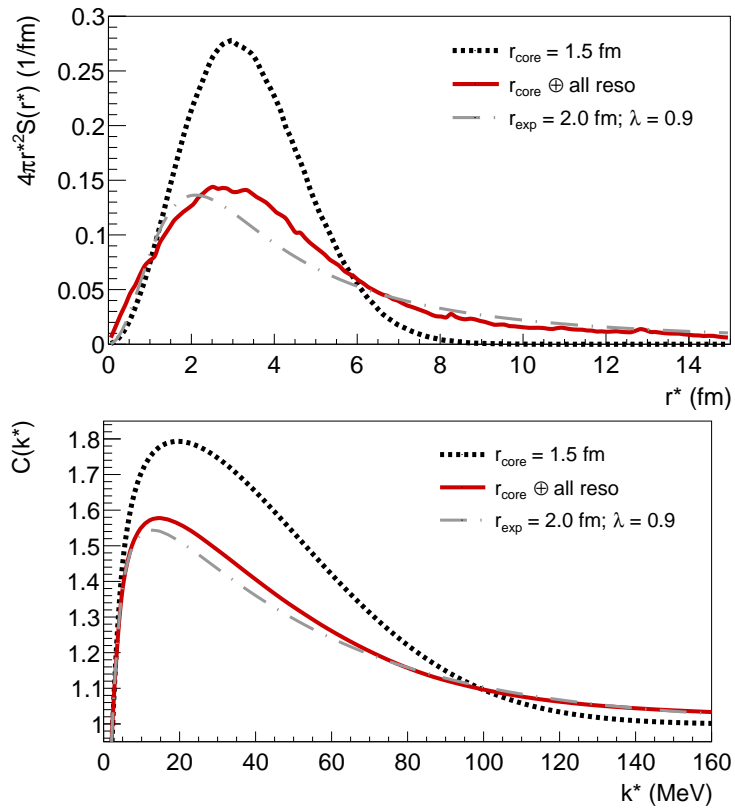


FIGURE 4.6: A comparison between the Gaussian core with resonances included (red line) to a Cauchy source, scaled down appropriately. The size of 2.0 fm is consistent with existing experimental results employing a Cauchy source. The top (bottom) panel shows the corresponding source (correlation) function.

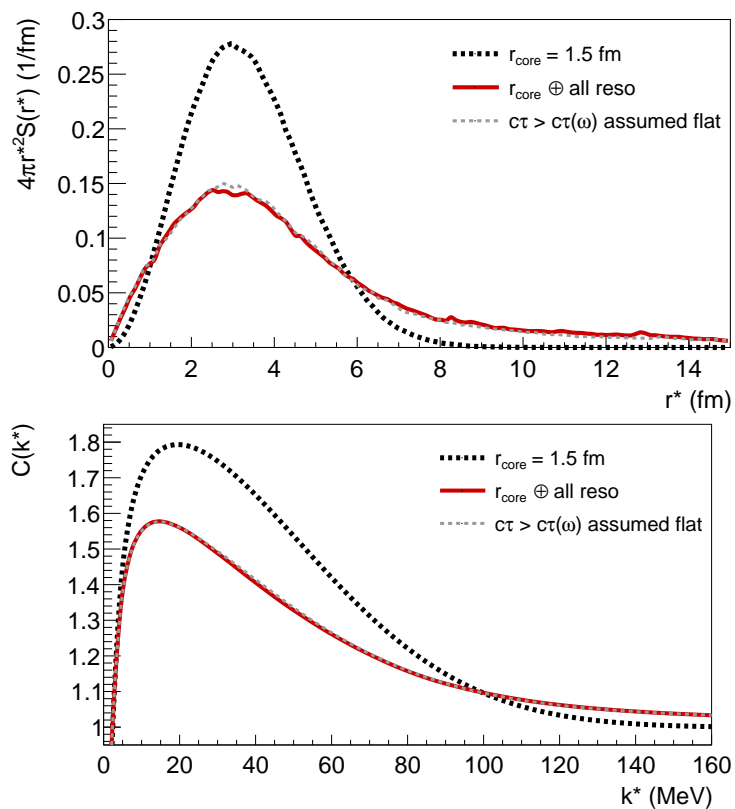


FIGURE 4.7: The inclusion of even longer lived resonances ($c\tau > 25$ fm) into the source can be perfectly described by absorbing them into the flat feed-down contribution. The top (bottom) panel shows the corresponding source (correlation) function.

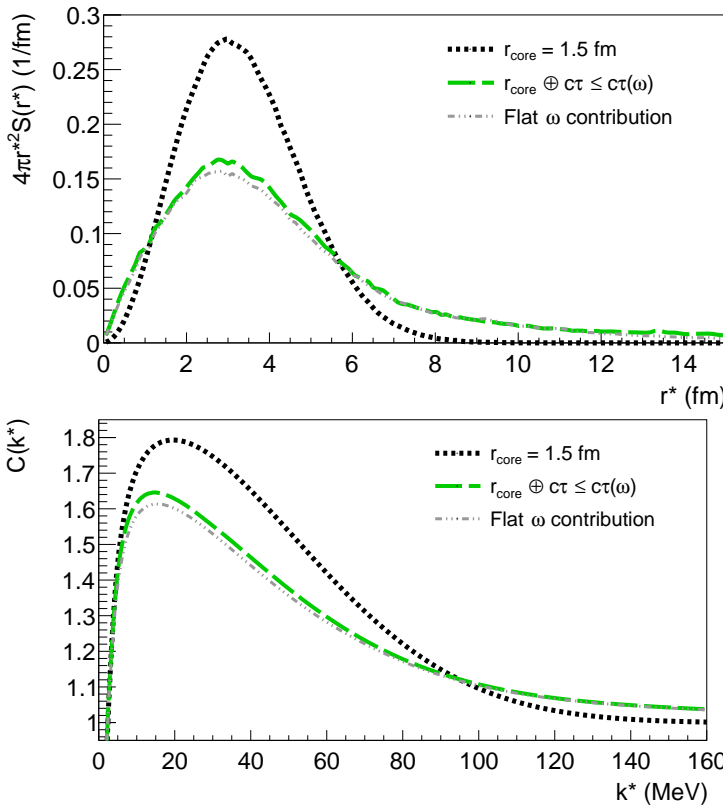


FIGURE 4.8: The contribution of ω meson into the pion yield can be modeled by an effective flat contribution ($\lambda_\omega = 0.86$) to a rather good precision. The top (bottom) panel shows the corresponding source (correlation) function.

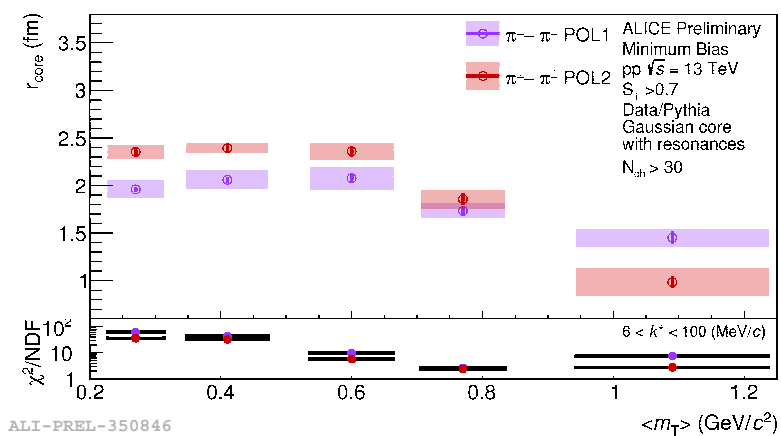


FIGURE 4.9: The r_{core} as a function of $\langle m_T \rangle$ for same charged pions studied in minimum-bias pp collisions at 13 TeV, in the highest available multiplicity bin [106]. The two colors correspond to different hypothesis on the non-femtoscopic background.

Chapter 5

The Λ - Λ interaction

5.1 Introduction and physics motivation

The Λ - Λ interaction has stirred many discussion among theorists and experimentalists, due to its exciting prospects. This interaction does not experience a single-pion interaction, thus the range of the final state interaction is more compact and sensitive to higher-order processes. Already in the 70's the idea of a six-quark ($uuddss$) bound state was put forward within the quark bag model [107]. Such a state is generally referred to as a *H-dibaryon*, and since a pair of Λ hyperons is the lightest dibaryon configuration with such quark content, the $\Lambda\Lambda$ system is thought as the most relevant for the search of this exotic state. The mass of the hypothetical H-dibaryon is largely unknown, with initial speculations that it is lower than the $\Lambda\Lambda$ threshold, although there are new calculations suggestive of a mass between the $\Lambda\Lambda$ and $\Lambda\Xi$. This scenario corresponds to a resonant nature of the H-dibaryon, with a possible final state of its decay into $\Lambda\Lambda$. A nice, albeit a bit outdated, overview is provided by Tsutomu Sakai et al [108].

Experimentally the most useful data stems from the Japanese National Laboratory for High Energy Physics (KEK), that used a beam of negative kaons to shoot on a carbon target and searched for a final state consisting of at least a positive kaon and two Λ baryons. At first a direct approach in searching for the H-dibaryon was adopted by the E224 collaboration, in which the identified events of a ($K^+\Lambda\Lambda\chi$) final state were used to build the invariant mass spectrum of the $\Lambda\Lambda$ pairs, hoping to find a signature (bump) of a decaying resonance [109]. The result, shown in the left panel of Fig. 5.1, suggests a minor enhancement near the threshold, yet it is statistically insignificant for any conclusion. A later study, identical to E224, was performed by the E522 collaboration, in which the statistical precision of the data was improved on, and the initial hint of an overall enhancement of the measured yield at low invariant mass is not visible any more, apart from a single speculative bin at 15 MeV above threshold, that deviates by about 2σ (Fig. 5.1, right panel) [110]. The study performed by E224 was followed up by the emulsion experiment E373 [14], that claimed an observation of a single event (called the *Nagara event*) corresponding to the production and decay of a double-hypernucleus $^{6}\Lambda\Lambda\text{He}$, which is in essence a normal ^{4}He with two Λ hyperons attached to it. The existence of such a state points towards an overall attractive interaction between the protons, neutrons and Λ particles, while the measured binding energy of $1.01 \pm 0.20^{+0.18}_{-0.11}$ MeV, later updated to 0.67 ± 0.16 MeV [112], allows to quantify the genuine $\Lambda\Lambda$ interaction. This is possible as the NN potential is well known and the $N\Lambda$ is modeled to a good precision as well. Nevertheless, the in-medium potential due to the multi-body interaction is not well constrained, leading to a large systematic uncertainty in the determination of the genuine $\Lambda\Lambda$ potential. Dedicated theoretical studies related to the *Nagara event*

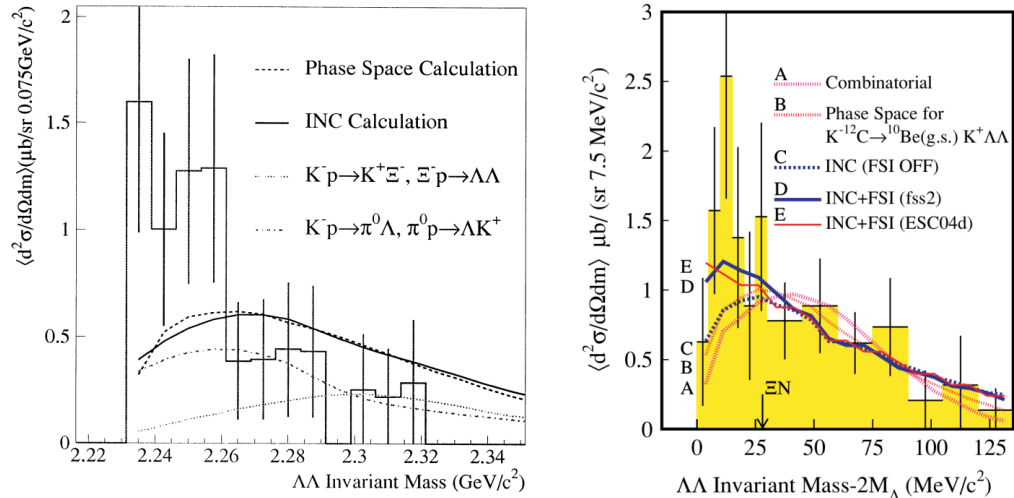


FIGURE 5.1: Result from KEK-E224 [109] (left) and KEK-E522 [110] (right) on the invariant mass of $\Lambda\Lambda$. The measured data points are compared to an intranuclear cascade model (INC) [111] that accounts for the in-medium scattering of the Λ particles. The data sits consistently above this prediction, nevertheless KEK-E522 showed that including a final-state interaction (FSI) model drives the theory prediction further up, leading to a good description of the data without the need for a contribution from $H \rightarrow \Lambda\Lambda$.

lead to the conclusion that the $\Lambda\Lambda$ interaction is attractive in nature, most likely mildly [113, 114]. However, a bound state could not be excluded, although an upper limit of the allowed binding energy of 7 MeV was obtained.

The studies performed by the KEK collaboration, in particular the observation of $\Lambda\Lambda$ -He, provided the theorists with solid results on the H-dibaryon for the first time in more than 20 years, yet their interpretation was rather inconclusive. The STAR collaboration made a solid attempt to address this issue by implying two particle correlation techniques in Au–Au collisions at $\sqrt{s_{NN}} = 200$ GeV to extract the scattering parameters of the Λ - Λ system. Their final conclusions were rather controversial, as they claimed a repulsive interaction with an inverse scattering length of $f_0^{-1} = -0.91 \pm 0.31^{+0.07}_{-0.56}$ fm $^{-1}$ [36]. Nevertheless, a later re-analysis of the data outside of the STAR collaboration demonstrated that there are large systematic biases related to non-femtoscopic and residual contributions, and should they be treated differently the data is compatible with both a slightly attractive interaction or a bound state, leaving the question about the H-dibaryon unanswered [37]. The ALICE collaboration investigated the Λ - Λ system in the initial femtoscopic analysis performed on the subject of final state interactions in small collision systems [38], however the poor statistics of the data sample did not allow any quantitative statements.

The knowledge, prior to this work, on the $\Lambda\Lambda$ interaction is summarized in Fig. 5.2 (Fig. 4 in [38]), where the two axes correspond to the *inverse scattering length*¹ f_0^{-1} and the *effective range* d_0 . The color code on the plot represents the compatibility of the measured ALICE correlation function to the prediction of the Lednický model

¹The sign convention is such that a positive scattering length corresponds to an attractive interaction.

for a certain set of f_0 and d_0 . The regions above 3σ can be excluded, while the shaded area represents a region in which the Lednický model is not applicable, and the interpretation is difficult. To understand this plot better, consider that a positive f_0^{-1} corresponds to an attractive interaction that gets weaker at large values. Values close to $f_0^{-1} = 0$, i.e. $f_0 \rightarrow \infty$, point towards a strong attraction that can transition into a bound state ($f_0^{-1} < 0$). Based on quantum scattering theory, the *effective range expansion* satisfies

$$k \cot(\delta(k)) \xrightarrow{k \rightarrow 0} \frac{1}{f_0} + \frac{1}{2} d_0 k^2 + \mathcal{O}(k^4), \quad (2.15)$$

while in the presence of a *bound state* the binding energy is

$$B_{\Lambda\Lambda} = \frac{1}{m_{\Lambda} d_0^2} \left(1 - \sqrt{1 + 2d_0 f_0^{-1}} \right)^2. \quad (5.1)$$

The above relation produces a meaningful (real) binding energy only if the expression under the square root is positive, imposing the condition $|2d_0 f_0^{-1}| < 1$. This implies that on the plot in Fig. 5.2 a bound state is located at small $|f_0^{-1}|$ and d_0 , for $f_0^{-1} < 0$. Indeed the first few plotted points of the ND and NF theoretical models correspond to binding potentials (ND46, ND48, NF42 and NF44). Further, a deep bound state (large $B_{\Lambda\Lambda}$) corresponds to small f_0^{-1} and d_0 . All other values located at $f_0^{-1} < 0$, such as the STAR result, relate to a repulsive interaction. The colored

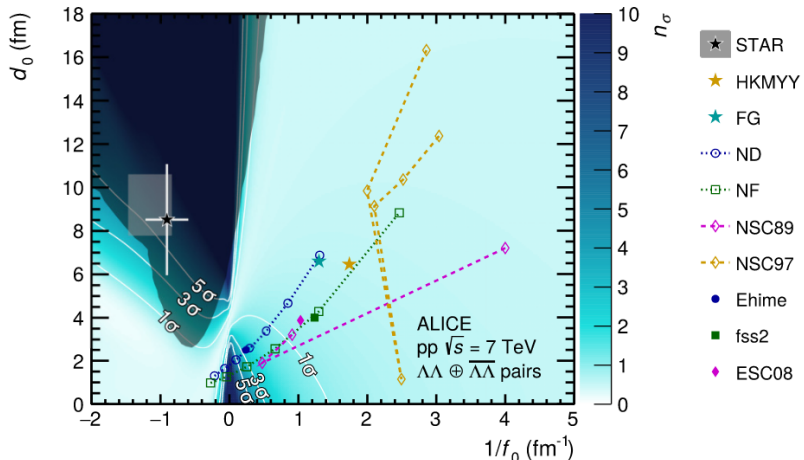


FIGURE 5.2: Result from ALICE [38] on the Λ - Λ interaction, based on femtoscopy in pp collisions at 7 TeV. This is an exclusion plot based on the deviation between the measured data, and the prediction by the Lednický model for different scattering parameters f_0 and d_0 . In addition, the predictions of several models are plotted (see the text for details).

points and lines in Fig. 5.2 represent different theoretical prediction, where the two colored stars correspond to models constrained directly by the hypernuclei results of KEK E373. The Ehime boson exchange model [115] is constrained simultaneously to the Nagara event and to a rather old photomicrographic measurement at CERN, in which there is a single event speculated to be the decay of a $^{10}_{\Lambda\Lambda}\text{Be}$ or $^{11}_{\Lambda\Lambda}\text{Be}$ hypernucleus [116]. However, the analysis of the latter was proven to overestimate the corresponding binding energy, thus the Ehime potential is overly attractive [37]. The fss2 model is spin-flavored SU₆ quark-model that is constrained only to NN and NY data, but is claimed to predict accurately the binding energy of $^6_{\Lambda\Lambda}\text{He}$ (Nagara

event) [117, 118]. The rest of the potentials are provided by the the Nijmegen group and based on meson-exchange to describe the interaction. They posses a repulsive core, that is either hard or soft (SC). Similarly to the fss2, the Nijmegen models are fitted to NN and NY data. Due to the limited experimental results on YY, the related parameters are poorly constrained, providing many possible parameterizations of the $\Lambda\Lambda$ interaction, as indicated by the multitude of predictions shown in Fig. 5.2. The extended-soft-core model (ESC08 [119]) has been specifically fine-tuned to reproduce the Nagara event, while the others (ND, NF and NSC [120–122]) are not.

The scientific society converges towards the idea of a slightly attractive interaction in this channel, as suggested both by the HKMYY and FG models used to describe the hypernuclei data and the preliminary lattice results ($f_0^{-1} = 1.45 \pm 0.25 \text{ fm}^{-1}$ and $d_0 = 5.16 \pm 0.82 \text{ fm}$) [41, 123]², yet there is not a single existing constraint that prohibits the existence of a sub-threshold bound state, leaving a lot of room for exciting new discoveries. Based on Fig. 5.2, it is evident that the ALICE 7 TeV data set is not capable of improving on the existing knowledge on $\Lambda\Lambda$ interaction. Even the Ehime potential, that is known to be overly attractive, cannot be completely excluded, as it sits below the 3σ limit. The present work addresses this issue by combining the results collected in minimum bias pp collisions at both 7 and 13 TeV together with measurements in p–Pb reactions at 5.02 TeV.

Next, let us point out the main goals and challenges of increasing the statistical significance of the femtoscopic studies. Even if the H-dibaryon does not exist, a H-dibaryon above the $\Lambda\Lambda$ threshold can still be present, and visible as an enhancement in the correlation function at larger k^* values. Moreover, there are several coupled channels that could be resolved as a non-flat structure in the correlation function. These channels and their corresponding thresholds are summarized in Table 5.1. Note that the coupling occurs only in the isospin 0 component, implying that a certain fraction $\omega_{I=0}$ of the yield of each pair contributes to $\Lambda\Lambda$. The most relevant

$\Lambda\Lambda \leftrightarrow XY$	$\Lambda\Lambda$	$n\Xi^0$	$p\Xi^-$	$\Sigma^0\Sigma^0$	$\Sigma^+\Sigma^-$
Mass threshold (MeV/ c^2)	2231	2254	2260	2385	2387
k^* threshold (MeV/ c)	0	161	179	421	424
$\omega_{I=0}$	1	1/2	1/2	1/3	1/3

TABLE 5.1: The mass threshold of the $\Lambda\Lambda$ system and all channels coupled to it, with their corresponding threshold in k^* and coupling strengths related to the isospin.

channels, due to their low threshold, are $\Lambda\Lambda \leftrightarrow n\Xi^0$ and $\Lambda\Lambda \leftrightarrow p\Xi^-$. Unfortunately, at the time of the conduction of this analysis, there were no theoretical calculations to account for these coupling effects, thus they are *not considered*. Newly, there is one theoretical work based on χ EFT that addresses this issue [124], and concludes that the effect of the $\Lambda\Lambda \leftrightarrow N\Xi$ coupling onto the Λ - Λ correlation function is comparable to the statistical uncertainties of the (published) ALICE data. Thus, as expected, it is unlikely that the conclusions are significantly biased by these effects.

²The values quoted here and published in [41] were obtained in a private communication with the authors of [123], before their results were published. Thus there is slight deviations in the values from [41] and [123], but entirely within the uncertainties.

The results of this Λ - Λ analysis were published in PLB [41] by the ALICE collaboration, where I was the main analyzer and chaired the publication process.

5.2 Analysis techniques

The aim of the Λ - Λ analysis is the direct study of the scattering parameters, by performing a scan of the corresponding phase space to create a plot such as Fig. 5.2. The strategy is to measure the p-p and Λ - Λ correlation functions, fix the source radius from the p-p correlation (chapter 4), fix all feed-down contributions (chapter 3.1.5) and use the Lednický model (chapter 1.5.4, Eq. 1.30) to determine the agreement of specific choice of scattering parameters (f_0^{-1} and d_0) to the Λ - Λ data by evaluating the corresponding χ^2 value. Assuming that the Lednický model is a viable theoretical framework containing the *true* solution, it makes possible to assign a confidence level to the scattering parameters by taking the result with lowest χ^2 (χ^2_{best}) as a *null hypothesis* and compare it to the χ^2 resulting from all other (f_0^{-1}, d_0) combinations by $\Delta\chi^2_v = \chi^2_v - \chi^2_{\text{best}}$ (Eq. 3.46), following the methods introduced in chapter 3.5.2. The index v corresponds to the number of free parameters in the theory, which in this specific case is 2. To combine the 3 different data sets, each of them is analyzed independently, however the final χ^2 values are summed up.

The correlation function for the pp data set at 7 TeV has already been obtained in [38], thus at present only the pp 13 TeV and p-Pb 5.02 TeV data sets have been analyzed [41]. The reconstruction of the correlation functions is identical in all systems, although the systematic variations are slightly different. A full summary is provided by Tables 3.2, 3.5, 3.9 and 3.10, although for this analysis in particular, the systematic uncertainties related to the variations of the cuts in the reconstruction procedure were *not* used. The reason is that the large statistical uncertainties caused some doubt about the significance of the systematic ones. There is a method, called the *Barlow test*, that can be used to quantify the relative significance between statistical and systematical uncertainties.

Digression: Barlow test

The Barlow test uses the relation

$$n_i^{(\sigma)} = \frac{|d_i - d_0|}{\sqrt{\sigma_i^2 - \sigma_0^2}}, \quad (5.2)$$

where i is indexing the systematic variations ($i = 0$ is the default one), d_i is the value of the studied observable in the i -th variation and σ_i is the corresponding statistical uncertainty. In essence, the denominator gives an estimate of the expected statistical fluctuations due to the slightly different amount of data for each variation, and the numerator shows the actual measured difference. If the latter is related purely to statistical fluctuations, one expects that 68% of the bins result in $n_i^{(\sigma)} < 1$, 95% in $n_i^{(\sigma)} < 2$ etc. The common convention is to apply the Barlow test to each bin in $C(k^*)$ and if deviations of $n_i^{(\sigma)} > 2$ happen with frequency of less than 1:20 (5%) the systematic uncertainties can be neglected.

Digression: Personal opinion on the Barlow test

In the coarse of my PhD I developed a dislike towards this method, as it is a bit hand-waving and for it to be applied the systematic uncertainties need to be evaluated anyways. Hence the only benefit of ignoring them is the smaller amount of iteration needed to be performed by the fit procedure, which is very often not a limiting factor in the analysis. Thus I would strongly recommend to be conservative and always propagate the uncertainties properly, and revert to the use of the Barlow test only in case of a CPU intensive fitting procedure, leading to a bottleneck in the analysis that can be avoided.

The λ parameters, listed in Tables 5.2 and 5.3, are evaluated based on the single particle fractions (Table 3.6) and purities (Table 3.7). The feed-down contributions

Pair	pp		Pair	p- Λ		Pair	p- Ξ^-	
	λ_i^{pp} (%)	$\lambda_i^{\text{p-Pb}}$ (%)		λ_i^{pp} (%)	$\lambda_i^{\text{p-Pb}}$ (%)		λ_i^{pp} (%)	$\lambda_i^{\text{p-Pb}}$ (%)
pp	74.8	72.8	p Λ	50.3	41.5	p Ξ^-	55.5	50.8
p Λ	15.1	16.1	p Λ_{Σ^0}	16.8	13.8	p $\Xi^-_{\Xi(1530)}$	8.8	8.1
± 0.7	± 0.8		p Λ_{Ξ^-}	8.3	12.1			
flat res.	8.1 \mp 0.7	8.0 \mp 0.8	flat res.	20.4	24.9	flat res.	30.3	28.3
fake	2.0	3.1	fake	4.2	7.7	fake	5.4	12.8

TABLE 5.2: The λ parameters, with uncertainties used to model the p-p correlation function, and the associated feed-down correlations, in the analysis of the data sets taken in MB pp collisions at 13 TeV and p-Pb collisions at 5.02 TeV. The sub-indexes are used to indicate the mother particle in case of feed-down. Only the non-flat feed-down (residual) contributions are listed individually, while all other contributions are flat and listed as “flat res.”. All misidentified (fake) pairs are assumed to be uncorrelated, thus resulting in a flat correlation signal.

explicitly accounted for are p- Λ \rightarrow p-p, p- Σ^0 \rightarrow p- Λ \rightarrow p-p, p- Ξ^- \rightarrow p- Λ \rightarrow p-p and p $\Xi(1530)$ \rightarrow p- Ξ^- \rightarrow p- Λ \rightarrow p-p. For practical purposes all non-direct feed-down contributions can be assumed flat as they have a negligible effect on the p-p correlation, nevertheless the initial goal of the analysis framework was to perform a global fit over all measured correlation functions (p-p, p- Λ , p- Ξ^- and Λ - Λ)³, for

³The reason not to finish the global analysis was physics motivated, as it was realized that while there are many unknowns on the interaction in each individual channel, they are not strongly coupled to one another. Thus it was more sensible to perform multiple cleaner (dedicated) analyses.

Pair	λ_i^{pp} (%)	$\lambda_i^{\text{p-Pb}}$ (%)
$\Lambda\Lambda$	33.8 ± 3.1	23.9 ± 2.2
flat res.	59.8 ± 3.1	64.0 ± 2.2
fakes	6.4	12.1

TABLE 5.3: The λ parameters, with uncertainties, used to model the Λ - Λ correlation function in the analysis of the data sets taken in MB pp collisions at 13 TeV and p-Pb collisions at 5.02 TeV.

which reason the full chain of the feed-down was already in place and adopted. For the Λ - Λ pairs the feed-down is considered flat, although it is worth pointing out that the main contributors are Σ^0 (c.a. 15-20%), Ξ^- and Ξ^0 (each c.a. 10-15%), building 60%-64% of the correlation function. Since both $\Lambda\Sigma$ and $\Lambda\Xi$ interactions are completely unknown, there is no way to have an estimate on their functional shape in $C(k^*)$. Nevertheless, they are unlikely to be much stronger than the Λ - Λ signal and given the flattening effect of the kinematical transformation into Λ - Λ (see chapter 2.7.1) as well the rather large uncertainties of all data sets, it is justified to assume a flat contribution to the correlation function associated to these feed-downs. The systematic uncertainties on the λ parameters are related to the $\Sigma^0:\Lambda$ ratio, which is expected to be $1/3 \pm 20\%$ based on theoretical (thermal model) and experimental considerations [75, 77]. These uncertainties are applied only to the primary and direct feed-down contributions.

The theoretical modeling of the correlation functions is based on the Argonne $v18$ potential for p-p [7], chiral effective field theory⁴ in next-to-leading order (default) [8] and leading order (systematics) [102] for p- Λ and the preliminary lattice results for p- Ξ^- [125]. For the p- Ξ^- (1530) only the Coulomb interaction was considered. The p- Σ^0 interaction is accounted for as described in [126]. Finally, as already mentioned, the Lednický model is used to evaluate the Λ - Λ correlation, where the scattering parameters f_0 and d_0 are scanned over to find the best fit.

The p-p correlation functions were used to obtain the emission source, by assuming a common Gaussian source function for the p-p and Λ - Λ pairs. This is contradictory to the discussion in chapter 4, which claims that a common parameterization occurs only for a core Gaussian source corrected for the effect of short lived resonances. The reason no to use the resonance source model in this analysis, is simply as it was not yet developed. Nevertheless, it was exactly the analyses performed in MB pp collisions, including this one, that triggered the discussion on the importance of modelling the source more accurately. Preliminary studies on the subject were performed, attempting to gauge on the effect of both the m_T scaling and the amount of short-lived resonances onto the correlation function. This was done by implying a much more simplified treatment of the resonances, assuming that the emitted resonances and particles sketched in Fig. 4.2 are always oriented back-to-back (180 degree angle), motivated by the overall outwards expansion of the colliding system. Compared to the p-p system, this study predicted approximately 5% larger effective Gaussian source size for the Λ - Λ system, which was now verified to be consistent with the prediction of the resonance source model described in chapter 4. This uncertainty is accounted for as a systematic variation of r_0 for Λ - Λ . To obtain r_0 the p-p correlation functions were fitted using Eq. 3.41 (simplified as 5.3), where only the constant term \mathcal{N} is considered by default. This is done so, as the correlation functions are consistent with unity in the region $k^* \in (200, 400)$ MeV/c. As a systematic check the fits were also performed by including a linear term into the non-femtoscopic baseline.

$$C_{\text{fit}}(k^*) = \mathcal{N} (1 + p_1 k^*) C_{\text{femto}}(k^*). \quad (5.3)$$

The fit range is up to 375 MeV/c, with ± 25 MeV/c variations for the evaluation of the systematic uncertainties. The final result on r_0 (Fig. 5.3) is $1.188 \pm 0.009^{+0.016}_{-0.009}$ for

⁴Here a simplified approach was used, where only the scattering parameters were taken from the theory, while the modelling of the correlation function is done using the Lednický model.

the pp data set and $1.437 \pm 0.0011^{+0.013}_{-0.006}$ for the p-Pb data set, with an additional $+5\%$ uncertainty when applied to Λ - Λ . Note, that the effect of the momentum resolution in this analysis, for both p-p and Λ - Λ , is not explicitly corrected for, instead the fit function itself is smeared by using the detector response matrix, following the procedure introduced in chapter 2.7.3. The required matrices, such as the one for p-p shown in Fig. 2.12, are obtained from the full scale MC simulations, by accessing the true momentum for each particle, enabling to obtain the probabilistic relation between the reconstructed k^* and the “true” k^* of the pair at the generator level of the simulation, i.e. before the detector effects were applied.

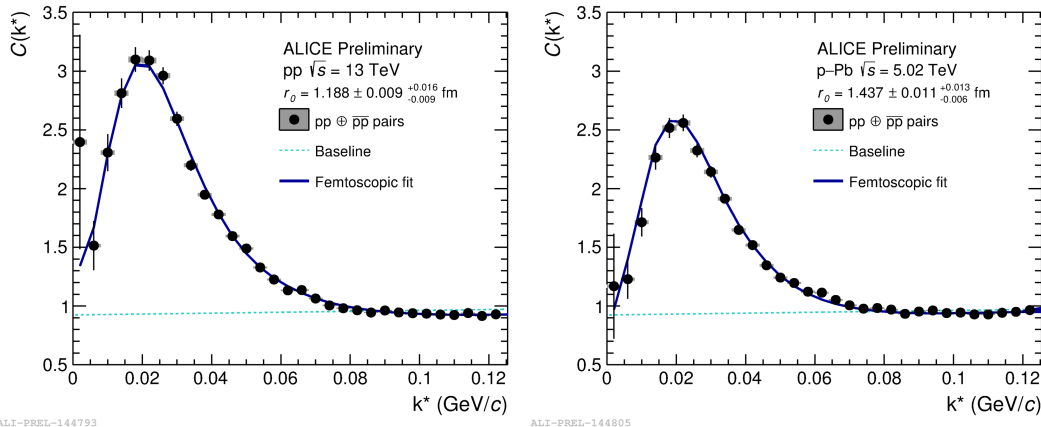


FIGURE 5.3: The p-p correlation functions as measured in pp collisions at 13 TeV (left) and p-Pb collisions at 5.02 TeV (right). The femtoscopic fits (blue lines) are performed by constraining the interaction, leaving r_0 and the non-femtoscopic baseline as free fit parameters.

The Λ - Λ correlation functions are fitted by Eq. 5.3 as well, with the source size fixed from the p-p result, while the interaction is accounted for by the Lednický model using fixed scattering parameters f_0 and d_0 , leaving only the non-femtoscopic baseline free to vary. In contrast to p-p, the Λ - Λ correlation functions manifest a slight linear slope at larger k^* (above 200 MeV/c), thus the baseline polynomial is always assumed to be of first order. This also allows for adjustment of the baseline to the unmodeled effects of the coupled channel dynamics and the feed-down contributions. The data is fitted up to 460 MeV/c, with systematic variations to 420 and 500 MeV/c. Further, it was noticed that the coarse default binning of 20 MeV/c causes small artificial biases, thus the systematic variations also include a reevaluation of the correlation function in 16 and 12 MeV/c sized bins⁵. The fits to $C(k^*)$ are performed for each set of (f_0^{-1}, d_0) and the total $\chi^2 = \chi^2_{\text{pp7TeV}} + \chi^2_{\text{pp13TeV}} + \chi^2_{\text{pPb}}$ evaluated based on the results from all three studied collision systems. The parameter set with the lowest χ^2_{best} is selected as the null hypothesis, to which all other (f_0^{-1}, d_0) are compared by their $\Delta\chi^2 = \chi^2 - \chi^2_{\text{best}}$. Following the recipe in chapter 3.5.2 the corresponding confidence level n_σ is evaluated, leading to the exclusion plot shown in Fig. 5.6. There are a couple of “special” regions within the parameter space spanned by (f_0^{-1}, d_0) . First, the Lednický model has a term to correct for the effect of a small source $(1 - d_0/(2\sqrt{2}\pi r_0))$ in Eq. 1.23), which breaks down for large values of the ratio between the effective range and the source size (d_0/r_0). While

⁵This particular systematic variation is *not* applied to the pp 7 TeV data, as it was directly used from the existing results [38].

it is difficult to determine the exact point at which this term loses its applicability, it is certain that the correlation function has to be positive, thus if some d_0/r_0 ratio results in a negative $C(k^*)$ it is evident that the approximation no longer works. This region of the phase space is marked by a dark shaded color in Fig. 5.6, and should not be used for any physics conclusions. It is important to stress, that this is not a big limitation, as there are no realistic theoretical predictions with scattering parameters within this nonphysical region, in which the only data point is the original, and currently considered wrong, measurement by the STAR collaboration. Further, it was explicitly verified (Fig. 5.5) that for all models plotted in Fig. 5.6 the Lednický model gives identical results as an evaluation of the wave and correlation function, using CATS, with an effective parameterization of the interaction potential $V(r)$ as suggested in [37] and discussed in chapter 2.5, justifying the use of the Lednický equation for all physically motivated scattering parameters. The second region of interest is the phase space corresponding to a bound state. We have seen that the binding energy $B_{\Lambda\Lambda}$ associated with a set of scattering parameters can be evaluated by Eq. 5.2, providing an opportunity to assign a confidence level to each $B_{\Lambda\Lambda}$. Note, that Eq. 5.2 projects two parameters onto one, meaning that there is no unique transformation $(f_0^{-1}, d_0) \rightarrow B_{\Lambda\Lambda}$, and a single value for the binding energy could result from multiple parameterizations. Thus the assigned confidence level to $B_{\Lambda\Lambda}$ has to be the lowest (best) one obtained.

5.3 Results and outlook

The experimental correlations function for Λ - Λ in the different data sets are plotted in Fig. 5.4. The yellow line is a dummy fit with free scattering parameters, but the results will not be discussed or interpreted due to the very large uncertainties, leading to the necessity of a parameter scan. These data points are similar among all systems, and point towards a correlation function that is consistent with a pure quantum statics term, relevant in this system as it consists of two identical particles. This observations suggest that the strong interaction is shallow, although its strength could be screened by the low (c.a. 30%) amount of genuine Λ - Λ signal. Further, there is no visible hint on the opening of the $\Lambda\Xi$ coupled channels (160-180 MeV/c) or a bump corresponding to a possible H-dibaryon resonance above the $\Lambda\Lambda$ threshold. The former certainly exists, the fact that it is not resolved also implies that the latter cannot be excluded. Fig. 5.5 shows the correlation functions for the ND model family, and reveals that even when they are scaled down by a λ parameter certain predictions deviate substantially from the quantum-statistics baseline. In particular, strongly attractive interaction, such as ND50 (pink), ND52 (cyan) and ND54 (yellow), are significantly enhanced above unity, and will be for sure excluded by the data. The same holds for the ND48, pointing a very shallow (small $B_{\Lambda\Lambda}$) bound state. A slightly deeper bound state, such as ND46, develops a mild dip around 60 MeV/c, but does not deviate significantly from the baseline, it is thus unlikely to be excluded by the data. However, an even deeper bound state will create a more substantial dip structure, leading to a discrepancy to the data. These simple considerations set up the expectations for the full analysis: exclusion of the very attractive potentials and the very shallow or very deep bound states. The final results are presented in Fig. 5.6 and 5.7. The former is the confidence level (exclusion) plot of the scattering parameters (f_0^{-1}, d_0) , done analogously to Fig. 5.2 [38]. The latter is the transformation of this plot to $(B_{\Lambda\Lambda}, d_0)$, where only the standard 1σ

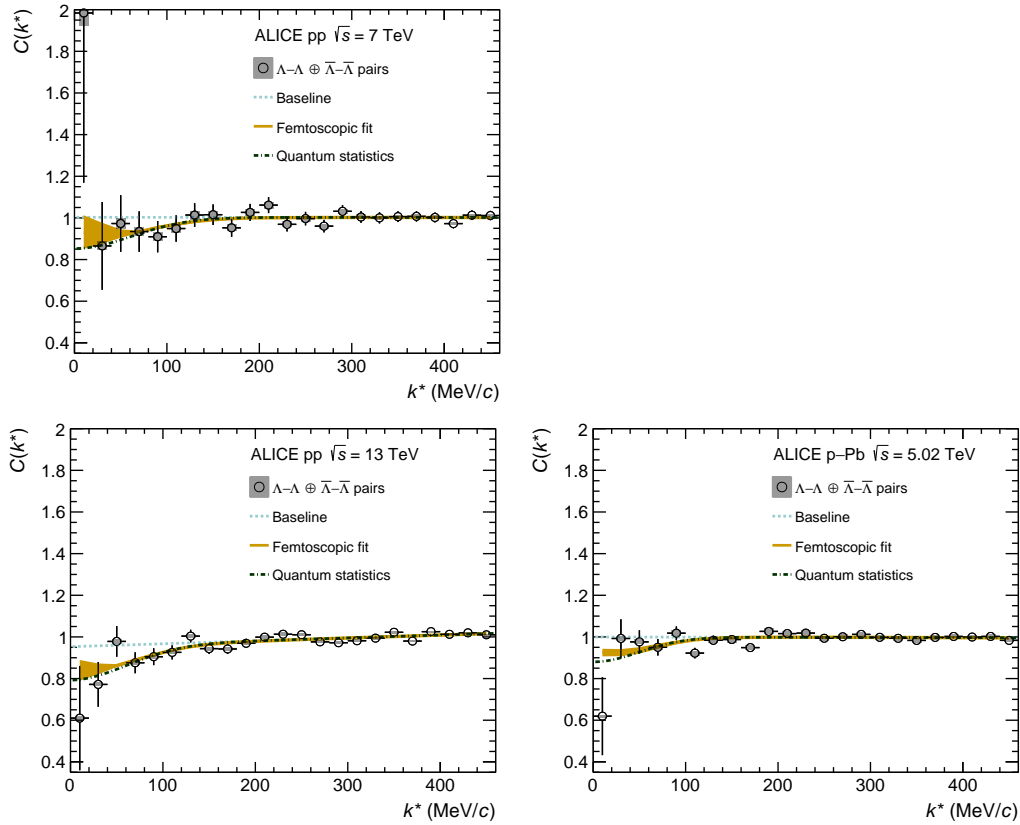


FIGURE 5.4: The Λ - Λ correlation functions for the different collision systems. The upper left panel is the result from [38], while the lower panels relate to the present analysis [41]. The gray boxes denote the systematic uncertainties, which are neglected based on the Barlow test. Visually, the justification becomes obvious from their small relative size compared to the statistical uncertainties.

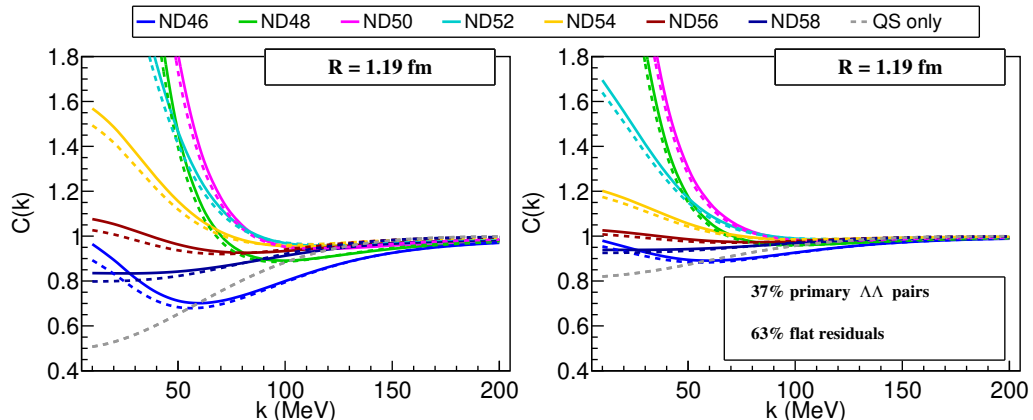


FIGURE 5.5: Theoretical $\Lambda\Lambda$ correlation functions. The solid lines represent the CATS solutions based on the potentials from [37], while the dashed lines are the corresponding results from the Lednický model. The right panel shows the genuine Λ - Λ correlations, the left panel shows the same functions scaled according to the λ parameters.

uncertainty is plotted, including the systematic uncertainties⁶. Indeed these results

⁶The systematic uncertainties are related to the variations of the fit parameters only, and are omitted from Fig. 5.6 for visual purposes.

confirm our naive expectations, nevertheless it is now possible to make quantitative statements. The color code in Fig. 5.6 is such that the white regions provide

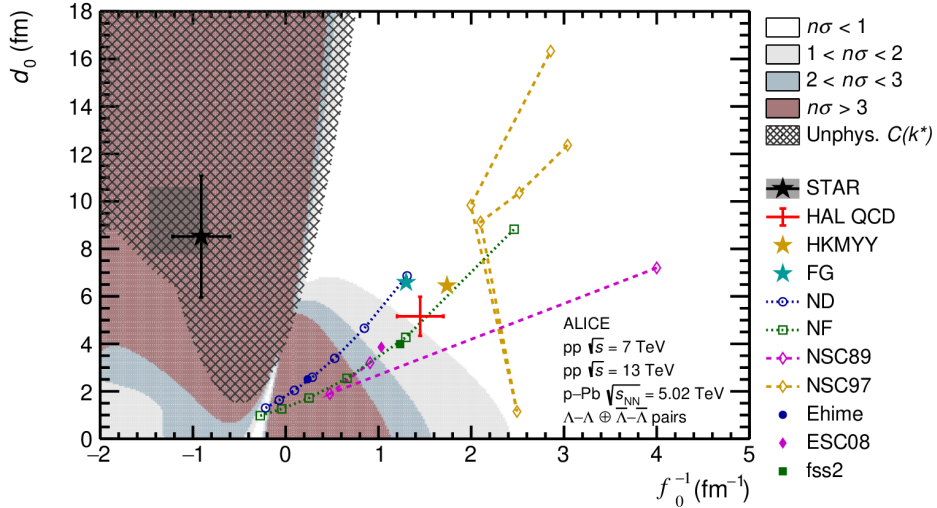


FIGURE 5.6: [41] Confidence levels for the scattering parameters of Λ - Λ .

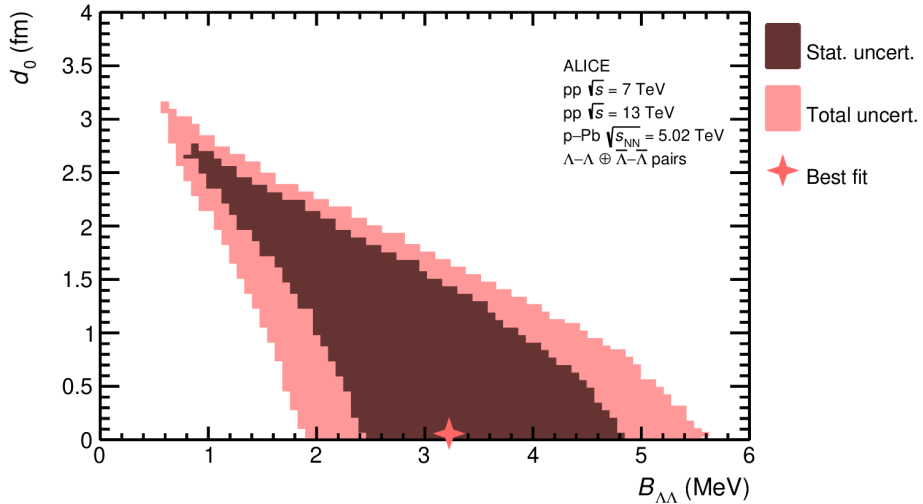


FIGURE 5.7: [41] Confidence level (1σ) for the binding energy, as a function of the effective range, of Λ - Λ .

the best compatibility to the data ($n_\sigma < 1$), the gray and dark blue regions are not favoured but cannot be excluded ($n_\sigma < 3$) while the dark red region is disfavoured with more than $3n_\sigma$ and highly unlikely (less than 0.3%) to be a statistical fluctuation. The models anchored to the hypernuclei measurements (the two colored stars), as well as the preliminary lattice computation (red cross), are well in agreement to the ALICE data. The corresponding scattering parameters are associated with a mildly attractive interaction and a large effective range. Nevertheless, there is another family of good solutions, namely the *bound state island* seen at small d_0 and slightly negative f_0^{-1} . From an experimental perspective this seems disappointing at first, as no firm conclusion on the existence of the H-dibaryon can be made, just as in the case of all previous measurements. However, the phase space is significantly constrained, and Fig. 5.7 imposes strict limits on the allowed binding energy as a

function of the effective range. Integrating over the dependence of the latter leads to $B_{\Lambda\Lambda} \in (0.6, 5.6)$ MeV/ c , setting limits on both the minimum and maximum allowed $B_{\Lambda\Lambda}$. The existing restriction was $B_{\Lambda\Lambda} < 7$ MeV/ c , making the present data the new benchmark for the theoretical studies. Moreover, with view of the newer data set corresponding to high-multiplicity pp collisions at 13 TeV and the upcoming RUN3 of the LHC, one can be confident that most of the remaining questions can be answered within the next few years.

I would like to conclude with my personal opinion on the main experimental challenges for ALICE, which need to be addressed in order to reach a definite conclusion from the upcoming data sets. The latest analyses of the high-multiplicity pp data set lead to the observation that the non-femtoscopic baseline becomes an issue for precision studies, and if it is modeled by a polynomial function it can contribute by up to 3% to the correlation function, which is comparable with the expected difference in the signal for the two scenarios, e.g. ND58 and ND46 models (the two dark blue lines) in Fig. 5.5. The best way to resolve this issue, is to achieve a reliable description of the long-range k^* correlations and angular correlation of the baryon-baryon pairs from an advanced transport model, such as AMPT [88] (see chapter 3.4.1). Further, there are multiple coupled channels to $\Lambda\Lambda$ ($N\Xi$ and $\Sigma\Sigma$), where the low $N\Xi$ threshold of 160-180 MeV/ c can cause significant modification within the femtoscopic region. Moreover, the Λ - Σ^0 feed-down into Λ - Λ is substantial (more than 20%) and the small mass difference between Λ and Σ implies a large impact of the residual correlation. At present, the $\Lambda\Sigma^0$ interaction is theoretically completely unknown, however there are claims by the HAL QCD collaboration that a full coupled-channel evaluation of the Λ - Λ system will be performed in the future [123]. If this is achieved it would be possible to test the Λ - Λ system in much greater depth, although, unlike at present, this will be done in a model dependent way. Finally, from the experimental side the amount of misidentified particles is substantial in the context of precision studies (5-13%), demanding the use of a side-band analysis, or similar methods (see section 3.3), to correct the correlation signal.

The issues highlighted in the above paragraph are certainly not trivial. In particular, the coupled channels dynamics will become important, as well as the feed-down from Λ - Σ^0 . Nevertheless, there are theoretical developments on that subject, making the prospect of the future results very exciting. The present work demonstrates that the correlation studies have already reached superiority over traditional experimental methods, such as measurements of hypernuclei, in the study of the Λ - Λ interaction, and are the best currently available option to resolve the speculations surrounding the H-dibaryon.

Chapter 6

The p- Λ interaction

6.1 Introduction an physics motivation

Summarizing the introductory discussion from chapter 1.4, the Λ particle is the lightest hyperon (baryon with a strange quark), it is neutral and composed of uds quarks. It has attracted a lot of theoretical interest, as it relates to multiple interesting physics topics, such as the study of *neutron stars* (NS). Experimentally it is the most accessible hyperon, making possible to constrain the theoretical models. A long standing goal of nuclear physics is to determine the *Equation of State* (EoS), capable of providing effective treatment of the properties of dense nuclear matter, that goes beyond the density of the nucleus ρ_0 . The relevance of hyperons, Λ in particular, for neutron stars is related to the fermionic nature of all baryons, leading to a limitation on their allowed quantum states (Pauli exclusion principle). This imposes a large increase of the chemical potential for nucleons, eventually making it energetically favorable to produce hyperons. Nevertheless, the density at which this effect occurs depends on the interaction between the baryons in medium ($\rho > \rho_0$), which is experimentally extremely challenging to study. The investigation of these effects is thus model dependent, where a theoretical extrapolation to high densities is needed. The corresponding constraints are based on the existing results from scattering and hypernuclei experiments, which mostly provide information about the 2-body interaction in vacuum, nevertheless the latter can also be used to examine the genuine 3-body force. The state of the art theory regarding the $N\Lambda$ interaction is the *chiral effective field theory* (χ EFT). It has two main results, based on leading order (LO) and next-to-leading order (NLO) calculations, where the former is very much outdated and incompatible with the scattering data. The theory includes a full treatment of the *coupled channel* $N\Sigma \leftrightarrow N\Lambda$, where the genuine $N\Sigma$ interaction and the coupling strength to $N\Lambda$ are not strongly constrained by the existing data. The authors of χ EFT demonstrated that this allows to find multiple parameterizations (NLO13 and NLO19) of the theory for which the coupling strength is different (smaller for NLO19) but the description of the experimental data is equally good. Most notably, these two versions of the theory lead to a different genuine 3-body interaction, where the NLO19 leads to more repulsion (see chapter 1.4.3). This can influence the EoS of NS a little, although for both NLO13 and NLO19 the approximate treatment of the 3-body problems provides enough repulsion to explain the delayed appearance of Λ hyperons within the NS interior, giving a possible explanation to the hyperon puzzle.

Figure 6.1 summarizes the existing scattering data, as well as the differences in the predictions of NLO13 and NLO19. It is evident that the precision of the theory surpasses that of the data, and it is impossible to separate between these models.

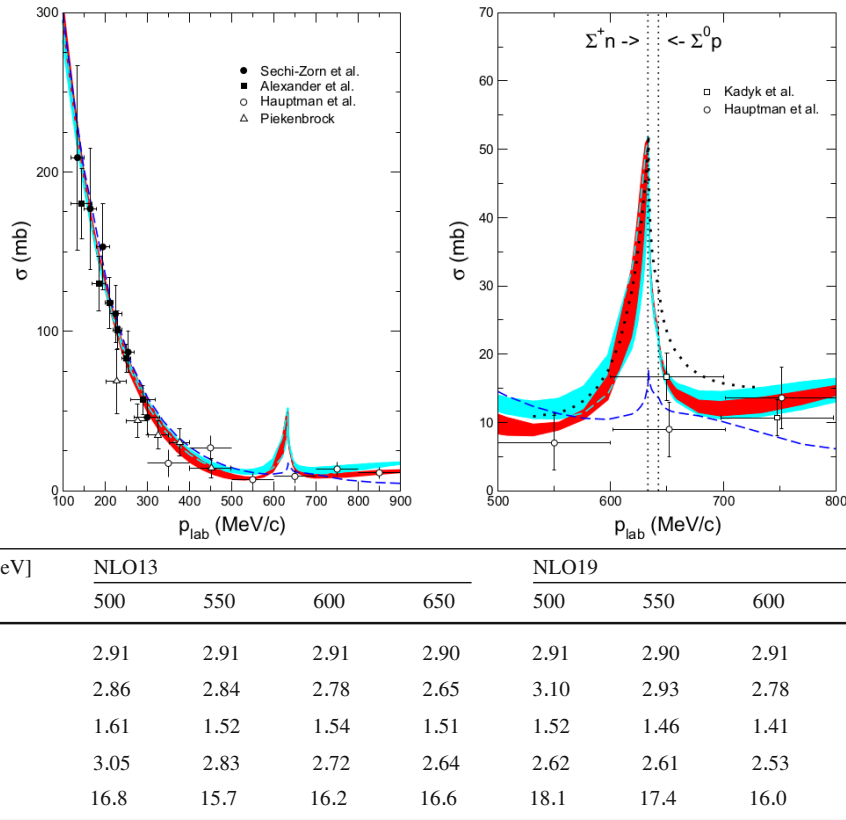


FIGURE 6.1: The $p\text{--}\Lambda$ cross section from experiment and χ EFT. The bands represent the NLO13 (red) and NLO19 (red) parameterizations. The table provides information on the scattering length f and effective range d in the singlet ($S = 0$) and triplet ($S = 1$) configuration, as well as the total χ^2 of the 36 data points.

Moreover, the cusp corresponding to the $\text{N}\Sigma \leftrightarrow \text{N}\Lambda$ coupling is not resolved experimentally and the first data point is at $p_{\text{lab}} \approx 130 \text{ MeV}/c$ ($k^* \approx 60 \text{ MeV}/c$). By contrast, non-traditional femtoscopy excels at measuring the interaction at very low energy. Figure 6.2 shows the same theoretical models translated onto the $p\text{--}\Lambda$ correlation function, scaled by the expected experimental λ parameter for the current analysis. The width of the bands corresponds to the statistical uncertainties achieved by ALICE in the high-multiplicity triggered pp collisions at 13 TeV. Apart from the obvious opportunity to separate between LO and NLO, the interesting observation is that the strength of the cusp corresponding to the coupling to $p\Sigma^0$ is substantially different between the individual variations of the NLO model, hinting that it could be possible to experimentally discriminate, albeit slightly, between the differences of the NLO13 and NLO19 calculations. Further, these two models also show a slight systematic difference in their slope over the k^* range below 200 MeV/c , due to the small differences in their s -wave scattering length for $S = 1$, that could add up to a statistically significant difference in the fit to the data. Moreover, the feed-down contribution of the $p\text{--}\Sigma^0$ channel contributes by a non-flat amount at $k^* > 40 \text{ MeV}/c$, implying that the $p\text{--}\Lambda$ correlation function measured by ALICE will be sensitive to the genuine $p\text{--}\Sigma^0$ correlation, providing an extension, if not even an improvement, over the direct measurement [42]. The momentum reach of the data extends essentially to zero momentum, where the maximum uncertainty is only around 4% and for k^* below 20 MeV/c . For comparison, the first data point of the scattering data is

at $k^* \approx 60$ MeV/c with an uncertainty of 25%, which for the present data is reduced to c.a. 0.5%.

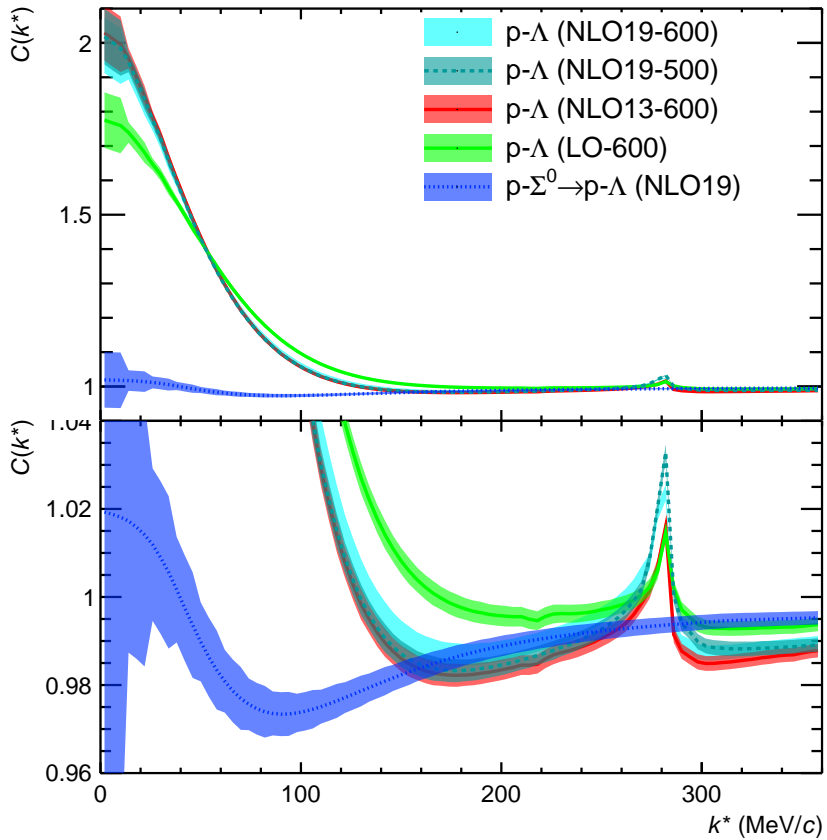


FIGURE 6.2: The p- Λ theoretical correlation based on χ EFT [8, 21, 102]. The strength of the signal is scaled according to the experimental λ parameters, and the default cusp strength ω of 1/3 is used. In addition, the dark-blue color represents the expected residual p- Σ^0 contribution to the p- Λ .

6.2 Analysis techniques

6.2.1 Overview

The details on the data analysis follow exactly the description provided in chapter 3. The data set used is from pp collisions at 13 TeV triggered for high-multiplicity, which provides the largest statistical significance as of this moment. The total amount of events is roughly 1 billion, resulting in c.a. 1 billion p \oplus \bar{p} candidates, 250 million $\Lambda \oplus \bar{\Lambda}$ candidates and 1.3 million p $\Lambda \oplus \bar{p}\bar{\Lambda}$ pairs with k^* below 200 MeV. The measured raw experimental function is plotted in Fig. 6.3, and demonstrates its excellent statistical significance, above all, by the very clear observation of the kinematic cusp corresponding to the $N\Sigma \leftrightarrow N\Lambda$ coupled channel at the threshold of $k^* = 289$ MeV/c. Overall, the uncertainties are small enough to separate differences even of $\sim 1\%$ in the correlation function at intermediate k^* ranges and 1-3% at the very low k^* . Based on Fig. 6.2 all theoretical differences are of that order, including the feed-down contribution of p- Σ^0 , meaning that this data set should indeed provide a very precise benchmark to the theory. Still, the very high statistical precision

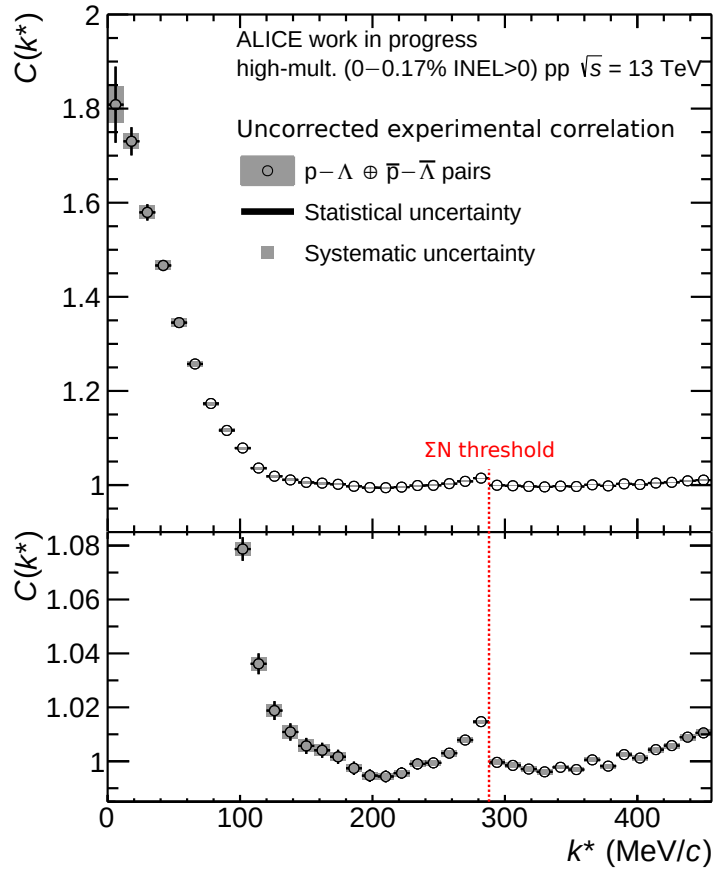


FIGURE 6.3: The uncorrected experimental $p-\Lambda$ correlation function, normalized in the region 200 – 400 MeV/c for visualization purpose. The main highlight is the extremely large precision, allowing for the first direct observation of the coupling to ΣN in the $\Lambda\Lambda$ system.

makes any comparison susceptible to be biased by small contamination or systematic uncertainties related to the modelling. The purity of the protons is 99.43%, and of the Λ candidates it is 96.0%. The latter implies 4% of misidentified Λ particles, which could play a substantial role for the correlation function. For that reason the experimental correlation function has been corrected by implying a sideband analysis (see chapter 3.3.3), using the following two equations

$$C_{\text{misid}}(k^*) \approx \omega_{\text{left}} C_{\text{misid},\text{left}}(k^*) + \omega_{\text{right}} C_{\text{misid},\text{right}}(k^*), \quad (3.28)$$

$$C_{\text{pure}}(k^*) = \frac{C(k^*) - \lambda_{\text{misid}} C_{\text{misid}}(k^*)}{\lambda_{\text{pure}}} = \frac{C(k^*) - (1 - \lambda_{\text{pure}}) C_{\text{misid}}(k^*)}{\lambda_{\text{pure}}}, \quad (3.29)$$

where $C(k^*)$ is the measured correlation function, based on the ratio of the same- and mixed-event samples¹, $C_{\text{misid}}(k^*)$ is the sideband correlation function built with fake Λ candidates selected from the left/right (weighted by $\omega_{\text{left}} = 1 - \omega_{\text{right}}$) side of the Λ invariant mass peak, $\lambda_{\text{pure}} = \mathcal{P}(\Lambda)$ is the purity of the Λ candidates and $C_{\text{pure}}(k^*)$ is the correlation function corrected for the Λ impurities. The latter will be

¹As discussed in chapter 3.2, to be able to perform the correct arithmetic for summation of correlations, the normalization has to be done over the total yield of the same- and mixed-event samples, i.e. the integral of both over the full k^* range has to be 1. This has been consistently done so throughout the analysis, however, to have a more intuitive femtoscopy oriented representation on the figures, unless stated otherwise the plotted correlations have been normalized in different k^* ranges, chosen such that $C(k^*) \approx 1$ outside of the femtoscopy region.

used further in the analysis, using its full decomposition into

$$C_{\text{pure}}(k^*) = b(k^*)[\lambda_{p\Lambda} C_{p\Lambda}(k^*) + \lambda_{p(\Sigma^0)} C_{p(\Sigma^0)}(k^*) + \lambda_{p(\Xi)} C_{p(\Xi)}(k^*) + \lambda_{\text{ff}} + \lambda_{\tilde{p}\Lambda}], \quad (6.1)$$

$$\lambda_{\tilde{p}\Lambda} C_{p(\Xi)}(k^*) + \lambda_{\text{ff}} + \lambda_{\tilde{p}\Lambda}], \quad (6.2)$$

where $b(k^*) = C_{\text{non-femto}}(k^*)$ is the non-femtoscopic baseline (Eq. 3.35) and the terms in the square brackets represent the individual contributions to the correlation signal, scaled by the corresponding λ parameters of the genuine $p\Lambda$, feed-down related to $p(\Sigma^0) \rightarrow p\Lambda$ and $p(\Xi) \rightarrow p\Lambda$. The term λ_{ff} is related to all other feed-down contributions, that are here considered to result in a flat correlation signal, while $\lambda_{\tilde{p}\Lambda} = 1 - \mathcal{P} = 0.57\%$ relates to the misidentified protons and the corresponding signal is assumed flat. Note, that since $C_{\text{pure}}(k^*)$ is explicitly corrected for the misidentified Λ particles, the associated contribution drops out of the decomposition presented in Eq. 6.1, and the evaluation of the remaining λ parameters is performed by using a Λ purity of 100%. To make the results more accessible for direct comparison to theoretical predictions, the correlation function has been unfolded for the effect of momentum resolution. Finally, the corrected and unfolded correlation function is compared to the different hypotheses on the interaction, where only the non-femtoscopic baseline $b(k^*)$ is determined by the fitting procedure.

6.2.2 Decomposition of the correlation signal

Next, let us examine in more details the decomposition of the correlation signal, and motivate the two parameters λ_{ff} and $\lambda_{\tilde{p}\Lambda}$ used to approximate several contributions with a flat signal. The details regarding the fraction of protons and Λ s are provided, respectively, in chapters 3.1.4 and 3.1.5. The feed-down contributions to the protons are the decays of Λ and Σ^+ , where the ratio between them is 70:30, thus the dominant residual is related to $\Lambda \rightarrow p$. The corresponding residual correlation into $p-\Lambda$ is $(\Lambda)\Lambda \rightarrow p\Lambda$, nevertheless it is known that the $\Lambda-\Lambda$ correlation function exhibits a rather flat behaviour (chapter 5 and [41]) and due to the additional flattening effect of the kinematic transformation of the residual correlation (see chapter 2.7.1) it is safe to assume that the overall contribution into $p-\Lambda$ is approximately flat. Further, the $\Sigma^+\Lambda$ interaction is completely unknown, but given its lower weight into the $p-\Lambda$ decomposition, it is justified to assign a flat residual signal. Regarding the feed-down into Λ , there are two relevant channels associated with Σ^0 and Ξ decays, where the latter is equally split between the contribution of Ξ^- and Ξ^0 . Both Σ^0 and Ξ have considerable contributions ($\sim 20\%$ each) to the total Λ yield, thus they are explicitly accounted for in the decomposition.

The $p-\Xi^-$ interaction has been studied by colleague Bernhard Hohlweger, and his findings confirm the lattice potential obtained by the HAL-QCD collaboration as a valid description of this channel [40, 45, 62]. For this reason both the $p(\Xi^-) \rightarrow p\Lambda$ and $p(\Xi^0) \rightarrow p\Lambda$ feed-down contributions have been modeled using the lattice results. The amount of feeddown Ξ particles into Λ has been estimated to be 23.2% (chapter 3.1.5), however that study evaluates the amount of fractions averaged over all reconstructed single particles, independent on k^* . Fig. 3.15 however reveals that for the high-multiplicity pp data set there is a slight p_T dependence in the amount of fractions, which can be translated into a relation to k^* . By relating the average p_T of the Λ particles used in the reconstruction of $p-\Lambda$ pairs with k^* below 480 MeV/ c , it has been revealed that the average fraction of secondary Ξ s is modified to 27%. This value has been included as part of the systematic variations.

Pair	$p\Lambda$	$p(\Sigma^0)$	$p(\Xi)$	Flat feed-down	$\tilde{p}\Lambda$
$\lambda_{\text{Pair}} (\%)$	47.1	15.7	19.0	17.6	0.6
$\min\{\lambda_{\text{Pair}}\} (\%)$	42.7	12.6	—	—	—
$\max\{\lambda_{\text{Pair}}\} (\%)$	49.6	18.0	22.1	—	—

TABLE 6.1: Weight parameters of the individual components of the $p\text{-}\Lambda$ correlation function. The two last rows correspond to the minimum and maximum value of the λ parameters within the systematic variations.

The $p\Sigma^0$ is experimentally very poorly constrained, even by correlation studies [42], thus the theoretical treatment of this channel is far from being refined. Nevertheless, there are several calculation available, the most prominent being χ EFT. Since this model is also providing the state of the art description of the $N\Lambda$ interaction, including its coupling to $N\Sigma$, the most natural choice is to use χ EFT for the entire $N\Sigma \leftrightarrow N\Lambda$ system. Indeed any physics conclusion related to the measured $p\text{-}\Lambda$ correlation function have to be model-dependent due to the complex coupled channel dynamics, hence the main goal of the present analysis is to test the accuracy of χ EFT and draw all the conclusions based on the goodness of the fit. Both the $\lambda_{p(\Sigma^0)}$ parameter and the strength of the cusp corresponding to the coupled channel depend on the relative amount of initial state Λ and Σ^0 particles. As discussed in chapter 3.1.5, the expected value based on naive isospin considerations is 0.33, however accounting for the theoretical and experimental predictions, the systematic variations are including a ± 0.07 variation of this parameter.

Further, the rest of the residual correlations, related to pairs for which both the proton and the Λ stem from feed-downs, have small weights and are significantly flattened due to the transformation into $p\text{-}\Lambda$, thus they have been considered approximately flat and included in the λ_{ff} factor of Eq. 6.1. The last contribution into $p\text{-}\Lambda$ relates to the misidentified protons ($\lambda_{\tilde{p}\Lambda} = 0.57\%$). While this number is very small, the precision of the data is of the same order, thus it is important to examine the largest possible correlation signal in this channel. The misidentifications are mostly π^+ or K^+ particles. Both the $\pi^+\Lambda$ and $K^+\Lambda$ are probably not very strongly interacting, e.g. at low energies the cross sections of π^+p and K^+p are an order of magnitude lower compared to $p\Lambda$, and the situation is unlikely to be significantly different for interactions with Λ . The $K^+\Lambda$ channel has been already studied by correlation techniques in heavy-ion collisions by ALICE [127], where a mild repulsion was found. Assuming the exaggerated scenario that $\lambda_{\tilde{p}\Lambda}$ is entirely attributed to the $K^+\Lambda$ channel and that the interaction is described based on the scattering parameters extracted in [127], Eq. 3.27 has been employed to evaluate the significance of this contribution into $p\text{-}\Lambda$. It was found that it is c.a. factor 10 smaller than the statistical uncertainties of the data, for this reason the associated residual signal is assumed flat. The λ parameters and their associated uncertainties, evaluated based on the above discussion, are summarized in Table 6.1.

6.2.3 Sideband analysis

The *sideband analysis* composes of two aspects, first to evaluate better the uncertainties associated with the purity determination (λ_{pure}), and second to determine

all components of Eq. 3.28 in order to obtain the final result on the p- Λ correlation. So far the discussion on the purity of the Λ candidate focused on the invariant mass spectrum of the single particles (Fig. 3.10), where the fit, performed with the sum of two Gaussians (signal) and a second order polynomial (background), results in $\mathcal{P}(\Lambda) = 96.0\%$. Nevertheless, there are a few considerations to be made, first the quality of the fits were rather poor, mostly due to the shoulder above $M(p\pi^-)$ of $1.13 \text{ GeV}/c^2$, which could not be described properly. Second, the purity could depend on k^* , hence to get a more precise determination it has to be evaluated not from the single particle spectra, but rather from the Λ candidates used to build the p- Λ pairs at specific k^* . In chapter 3.3 it was discussed that the λ parameters have to be determined from the reference (mixed-event) sample, since the purity of the same-event sample is biased by the final state interaction. Thus it was concluded to reevaluate the purity of the Λ candidates, by fitting their invariant mass spectra obtained deferentially in k^* from the Λ s used to build the p- Λ mixed-event sample. To obtain a more accurate description of the background, the polynomial function has been substituted by a 3-rd order spline. This introduces further degrees of freedom to the fit, allowing for larger systematic uncertainties related to the structures present in the background. For the single particle fits the Λ and $\bar{\Lambda}$ candidates were fitted separately, each by using a the sum of two Gaussians to model the signal, meaning that the total $\Lambda \oplus \bar{\Lambda}$ yield has been characterized by 4 Gaussians. However, the shapes of their invariant mass spectra are quite similar, thus it is possible to combine the two spectra to obtain a bit more stable fit to determine the shape of the background spline, and attempt to model the peak corresponding to $\Lambda \oplus \bar{\Lambda}$ by the sum of two Gaussians only. Still, the fits showed some systematic discrepancies at the “edges” around the Λ peak, that are resolved by introducing a 3-rd Gaussian. Such a fit procedure resulted in a significantly improved description of the invariant mass spectrum compared to the initial attempt in chapter 3.1.5. The analytical expression describing the fit is

$$f_M(M) = \sum_{i=1}^3 \frac{\mathcal{A}_i}{\sigma_M^{(i)} \sqrt{2\pi}} \exp \left[-\frac{1}{2} \left(\frac{M - M_\Lambda}{\sigma_M^{(i)}} \right)^2 \right] + B_S(M), \quad (6.3)$$

where $f_M(M)$ is the fit function for the invariant mass spectrum, \mathcal{A}_i are the amplitudes associated with each of the 3 Gaussians used to model the Λ peak, M_Λ is the position of the peak and common to all Gaussians, $\sigma_M^{(i)}$ is the width of each Gaussian and $B_S(M)$ is the spline function describing the background. The corresponding *purity* is evaluated by

$$\mathcal{P}(\Lambda) = \frac{\int_{M_{\min}}^{M_{\max}} f_M(M) - B_S(M)}{\int_{M_{\min}}^{M_{\max}} f_M(M)} = 1 - \frac{\int_{M_{\min}}^{M_{\max}} B_S(M)}{\int_{M_{\min}}^{M_{\max}} f_M(M)}, \quad (6.4)$$

where the integration limits are based on the minimum and maximum allowed invariant mass of the Λ candidates, which in the present analysis are located at $\pm 4 \text{ MeV}/c^2$ around the nominal Λ mass of $M_{\Lambda, \text{pdg}} = 1115.683 \text{ MeV}/c^2$. The systematic variations includes the usage of only 2 Gaussians in the signal, i.e. setting $\mathcal{A}_3 = 0$. The fit range is extended to $M \in [1088, 1144] \text{ MeV}/c^2$ in order to obtain a more stable and accurate description of the background function. Further, to insure a smooth behaviour of the background underneath the peak region, the nodes of the splines are placed at least $10 \text{ MeV}/c^2$ away from it. A total of 8 spline nodes

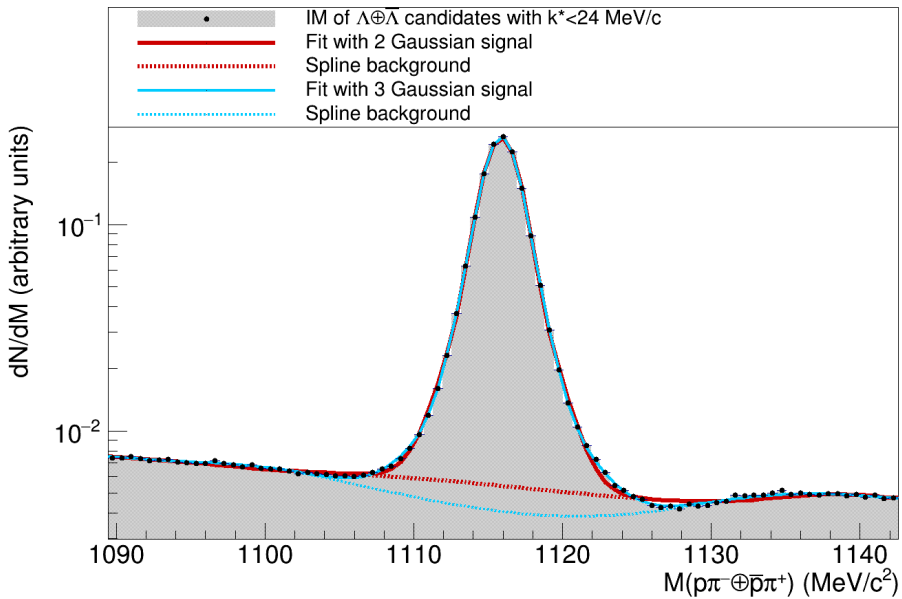


FIGURE 6.4: Invariant mass of Λ candidates with k^* below 24 MeV/ c , and the corresponding fits using the sum of 2 (red) or 3 (blue) Gaussians to model the signal.

are used, located at $M = 1116 \pm (10 + 6n)$ MeV/ c^2 with $n \in \{0, 1, 2, 3\}$. An example of a single fit, for $k^* \in [0, 24]$ MeV/ c , is shown in Fig. 6.4. The resulting purity, as a function of k^* , is presented in Fig. 6.5. Clearly, at low k^* the purity remains rather constant, where the values averaged below k^* of 480 MeV/ c are 95.3% for the 2-Gaussian signal and 96.3% for the 3-Gaussian case. These results are consistent with the single particle analysis (96.0%), nevertheless it is evident that there is a significant systematic uncertainty of c.a. 1%, which is now considered and will be propagated to the later stages of the analysis.

With the issue on the purity solved, we can now return to the problem of obtaining $C_{\text{misid}}(k^*)$. The definition, according to Eq. 3.28, requires the measurement of the left and right sideband correlation functions ($C_{\text{misid},\text{left}}(k^*)$, $C_{\text{misid},\text{right}}(k^*)$), achieved by sampling fake Λ candidates at values smaller or larger than the position of the Λ peak on the IM spectrum. Ideally, $C_{\text{misid}} \approx C_{\text{misid},\text{left}}(k^*) \approx C_{\text{misid},\text{right}}(k^*)$. However, in reality the reconstructed sideband correlations show substantial differences depending on the selected range (Fig. 6.6). There are two main issues, on one hand the left and right sidebands differ from one another, on the other hand each sideband function depends on the selected invariant mass interval, implying an overall instability of the method. The latter is addressed by selecting only a narrow window of invariant mass range, situated as close as possible to the Λ peak². The final choice for the invariant mass windows are $M \in [1095, 1108]$ MeV/ c^2 for the left sideband and $M \in [1124, 1135]$ MeV/ c^2 for the right one. At this point no systematic uncertainty is assigned, as the ranges are tuned to provide the most accurate estimate of the sidebands, and any further variations will result in a larger discrepancy to the unknown true solution, which is supposedly given by the correctly weighted sum of the two sidebands. Thus the systematic uncertainties will be integrated into the weight parameter $\omega_{\text{left}} = 1 - \omega_{\text{right}}$ (Eq. 3.28), which is, by construction, the relative

²Further quality assessments were performed, to guarantee that the selected intervals are close to the peak region, without being significantly biased by the true $p-\Lambda$ signal.

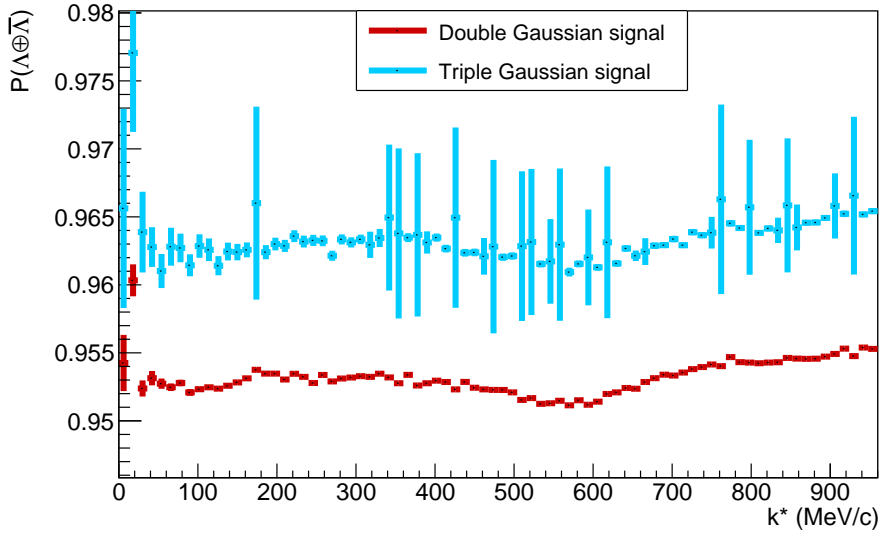


FIGURE 6.5: Purity of the Λ candidates as a function of k^* , depending on the fit hypotheses. The uncertainties are estimated using a Bootstrap method, where for the assumption of a triple Gaussian signal there are often some instabilities, however it was verified they can be reduced by making the binning in k^* coarser and do not influence the final result.

amount of background stemming from the left sideband. Hence it is defined as the ratio of the integrals of the background function $B_S(M)$ evaluated in different mass intervals

$$\frac{\omega_{\text{left}}}{1 - \omega_{\text{left}}} = \frac{\int_{L_{\min}}^{L_{\max}} B_S(M)}{\int_{R_{\min}}^{R_{\max}} B_S(M)}, \quad (6.5)$$

where the integration limits $L(R)$ correspond to the left (right) sideband. The systematic uncertainties are based on two different assumption. First, $(L(R)_{\min}, L(R)_{\max})$ are considered to correspond to the intervals from which the left/right sidebands are built, i.e. $(L_{\min}, L_{\max}) = (1095, 1108) \text{ MeV}/c^2$ and $(R_{\min}, R_{\max}) = (1124, 1135) \text{ MeV}/c^2$. Second, since the sideband signal has to be extrapolated to the Λ peak region, the integration limits can be selected as the left-/right part of the IM range $(M_{\Lambda, \text{pdg}} \pm 4 \text{ MeV}/c^2)$ used for the reconstruction of the true Λ candidates, just as for the determination of the purity (Eq. 6.6). This leads to $(L_{\min}, L_{\max}) = (M_{\min}, M_{\Lambda, \text{pdg}})$ and $(R_{\min}, R_{\max}) = (M_{\Lambda, \text{pdg}}, M_{\max})$. The resulting ω_{left} parameters also depend on the choice of the signal function for the fit of the invariant mass, leading to a total of 4 different systematic variations, summarized in Table 6.2. The resulting $C_{\text{misid}}(k^*)$ is plotted in Fig. 6.7. Finally, $C_{\text{pure}}(k^*)$ is evaluated based on Eq. 3.29, where the systematic uncertainties include independent all 4 variations presented in Table 6.2, with the purity variation being applied to λ_{pure} as well. As discussed in chapter 3.5.2, the systematic uncertainties of the reconstruction procedure results in 45 different cut variations, each yielding a unique $C_{\text{pure}}(k^*)$ ³, implying that after the sideband correction there are 180 instances of $C_{\text{pure}}(k^*)$ to sample from for the systematic uncertainties. Figure 6.8 shows the effect of the purity correction, that leads to a statistically significant modification at the intermediate

³Strictly speaking, there are also 45 different sidebands, however due to limitations in the computing resources $C_{\text{misid}}(k^*)$ is assumed independent on the applied cuts.

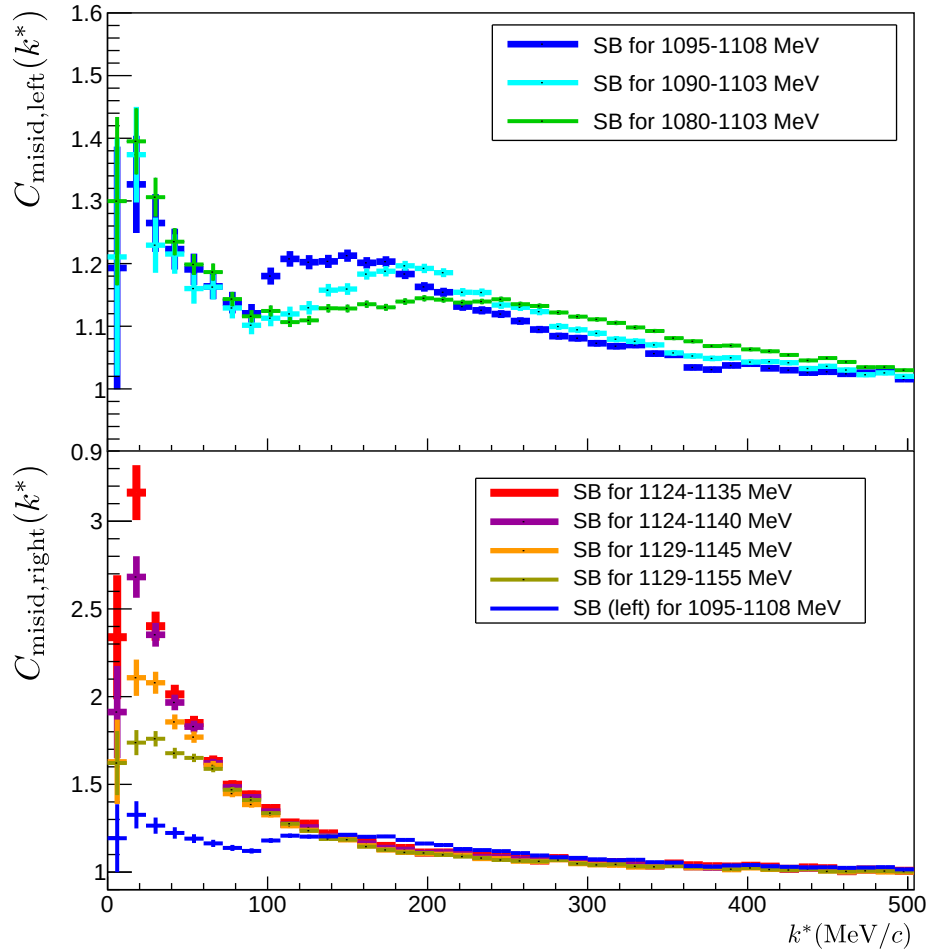


FIGURE 6.6: Sideband correlations for $p-\Lambda$. The normalization is performed for $k^* \in [600, 900]$ MeV/c, as the functional shape becomes flat in this region. The final selection corresponds to the blue points (left sideband) and red points (right sideband).

	Double Gaussian	Triple Gaussian
Peak region	52.0%	52.9%
Outside peak	55.4%	57.4%

TABLE 6.2: The weight of the left sideband to the total yield of the background, extracted for different fit hypotheses. The columns represent the different parameterization of the signal, while each row represents a different integration region used to evaluate these ratios (see the text).

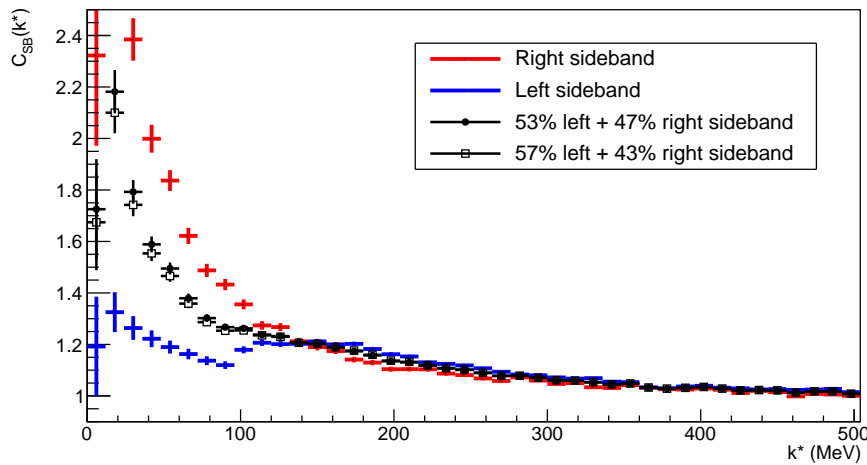


FIGURE 6.7: Comparison of the different linear combinations of right and left sidebands with the two extracted weights corresponding to the IM fit using a triple Gaussian. The systematic deviations are quite small, and the differences due to using a double Gaussian (not plotted here) are even less pronounced.

k^* region.

6.2.4 Unfolding

The big impact of the recent femtoscopy analyses on the theoretical constraints in various systems demonstrated one small inconvenience in the presentation of the results. Namely, to account for the effect of detector resolution the correlation function has to be smeared by a matrix (chapter 2.7.3). Thus to allow the use of the data outside of the ALICE collaboration, for each published correlation function a supplementary material is needed to include the corresponding momentum smearing matrix. This adds an additional layer of complexity in interpreting the data quantitatively, which can, however, be avoided by performing an unfolding procedure.

The main issue with unfolding, is that mathematically it translates to obtaining the inverse of the smearing matrix. However, as e.g. seen in Fig. 2.11, the experimental matrix has no fixed analytical form and it is not smooth due to the statistical noise. Thus obtaining the inverse smearing matrix is not possible. There are many numerical methods to address this issue, however they are often depending on the properties of the studied functions and their smearing matrices, making it rather challenging to fine-tune them to the specific analysis. For this reason, and since the studied correlation function has a relatively small number of bins, a different strategy was employed for the p - Λ analysis, namely a brute-force method. The idea is to make a reasonable guess for the true unfolded distribution $C_{\text{unfold}}(k^*)$ and apply the momentum smearing on it to obtain the corresponding $C_{\text{fold}}(k^*)$, which should ideally be equal to $C_{\text{pure}}(k^*)$ ⁴. A good initial guess will result in small deviations between $C_{\text{fold}}(k^*)$ and $C_{\text{pure}}(k^*)$, that can be accounted for by bootstrapping $C_{\text{unfold}}(k^*)$ and reevaluating $C_{\text{fold}}(k^*)$ until it matches $C_{\text{pure}}(k^*)$ within a desired precision. The bootstrap has to be slightly modified in order to result in a converging behaviour. This

⁴Note that the sideband correction is much more easy to apply to the raw experimental data, thus the unfolding procedure has to be performed after correcting the correlation function.

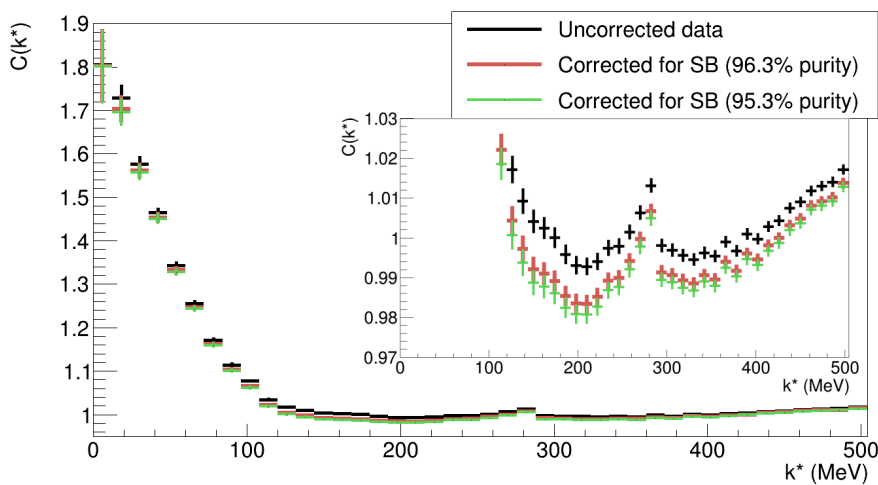


FIGURE 6.8: Corrected experimental correlation function for the two different purities. The systematic uncertainties are omitted for visual purposes. To gauge better on the relative behaviour of the correlation functions, the femtoscopic re-normalization is determined only for the uncorrected set, and the same factor is applied to the rest.

is done by monitoring the best achieved agreement (based on χ^2) between $C_{\text{fold}}(k^*)$ and $C_{\text{pure}}(k^*)$, and updating $C_{\text{unfold}}(k^*)$ each time when χ^2 is reduced. The computation is cut-off after a time-limit on the CPU, chosen such that the obtained χ^2_{ndf} is around 0.2. Note, that a value of 1 would imply that the unfolding procedure acts as a good fit model, but this is not enough since the true solution certainly exists and contains all statistical fluctuations observed in $C_{\text{pure}}(k^*)$, this having a χ^2_{ndf} much lower than 1 is a necessity⁵. Unfortunately, the obtained solution does not have any associated uncertainty, but thus can be addressed by applying the bootstrap method to the initial reference sample $C_{\text{pure}}(k^*)$ and redoing the whole procedure. The obvious disadvantage of this workflow is that it requires the use of two nested bootstraps, translating into a (brute force)² computing requirements, which can create a big bottleneck based on the available computing resources. This is further complicated by the need to unfold all of the 180 correlation functions corresponding to the different cut and sideband variations. For the present analysis the local computing cluster available to our group, containing c.a. 500 CPUs, was capable of performing the unfolding within several hours.

The effect of the unfolding is expected to be quite small and only relevant in the first few bins of the p – Λ correlation function, due to the observation that the smearing of the theoretical function has these properties. For that reason a good choice of an initial $C_{\text{unfold}}(k^*)$ can be made by simply using the measured $C_{\text{pure}}(k^*)$. To make the convergence faster, a spline function $C_{\text{spline}}(k^*)$ is adopted to model $C_{\text{unfold}}(k^*)$ and using it as a theoretical model for the correlation function within the CATS framework. Then $C_{\text{unfold}}(k^*)$ is fitted to describe the experimental to $C_{\text{pure}}(k^*)$, using the standard procedure involving momentum smearing. In this way the resulting $C_{\text{spline}}(k^*)$ provides a solution that is very close to the true unfolded correlation, nevertheless the splines smooth the solution too much, hence the statistical fluctuations are not fully propagated. The typical χ^2 of the fit is indeed just below one.

⁵Further analysis based on the p -value and the number of data points confirmed that in this study the unfolding procedure can be considered successful for values of $\chi^2_{\text{ndf}} < 0.5$.

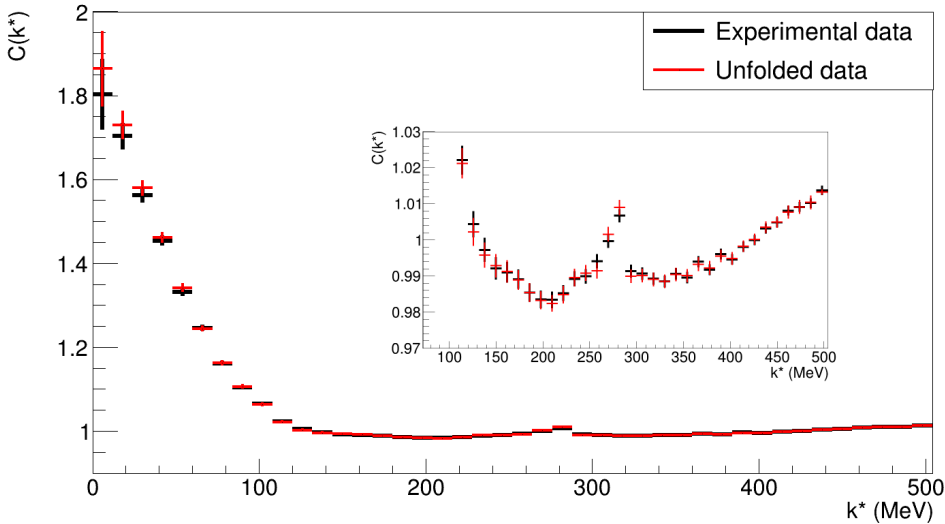


FIGURE 6.9: The effect of the unfolding is very mild, mostly consisting of a small systematic enhancement in the first 3 bins.

However, if this function is used in the doubly iterative procedure described above, it converges rather fast towards the desired precision of $\chi^2 \approx 0.2$.

An example of one unfolded correlation function, without systematic uncertainties, is shown in Fig. 6.9. As expected, the effect is quite small and only relevant at very small k^* . The same holds for the statistical uncertainties, which are increased by an negligible amount.

6.2.5 Data modelling

The theory to be tested by the ALICE data is the χ EFT calculation of the $N\Sigma \leftrightarrow N\Lambda$ system, where by default the NLO19 version with a cutoff scale of 600 MeV is used for both the $p\text{-}\Lambda$ and $p\text{-}\Sigma^0$ wave functions, the latter being relevant for the feed-down. The main questions to address are if the theory is capable of describing the data well, and study the sensitivity of the data to the different versions (NLO19, NLO13 and LO) of χ EFT for the $p\text{-}\Lambda$ channel and to the different cutoff scales (500, 550, 600 and 650 MeV). Any deviations in the $p\text{-}\Sigma^0$ residual correlations will not be resolved by the data for sure, thus not tested, however one extreme case will be investigated. It will be assumed that the $p\Sigma^0$ interaction is weaker than predicted, resulting in a completely flat correlation function. The goal is to see if the data has the sensitivity to discriminate large inaccuracies in the determination of $p\text{-}\Sigma^0$, which could occur in the theory due to the essentially non-existing experimental constraints for this system. Further, the strength of the coupling $N\Sigma \leftrightarrow N\Lambda$ can be tested by the cusp structure at $k^* = 289 \text{ MeV}/c$, corresponding to the threshold of this channel. As already discussed, this amplitude also depends on the $\Sigma^0\text{:}\Lambda$ ratio, which is expected to be 0.33 ± 0.07 , where the theoretical predictions suggest a value closer to the upper limit of 0.4.

The non-femtoscopic baseline present in Eq. 6.1 is modeled as described in chapter 3.4.2, where the parameterization is based on Eq. 3.38 using a 3-rd order polynomial, resulting in

$$b(k^*) = \mathcal{N} (1 + p_2 k^{*2} + p_3 k^{*3}). \quad (6.6)$$

As a reminder, this function is motivated by the requirement of a flat baseline at $k^* = 0$ and as the MC data can be successfully modeled by such function. To constrain the baseline better, it has been fitted up to $k^* = 456 \text{ MeV}/c$, with systematic variations of this limit to 432 and 480 MeV/c .

The final fit is performed using Eq. 6.1, where by now we have determined all of the input, apart from the baseline which contains 3 free fit parameters. Following the discussion in chapter 3.5.2, the systematic uncertainties are evaluated by fitting the data multiple times, each with different systematic variations. To obtain the full uncertainties, the bootstrap procedure has been included. To evaluate the χ^2 the bootstrap was switched off, as it introduces a bias to the χ^2_{ndf} of up to 1 (see chapter). Importantly, all variations of the physics observables are considered as different hypotheses, and the final χ^2_{ndf} correspond to the average value of the best hypothesis. The observables in question are the source radius, Λ purity, $\Sigma^0:\Lambda$ ratio and the $\Xi : (\Lambda + \Sigma^0)$ ratio. The different hypotheses related to the $p\text{-}\Lambda$ and $p\text{-}\Sigma^0$ models are the direct subject of this study, as such they have been analyzed independently from one another.

6.3 Results

The final results of the $p\text{-}\Lambda$ analysis are summarized by Fig. 6.10 and 6.11. The upper and middle panels of the figures show the fully corrected and unfolded data, fitted by Eq. 6.1 using different hypothesis for the interaction. The red band corresponds to the obtained $C_{\text{pure}}(k^*)$, the gray band is the baseline $b(k^*)$, while the orange and cyan bands correspond to the contributions of the residual $p\text{-}\Sigma^0$ and $p\text{-}\Xi$ correlation with respect to the baseline⁶. The width of the bands represent the total uncertainty of the fit. The middle panels are zoomed on the y -axis in order to better visualize the $N\Sigma \leftrightarrow N\Lambda$ cusp. The lower panels correspond to the deviation between the fit and the data as a function of k^* . Since the baseline function has only slight deviations from a flat function for k^* below 300 MeV/c , which is in agreement with the MC data (Fig. 3.17), an additional systematic check was performed by fitting the $p\text{-}\Lambda$ correlation only up to k^* of 336 MeV/c using a flat baseline function ($p_2 = p_3 = 0$). Table 6.3 shows the χ^2_{ndf} values in the range $k^* \in [0, 300] \text{ MeV}/c$ corresponding to each fit, where the default values correspond to the standard baseline and the values in brackets are based on the flat baseline. The different columns represent the two assumptions on the $p\text{-}\Sigma^0$ residual, while the different rows correspond to the different variations of the χ^2 EFT used to model the $p\text{-}\Lambda$ interaction. A careful examination of these results reveals several interesting patterns. First, the baseline hypothesis does not significantly change the ordering of the obtained χ^2 , implying that any physics conclusions based on the relative comparisons of the physics models are solid. Concentrating on the different $p\text{-}\Lambda$ models, the noticeable pattern is that, independently on the assumed $p\text{-}\Sigma^0$ residual, the χ^2 decreases in the order LO, NLO13, NLO19, with the latter providing the best χ^2 for the case of a cutoff scale at 600 MeV. The LO, which is incompatible to the existing scattering data, is completely excluded, mostly as it fails to describe the coupling effect. However, while the NLO13 and NLO19 provide similar level of agreement, there is a systematic preference towards

⁶This means the plotted curves correspond to Eq. 6.1 with the assumption that the only non-flat correlation function is either $C_{p(\Sigma^0)}(k^*)$ or $C_{p(\Xi)}(k^*)$. For the former it means $C_{\text{plot}}(k^*) = b(k^*) \left[\lambda_{p(\Sigma^0)}(C_{p(\Sigma^0)}(k^*) - 1) + 1 \right]$ and analogous for the latter.

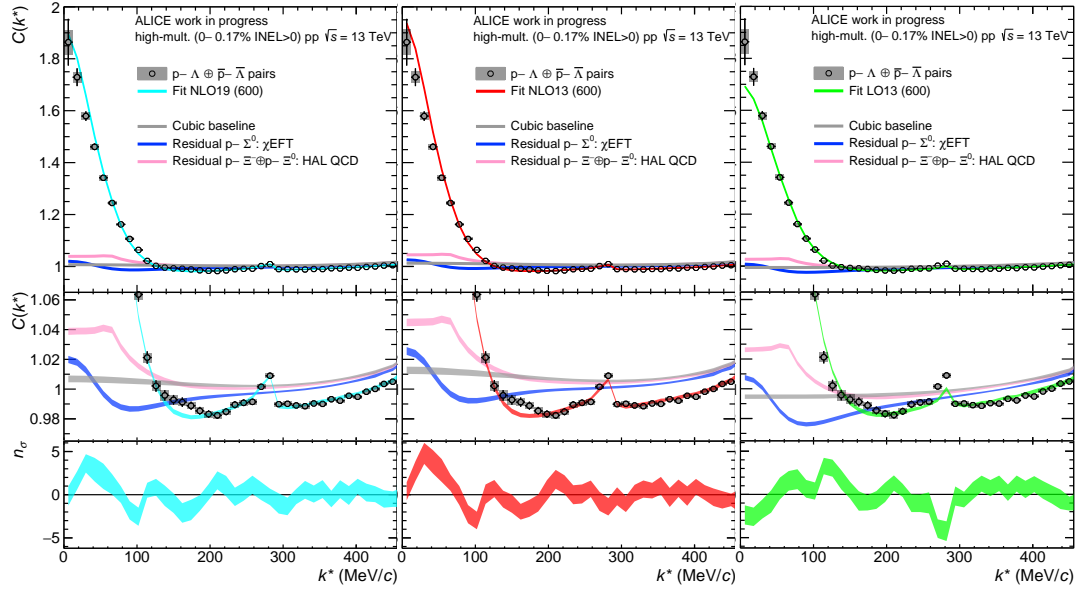


FIGURE 6.10: The $p\text{-}\Lambda$ correlation function, sideband corrected and unfolded, and the corresponding fit results for the different $p\Lambda$ predictions of χ EFT. From left to right these are the NLO19, NLO13 and LO calculations, all performed at a cutoff energy of 600 MeV. The $p\Sigma$ interaction is modeled by the NLO19 in all cases.

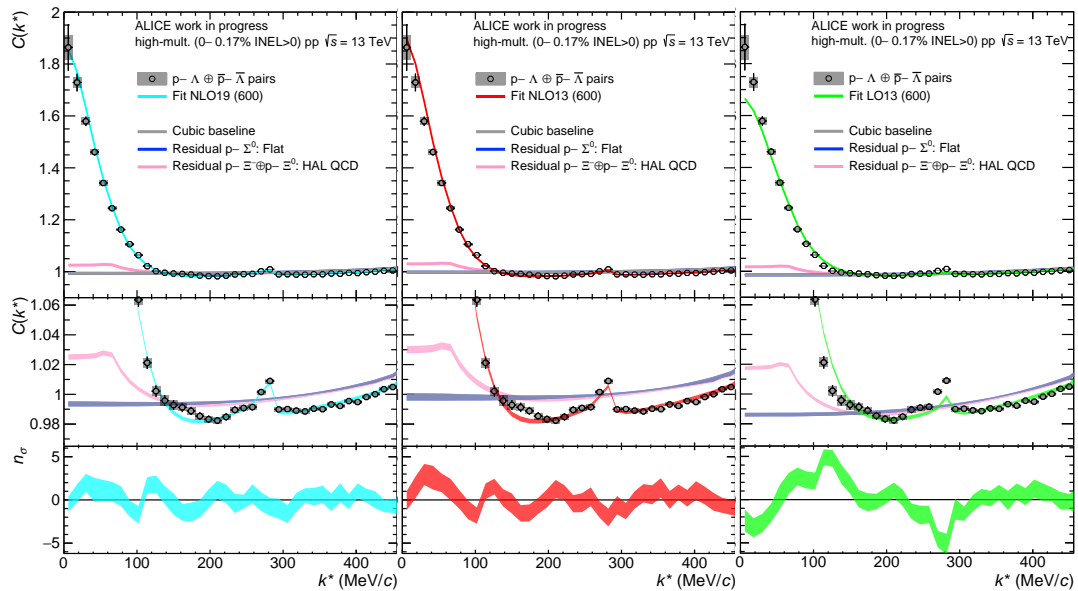


FIGURE 6.11: The $p\text{-}\Lambda$ correlation function, sideband corrected and unfolded, and the corresponding fit results for the different $p\Lambda$ predictions of χ EFT. From left to right these are the NLO19, NLO13 and LO calculations, all performed at a cutoff energy of 600 MeV. The $p\text{-}\Sigma^0$ correlation is assumed flat in all cases.

$p\text{-}\Sigma^0$ (\rightarrow) $p\text{-}\Lambda$ (\downarrow)	$\chi^2\text{EFT}$	Flat
LO13-600	3.4 (4.7)	7.0 (9.9)
NLO13-500	4.6 (7.4)	2.8 (3.2)
NLO13-550	2.7 (3.9)	1.6 (1.6)
NLO13-600	3.5 (3.5)	2.1 (2.2)
NLO13-650	3.3 (3.3)	2.6 (3.0)
NLO19-500	3.4 (4.4)	2.0 (2.0)
NLO19-550	2.7 (2.6)	1.4 (1.6)
NLO19-600	2.3 (2.4)	1.3 (2.0)
NLO19-650	2.3 (2.3)	1.7 (2.5)

TABLE 6.3: Values of χ^2/NDF for the different interaction hypotheses of $p\text{-}\Lambda$ and $p\text{-}\Sigma^0$, evaluated for $k^* \in [0, 300]$ MeV. The default values correspond to the fit with a cubic baseline and the values in brackets represent the results from using a constant baseline. The default model (in bold) is the $\chi^2\text{EFT}$ NLO19 calculation, at a cutoff parameter of 600 MeV.

NLO19, something that was not possible to observe based on the available scattering data [21]. Discriminating between these two models is important, as the different strength of the $\text{N}\Sigma \leftrightarrow \text{N}\Lambda$ coupling influences the the balance between the 2 and 3 body forces required to explain hypernuclei results. This is relevant for the study of dense matter (neutron stars), and while both NLO13 and NLO19 give similar predictions for the EoS under the consideration of both 2 and 3 body interaction, the NLO19 results in a much softer genuine 2 body EoS, requiring more repulsion from the 3-body sector. Finally, comparing the two $p\text{-}\Sigma^0$ hypotheses, it is evident that assuming an approximately flat residual signal results in a substantial improvement in the fit, highlighting the sensitivity of the present data to the genuine $p\text{-}\Sigma^0$ correlation function, in addition to the genuine $p\text{-}\Lambda$ signal and the $\text{N}\Sigma \leftrightarrow \text{N}\Lambda$ coupling. Nevertheless, since all these contributions to the correlation function are highly correlated in the fit function, it is difficult to disentangle them in a model independent way. In fact, based on the deviation plots seen in the lower panels of Fig. 6.10 and 6.11, one can understand that the better description of the data with the flat $p\text{-}\Sigma^0$ correlation is due to the improved χ^2 at low relative momentum ($k^* < 100$ MeV/c), which could also be achieved by other effects. For example, a slightly weaker attraction in the $p\text{-}\Lambda$ channel, in particular in the S=1 channel as it has the largest contribution (3/4) to the signal, would lead to a slightly reduced strength of $C(k^*)$ precisely in that k^* region, providing an alternative explanation of the deviation. Should this be true, it is likely that the hypernuclei results will require even stronger repulsion for the 3-body interaction. It would be thus best to use the present data as a direct constrain for the theoretical calculations. This of course has to be done by theoreticians outside of the ALICE collaboration, as we remain excited about the future results and interpretations of our data.

In addition, it is interesting to note that the best fit hypothesis has a strong preference towards a $\Sigma^0\text{:}\Lambda$ ratio of 0.4, which is inline with the predictions from theory and recent ALICE preliminary results on the subject [75, 77]. The amount of secondary Ξ s is expected to be the upper limit of 27.0%, as suggested by the k^* dependence of the template fits for the Λ (Fig. 3.15), and this is indeed confirmed by the fit.

Consequently, the lower value for the genuine $\lambda_{p\Lambda}$ of 42.7% is resulting in the best description of the data. Further, the upper limit of $r_{\text{core}} = 1.06$ fm is consistently providing better fit results, a fact which will be further discussed below. Regarding the purity, the fit seems incapable of discriminating between the two cases of 95.3% or 96.3%, although a slight tendency towards the latter, which corresponds to the better fits of the invariant mass spectrum, is present. These considerations imply that the best fit hypotheses of the fits are physically meaningful, giving further confidence on the quality of the data and the corresponding fit procedure.

However, there is one big caveat to address, namely the effects other than the strong interaction, that can provide explanation to the observed discrepancy at low k^* . For that let us assume the chiral effective field theory is completely accurate, and pose the question what can cause similar modification of $C(k^*)$. Two obvious candidates are the λ parameters and the source function. In the present work a lot of effort went into the investigation of the associated systematic uncertainties. Regarding the λ parameters, a better fit can be obtained by lowering the value of the genuine $p\text{-}\Lambda$ contribution, however at present the systematic uncertainties already include very conservative variations of all known parameters capable of reducing $\lambda_{p\Lambda}$. Moreover, the systematic variation of the CPA (from 0.99 to 0.995) is large enough to increase the amount of Λ primaries and the Λ purity by a statistically significant amount, making the genuine amount of $p\text{-}\Lambda$ higher in the data. This would enhance the experimental correlation function, leading to a better fit to the theoretical model⁷. In that sense the larger CPA variation is a very conservative choice, but still this discrepancy persists, excluding the λ parameters as a possible explanation. Regarding the source function, the constraints obtained from the $p\text{-}p$ correlation assume an uncertainty corresponding to 3σ of the statistical error, given that the standard uncertainty corresponds to 1σ . This is done so, as the resonance source model has not been verified in systems other than $p\text{-}\Lambda$ itself, which obviously biases the study of the interaction, and the increased uncertainty allows to reach the best $r_{\text{core}} = 1.06$ fm obtained by fitting the $p\text{-}\Lambda$ using χEFT . For this reason it is impossible to improve the fit by further variations of the source size. Nevertheless, a profile of the core source different than a Gaussian will modify the shape of the correlation function as well. A non-Gaussian core can be related to the hadronization process, as it is possible to describe random processes with of large discrete steps by a Lévy flight (see chapter 4). This leads to an emission profile of a transitional shape between a Cauchy ($\alpha = 1$) and a Gaussian distribution ($\alpha = 2$). Such an emission profile will have a larger tail, that acts approximately as having more flat signal to the correlation and has similar effect⁸ as the reduction of the $\lambda_{p\Lambda}$ parameter. The Lévy scenario has been investigated in this work, by fitting the r_{core} from the $p\text{-}p$ and $p\text{-}\Lambda$ correlation functions scanning over the stability parameter α . This study revealed that the $p\text{-}\Lambda$ can be better described by a pure Cauchy distribution ($\alpha = 1$), however the $p\text{-}p$ correlation was incompatible with $\alpha < 1.5$ and the best solution was provided for $\alpha > 1.7$. As there is no physics motivated reasoning to explain a completely different profile of the emission source for $p\text{-}p$ and $p\text{-}\Lambda$, and the interaction of the former is much better constrained, it was concluded that an $\alpha = 1$ is a nonphysical solution, and hence the Lévy parameterization cannot be used to model the low k^* behaviour

⁷If the experimental correlation has larger genuine $p\text{-}\Lambda$ contribution than used by the fit, this is similar to fitting the default correlation function by applying lower $\lambda_{p\Lambda}$ parameters onto the fit function.

⁸It should be mentioned, that the Lévy source changes both the width and amplitude of the femtoscopic signal, nevertheless both modify the small k^* region.

of the $p\text{--}\Lambda$ correlation function. An additional caveat, that has not been investigated explicitly, is the effect of the Lorentz boost onto the source function when changing the system from the laboratory frame to the pair center of mass frame. Still, it was verified that for the EPOS source function, for which both the $p\text{--}p$ and $p\text{--}\Lambda$ pairs can be modeled reasonably well by a Lévy distribution, the change of the coordinate system leads to an increased α parameter, making the source for $p\text{--}p$ and $p\text{--}\Lambda$ closer to a Gaussian in the pair center of mass frame. Thus, it was concluded that the effect of Lorentz boost can be ignored. Finally, the shape of the correlation function is influenced by the non-femtoscopic baseline, however this is already modeled by a very “flexible” function, and its effect tends not to be localized only at low k^* , but rather spread across the whole correlation function, resulting in a smooth behaviour over any narrow k^* window. For this reason the non-femtoscopic effects are not a suitable explanation of the localized modification for $k^* < 100 \text{ MeV}/c$. Having performed all these checks, it is safe to claim that the non-perfect χ^2 of the fit to the $p\text{--}\Lambda$ correlation function is related to the modelling of the strong final state interaction.

In conclusion, the ALICE $p\text{--}\Lambda$ correlation function measured in high-multiplicity triggered pp collisions at 13 TeV provides the most precise measurement of this system up to date. The result is a convolution of both $p\text{--}\Lambda$ spin channels, the genuine $p\text{--}\Sigma^0$ correlation due to the feed-down effects, and the $N\Sigma \leftrightarrow N\Lambda$ coupled channel. This makes any conclusions model dependent, and the state of the art χ EFT calculations were employed to model the strong interaction. The general description of the data is quite good, in particular around the kinematic cusp corresponding to the opening of the $N\Sigma$ channel, nevertheless at low k^* a slight systematic discrepancy in the slope of the correlation is observed. It was demonstrated that the $p\text{--}\Sigma^0$ residual correlation, which is not well constrained experimentally, has a strong effect on the correlation function exactly in that region, and if a weaker $p\Sigma$ interaction is assumed the quality of the fit improves. This is not a unique explanation, alternatively an over-prediction of the $p\Lambda$ interaction strength can cause a similar effect. Regardless of the underlying reason for the deviation, the most important message is that the data itself is driving the study of the nucleon–hyperon system into a precision era, where the major uncertainties are related to the systematic bias of the λ parameters, the non-femtoscopic baseline and the modelling of the source function. Arguably, the latter is the least well understood, as it relies on the effectiveness of the resonance source model, that is yet to be better constrained by studying the baryon–meson and meson–meson correlations. Nevertheless, multiple systematic cross-checks were performed on all known possible pitfalls, and there were no hints about a viable explanation of the low k^* behaviour of the $p\text{--}\Lambda$ correlation function, leading to the conclusion that the dominant effect has to be traced back the strong interaction of the $N\Sigma \leftrightarrow N\Lambda$ system. As such, the present data provide a valuable new constraint for the theoretical models to consider in the future, allowing to construct a more realistic nuclear equation of state and relate to the study of neutron stars.

Personal remarks

I consider this chapter, devoted to the study of the $p\Lambda$ interaction, as the most important result of this thesis due to its obvious interconnection to other fields in physics. It also took the longest time to analyze, due to the complexity of the systematic uncertainties, leading to the “casual” intermediate study of the emission source and the subsequent publication in PLB. I would like to express my sincere gratitude to the people directly involved in this study, which are my official supervisor Laura

Fabbietti, my unofficial supervisor Valentina Mantovani Sarti and the main author of the χ EFT Johann Haidenbauer.

I happened to know that Laura had a large interest in the $p\Lambda$ interaction, that triggered her to initiate all femtoscopic activities in our group. I am very thankful that she put her trust in me to lead the analysis of this system, and I am very thankful for her never-ending determination, inspiration and patience that lead this study to an successful end, revealing many interesting physics effects on the way.

On the other hand, Valentina (Vale) earned her nickname “grandma” in our group for a good reason, as she has been the one person to which everyone, myself in particular, went to seek comfort in the most difficult moments, and Vale always found the strength to provide support both as a professional and as a friend, keeping a spark alive in the dark!

Finally, a good analysis requires a good theory. As discussed, the $p-\Lambda$ data set is essentially impossible to analyse in a model-independent way, thus any conclusions had to be based on a solid theoretical basis. The χ EFT theory is the best tool to study the $p\Lambda$ interaction, in particular as it includes the coupled channel dynamics. The close collaboration with Johann resulted in many interesting discussions, that helped us understand the physics of this channel to a much better level. Moreover, Johann provided privately all relevant wave functions, including their systematic variations, to include in our framework. Hence, all of the physics conclusions of this analysis are based on Johann’s work, for which it is needless to say I am personally extremely thankful, and hope that these results will be useful for his future work.

Chapter 7

Final remarks and outlook

The use of two particle correlations to study the strong final state interaction has proven to be a powerful tool when applied to small collision systems such as pp . The reason is the accurate determination of the emission source, based on the assumption of similar hadronization scale based on the underlying QCD principles, where the only additional effects stem from non-primordial particle production. The latter corresponds to strongly decaying resonances that produce the measured particles, introducing a slight offset in the emission compared to the primordial source. These effects have been studied and accounted for in a Monte-Carlo based procedure (chapter 4). In the scope of this work the CATS framework has been developed (chapter 2) and used, by me and colleagues, to analyze a multitude of particle pair species. The full list of published results consists of the CATS paper [39], the maiden study on non-traditional femtoscopy in small collision systems [38], the resonance source model [44] and the subsequent investigations of Λ - Λ , p - Σ^0 , p - Ξ^- , p - K^- , p - Ω^- [40–43, 45], while the analysis of p - Λ is finalized and the publication is under collaboration review. In the present work the Λ - Λ and p - Λ analyses have been described in details in chapters 5 and 6.

Many of these interesting results have not been described in the present work, but can be found under the corresponding references. Nevertheless, I have been directly or indirectly involved in all of them by participating in many interesting discussion with my colleagues. Thus a brief summary is presented in this section, alongside with an outlook based on my view on the most important femtoscopic studies to follow.

7.1 Proton–Kaon

The kaon is a meson containing one strange and an up or a down quark. The pK^+ interaction is reasonably well understood, the pK^- provides many interesting physics questions, as it couples to 5 other channels ($n\bar{K}^0$, $\pi^-\Sigma^+$, $\pi^0\Sigma^0$, $\pi^+\Sigma^-$ and $\pi^0\Lambda$). It is also thought to be linked to the generation of the quasi-bound state of $\Lambda(1405)$. As the $\Lambda(1405)$ resonance sits below the threshold of pK^- , it is not directly accessible by scattering experiments, and has to be constrained by theoretical models. Nevertheless, as in the case of the $p\Lambda$, the available data on pK^- is very limited at low momenta, and the coupling effects are unresolved. Nevertheless, there was a dedicated experiment (SIDDHARTA [128]) to study the interaction exactly at the threshold, which has been able to provide valuable constraints, however unable to study the complex nature of the coupled channels. On the other hand, the ALICE femtoscopic data has been able to resolve the coupling $pK^- \leftrightarrow n\bar{K}^0$ for the first time, and showed that the existing theoretical models do not describe the data (Fig. 7.1).

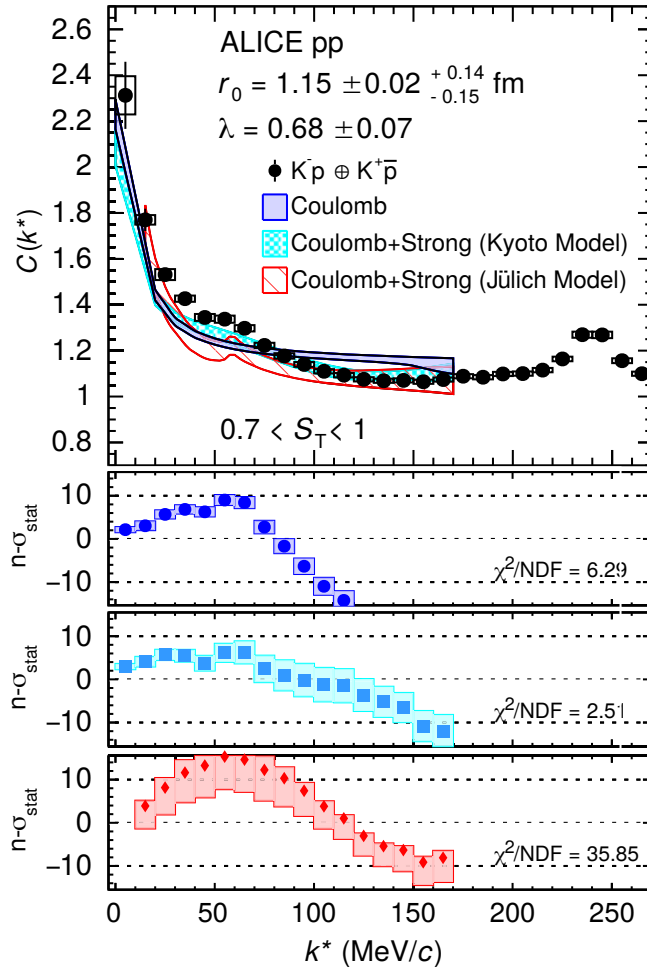


FIGURE 7.1: [43] Experimental $p\text{-}K^-$ correlation function. Combined result based on pp collisions at 5 TeV, 7 TeV and 13 TeV. The correlation is fitted only below k^* of 170 MeV/ c , to avoid interference with the peak corresponding to $\Lambda(1520)$. The step-like structure at $k^* = 58$ MeV/ c corresponds to the threshold of *coupling* to the $n\bar{K}^0$ channel. Both of the presented models are constrained by the SIDDHARTA data, but the Kyoto model did not include the mass difference between K^- and \bar{K}^0 , hence the coupling effect is not reproduced.

This analysis was performed by Ramona Lea and I have been included in the paper committee for the publication. The results were actively discussed with theoreticians, which responded fast by improving their “Kyoto” model to include the coupled channel effects, and showed that in this way the ALICE data can be reproduced (Fig. 7.2) [59]. Nevertheless, the reproduction of the data was only possible by using a smaller source than the experimental estimation. Further, the result shows a strong dependence towards the contribution of the $\pi\Sigma$ coupling, which could interfere with extraction of the source. Thus, the questions are now back to the experimentalists, as the source has to be further constraint. This is likely to be achieved by extending the resonance source model to the $p\text{-}K$ system. Further, theoretically the effect of the coupled channels diminishes rather quickly for large source sizes, as the modification of the wave function is only large at very small distances. For that reason, the ALICE collaboration is currently investigating the $p\text{-}K^-$ correlations in $p\text{-}Pb$ and $Pb\text{-}Pb$ collisions, with the final goal of making a scan over many different source sizes to provide the theory with much needed constraints on the range of these coupled channels. For the case of $Pb\text{-}Pb$ the expectation is to reach the asymptotic solution that can be described with the genuine $p\text{-}K^-$ scattering parameters only. These additional constraints would eventually make the extrapolation accuracy below the $p\text{-}K^-$ threshold better, and shed more light on the nature of the $\Lambda(1405)$.

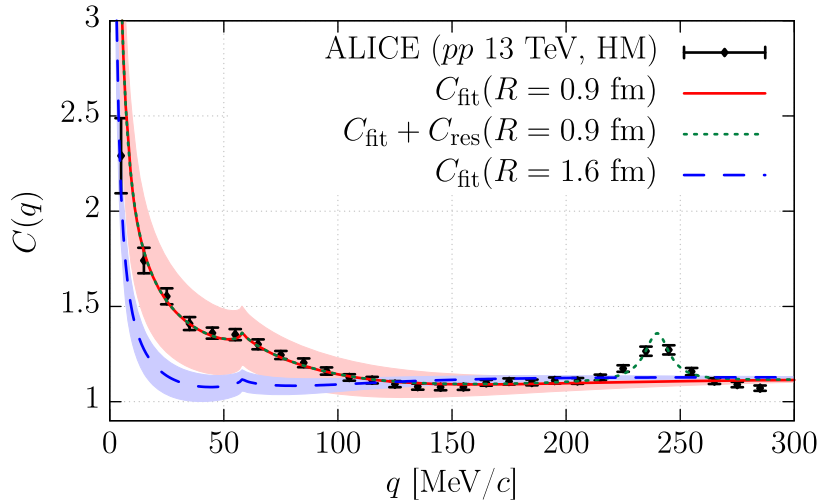


FIGURE 7.2: [59] Improved modelling of the p- K^- correlation function. The proper theoretical treatment of the coupled channels by the Kyoto model leads to a better description of the data, posing questions on the source size and the strength of the coupling to $\pi\Sigma$.

7.2 Proton- Ξ and proton- Ω

The p- Ξ^- and p- Ω^- systems¹ have been the perfect playground to test lattice computations, as these claim to provide rather accurate results in the multi strangeness sector. Moreover, the Ξ baryon is the heaviest particle though to play a potential role for the description of neutron stars, and the lattice prediction on the interaction of n Ξ suggests that the onset of Ξ^- particles inside the NS is not favoured [129]. The analysis of p- Ξ^- showed a very clear attractive interaction, which could be well described by the lattice prediction (Fig. 7.3). This is seen as the first direct observation of the

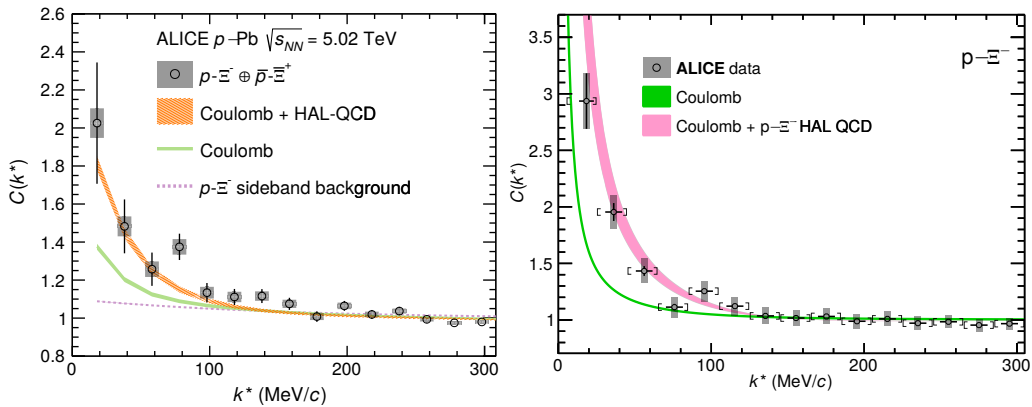


FIGURE 7.3: [40] Experimental p- Ξ^- correlation function extracted by ALICE. Left panel: in p-Pb collisions at 5.02 TeV, right panel: in pp collisions at 13 TeV triggered for HM.

p Ξ^- attraction and the first direct test of the lattice predictions for a multi strange system. Further, as discussed in the Λ - Λ section, it is believed that *bound states* of di-baryons should exist, and the latest lattice results suggest that a very shallow one could be formed by p Ω (E_B below 1.6 MeV/c) [130, 131]. However, due to the yet non-physical quark masses used in the calculations and the unknown character of

¹The Ξ^- consists of uss quarks, while the Ω is sss.

the spin 2 channel, experimental results are essential to draw any final conclusions. The corresponding analysis was seen as utmost pioneering, and consequently published in *Nature Physics* [45]. The result is shown in Fig. 7.4 where the theoretical predictions are based on the lattice calculations done by the HAL QCD collaboration [130]. So far a sign of a bound state was not seen, as it is expected to have a

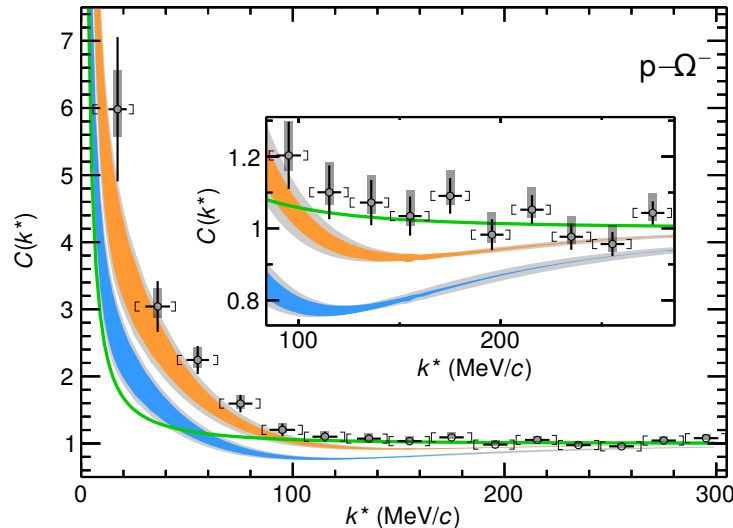


FIGURE 7.4: [45] Experimental $p-\Omega^-$ correlation function extracted by ALICE in pp collisions at 13 TeV triggered for HM. The colored bands represent different theoretical modelling, green is the Coulomb only case, orange and blue are the lattice result, depending on the treatment of the spin 1 channel, where the former assumes its identical as the spin 2 interaction and the latter includes a strong absorption due to the coupling to $\Xi\Lambda$.

signature dip at intermediate k^* values (Fig. 2.5). However, a very weakly bound state would have a correspondingly small dip, however as discussed in chapter 2.5 the best way to find a bound state, if it exists, is by performing an experimental scan over different source sizes, which could turn the dip into a genuine depletion of the correlation at larger source sizes. As a matter of fact, there is a chiral approach constrained to the lattice data, called the Sekihara model, that can be used to extrapolate down to the physical quark masses. It does result in a much lower binding energy (0.1 MeV), which could potentially explain the absence of a dip structure [131]. For these reason the next steps for the study of $p-\Omega^-$ is to investigate other collision systems, but as the statistical significance of the data is limited the follow up analyses are perhaps best suited for the LHC RUN3.

7.3 Proton- Σ

The $p-\Sigma^0$ has been often considered impossible to study via correlation techniques, as the Σ^0 decays into a Λ and a very soft (low momentum) photon, and the latter is very difficult to reconstruct experimentally. Thus, when my colleague Andreas Mathis took this system as the prime physics analysis for his thesis, I honestly thought he made a mistake. But he was fast to prove me wrong, as using the reconstruction of e^+e^- pairs related to photon convergence inside the detector material, he was able to extract the $p-\Sigma^0$ correlation function, and estimate the huge background using a sideband analysis [42]. The result is plotted in Fig. 7.5, and while it lacks the

statistical sharpness of the rest of the discussed analyses and cannot really discriminate between the different theoretical models, the mere fact that it was measured suggests that in the future, e.g. at RUN3, it could be possible to achieve a level of precision to provide the theory with constraints better than from scattering experiments (Fig. 1.6). Moreover, in chapter 6 it was discussed that the p- Λ system is

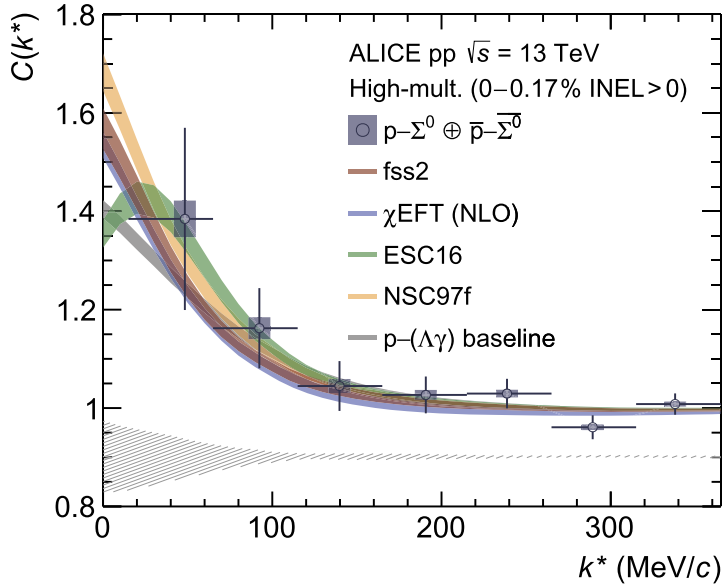


FIGURE 7.5: [42] Experimental p- Σ^0 correlation function extracted by ALICE in pp collisions at 13 TeV triggered for HM. The gray band represents the background extracted from a sideband analysis. The colored lines are the fits using several different interaction model, nevertheless at the moment it is not possible to separate between them.

sensitive to p- Σ^0 as well, both through the coupling and residual correlations, however it is extremely difficult to disentangle the multiple convoluted effects. As such, having a direct measurement of the p- Σ^0 channel will provide a very much needed differential information on the $N\Sigma \leftrightarrow N\Lambda$ system, that has been so far missing.

7.4 Outlook

There are further ongoing analysis at ALICE, which attempt to find further used cases for femtoscopy. One idea has been to combine it with studies related to coalescence models of light atomic nuclei, such as deuteron (pn) or ^3He (pd), as there are already theoretical links between the so called coalescence parameter (a measurable observable) and the the emission source of the hadrons building the nuclei [132]. E.g., the amount of produced deuterons has to be related to both the pd interaction and the pn emission source, which within the resonance source model is identical to the case of pp. Colleague Bhawani Singh is thus analysing the p-d correlation function, and already there are some interesting hints that the theoretical description of the interaction is incomplete. This study is extended by Stefan Heckel to perform a Λ -d analysis, as there are interesting theoretical predictions from J. Haidenbauer [133], suggesting an extremely strong attraction. This is relevant for both the better understanding of the spin dependence of the $N\Lambda$ interaction, as well as the *three-body* Λ NN forces, both of which are essential for the study of the EoS.

Another interesting project is lead by Valentina Mantovani Sarti, as she studies

baryon–antibaryon correlations in an attempt to access the coupled channel and annihilation dynamics for these systems. They are expected to be extremely relevant in many of these systems, nevertheless the theoretical work in that direction is very little, partially due to the lack of any data at low momenta. As such, femtoscopy is the only way to assess these effects, and is on the verge of providing yet another “first” result. This work is challenged by the presence of mini-jet background, that is currently treated mostly empirically, although if this pioneering analysis is successful it would demand the future investigation of the QCD related emission effects in further details.

The study of 2 body interactions by means of correlations has developed a lot in the last few years, and in many systems it reached the level of high precision (e.g. $p\text{-}\Lambda$). The main source of systematic uncertainties is currently related to the extraction of the λ parameters, the source function and the non-femtoscopic baseline. To obtain any new information from future studies, it would be important to investigate the hadronization process in further details, using advanced transport models such as AMPT (see the discussion in chapter 3.4). Such studies will go back in the direction of traditional femtoscopy, and could help to understand some of the fundamentals of the QCD, in particular the hadronization process in small collision systems and potentially the link to some of the similarities in HI collisions. The best suited system to perform such studies are $p\text{-}p$ and $p\text{-}\Lambda$, as the interaction is best constrained for these baryon–baryon pairs. Moreover, should the long-range effects of the correlation function are better understood, the non-traditional femtoscopy by means of baryon–antibaryon correlations will hugely benefit.

In my view, the Crown Jewels of femtoscopy is related to the study of 3-body correlations. The reason is that from an experimental perspective it would be much easier to perform compared to the reduction of the systematic uncertainties in the 2-body sector, where the only real bottleneck is the available statistics. Colleague Laura Šerkšnytė has gauged this issue using the HM $p\text{-}p$ collisions at 13 TeV, and the upshot is that even now there is a significant NNN and an “almost” significant $NN\Lambda$ signal. The latter will be no problem to investigate in RUN3, and if the ALICE collaboration allows for a dedicated $N\Lambda\Lambda$ trigger, an option that is under consideration, even that system could be measured. Given the discussion in chapter 1.4.3, this would be an incredible result for constraining the theoretical modelling of the 3-body forces, that are essential for an accurate EoS at large densities, and subsequently the description of neutron stars. I firmly believe that the hyperon puzzle could easily find its master and either be solved or promoted into a hyperon enigma, depending on if the results show a repulsive or an attractive 3-body force. Both cases would be extremely interesting, as the former would simply provide an elegant solution to the puzzle, while the latter would require many new theoretical ideas to be put forth, e.g. investigate the possibility of QCD phase transition into quark matter at relatively low densities, other sources of repulsion in the multi-body sector etc. In any case one thing is certain, namely that femtoscopy is the only experimental technique capable of investigating these effects with a minimalistic model dependence and with reasonable precision.

Appendix A

CATS tutorial

A.1 Overview

This chapter of the appendix, aims at providing more technical information regarding the CATS framework, and a lot of examples regarding the actual usage of CATS in term of coding. In the following sections, the following topics will be presented in that order:

- Basic use of CATS to evaluate the theoretical correlation function for simple source and interaction models.
- The CATS extensions, which provide utilities to apply momentum smearing onto the theoretical correlation, and include the effects of feed-down. Additionally, the predefined interaction potentials will be discussed.
- Suggestions for fitting experimental data with ROOT, using CATS to model the correlation function.
- Inclusion of external wave functions.
- Using the Monte-Carlo based source developed to model the universal core source including short-lived resonances.

One of the design goal of CATS is to use a minimal set of required packages, so that the framework can (almost) be used as a stand alone package. The only requirement of external libraries is the *GNU Scientific Library (GSL)* [52], which is used to evaluate the free wave solutions to the Schrödinger equation. For various applications of the CATS extensions, histogram classes are required. In order to avoid the requirement of a ROOT¹ installation [46], a custom made class called *DLM_Histo* is used instead. The main highlights of this class, is that it can be defined with any dimensionality, and evaluated not only at the bin center, but at any desired position. To achieve that a multidimensional linear interpolation is employed. This is particularly relevant for the input of external wave functions to model the interaction, as these are often provided with limited binning in k^* . The extrapolated result for the wave function is approximate, thus a very coarse initial binning could lead to uncontrolled systematic biases.

The C++ code examples are only limited to the sections relevant to the CATS framework, any further theoretical curves or plotting macros will not be shown here. *The units assumed by CATS are MeV and fm*. These units will be used for all examples, unless explicitly stated otherwise.

¹The standard analysis framework in high energy physics.

Some of the dependencies are also not shown, below a list of commonly used constants that will be used in the examples

```

1  const double Mass_pi0 = 134.9766;
2  const double Mass_pic = 139.57018;
3  const double Mass_Kch = 493.677;
4  const double Mass_K0 = 497.648;
5  const double Mass_p = 938.272;
6  const double Mass_L = 1115.683;
7  const double Mass_Xim = 1321.7;
8  const double MassOmega = 1672.45;
9
10 const double Pi(3.141592653589793);
11 //fine-structure constant (==e^2 in Gaussian units)
12 const double AlphaFS(0.0072973525664);
13 const double RevSqrt2(0.7071067811865475);
14 const std::complex<double> i(0,1);
15 const double EulerConst = 0.57721566490153;
16 //convert fm into natural units (1/MeV)
17 const double FmToNu(5.067731237e-3);
18 const double NuToFm(197.3269602);
19 const double RadToDeg(57.295779513082);
20 const double DegToRad(0.017453292519943);

```

The “Correlation Analysis Tool using the Schrödinger equation” is a C++ based framework, the purpose of which is evaluate the correlation function between a pair of particles, using the relation

$$C_{\text{th}}(k^*) = \int S(\vec{k}^*, \vec{r}^*) \left| \Psi(\vec{k}^*, \vec{r}^*) \right|^2 d^3 r^*. \quad (1.10)$$

The main design goal is to allow for a maximum customizability of the source function and the interaction leading to the wave function. For the source this is achieved by allowing to use as input any user-defined C++ function or class². The wave function is decomposed in partial waves, and the CATS allows to define multiple interaction channels (see section 2.3). For each channel and partial wave, there is a unique solution $u(k, r)$ describing the interaction, which in CATS can either be evaluated from a real local potential $V(r)$, or provided externally in discretized form. In the latter case $u(k, r)$ is allowed to be defined in the complex plane. The final correlation function is computed by

$$C_{\text{th}}(k^*) = \int S(\vec{k}^*, \vec{r}^*) \sum_{\text{channel}} w_{\text{channel}} \sum_l |\Psi_{k,l}(r^*)|^2 d^3 r^*, \quad (A.1)$$

where all individual channels are summed up with their corresponding weights w_{channel} and the total wave function computed from the individual partial waves. The details on the physics aspects of the computation are placed in chapter 2.

A.2 Simple source functions in π – π correlations

Let us move to exact C++ examples of code snippets representing the computation of different correlation functions. The focus here will be on the *set up the emission source*. In the example below, we will study how to use a *pointer to a user defined function* as an input. The function should be of the following type

```
1  double Function(double* Pars);
```

where “Pars” is an array containing information on the relative momentum k^* ($Pars[0]$), the relative distance between the particles r^* ($Pars[1]$) and the $\cos(\angle \vec{k}^*, \vec{r}^*)$

²Further details will be presented with the following examples.

r^* ($\text{Pars}[2]$) and any further parameters that might be required ($\text{Pars}[>2]$). The first 3 elements of this array are variables that are directly controlled by CATS, as such they should always correspond to the above definition. Any other elements are treated as *source parameters*, to which CATS has an interface with the help of the class “CATSparameters”. Objects of this type save the user-defined parameters and are used by CATS to store them. **N.B.** Since these parameters are placed in $\text{Pars}[>2]$, the 0–th parameter in “CATSparameters” corresponds to $\text{Pars}[3]$ and so on, i.e. there is a displacement of 3 units in the counting.

The CATS package contains a lot of additional extensions, which are expected to be commonly used in any femtoscopic analysis. The function and objects declared in “DLM_Source.h” contain the definitions of the most commonly used source functions, as for example a Gaussian or a Cauchy³ source function (Eq. A.2 and Eq. A.3).

$$S(r) = (4\pi r_0^2)^{-1.5} \exp\left(-\frac{r^2}{4r_0^2}\right) \quad (\text{A.2})$$

$$S(r) = \frac{r_0}{\pi} (r_0^2 + r^2)^{-2} \quad (\text{A.3})$$

If the source distribution does not have any angular dependence, this is trivially integrated out of Eq. 1.10 by obtaining an additional factor of $4\pi r^2$. The input into CATS for a source without any angular dependence is given in the form of $4\pi r^2 S(r)$, which, for the above two sources, reads in the source code as

```

1 double GaussSource(double* Pars){
2     double& Radius = Pars[1];
3     double& Size = Pars[3];
4     return 4.*Pi*Radius*Radius*pow(4.*Pi*Size*Size, -1.5)*
5         exp(-(Radius*Radius)/(4.*Size*Size));
6 }
7 double ExponentialSource(double* Pars){
8     double& Radius = Pars[1];
9     double& Size = Pars[3];
10    return 4.*Radius*Radius*Size*pow(Radius*Radius+Size*Size, -2.);
11 }
```

With these steps completed, let us proceed with an example of using these sources to study the π – π correlation function, in the case of non-identical charged pions. In this case both the Coulomb interaction and quantum statistics are present, but there is no significant strong interaction. The first step is to define a “CATS” object and set up the binning.

```

1 //ExpSource==true => use exponential source
2 //ExpSource==false => use Gaussian source
3 TGraph* Basics_PiPiCATS(const bool& ExpSource){
4
5     //constants related to the number of bins and range (in MeV)
6     const unsigned NumMomBins = 300;
7     const double kMin = 0;
8     const double kMax = 300;
9
10    //initialize the CATS object
11    CATS PionKitty;
12    //(#bins, min, max) or (#bins, BinRangeArray[] as in ROOT)
13    PionKitty.SetMomBins(NumMomBins, kMin, kMax);
```

³The Cauchy source distribution is commonly referred to as *exponential* source, as the resulting correlation function for non-charged, non-interacting identical particles has an exponential shape.

The next step is to *set up the emission source*, by defining the object containing the parameters⁴, as well as passing a pointer of the desired source function to the CATS object.

```

1 //object for the parameters to be used by the source function
2 CATSparameters SOURCE_PARS(CATSparameters::tSource,1,true);
3 //set the first and only par (source size)
4 SOURCE_PARS.SetParameter(0,1.5);
5 //say to CATS which Source function to use, and with which parameter set
6 PionKitty.SetAnaSource(ExpSource?ExponentialSource:GaussSource,SOURCE_PARS);
7 //this step is needed, to set up CATS for a source from a function
8 //there is one more possibility, namely to use the source as a
9 //direct input from a transport model. This method will not be discussed here
10 PionKitty.SetUseAnalyticSource(true);
11 //reduces CPU time, for a source that does not has a
12 //momentum or an angular dependence
13 Kitty.SetMomentumDependentSource(false);
14 Kitty.SetThetaDependentSource(false);
15 //if true, the source is automatically renormalized in the range 0–64 fm.
16 //Nice to dummy proof the source, but problematic for sources with large tails
17 //for the Gaussian example above, both options should be completely identical
18 Kitty.SetAutoNormSource(false);

```

The next input is related to the interaction, namely the number of interaction channels, including their spin quantum number, number of non-trivial partial waves and weight to the total correlation function. The pions are spin 0 particles, thus there is only a single configuration of the total spin (0), resulting in a single interaction channel. Since there is no strong interaction present, this channel does not have any partial waves that deviate from a free wave solution.

```

1 //standard settings for a CATS object which has
2 //no strong interaction potential included
3 PionKitty.SetNumChannels(1);
4 //which channel, how many PWs
5 PionKitty.SetNumPW(0,0);
6 //which channel, spin value
7 PionKitty.SetSpin(0,0);
8 //which channel, weight
9 PionKitty.SetChannelWeight(0, 1);

```

At this stage one could include information about the strong interaction. Since this is not needed in the current example, we proceed to the final input needed, which is related to the properties of the particle pair, in particular the charge, mass and identity

```

1 //standard settings for a CATS object which has
2 //no strong interaction potential included
3 PionKitty.SetNumChannels(1);
4 //which channel, how many PWs
5 PionKitty.SetNumPW(0,0);
6 //which channel, spin value
7 PionKitty.SetSpin(0,0);
8 //which channel, weight
9 PionKitty.SetChannelWeight(0, 1);
10
11 //include the coulomb interaction.
12 //Q1Q2 is the multiplied charge numbers of the two particles
13 PionKitty.SetQ1Q2(1);
14 //the reduced mass of the two pions
15 PionKitty.SetRedMass( 0.5*Mass_pip );
16 //for identical particles, we need to include the quantum statistics
17 PionKitty.SetQuantumStatistics(true);
18 }

```

So far the “CATS” object is set up, but to run the computation and evaluate the correlation function one has to run the command

⁴In the examples of a Gaussian and an exponential source there is a single parameter defining the width of the distributions.

```
1 PionKitty . KillTheCat();
```

The results are save internally, and the values of the correlation function can be obtained in the following way

```
1 // save the result in a TGraph (ROOT)
2 TGraph* grCk = new TGraph();
3 grCk->SetName("grCk");
4 grCk->Set(NumMomBins);
5 // iterate over all momentum bins
6 for(unsigned uMom=0; uMom<NumMomBins; uMom++){
7     // the GetMomentum() function sets the x-axis
8     // the GetCorrFun() function evaluates C(k) (y-axis)
9     grCk->SetPoint(uMom, PionKitty .GetMomentum(uMom) , PionKitty .GetCorrFun(uMom));
10 }
11
12 }
```

The results from the above example is shown in Fig. A.1 and compared to the result from the *Bowler-Sinyukov* (Eq. A.4) approach including Coulomb correction [134–136].

$$C(k^*) = 1 - \lambda + \lambda K(k^*) [1 + \exp(-(2r_0 k^*)^\alpha)], \quad (\text{A.4})$$

where λ is a simple scaling parameter, α controls the profile of the source ($\alpha = 1(2)$ corresponds to an exponential (Gaussian) source) and $K(k^*)$ is rather complicated Coulomb correction factor, based on a Gaussian parameterization. The Bowler-Sinyukov model is commonly used to study correlations between identical pions. The good agreement between the CATS and the Bowler-Sinyukov result for a Gaus-

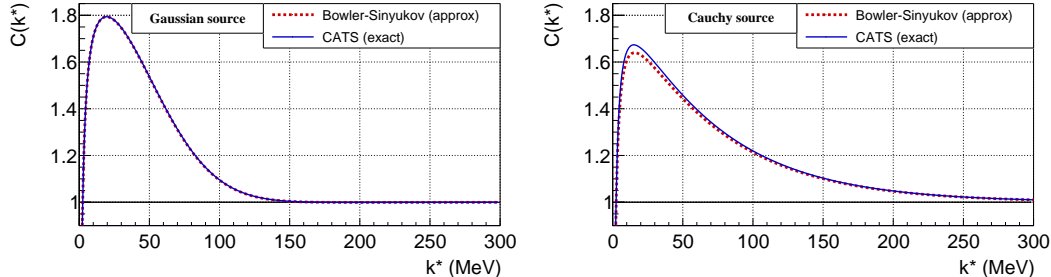


FIGURE A.1: Correlation of charged identical pions for different source profiles and different theoretical modelling. The width of the sources is fixed to 1.5 fm, the λ parameter assumed to be 1.

sian source can serve as a proof that the CATS computation is accurate. The slight difference observed for an exponential source can be attributed to the Gaussian treatment of the Coulomb interaction within the correction to the Bowler-Sinyukov model [136].

A.3 Inclusion of the strong interaction in potential form

In this next example, the focus will be on including the *strong interaction* in CATS, based on a real local potential $V(r)$. Referring back to section 2.2, let us remind us that one way of including the strong interaction in CATS is by setting $V(r)$ for each partial wave of each interaction channel. As an example, we will look at the p- Λ correlation function, based on the assumption of s -wave interaction, modeled via the Usmani potential [60]. This potential is a meson-exchange model, with a phenomenological repulsive core. The p- Λ system consists of two fermions, as such the possible total spin configuration is either 0 (singlet state) or 1 (triplet state). The

Usmani potential contains both spin channels. The singlet/triplet configuration of the spin channels results in 1:3 ratio of the weights of each channel to the correlation function. Technically, the inclusion of an interaction potential into CATS is realized in a similar manner as for the previous example for the source function, i.e. by defining a function of the type

```
1 double Function(double* Pars);
```

The array “Pars” is defined such that the variables controlled by CATS are *Pars[0]*, corresponding to the relative distance r , and *Pars[1]*, correponding to the relative momentum k^* . The interaction is assumed to be spherically symmetric, thus the angle between \vec{r}^* and \vec{k}^* is omitted. The rest of the array *Pars[>1]* can be used to store the potential parameters. Just as in the case of the emission source, the interface to CATS is realized by the class “CATSparameters”, where the displacement between the parameter number and its position in *Pars[]* is 2. There are multiple predefined potentials in “DLM_Potentials.h”, one of which is the Usmani potential

```
1 double UsmaniPotentialCats(double* Pars){
2     double& r = Pars[0];
3     double& Spin = Pars[2];
4     // Values for the potential
5     const double vbar = 6.2;
6     const double vsigma = 0.25;
7     const double wc = 2137;
8     double x=r*0.7;
9     double vc = wc/(1+exp((r-0.5)/0.2));
10    double tpi = (1.0+3.0/x+3.0/(x*x)) * (exp(-x)/x) * pow(1.-exp(-2.*r*r),2.);
11    double v = 0.;
12    if (Spin == 0) v = vc - (vbar + 0.75*vsigma)*tpi*tpi;//Usmani singlet
13    else if (Spin == 1) v = vc - (vbar - 0.25*vsigma)*tpi*tpi;//Usmani triplet
14    else printf ("wrong_polarization\n");
15    return v;
16 }
```

For this example, *Pars[2]* is the only parameter of the interaction, and it represents the total spin of the system. To evaluate the p - Λ correlation function with CATS, we follow the previous example of the π - π correlation, but by updating all set up parameters to match the p - Λ system, and adding 2 interaction channels, each being represented by a single partial wave modeled by the Usmani potential. We will make the following example much more modular, in order to reuse the same definition later on. We start with a function to set up the Gaussian source.

```
1 void CATS_GaussSource(CATS& Kitty, const double& SourceSize){
2     CATSparameters cPars(CATSparameters::tSource,1,true);
3     cPars.SetParameter(0,SourceSize);
4     Kitty.SetAnaSource(GaussSource, cPars);
5     Kitty.SetUseAnalyticSource(true);
6     Kitty.SetMomentumDependentSource(false);
7     Kitty.SetThetaDependentSource(false);
8     // if true, the source is automatically renormalized in the range 0-64 fm.
9     // Nice to dummy proof the source, but problematic for sources with large tails
10    // for the Gaussian example above, both options should be completely identical
11    Kitty.SetAutoNormSource(false);
12 }
```

Next a function to setup the basic properties of the p - Λ system.

```
1 void CATS_pL_Basic(CATS& Kitty, const unsigned& NumMomBins, const double& kMin, const double& kMax){
2     Kitty.SetMomBins(NumMomBins,kMin,kMax);
3     //should you include in the result any bins,
4     //where the Schroedinger solver failed
5     Kitty.SetExcludeFailedBins(false);
6     Kitty.SetQ1Q2(0);
7     Kitty.SetQuantumStatistics(false);
8     Kitty.SetRedMass( (Mass_p*Mass_L)/(Mass_p+Mass_L) );
9 }
```

Next a function to setup the interaction for the p- Λ system using the Usmani potential.

```

1 //setup the CATS interaction for pLambda (Usmani)
2 void CATS_pL_Usmani(CATS& Kitty){
3     Kitty.SetNumChannels(2);
4     Kitty.SetNumPW(0,1);
5     Kitty.SetNumPW(1,1);
6     Kitty.SetSpin(0,0);
7     Kitty.SetSpin(1,1);
8     //set up the weights of the spin 0 and 1 channel.
9     //the singlet/triplet configuration leads to these weights
10    Kitty.SetChannelWeight(0, 1./4.);
11    Kitty.SetChannelWeight(1, 3./4.);
12
13    //define the parameters for the 1S0 partial wave
14    CATSparameters POT_PARS_1S0(CATSparameters::tPotential,1,true);
15    //the only parameter is the spin (here 0)
16    POT_PARS_1S0.SetParameter(0,0);
17    //define the parameters for the 3S1 partial wave
18    CATSparameters POT_PARS_3S1(CATSparameters::tPotential,1,true);
19    //the only parameter is the spin (here 1)
20    POT_PARS_3S1.SetParameter(0,1);
21    //For each channel and each partial wave, the strong potential
22    //has to be added using this function, taking as input arguments
23    //##WhichChannel,#WhichPW,PotentialFunction,Parameters
24    Kitty.SetShortRangePotential(0,0,UsmaniPotentialCats,POT_PARS_1S0);
25    Kitty.SetShortRangePotential(1,0,UsmaniPotentialCats,POT_PARS_3S1);
26 }
```

To obtain the p- Λ correlation function we need to run the CATS object (the example below) and plot the result (Fig. A.2).

```

1 TGraph* Basics_ProtonLambda(){
2
3     const unsigned NumMomBins = 150;
4     const double kMin = 0;
5     const double kMax = 300;
6
7     CATS Kitty_pL;
8     CATS_pL_Basic(Kitty_pL,NumMomBins,kMin,kMax);
9     CATS_GaussSource(Kitty_pL,1.5);
10    CATS_pL_Usmani(Kitty_pL);
11
12    //these are two optional functions, which can make the computing
13    //grid finer, at the expense of increased CPU time to solve
14    //the Schroedinger equation. The default value is 5e-6. Here we choose
15    //a very fine grid, in order to produce a smooth 2 MeV binned correlation
16    Kitty_pL.SetEpsilonConv(5e-8);
17    Kitty_pL.SetEpsilonProp(5e-8);
18    Kitty_pL.KillTheCat();
19
20    //save the result in a TGraph (ROOT)
21    TGraph* grCk = new TGraph();
22    grCk->SetName("grCk");
23    grCk->Set(NumMomBins);
24    //iterate over all momentum bins
25    for(unsigned uMom=0; uMom<NumMomBins; uMom++){
26        //the GetMomentum() function sets the x-axis
27        //the GetCorrFun() function evaluates C(k) (y-axis)
28        grCk->SetPoint(uMom,Kitty_pL.GetMomentum(uMom),Kitty_pL.GetCorrFun(uMom));
29    }
30
31    return grCk;
32 }
```

The scattering length f_0 of the Usmani potential for the 1S0 (3S1) channel is 2.88 (1.66) fm, while the effective range d_0 is 2.92 (3.78) fm [137]. This corresponds to a strongly attractive non-binding interaction, which according to the discussion in section 2.5 should result in a large enhancement at low k^* and slight depletion at intermediate k^* . This is consistent with Fig. A.2.

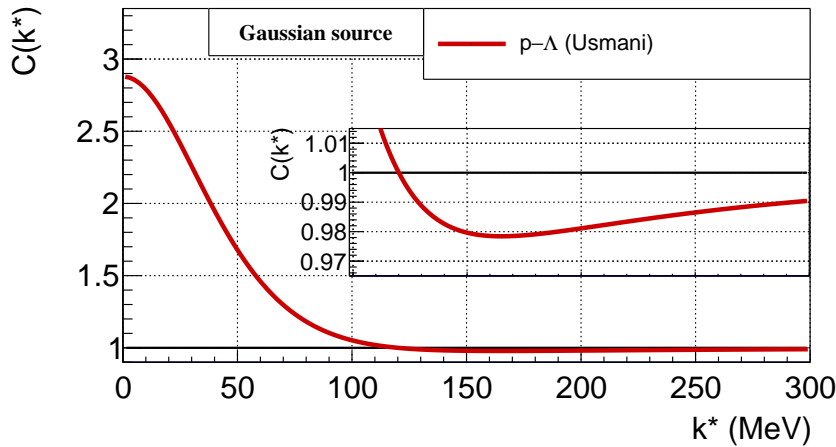


FIGURE A.2: Correlation of p- Λ (Usmani potential). The width of the sources is fixed to 1.5 fm.

A.4 The predefined interaction potentials

The CATS package contains a various interaction potentials, defined in “DLM_Potentials.cpp”. The most simple example is the function used to model the toy potentials presented in chapter 2.5, defined below in the form of the sum of three Gaussians

```

1 //V0*exp(-r^2/mu0^2)+V1*exp(-r^2/mu1^2)+V2*exp(-r^2/mu2^2)
2 // [0] - r; [1] = k; [2]=V0; [3]=mu0; [4]=V1; [5]=mu1; [6]=V2; [7]=mu2
3 double TripleGaussSum(double* Pars){
4     return Pars[2]*exp(-pow(Pars[0]/Pars[3],2))+  

5     Pars[4]*exp(-pow(Pars[0]/Pars[5],2))+  

6     Pars[6]*exp(-pow(Pars[0]/Pars[7],2));
7 }
```

The meaning of the array “Pars” is the same as presented in the previous section (A.3). In this example there are two input parameters per Gaussian, resulting in a total of six parameters. To set them up for the case of the V_B potential presented in chapter 2.5, one should use the following syntax

```

1 //... (standard definition of CATS object, binning, source etc.)
2 CATSparameters ParsPot(CATSparameters::tPotential,6,true);
3 //strength of the attractive part
4 ParsPot.SetParameter(0,-150);
5 //range of the attractive part
6 ParsPot.SetParameter(1,1.0);
7 //strength of the repulsive core
8 ParsPot.SetParameter(2,125);
9 //range of the repulsive core
10 ParsPot.SetParameter(3,0.5);
11 //put this parameter to zero to remove the contribution
12 //from the third Gaussian
13 ParsPot.SetParameter(4,0.0);
14 //dummy parameter
15 ParsPot.SetParameter(5,100.0);
16 //... (execute CATS, plotting macros etc.)
17 }
```

Another useful potential is the pure repulsive core

$$A \left[1 + \exp \left(\frac{r - R}{S} \right) \right]^{-1}, \quad (\text{A.5})$$

where A is an amplitude, R is the range of the repulsive core and S is a slope parameter. The source code corresponding to this potential is

```

1 // [2] is the amplitude
2 // [3] is the range
3 // [4] is the slope
4 double RepulsiveCore(double* Pars){
5     return Pars[2]/(1+exp((Pars[0]-Pars[3])/Pars[4]));
6 }
```

This potential can be used to insert an infinite barrier at some point, which has a used case to simulate absorption below a certain distance. Fig. A.3 shows an example for such a repulsive core.

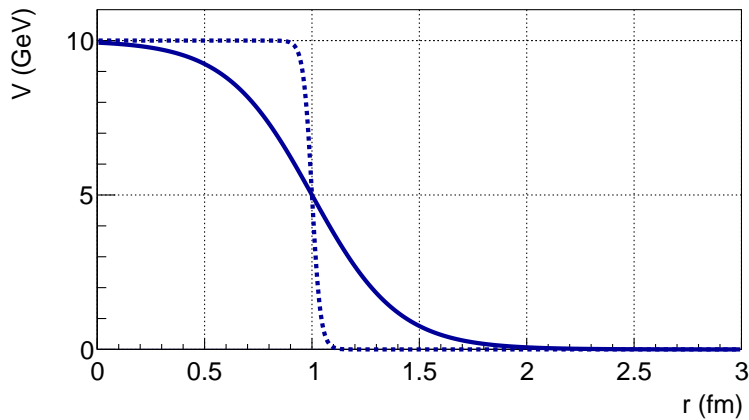


FIGURE A.3: Two repulsive cores with equal amplitudes (10 GeV) and ranges (1 fm), but different slope parameters. The solid line represents a soft repulsion with a slope parameter of 0.2 fm^{-1} , while the dashed line has $S = 0.02 \text{ fm}^{-1}$ and as such can be used as a “potential barrier”.

All other interaction potentials that were used in this work, are defined using the same function, but called with different input parameters, many of them serving as flags to specify the interaction.

```
1 double fDlmPot(double* Parameters);
```

The first two arguments of this function, as always, are controlled by CATS and serve the purpose of passing the variables r^* and k^* . The rest of the parameters are used as described in Table A.1. Note that there are many input parameters, and depending on the interaction type not all of them are used. An executive summary showing which flags are needed by a specific potential are shown in Table A.1. Listed below are all currently (year 2020) implemented potentials and their flags.

- **NN_AV18:** The Argonne $v18$ potential for N–N interaction [7]. This potential can be used to study any N–N interaction, as long as all the parameters listed in Table A.1 are appropriately set. Nevertheless, the potential was tested only for the pp interaction, for all other system the code is to be used “as it is”, without guarantee. For pp, there were several complications with the inclusion of the 3P2 partial waves, as it couples to 3F2. We tested multiple solutions, and concluded that the best way to treat this partial wave is by taking the coupled channel solution and using the first diagonal element of the Hamiltonian (direct contribution of $3\text{P}2 \rightarrow 3\text{P}2$) as a single channel potential. This scenario is invoked by setting $DlmPotFlag == v18_Coupled3P2$ ⁵. This

⁵ $v18_Coupled3P2$ is an enumerator representing the number 2

double* Parameters;	CATSpараметр CatsPar;	Description
[2]	<code>.SetParameter(0)</code>	A flag (DlmPot) for the interaction type (e.g. pp, p- Λ etc.). The available flags are discussed in the text.
[3]	<code>.SetParameter(1)</code>	A flag (DlmPotFlag) to be passed to the potential. The meaning of the flag depends on the definition of the potential, and is discussed individual for each potential in the text.
[4]	<code>.SetParameter(2)</code>	Isospin I of the pair
[5]	<code>.SetParameter(3)</code>	Two times the isospin of particle 1 ($2I_1$)
[6]	<code>.SetParameter(4)</code>	Two times the isospin of particle 2 ($2I_2$)
[7]	<code>.SetParameter(5)</code>	Spin S of the pair
[8]	<code>.SetParameter(6)</code>	Angular momentum L of the pair
[9]	<code>.SetParameter(7)</code>	Total angular momentum J of the pair
[≥ 10]	<code>.SetParameter(≥ 8)</code>	Further optional parameters

TABLE A.1: The parameters of “fDlmPot”. The first column is the position within the array `double* Parameters`, the second column is the corresponding input into CATS via the `CATSpараметр` object and the third column describes the parameters.

flag was used for all pp analyses presented in this work, **please use *DlmPot-Flag == v18_Coupled3P2*** for your own analyses, unless the implementation of the 3P2 is updated and improved.

- **NN_ReidV8:** The Reid $v8$ potential for N–N interaction [138]. Similar implementation as for the Argonne $v18$ (*NN_AV18*) case.
- **pp_ReidSC, pp_ReidOli, pp_ReidCrab, pp_ReidVale**
Several implementations of the Reid potential. All were used for testing purposes, resulting in inaccurate results for the interaction, and should **not be used**.
- **pL_UsmaniOli:** The Usmani potential for p– Λ interaction [60]. Uses exactly the same expression for the interaction as in the example shown previously in the chapter. The only relevant input parameter is the spin S of the pair.
- **pXim_Lattice:** The *preliminary* HAL-QCD potential for p– Ξ interaction [125]. This is an outdated potential, based on the preliminary lattice results. The exact potential has been provided to us, to be used in CATS, in a private communication with Prof. Tetsuo Hatsuda and Prof. Kenji Morita. Depending on the euclidean time t , multiple parameterizations are available. These are set using “*DlmPotFlag*”. For the $I = 0$ one can pass $t \in \{9, 10, 11, 12\}$, while for $I = 1$ the argument passed is $(t - 8) \in \{1, 2, 3, 4, 5, 6\}$. The functional parameterization and the uncertainties related to this potential were improved, and now included in CATS to be used with the flag “*pXim_HALQCD1*”.
- **pXim_HALQCD1:** An *updated* version of the HAL-QCD potential for p– Ξ interaction [123, 139].

This potential is based on the final published lattice data [123], however the parameterization of the fit to the potential was provided to us in a private communication by K. Sasaki and T. Miyamoto. This is the version used to model the $p-\Xi$ interaction in our publication [40]. Depending on the euclidean time $t \in \{11, 12, 13\}$, multiple parameterizations are available. These set using “DlmPotFlag”.

- *pXim_LatticeAvg, pXim_LatticeSqrtAvg*: Potentials used for various tests of the HAL-QCD potentials for $p-\Xi$. **Do not use**.
- *pOmega_Lattice*: $p-\Omega^-$ potentials obtained from the lattice [130, 140]. There are two sets of potentials. The first set is from the result for non-physical pion masses [140] and contains three potentials corresponding to the V_I , V_{II} and V_{III} potentials used in the publication on $p-\Omega^-$ from STAR [141]. These three potentials are called with “DlmPotFlag” set to 121, 122 and 123 respectively.

The second set of potentials are obtained from the lattice computation for pions with near the physical point masses [130]. These potentials are called with “DlmPotFlag” set set to 11,12,13 or 14, where the number corresponds to the euclidean time used. The parameterization of these potentials follows the prescription presented in [130].

N.B. All lattice $p-\Omega^-$ potentials model only the 5S2 component of the interaction. The spin one channel (3S1) is inaccessible at the moment.

- *pOmega_Tetsuo*: The Sekihara meson exchange model for $p-\Omega^-$ [131]. The Sekihara meson exchange model is partially fitted to the HAL-QCD calculation, and is used to provide an effective “extrapolation” to the physical masses of the pions. Just as for the lattice potentials, only the 5S2 channel is modeled and only the real part of the potential is considered.
- *pKm_Tetsuo*: The Kyoto model for $p-K^-$ interaction, based on an outdated computation, in which the mass difference between charged and neutral kaons is not accounted for [142]. The interaction is mapped onto an effective single channel energy dependant potential (Eq. 8 in [142]), which has a real an imaginary part (Table VI in [142]). Since CATS can only work with a real valued potential, the imaginary part was omitted. The authors of the above reference confirmed that this should be a reasonable approximation. Nevertheless, new theoretical developments of this model resulted in much more complete calculations [59], thus ***pKm_Tetsuo should be considered as an outdated and inaccurate model*** for $p-K^-$. The new model is unavailable in a simplified form, thus the $p-K^-$ interaction is included in CATS by the direct use of the wave function (see section ??).

A.5 DLM_Ck: The correlation function as a histogram

The extensions to the CATS framework within the classes *DLM_Ck* and *DLM_CkDecomp*⁶ contain the tools needed to apply the momentum smearing and

⁶There is a derived class called *DLM_CkDecomposition*, which is identical up to the input of the smear matrices. In *DLM_CkDecomposition* the input is ROOT based (*TH2F*), while in *DLM_CkDecomp* the *DLM_Histo* class is used instead.

feed-down effects onto the theoretical correlation function (introduced in chapter 2.7). For the use in CATS, the correlation function is wrapped in the class *DLM_Ck*, which inherits from *DLM_Histo*, but has several functionalities making it particularly useful for femtoscopy analyses. The initialization of such an object can be done in two ways. The first option is to use a CATS object to set up the histogram, achieved by invoking the constructor

```
1 DLM_Ck(const unsigned& nSourcePar, const unsigned& nPotPar, CATS& cat,
2   const unsigned& numbin, const double& minMom, const double& maxMom);
```

where *nSourcePar* (*nPotPar*) are the number of source (potential) parameters associated with a CATS object *cat*. By default the binning is inherited from CATS, although by desire one could change it by setting *numbin*, *minMom* and *maxMom*. It is often a good practice to set up a binning slightly larger than needed for the analysis and plotting, as the smearing procedures could lead to edge effects in the last couple of bins.

Alternatively one can use a function as an input for the correlation function.

```
1 double CkFunction(const double &Momentum,
2   const double* SourcePar, const double* PotPar)
```

This function should have three arguments, a *double* for the momentum k^* and two pointers to arrays containing the source and potential parameters. Any user defined function with such a definition can be used as an input to *DLM_Ck*, which is set up by the constructor

```
1 DLM_Ck(const unsigned& nSourcePar, const unsigned& nPotPar,
2   const unsigned& numbin, const double& minMom, const double& maxMom,
3   double (*CorrFun)(const double&, const double*, const double*))
```

The arguments are similar as to the previous example.

The class *DLM_Ck* provides an interface to access and change the source and potential parameters, achieved via the functions

```
1 void SetSourcePar(const unsigned& WhichPar, const double& Value);
2 void SetPotPar(const unsigned& WhichPar, const double& Value);
```

In case the initialization is linked to a CATS object, *DLM_Ck* changes the parameters by calling the functions

```
1 void CATS::SetAnaSource(const unsigned& WhichPar, const double& Value,
2   const bool& SmallChange=false);
3 void CATS::SetShortRangePotential(const unsigned& usCh, const unsigned& usPW,
4   const unsigned& WhichPar, const double& Value);
```

If the initialization is based on a custom function, the corresponding elements of the arrays *SourcePar* and *PotPar* are changed.

It is often required to perform an analysis that extends beyond the femtoscopy range, e.g. in order to constrain the non-femtoscopy background. The correlation function has the property $C(k^* \rightarrow \infty) \rightarrow 1$, which can be modeled numerically by assuming the existence of a scale $k^* = k_\infty$, above which the condition for convergence is fulfilled. The numerical evaluation of $C(k^*)$ is often modeled only up to a certain $k^* = k_{\max} < k_\infty$, which leads to missing values $C(k_{\max} < k^* < k_\infty)$. The class *DLM_Ck* provides one simple solution to this problem, by assuming a linear relation of the correlation function in this region

$$C(k_{\max} < k^* < k_\infty) = \alpha k^* + \beta, \quad (\text{A.6})$$

invoking the boundary conditions

$$\begin{cases} C(k_{\max}) = \text{true solution} \\ C(k_{\infty}) = 1. \end{cases} \quad (\text{A.7})$$

A graphical representation of the idea is sketched in Fig. A.4. The set up of the cutoff

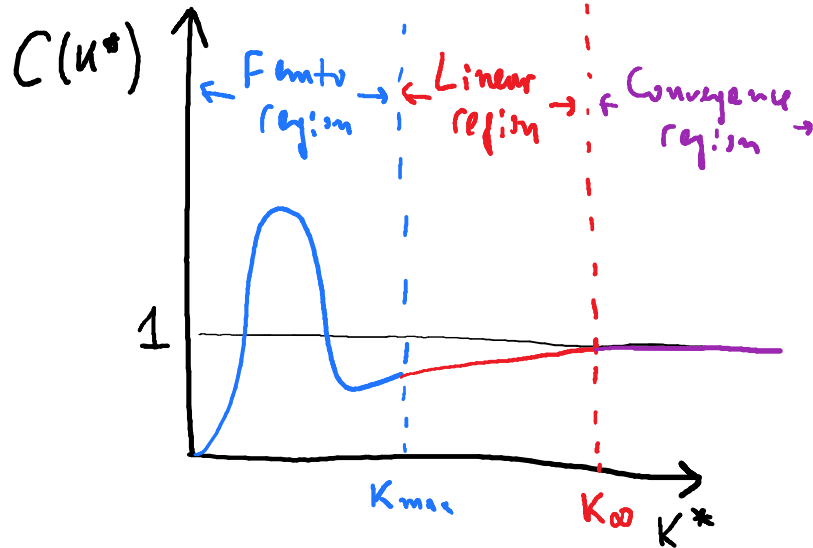


FIGURE A.4: A sketch of the correlation function modeled with *DLM_Ck*. After the value k_{\max} the correlation is assumed to approach unity with a linear function. Once unity is reached, the correlation becomes flat. In this example $C(k_{\max}) < 1$, but the same logic is applied if $C(k_{\max}) > 1$, however with inverted slope of the linear function.

is done by in *DLM_Ck* by the function

```
1 void SetCutOff( const double& Momentum=1e6, const double& kc=-1);
```

where *Momentum* plays the role of k_{\max} and *kc* is representing k_{∞} . If *kc* is set to a negative value, than the above considerations are ignored, and the correlation function is assumed to be flat above k_{\max} , obtaining the constant value $C(k^* > k_{\max}) = |kc|$. This option is not recommended, however it was kept and set as the default cutoff option due to issues with the backwards compatibility of the code.

The initialization of *DLM_Ck* happens by passing a pointer either to a CATS object, or a function of the type

```
1 double CkFunction( const double &Momentum,
2                      const double* SourcePar, const double* PotPar);
```

where the input arguments are the k^* (*Momentum*) and two arrays containing the source and potential parameters related to the correlation function.

A.6 Usage of the Lednický model and other custom correlation functions

As explained in the previous section, the class *DLM_Ck* can be defined with any custom function. The file “*DLM_CkModels.h*” contains multiple functions used to

model the correlation function, in the example below we will study the use of the Lednický model. In CATS there are multiple instances of this model, depending on the used case. The naming of the functions in “DLM_CkModels.h” is self explanatory, below a list of the most common Lednický based functions

```

1 // ... represents
2 //const double& Momentum, const double* SourcePar, const double* PotPar
3 double Lednický_Identical_Singlet(...);
4 double Lednický_Identical_Singlet_InvScatLen(...);
5 double Lednický_Singlet(...);
6 double Lednický_Singlet_InvScatLen(...);
7 double Lednický_Identical_Triplet(...);
8 double Lednický_Triplet(...);
9 double ComplexLednický_Identical_Singlet(...);
10 double ComplexLednický_Identical_Singlet_InvScatLen(...);
11 double ComplexLednický_Singlet(...);
12 double ComplexLednický_Singlet_InvScatLen(...);
13 double ComplexLednický_Identical_Triplet(...);
14 double ComplexLednický_Triplet(...);

```

All functions have a single source parameter corresponding the the Gaussian source size. There are two main groups of functions, those with a real scattering length (name begins with *Lednický*) and those with a complex scattering length (name begins with *Complex*). Further, the name of the functions contains either *Singlet* or *Triplet*. The former refers to a single channel interaction, the latter to two-channel interactions, for which the first channel plays the role of a singlet state (weight of 1/4) and the second channel is a triplet state (weight of 3/4). If the name of the function contains *Identical*, quantum statistics is included. Finally, the key work *InvScatLen* implies that the input for the scattering length f_0 is given as $1/f_0$. The potential parameters (*PotPar*) follow the ordering scheme $\{\Re f_0, \Im f_0, d_0$ (effective range) $\}$ for the first channel, followed by the same parameters for the second channel (if present). The imaginary part of f_0 is dropped out in case of non-complex functions. E.g. for *Lednický_Triplet* there are 4 input parameters, the first two represent f_0 and d_0 of the singlet, the next two of the triplet. The corresponding complex function will obtain 6 input parameters, due to the imaginary part of f_0 .

As a practical example, let us compute the p - Λ correlation function using the Lednický model and compare the result to the Usmani potential. To make a fair comparison, the scattering parameters will be set to those of the Usmani potential.

```

1 TGraph* Lednický_ProtonLambda(){
2     const unsigned NumMomBins = 150;
3     const double kMin = 0;
4     const double kMax = 300;
5     const double SourceSize = 1.5;
6     //anchored to the Usmani potential
7     const double ScattLen_1S0 = 2.88;
8     const double EffRan_1S0 = 2.92;
9     const double ScattLen_3S1 = 1.66;
10    const double EffRan_3S1 = 3.78;
11
12    //initialize the histogram object using the Lednický model
13    //the first two arguments represent the number of source parameters
14    //and the number of potential parameters required by the function
15    DLM_Ck CkProtonLambda_Lednický(1,4,NumMomBins,kMin,kMax,Lednický_Triplet);
16    //set the source and interaction parameters
17    CkProtonLambda_Lednický.SetSourcePar(0,SourceSize);
18    CkProtonLambda_Lednický.SetPotPar(0,ScattLen_1S0);
19    CkProtonLambda_Lednický.SetPotPar(1,EffRan_1S0);
20    CkProtonLambda_Lednický.SetPotPar(2,ScattLen_3S1);
21    CkProtonLambda_Lednický.SetPotPar(3,EffRan_3S1);
22    //fill the histogram
23    CkProtonLambda_Lednický.Update();
24

```

```

25 // save the result in a TGraph (ROOT)
26 TGraph* grCk = new TGraph();
27 grCk->SetName("grCk_Lednicky_ProtonLambda");
28 grCk->Set(NumMomBins);
29 // iterate over all momentum bins
30 for(unsigned uMom=0; uMom<NumMomBins; uMom++){
31     //DLM_Ck has similar function naming as a ROOT TH1F.
32     //however the bin counting starts from zero, and the GetBinCenter
33     //has an extra parameter corresponding to the axis number.
34     //DLM_Ck is 1D, thus this parameter can only be zero
35     grCk->SetPoint(uMom, CkProtonLambda_Lednicky.GetBinCenter(0,uMom),
36                      CkProtonLambda_Lednicky.GetBinContent(uMom));
37 }
38
39 return grCk;
40 }

```

The output of this function is combined with the result for the Usmani potential (section A.3, Fig. A.2) is plotted in Fig. A.5

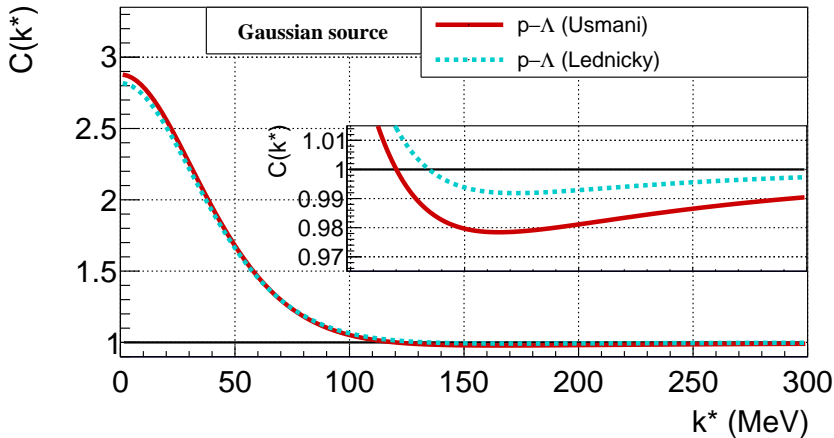


FIGURE A.5: Correlation of p- Λ . The width of the sources is fixed to 1.5 fm. The comparison between the true solution to the Usmani potential (red solid line) and the approximate Lednický model (cyan dotted line) shows that for this source size the Lednický model model is accurate within 1-2%.

A.7 DLM_CkDecomp: Correcting the correlation function

This is the base class to handle the momentum smearing and feed-down effects. An object of this class is initialized from a correlation function in the format of *DLM_Ck*, and the momentum smear and decay matrices are passed as 2-dimensional *DLM_Histo* objects. Alternatively there is a derived ROOT based class, called *DLM_CkDecomposition*, allowing the matrices to be in *TH2F* format. The theoretical idea related to the decomposition of the correlation function is presented in chapter 2.7. The momentum smearing is rather trivial and effecting only the measured correlation function. The feed-down is a physics effect related to the production of the particles, as such it affects each particle and modifies the theoretical correlation function. Naturally, this effect is recursive, e.g. due to the decay of $\Lambda \rightarrow p$, the p-p correlation contains a residual signal of the p- Λ correlation. However, the Λ itself could be produced from feed-down related to Ξ^- , thus the p- Λ correlation has a residual contribution from p- Ξ , implying that the p-p correlation carries an indirect

contribution from $p-\Xi$ as well ($p-\Xi \rightarrow p-\Lambda \rightarrow p-p$). The class *DLM_CkDecomp* is considering these effects, by allowing to set up all feed-downs to a particular channel by passing the theoretical correlations in the format of another *DLM_CkDecomp* object, which itself carries certain feed down correlations etc. The example below is based on the $p-p$ correlation function, for which the feed-down is assumed to be non-flat only for the $p-\Lambda \rightarrow p-p$ channel. For the feed-down to $p-\Lambda$ we will consider the contributions from $p-\Sigma^0$ and $p-\Xi$ and neglect any feed-down into those two channels. To model the interaction we will use the Argonne *v18* potential for $p-p$, the Usmani potential for $p-\Lambda$ and the HAL-QCD lattice results for $p-\Xi$. The $p-\Sigma^0$ is modeled via the *fs2* model [118], exactly as done in the ALICE pp high-multiplicity analysis [42]. Further details regarding these interactions, in particular their channels and weights, refer to the main body of the thesis???. The technical implementation of $p-\Sigma^0$ is done using the predefined function *Lednicky_gauss_Sigma0*. The rest of the above interactions are modeled with the potentials introduced in section A.4. The setup related to the $p-p$ interaction is performed with the following functions

```

1 //Basic initialization of a CATS object for pp
2 void CATS_pp_Basic(CATS& Kitty,
3   const unsigned& NumMomBins, const double& kMin, const double& kMax){
4   Kitty.SetMomBins(NumMomBins,kMin,kMax);
5   //should you include in the result any bins ,
6   //where the Schroedinger solver failed
7   Kitty.SetExcludeFailedBins(false);
8   Kitty.SetQ1Q2(1);
9   Kitty.SetQuantumStatistics(true);
10  Kitty.SetRedMass( 0.5*Mass_p );
11 }
12 //initialize the interaction for pp, using the AV18 potential.
13 //the s,l and d waves are included
14 void CATS_pp_AV18(CATS& Kitty, const bool& pwaves, const bool& dwaves){
15   //the 4 channels for pp are:
16   //s=0: 1S0 + 3D1
17   //s=1: 3P0
18   //s=1: 3P1
19   //s=1: 3P2
20   //note that for s=0 the p-waves are Pauli blocked ,
21   //for s=1 these are the s and d waves
22   if(pwaves){
23     Kitty.SetNumChannels(4);
24     if(dwaves) Kitty.SetNumPW(0,3);
25     else Kitty.SetNumPW(0,1);
26     Kitty.SetNumPW(1,2);
27     Kitty.SetNumPW(2,2);
28     Kitty.SetNumPW(3,2);
29     Kitty.SetSpin(0,0);
30     Kitty.SetSpin(1,1);
31     Kitty.SetSpin(2,1);
32     Kitty.SetSpin(3,1);
33     Kitty.SetChannelWeight(0, 3./12.);
34     Kitty.SetChannelWeight(1, 1./12.);
35     Kitty.SetChannelWeight(2, 3./12.);
36     Kitty.SetChannelWeight(3, 5./12.);
37   }
38   else{
39     //important: even with the p-waves switched off ,
40     //physics wise the spin 1 state still exists and
41     //the p-waves are there, just in there asymptotic state (free wave).
42     //To include this in the computation ,
43     //CATS still needs a second channel, even if it is 'empty'!
44     Kitty.SetNumChannels(2);
45     if(dwaves) Kitty.SetNumPW(0,3);
46     else Kitty.SetNumPW(0,1);
47     Kitty.SetNumPW(1,0);
48     Kitty.SetSpin(0,0);
49     Kitty.SetSpin(1,1);
50     Kitty.SetChannelWeight(0, 1./4.);
51     Kitty.SetChannelWeight(1, 3./4.);
```

```

52 }
53
54 //to set up the strong interaction , one can use the
55 //predefined functions available in DLM_Potentials.h
56 //The input parameters are by default 9 and are defined as follows:
57 //0: potential flag
58 //1: a second flag , that can be used if needed
59 //2: total isospin
60 //3: 2 x isospin of particle 1
61 //4: 2 x isospin of particle 2
62 //5: total spin
63 //6: l quantum number
64 //7: j quantum number
65 CATSparameters cPars_pp_1S0(CATSparameters::tPotential,8,true);
66 cPars_pp_1S0.SetParameter(0,NN_ReidV8); //choose the AV18
67 cPars_pp_1S0.SetParameter(1,v18_Coupled3P2);
68 cPars_pp_1S0.SetParameter(2,1);
69 cPars_pp_1S0.SetParameter(3,1);
70 cPars_pp_1S0.SetParameter(4,1);
71 cPars_pp_1S0.SetParameter(5,0);
72 cPars_pp_1S0.SetParameter(6,0);
73 cPars_pp_1S0.SetParameter(7,0);
74
75 //copy all settings from cPars_pp_1S0 , and just change quantum numbers s,l,j
76 CATSparameters cPars_pp_3P0(cPars_pp_1S0);
77 cPars_pp_3P0.SetParameter(5,1);
78 cPars_pp_3P0.SetParameter(6,1);
79 cPars_pp_3P0.SetParameter(7,0);
80
81 CATSparameters cPars_pp_3P1(cPars_pp_1S0);
82 cPars_pp_3P1.SetParameter(5,1);
83 cPars_pp_3P1.SetParameter(6,1);
84 cPars_pp_3P1.SetParameter(7,1);
85
86 CATSparameters cPars_pp_3P2(cPars_pp_1S0);
87 cPars_pp_3P2.SetParameter(5,1);
88 cPars_pp_3P2.SetParameter(6,1);
89 cPars_pp_3P2.SetParameter(7,2);
90
91 CATSparameters cPars_pp_1D2(cPars_pp_1S0);
92 cPars_pp_1D2.SetParameter(5,0);
93 cPars_pp_1D2.SetParameter(6,2);
94 cPars_pp_1D2.SetParameter(7,2);
95
96 //plug in the strong potential for each channel and partial wave
97 //the arguments are:
98 //##WhichChannel,#WhichPartialWave,#PotentialFunction,#PotentialParameters
99 Kitty.SetShortRangePotential(0,0,fDlmPot,cPars_pp_1S0);
100 if(pwaves){
101     Kitty.SetShortRangePotential(1,1,fDlmPot,cPars_pp_3P0);
102     Kitty.SetShortRangePotential(2,1,fDlmPot,cPars_pp_3P1);
103     Kitty.SetShortRangePotential(3,1,fDlmPot,cPars_pp_3P2);
104 }
105 if(dwaves){
106     Kitty.SetShortRangePotential(0,2,fDlmPot,cPars_pp_1D2);
107 }
108 //if later on you would like to switch some contribution off ,
109 //this can be done with:
110 //Kitty.RemoveShortRangePotential(#WhichChannel,# WhichPartialWave);
111 }

```

New, let us look at the set up for the $p\text{-}\Xi$ correlation with the latest lattice potential.

```

1 void CATS_pXim_Basic(CATS& Kitty,
2     const unsigned& NumMomBins, const double& kMin, const double& kMax){
3     Kitty.SetMomBins(NumMomBins,kMin,kMax);
4     //should you include in the result any bins ,
5     //where the Schroedinger solver failed
6     Kitty.SetExcludeFailedBins(false);
7     Kitty.SetQ1Q2(-1);
8     Kitty.SetQuantumStatistics(false);
9     Kitty.SetRedMass( (Mass_p*Mass_Xim)/(Mass_p+Mass_Xim) );
10 }

```

```

11 void CATS_pXim_Hal(CATS& Kitty){
12     // 0: S=0 I=0
13     // 1: S=1 I=0
14     // 2: S=0 I=1
15     // 3: S=1 I=1
16     Kitty .SetNumChannels(4);
17     Kitty .SetNumPW(0,1);
18     Kitty .SetNumPW(1,1);
19     Kitty .SetNumPW(2,1);
20     Kitty .SetNumPW(3,1);
21     Kitty .SetSpin(0,0);
22     Kitty .SetSpin(1,1);
23     Kitty .SetSpin(2,0);
24     Kitty .SetSpin(3,1);
25     Kitty .SetChannelWeight(0, 1./8.);
26     Kitty .SetChannelWeight(1, 3./8.);
27     Kitty .SetChannelWeight(2, 1./8.);
28     Kitty .SetChannelWeight(3, 3./8.);
29
30     CATSparameters cPars_pXim_HalI0S0(CATSparameters :: tPotential ,8 ,true );
31     cPars_pXim_HalI0S0 .SetParameter(0 ,pXim_HALQCD1 );
32     //the euclidean time
33     cPars_pXim_HalI0S0 .SetParameter(1 ,12);
34     cPars_pXim_HalI0S0 .SetParameter(2 ,0);
35     cPars_pXim_HalI0S0 .SetParameter(3 ,−1);
36     cPars_pXim_HalI0S0 .SetParameter(4 ,1);
37     cPars_pXim_HalI0S0 .SetParameter(5 ,0);
38     cPars_pXim_HalI0S0 .SetParameter(6 ,0);
39     cPars_pXim_HalI0S0 .SetParameter(7 ,0);
40
41     CATSparameters cPars_pXim_HalI0S1(CATSparameters :: tPotential ,8 ,true );
42     cPars_pXim_HalI0S1 .SetParameter(0 ,pXim_HALQCD1 );
43     //the euclidean time
44     cPars_pXim_HalI0S1 .SetParameter(1 ,12);
45     cPars_pXim_HalI0S1 .SetParameter(2 ,0);
46     cPars_pXim_HalI0S1 .SetParameter(3 ,−1);
47     cPars_pXim_HalI0S1 .SetParameter(4 ,1);
48     cPars_pXim_HalI0S1 .SetParameter(5 ,1);
49     cPars_pXim_HalI0S1 .SetParameter(6 ,0);
50     cPars_pXim_HalI0S1 .SetParameter(7 ,1);
51
52     CATSparameters cPars_pXim_HalI1S0(CATSparameters :: tPotential ,8 ,true );
53     cPars_pXim_HalI1S0 .SetParameter(0 ,pXim_HALQCD1 );
54     //the euclidean time
55     cPars_pXim_HalI1S0 .SetParameter(1 ,12);
56     cPars_pXim_HalI1S0 .SetParameter(2 ,1);
57     cPars_pXim_HalI1S0 .SetParameter(3 ,1);
58     cPars_pXim_HalI1S0 .SetParameter(4 ,1);
59     cPars_pXim_HalI1S0 .SetParameter(5 ,0);
60     cPars_pXim_HalI1S0 .SetParameter(6 ,0);
61     cPars_pXim_HalI1S0 .SetParameter(7 ,0);
62
63     CATSparameters cPars_pXim_HalI1S1(CATSparameters :: tPotential ,8 ,true );
64     cPars_pXim_HalI1S1 .SetParameter(0 ,pXim_HALQCD1 );
65     //the euclidean time
66     cPars_pXim_HalI1S1 .SetParameter(1 ,12);
67     cPars_pXim_HalI1S1 .SetParameter(2 ,1);
68     cPars_pXim_HalI1S1 .SetParameter(3 ,1);
69     cPars_pXim_HalI1S1 .SetParameter(4 ,1);
70     cPars_pXim_HalI1S1 .SetParameter(5 ,1);
71     cPars_pXim_HalI1S1 .SetParameter(6 ,0);
72     cPars_pXim_HalI1S1 .SetParameter(7 ,1);
73
74     Kitty .SetShortRangePotential(0 ,0 ,fDlmPot ,cPars_pXim_HalI0S0 );
75     Kitty .SetShortRangePotential(1 ,0 ,fDlmPot ,cPars_pXim_HalI0S1 );
76     Kitty .SetShortRangePotential(2 ,0 ,fDlmPot ,cPars_pXim_HalI1S0 );
77     Kitty .SetShortRangePotential(3 ,0 ,fDlmPot ,cPars_pXim_HalI1S1 );
78 }
```

As of this moment, we have defined all the needed correlation functions either in term of CATS objects, or a separate function ($p-\Sigma^0$). The next step is to create the

corresponding histograms of type *DLM_Ck*, a rather trivial step based on the function definitions discussed so far.

```

1 void Ck_pp_Decomposition(){
2
3     //the same source profile and size will be assumed for all
4     //contributions. This does NOT need to be the case
5     const double SourceSize = 1.5;
6     const double NumMomBins = 75;
7     const double kMin = 0;
8     const double kMax = 300;
9
10    //set up pp
11    CATS Kitty_pp;
12    CATS_GaussSource(Kitty_pp, SourceSize);
13    CATS_pp_Basic(Kitty_pp, NumMomBins, kMin, kMax);
14    //setup the pp interaction with s,p,d waves
15    CATS_pp_AV18(Kitty_pp, true, true);
16    Kitty_pp.KillTheCat();
17    //create the C(k) histogram
18    DLM_Ck dlmCk_pp(1,0,Kitty_pp);
19
20    //set up pLambda
21    CATS Kitty_pL;
22    CATS_GaussSource(Kitty_pL, SourceSize);
23    CATS_pL_Basic(Kitty_pL, NumMomBins, kMin, kMax);
24    CATS_pL_Usmani(Kitty_pL);
25    Kitty_pL.KillTheCat();
26    DLM_Ck dlmCk_pL(1,0,Kitty_pL);
27
28    //set up pXi
29    CATS Kitty_pXim;
30    CATS_GaussSource(Kitty_pXim, SourceSize);
31    CATS_pXim_Basic(Kitty_pXim, NumMomBins, kMin, kMax);
32    CATS_pXim_Hal(Kitty_pXim);
33    Kitty_pXim.KillTheCat();
34    DLM_Ck dlmCk_pXim(1,0,Kitty_pXim);
35
36    //set up pSigma0
37    DLM_Ck dlmCk_pSigma0(1,0,SourceSize, kMin, kMax, Lednicky_gauss_Sigma0);
38    dlmCk_pSigma0.SetSourcePar(0, SourceSize);

```

The new step is to define the decomposition objects, which will be used for momentum smearing and accounting for the feed-down. A required input are the corresponding smear and decay matrices, as discussed in chapter 2.7. These can be either in *TH2F* (ROOT) format, or in 2D *DLM_Histo<float>* format. The former requires the use of the *DLM_CkDecomposition* object, the latter uses *DLM_CkDecomp*. Figures ??? (PUT IN MAIN BODY) are examples of such histograms. Please note, that using matrices with binning coarser than the correlation function will lead to numerical artefacts. It is recommended to use binning that is the same as the correlation, or finer by an integer factor. In the results presented in this thesis, these bins were binned in 1 MeV. The technical implementation of obtaining these matrices is omitted from this work, hence we assume that these are well defined and called into our code by

```

1 //momentum smearing matrix.
2 //it is applied only to the final correlation (pp)
3 DLM_Histo<float>* hResolution_pp = GetSmearMatrix_pp();
4 //the decay matrix for the feeddown of pLambda->pp
5 DLM_Histo<float>* hFeedDown_pL_pp = GetDecayMatrix_pL_pp();
6 //the decay matrix for the feeddown of pXim->pLambda
7 DLM_Histo<float>* hFeedDown_pXim_pL = GetDecayMatrix_pXim_pL();
8 //the decay matrix for the feeddown of pSigma0->pL
9 DLM_Histo<float>* hFeedDown_pSigma0_pL = GetDecayMatrix_pSigma0_pL();

```

To define the objects to handle the decomposition, we need to set in the constructor a name (as a string), the number of non-primary contributions to the correlation function, a *DLM_Ck* object for the pair of interest and (optionally) a momentum smearing

matrix. The number of non-primary contribution is to be understood as the number of $\lambda_{ij} \neq \lambda_{00}$ parameters (see Eq. ??). Later on we will need to provide $\lambda_{ij} \neq \lambda_{00}$ as an input into *DLM_CkDecomp*, where λ_{00} is automatically set to $1 - \sum_{ij} \lambda_{ij}$. In order to keep the normalization related to the feed-downs correct thought the computation, it is important to always separate the feed-down contribution from the misidentifications, even if both are modeled with the same (e.g. flat) function. In the present example, the p-p correlation will have a non-flat feed-down contribution from p- Λ , a flat feed-down component related to any other channel and a flat contribution from misidentifications. This results in 3 non-primary entries. For all other channels we will neglect the misidentified component⁷, consequently resulting in 3, 1 and 1 non-primary components for the p- Λ , p- Ξ and p- Σ^0 respectively. The implementation in the code is

```

1  //the object is initialized by: a name of your choice ,
2  //number of contributions to C(k) APART from the primary ,
3  //DLM_Ck object , resolution matrix (NULL to avoid mom. smear)
4  DLM_CkDecomp CkDec_pp ("pp",3,dlmCk_pp,hResolution_pp);
5  DLM_CkDecomp CkDec_pL ("pLambda",3,dlmCk_pL,NULL);
6  DLM_CkDecomp CkDec_pXim ("pXim",1,dlmCk_pXim,NULL);
7  DLM_CkDecomp CkDec_pSigma0 ("pSigma0",1,dlmCk_pSigma0,NULL);
```

Adding the non-primary contributions to p-p is performed as follows

```

1  //example lambda pars (more or less realistic values)
2  const double lambda_pL_pp = 0.15;
3  const double lambda_pp_flat = 0.08;
4  const double lambda_pp_misid = 0.02;
5  //the primary lambda is assumed to be:
6  //1. - lambda_pL_pp - lambda_pp_flat - lambda_pp_misid
7  //to add the different contributions to the correlation , we need to specify:
8  //#WhichContribution ,#Type(cFeedDown or cFake),
9  //OPTIONALLY: DLM_CkDecomp of the feed-down contribution , transformation matrix
10 // if the last two entries are not given ,
11 // it is assumed that the feed-down correlation is flat
12 CkDec_pp.AddContribution(0,lambda_pL_pp,DLM_CkDecomp::cFeedDown,
13                         &CkDec_pL,hFeedDown_pL_pp);
14 CkDec_pp.AddContribution(1,lambda_pp_flat,DLM_CkDecomp::cFeedDown);
15 CkDec_pp.AddContribution(2,lambda_pp_misid,DLM_CkDecomp::cFake);
```

The same is performed for the rest of the correlations

```

1  double lambda_pXim_pL = 0.10;
2  double lambda_pSigma0_pL = 0.17;
3  double lambda_pL_flat = 0.23;
4  CkDec_pL.AddContribution(0,lambda_pXim_pL,DLM_CkDecomp::cFeedDown,
5                           &CkDec_pXim,hFeedDown_pXim_pL);
6  CkDec_pL.AddContribution(1,lambda_pSigma0_pL,DLM_CkDecomp::cFeedDown,
7                           &CkDec_pSigma0,hFeedDown_pSigma0_pL);
8  CkDec_pL.AddContribution(2,lambda_pL_flat,DLM_CkDecomp::cFeedDown);
9
10 double lambda_pXim_flat = 0.37;
11 CkDec_pXim.AddContribution(0,lambda_pXim_flat,DLM_CkDecomp::cFeedDown);
12
13 double lambda_pSigma0_flat = 0.12;
14 CkDec_pSigma0.AddContribution(0,lambda_pSigma0_flat,DLM_CkDecomp::cFeedDown);
```

To compute the resulting correlation functions, one should update all these objects. The two arguments of the *Update* function are related to i) force the update regardless of the status of the object. The forced update is propagated to any linked correlations. ii) At the expense of extra CPU time, the updated result contains all of the individual contributions, which are otherwise inaccessible.

```

1  CkDec_pp.Update(true ,true );
2  CkDec_pL.Update(true ,true );
```

⁷It is not necessary to include it, since we will only model the p-p correlation function. However, one should be careful, as neglecting the misidentifications will change the λ parameters!

```

3   CkDec_pXim.Update(true, true);
4   CkDec_pSigma0.Update(true, true);

```

To evaluate the resulting corrected correlation function, one should use the function

```

1   double EvalCk(const double& Momentum);

```

The individual contributions to the correlation signal can be called using a series of functions, the name of which begins with *EvalSignal*. These functions return the value of

$$\lambda_i [C_i(k^*) - 1], \quad (\text{A.8})$$

where i is indexing the contributions. The functions do **not** include the momentum smearing, this can be included in the result by using the functions *EvalSignalSmeared*. Below an example code, saving the output from the above computation in a *TGraph*, decomposing the p-p correlation into its primary part and the feed-down from p- Λ ⁸. For visibility, the individual contributions are normalized to unity

$$1 + \lambda_i [C_i(k^*) - 1]. \quad (\text{A.9})$$

```

1   for(unsigned uBin=0; uBin<NumMomBins; uBin++){
2       //the momentum
3       double Momentum = dlmCk_pp.GetBinCenter(0, uBin);
4       //evaluates the total pp correlation,
5       //including momentum smearing and feed-downs
6       double Ck_pp = CkDec_pp.EvalCk(Momentum);
7       //the contribution of the primary correlation (smeared)
8       double Ck_pp_pp = CkDec_pp.EvalSignalSmearedMain(Momentum);
9       //the contribution of the pL->pp correlation (smeared)
10      double Ck_pL_pp = CkDec_pp.EvalSignalSmearedChild(0, Momentum);
11      gCk_pp->SetPoint(uBin, Momentum, Ck_pp);
12      gCk_pp_pp->SetPoint(uBin, Momentum, Ck_pp_pp+1);
13      gCk_pL_pp->SetPoint(uBin, Momentum, Ck_pL_pp+1);
14  }
15
16  //PLOTING MACROS
17  //...
18
19  //do not forget to free the memory
20  delete Ck_pp;
21  delete Ck_pp_pp;
22  delete Ck_pL_pp;
23  delete hResolution_pp;
24  delete hFeedDown_pL_pp;
25  delete hFeedDown_pSigma0_pL;
26  delete hFeedDown_pXim_pL;
27 }

```

The results are plotted in Fig. A.6.

⁸Which in term contains p- Ξ and p- Σ^0 contributions.

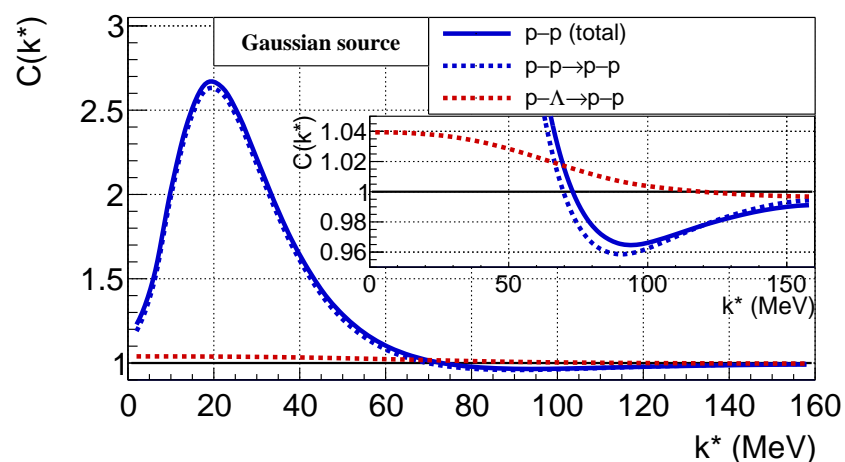


FIGURE A.6: Decomposition of the p-p correlation. The contribution from $p-\Lambda$ is very small, as it is flattened by the decay kinematics and suppressed by the λ parameter.

Appendix B

Details on the resonance source model

The full lists for resonances feeding into proton and Λ particles included in the SHM (see chapter 4.3) are given in Tables B.1 and B.2. They provide a detailed list of all resonances that are present in SHM as provided by F. Becattini. They are ordered by mass, and the different charged species are summed up together, with the exception of $\Sigma(1385)$, as they have the same mass and lifetime. Their fractions differ mostly due to the branching ratios (BR), which are included in SHM and applied to the EPOS selection manually. For example, the Δ^{++} , Δ^+ and Δ^0 decays into a proton with BR of 1, 2/3 and 1/3. The total fractions given in the tables refer to the amount of primary¹ protons and Λ s stemming from an intermediate decay of the corresponding resonance. The weights ω_{EPOS} are applied to the selected amount of resonance yield from EPOS, and are tuned manually to reproduce the effective mass predicted by SHM. The weights do *not* include the branching ratio, which is applied separately depending on the charge of the resonance. The last entry in both tables is the heaviest resonance included in EPOS, that has the effective role of representing all remaining heavy resonances. It is non-physical, thus not inside SHM and labeled as “other”. The EPOS simulation results in a substantial contribution of these effective resonances, thus they have been scaled down significantly.

An important detail is that the fraction provided by SHM are corrected for cascading decays into the ground state, meaning that if a heavier resonance decays into a lighter one before reaching the final state, consisting of proton or a Λ , it is counted towards the yield (fraction) of the light resonances and excluded from the heavy one. For example, the process $\Delta(1700) \rightarrow \Delta\pi \rightarrow p\pi\pi$ does not count as a 3-body decay of $\Delta(1700)$, but as a 2-body decay of Δ . In fact, in the case of resonances decaying into protons or Λ s the probability of a 2-body final state, where the second particle is a pion, is around 99%, justifying an additional assumption

Assumption 4: 2-body decay (optional)

All strongly decaying resonances have a 2-body final state, composed of proton or a Λ and a pion.

Assumption 4 is not required by our Monte-Carlo model, and while it is used in the study of p-p and p- Λ correlations it can be excluded for the study of π - π correlations.

¹The particles that are considered primaries are all that do not stem from weak or electromagnetic decays, e.g. the Σ^0 decay into Λ , and are included in the genuine λ parameter.

Resonance	Mass (MeV/c)	τ (fm/c)	Fraction (%)	ω_{EPOS} (%)
Δ	1232	1.67	43.67	100
$N(1440)$	1440	0.66	2.73	100
$N(1520)$	1520	1.72	2.64	100
$\Lambda(1520)$	1520	12.65	0.69	n/a
$N(1535)$	1535	1.32	1.53	100
$\Delta(1600)$	1600	0.56	1.00	100
$\Lambda(1600)$	1600	1.32	0.13	n/a
$\Sigma(1620)$	1600	2.27	0.21	n/a
$\Delta(1620)$	1620	1.36	0.78	100
$N(1650)$	1655	1.20	0.70	100
$\Sigma(1660)$	1660	1.97	0.18	0
$\Lambda(1670)$	1670	5.64	0.05	0
$\Sigma(1670)$	1670	3.29	0.33	0
$N(1675)$	1675	1.32	1.24	100
$N(1680)$	1685	1.52	1.72	100
$\Lambda(1690)$	1690	3.29	0.12	0
$\Delta(1700)$	1700	0.66	1.60	100
$N(1700)$	1700	1.97	0.13	100
$N(1710)$	1710	1.97	0.26	20
$N(1720)$	1720	0.99	1.07	100
$\Sigma(1750)$	1750	2.19	0.16	0
$\Sigma(1775)$	1775	1.64	0.57	0
$\Lambda(1800)$	1800	0.66	0.07	n/a
$\Lambda(1810)$	1810	1.32	0.10	n/a
$\Lambda(1820)$	1820	2.47	0.22	0
$\Lambda(1830)$	1830	2.08	0.04	n/a
$\Lambda(1890)$	1890	1.97	0.13	n/a
$\Delta(1905)$	1890	0.60	1.60	100
$\Delta(1910)$	1910	0.79	0.46	100
$\Sigma(1915)$	1915	1.64	0.07	0
$\Delta(\text{other})$	1925	n/a	n/a	20
Effective	1362	1.65	64.22	

TABLE B.1: The list of resonances from the SHM feeding into protons. The re-weight factors ω_{EPOS} used in the EPOS selection are based on the reduction of the yield to match the average mass of all resonances as predicted by SHM.

Resonance	Mass (MeV/c)	τ (fm/c)	Fraction (%)	ω_{EPOS} (%)
$\Sigma(1385)^+$	1383	5.51	16.40	100
$\Sigma(1385)^0$	1384	5.58	16.30	100
$\Sigma(1385)^-$	1387	5.01	15.94	100
$\Sigma(1620)$	1600	2.27	3.45	n/a
$N(1650)$	1655	1.20	0.26	0
$\Sigma(1660)$	1660	1.97	2.43	42
$\Sigma(1670)$	1670	3.29	2.19	42
$\Lambda(1670)$	1670	3.29	5.64	50
$\Lambda(1690)$	1690	3.29	0.82	50
$N(1710)$	1710	1.97	0.57	0
$N(1720)$	1720	0.99	0.37	0
$\Sigma(1750)$	1750	2.19	0.86	25
$\Sigma(1775)$	1775	1.64	1.60	18
$\Lambda(1820)$	1820	2.47	0.39	11
$\Xi(1820)$	1823	8.22	0.91	11
$\Sigma(1915)$	1915	1.64	1.36	3.7
$\Sigma(\text{other})$	1930	n/a	n/a	3.7
Effective	1463	4.69	64.38	

TABLE B.2: The list of resonances from the SHM feeding into Λ particles. The re-weight factors ω_{EPOS} used in the EPOS selection are based on the reduction of the yield to match the average mass of all resonances as predicted by SHM.

Index

- λ parameters, 28, 48, 80
- acceptance and efficiency, 29
- addition of correlations, 77
- angular correlations, 84
- Barlow test, 121
- bootstrap method, 95
- bound state, 35, 41, 119, 151
- Bowler-Sinyukov model, 159
- CATS, 29
- chiral effective field theory, 10, 129
- confidence interval, 99
- core-corona model, 85
- correlation function, 21
- cosine pointing angle, 65
- Coulomb interaction, 26, 31
- coupled channels, 10, 41, 129, 150
- data fitting, 93
- degenerate states in femtoscopy, 33
- distance of closest approach, 63
- effective Gaussian source, 111
- effective range, 24, 35, 118
- effective range expansion, 23, 35, 119
- emission source, 16, 21, 39, 41, 84, 101, 156
- equation of state, 11, 129
- event cuts, 62
- feed-down, 27, 29, 44, 63, 80
- femtoscopy, 15
- Gamow approximation, 27
- global tracks, 61
- H-dibaryon, 117
- HBT effect, 15
- Higgs boson, 53
- high-multiplicity trigger, 55
- hypernucleus, 9, 117
- hyperon, 3
- hyperon puzzle, 13
- identical particles, 25, 31
- Inner Tracking System, 56
- interaction channels, 33
- invariant mass, 67, 136
- jet, 5
- Koonin-Pratt relation, 20
- Lévy stable distribution, 104
- Large Hadron Collider, 53
- lattice calculations, 10
- Lednický model, 23, 38
- long-range correlations, 90
- mini-jets, 85
- minimum-bias trigger, 55
- misidentified particles, 44, 47, 81
- mixed event sample, 21, 73, 77, 84
- momentum dependent decomposition, 82
- momentum resolution, 29, 44, 49
- neutron star, 8, 129
- non-femtoscopic baseline, 74, 84, 88
- non-traditional femtoscopy, 17
- normalization in femtoscopy, 22, 74, 75, 78
- notation, 30
- pair cuts, 71
- partial waves, 30
- particle identification, 57
- particle reconstruction
 - Λ particles (V0), 65
 - charged tracks, 63
 - protons, 63
- phase shift, 35, 40
- pile-up, 56
- primary vertex, 56
- pseudorapidity, 54
- purity, 48, 63, 80, 135
- quantum chromodynamics, 3
- quark coalescence model, 86, 90
- quark-gluon plasma, 4, 84
- rapidity, 55
- reduced mass, 30

residual correlations, 27, 29, 44, 63, 80
resonance source model, 102, 105, 109
 Gaussian core, 105
 universal source model, 111

same event sample, 21, 73, 77
scattering length, 23, 35, 118
Schrödinger equation, 30
secondary vertex, 66
sideband analysis, 82, 134
source parameters in CATS, 157
standard model, 1, 53
statistical hadronization model, 104
strong interaction, 3, 34, 41, 159
systematic uncertainties, 94

template fit, 64
three-body interaction, 9, 153
Time Projection Chamber, 57
 TPC-only tracks, 61
Time-Of-Flight, 59
transverse mass, 102
transverse momentum, 54
triggering system, 55

unfolding, 139

Bibliography

- [1] David Griffiths.
Introduction to Elementary Particles.
 Wiley-VCH, 2008. ISBN 978-3-527-40601-2.
 Cited on page 2.
- [2] Wikipedia.
Standard Model
https://en.wikipedia.org/wiki/Standard_Model
 Accessed: 3rd Dec 2020.
 Cited on page 2.
- [3] Niels Walet Lectures (The University of Manchester).
The Feynman diagrams of QCD
<https://oer.physics.manchester.ac.uk/NP/Notes/Notesesse54.xht>
 Accessed: 3rd Dec 2020.
 Cited on page 3.
- [4] Michiel Botje Lectures (Nikhef, Science Park, Amsterdam).
Lecture notes Particle Physics II, Asymptotic Freedom
<https://www.nikhef.nl/~h24/qcdcourse/section-6.pdf>
 Accessed: 3rd Dec 2020.
 Cited on page 4.
- [5] Wit Busza, Krishna Rajagopal, and Wilke van der Schee.
Heavy Ion Collisions: The Big Picture, and the Big Questions.
Ann. Rev. Nucl. Part. Sci., 68:339–376, 2018. doi: 10.1146/annurev-nucl-101917-020852.
 Cited on pages 4 and 5.
- [6] ALICE Collaboration.
Enhanced production of multi-strange hadrons in high-multiplicity proton-proton collisions.
Nature Phys., 13:535–539, 2017. doi: 10.1038/nphys4111.
 Cited on pages 7, 55, and 85.
- [7] Robert B. Wiringa, V.G.J. Stoks, and R. Schiavilla.
An Accurate nucleon-nucleon potential with charge independence breaking.
Phys. Rev. C, 51:38–51, 1995. doi: 10.1103/PhysRevC.51.38.
 Cited on pages 8, 51, 103, 110, 123, and 163.
- [8] J. Haidenbauer, S. Petschauer, N. Kaiser, U.-G. Meissner, A. Nogga, and W. Weise.
Hyperon-nucleon interaction at next-to-leading order in chiral effective field theory.
Nucl. Phys. A, 915:24–58, 2013. doi: 10.1016/j.nuclphysa.2013.06.008.
 Cited on pages 9, 10, 13, 103, 123, and 131.

- [9] A. Gal, J.M. Soper, and R.H. Dalitz.
Shell-model analysis of lambda binding energies for p-shell hypernuclei. 1. Basic formulas and matrix elements for lambda N and lambda NN forces.
Annals Phys., 63:53–126, 1971. doi: 10.1016/0003-4916(71)90297-1.
 Cited on page 9.
- [10] A. Reuber, K. Holinde, and J. Speth.
Meson exchange hyperon - nucleon interactions in free scattering and nuclear matter.
Nucl. Phys. A, 570:543–579, 1994. doi: 10.1016/0375-9474(94)90073-6.
 Not cited.
- [11] O. Hashimoto and H. Tamura.
Spectroscopy of Lambda hypernuclei.
Prog. Part. Nucl. Phys., 57:564–653, 2006. doi: 10.1016/j.ppnp.2005.07.001.
 Not cited.
- [12] N. Kaiser and W. Weise.
Chiral SU(3) dynamics and Lambda-hyperons in the nuclear medium.
Phys. Rev. C, 71:015203, 2005. doi: 10.1103/PhysRevC.71.015203.
 Not cited.
- [13] D.J. Millener.
Shell-model calculations for p-shell hypernuclei.
Nucl. Phys. A, 881:298–309, 2012. doi: 10.1016/j.nuclphysa.2012.01.019.
 Cited on page 9.
- [14] H. Takahashi et al.
Observation of a (Lambda Lambda)He-6 double hypernucleus.
Phys. Rev. Lett., 87:212502, 2001. doi: 10.1103/PhysRevLett.87.212502.
 Cited on pages 10 and 117.
- [15] Tomofumi Nagae et al.
Search For A Ξ Bound State In The $^{12}\text{C}(K^-, K^+)X$ Reaction At 1.8 Gev/c in J-PARC.
PoS, INPC2016:038, 2017. doi: 10.22323/1.281.0038.
 Cited on page 10.
- [16] Tetsuo Hatsuda.
Lattice quantum chromodynamics and baryon-baryon interactions.
Front. Phys. (Beijing), 13(6):132105, 2018. doi: 10.1007/s11467-018-0829-4.
 Cited on page 10.
- [17] Stefan Petschauer, Johann Haidenbauer, Norbert Kaiser, Ulf-G. Meißner, and Wolfram Weise.
Hyperon-nuclear interactions from SU(3) chiral effective field theory.
Front. in Phys., 8:12, 2020. doi: 10.3389/fphy.2020.00012.
 Cited on pages 10 and 11.
- [18] LIGO and Virgo Collaborations.
GW170817: Measurements of neutron star radii and equation of state.
Phys. Rev. Lett., 121(16):161101, 2018. doi: 10.1103/PhysRevLett.121.161101.
 Cited on page 11.

- [19] Diego Lonardoni, Alessandro Lovato, Stefano Gandolfi, and Francesco Pedreira.
Hyperon Puzzle: Hints from Quantum Monte Carlo Calculations.
Phys. Rev. Lett., 114(9):092301, 2015. doi: 10.1103/PhysRevLett.114.092301.
Cited on page 12.
- [20] Dominik Gerstung, Norbert Kaiser, and Wolfram Weise.
Hyperon–nucleon three-body forces and strangeness in neutron stars.
Eur. Phys. J. A, 56(6):175, 2020. doi: 10.1140/epja/s10050-020-00180-2.
Cited on page 13.
- [21] J. Haidenbauer, U.-G. Meißner, and A. Nogga.
Hyperon–nucleon interaction within chiral effective field theory revisited.
Eur. Phys. J. A, 56(3):91, 2020. doi: 10.1140/epja/s10050-020-00100-4.
Cited on pages 13, 110, 131, and 144.
- [22] Wolfram Weise.
Dense Baryonic Matter and Strangeness in Neutron Stars.
JPS Conf. Proc., 26:011002, 2019. doi: 10.7566/JPSCP.26.011002.
Cited on page 14.
- [23] Gordon Baym, Shun Furusawa, Tetsuo Hatsuda, Toru Kojo, and Hajime Togashi.
New Neutron Star Equation of State with Quark-Hadron Crossover.
Astrophys. J., 885:42, 2019. doi: 10.3847/1538-4357/ab441e.
Cited on page 14.
- [24] Michael Annan Lisa, Scott Pratt, Ron Soltz, and Urs Wiedemann.
FEMTOSCOPY IN RELATIVISTIC HEAVY ION COLLISIONS: Two Decades of Progress.
Annual Review of Nuclear and Particle Science, 55(1):357–402, 2005. doi: 10.1146/annurev.nucl.55.090704.151533.
Cited on pages 15, 16, 21, and 23.
- [25] R. Hanbury Brown and R.Q. Twiss.
A New type of interferometer for use in radio astronomy.
Phil. Mag. Ser. 7, 45:663–682, 1954. doi: 10.1080/14786440708520475.
Cited on page 15.
- [26] R. Hanbury Brown and R.Q. Twiss.
A Test of a new type of stellar interferometer on Sirius.
Nature, 178:1046–1048, 1956. doi: 10.1038/1781046a0.
Cited on page 15.
- [27] Gordon Baym.
The Physics of Hanbury Brown-Twiss intensity interferometry: From stars to nuclear collisions.
Acta Phys. Polon. B, 29:1839–1884, 1998.
Cited on page 15.
- [28] Gerson Goldhaber, Sulamith Goldhaber, Won-Yong Lee, and Abraham Pais.
Influence of Bose-Einstein statistics on the anti-proton proton annihilation process.
Phys. Rev., 120:300–312, 1960. doi: 10.1103/PhysRev.120.300.
Cited on page 16.

- [29] M. Deutschmann et al.
Determination of the Fireball Dimensions from Second Order Interference Between Two-Pions.
Nucl. Phys. B, 103:198–212, 1976. doi: 10.1016/0550-3213(76)90043-2.
 Cited on page 16.
- [30] Edward V. Shuryak.
The Correlation of identical pions in multibody production.
Phys. Lett. B, 44:387–389, 1973. doi: 10.1016/0370-2693(73)90414-0.
 Cited on page 16.
- [31] G.I. Kopylov.
Like particle correlations as a tool to study the multiple production mechanism.
Phys. Lett. B, 50:472–474, 1974. doi: 10.1016/0370-2693(74)90263-9.
 Cited on page 16.
- [32] R. Lednicky and M.I. Podgoretsky.
The Interference of Identical Particles Emitted by Sources of Different Sizes.
Sov. J. Nucl. Phys., 30:432, 1979.
 Cited on page 16.
- [33] R. Lednicky and V.L. Lyuboshits.
Final State Interaction Effect on Pairing Correlations Between Particles with Small Relative Momenta.
Sov. J. Nucl. Phys., 35:770, 1982.
 Cited on pages 16 and 23.
- [34] STAR Collaboration.
Experimental and theoretical challenges in the search for the quark gluon plasma: The STAR Collaboration’s critical assessment of the evidence from RHIC collisions.
Nucl. Phys. A, 757:102–183, 2005. doi: 10.1016/j.nuclphysa.2005.03.085.
 Cited on page 16.
- [35] Huichao Song, Steffen A. Bass, Ulrich Heinz, Tetsufumi Hirano, and Chun Shen.
200 A GeV Au+Au collisions serve a nearly perfect quark-gluon liquid.
Phys. Rev. Lett., 106:192301, 2011. doi: 10.1103/PhysRevLett.106.192301. [Erratum: *Phys. Rev. Lett.* 109, 139904 (2012)].
 Cited on page 16.
- [36] STAR Collaboration.
 $\Lambda\Lambda$ Correlation Function in Au+Au collisions at $\sqrt{s_{NN}} = 200$ GeV.
Phys. Rev. Lett., 114(2):022301, 2015. doi: 10.1103/PhysRevLett.114.022301.
 Cited on pages 17 and 118.
- [37] Kenji Morita, Takenori Furumoto, and Akira Ohnishi.
 $\Lambda\Lambda$ interaction from relativistic heavy-ion collisions.
Phys. Rev. C, 91(2):024916, 2015. doi: 10.1103/PhysRevC.91.024916.
 Cited on pages 17, 34, 118, 119, 125, and 126.
- [38] ALICE Collaboration.
p-p, p- Λ and Λ - Λ correlations studied via femtoscopy in pp reactions at $\sqrt{s} =$

- 7 TeV.
Phys. Rev. C, 99(2):024001, 2019. doi: 10.1103/PhysRevC.99.024001.
Cited on pages 18, 20, 28, 48, 62, 63, 74, 102, 118, 119, 121, 124, 125, 126, and 149.
- [39] D.L. Mihaylov, V. Mantovani Sarti, O.W. Arnold, L. Fabbietti, B. Hohlweger, and A.M. Mathis.
A femtoscopic Correlation Analysis Tool using the Schrödinger equation (CATS).
Eur. Phys. J. C, 78(5):394, 2018. doi: 10.1140/epjc/s10052-018-5859-0.
Cited on pages 18, 20, 29, 108, and 149.
- [40] ALICE Collaboration.
First Observation of an Attractive Interaction between a Proton and a Cascade Baryon.
Phys. Rev. Lett., 123(11):112002, 2019. doi: 10.1103/PhysRevLett.123.112002.
Cited on pages 19, 20, 111, 133, 149, 151, and 165.
- [41] ALICE Collaboration.
Study of the Λ - Λ interaction with femtoscopy correlations in pp and p-Pb collisions at the LHC.
Phys. Lett. B, 797:134822, 2019. doi: 10.1016/j.physletb.2019.134822.
Cited on pages 19, 20, 120, 121, 126, 127, and 133.
- [42] ALICE Collaboration.
Investigation of the p- Σ^0 interaction via femtoscopy in pp collisions.
Phys. Lett. B, 805:135419, 2020. doi: 10.1016/j.physletb.2020.135419.
Cited on pages 20, 130, 134, 152, 153, and 170.
- [43] ALICE Collaboration.
Scattering studies with low-energy kaon-proton femtoscopy in proton-proton collisions at the LHC.
Phys. Rev. Lett., 124(9):092301, 2020. doi: 10.1103/PhysRevLett.124.092301.
Cited on pages 19, 20, 149, and 150.
- [44] ALICE Collaboration.
Search for a common baryon source in high-multiplicity pp collisions at the LHC.
Physics Letters B, 811:135849, 2020. doi: 10.1016/j.physletb.2020.135849.
Cited on pages 19, 20, 93, 102, 103, 106, 110, and 149.
- [45] ALICE Collaboration.
A new laboratory to study hadron-hadron interactions. 5 2020.
Cited on pages 18, 19, 54, 111, 133, 149, and 152.
- [46] R. Brun and F. Rademakers.
ROOT: An object oriented data analysis framework.
Nucl. Instrum. Meth. A, 389:81–86, 1997. doi: 10.1016/S0168-9002(97)00048-X.
Cited on pages 19, 45, and 155.
- [47] J. J. Sakurai and Jim Napolitano.
Modern Quantum Mechanics.
Pearson Education Limited, 2014. ISBN 978-1-292-02410-3.
Cited on pages 24 and 25.

- [48] David Griffiths.
Introduction to Quantum Mechanics.
 Pearson Prentice Hall, 2004. ISBN 978-1107179868.
 Cited on pages 24 and 25.
- [49] Richard Lednicky.
 Finite-size effects on two-particle production in continuous and discrete spectrum.
Phys. Part. Nucl., 40:307–352, 2009. doi: 10.1134/S1063779609030034.
 Cited on page 27.
- [50] M. Gmitro, J. Kvasil, R. Lednicky, and V.L. Lyuboshits.
 On the Sensitivity of Nucleon-nucleon Correlations to the Form of Short Range Potential.
Czech. J. Phys. B, 36:1281, 1986. doi: 10.1007/BF01598029.
 Cited on page 27.
- [51] Oliver Arnold.
 Study of the hyperon-nucleon interaction via femtoscopy in elementary systems with HADES and ALICE.
PhD thesis, Technical University of Munich, 2017.
 Cited on pages 28, 62, and 63.
- [52] M. Galassi et al.
GNU Scientific Library Reference Manual (3rd Ed.).
 Network Theory Limited, 2009. ISBN 978-0954612078.
 Cited on pages 31 and 155.
- [53] ATLAS Collaboration.
 Two-particle Bose–Einstein correlations in pp collisions at $\sqrt{s} = 0.9$ and 7 TeV measured with the ATLAS detector.
Eur. Phys. J. C, 75(10):466, 2015. doi: 10.1140/epjc/s10052-015-3644-x.
 Cited on pages 34 and 102.
- [54] CMS Collaboration.
 Bose-Einstein correlations in pp , $p\text{Pb}$, and PbPb collisions at $\sqrt{s_{NN}} = 0.9 - 7$ TeV.
Phys. Rev. C, 97(6):064912, 2018. doi: 10.1103/PhysRevC.97.064912.
 Cited on pages 102 and 104.
- [55] CMS Collaboration. Femtoscopic Bose-Einstein Correlations of charged hadrons in proton-proton collisions at $\sqrt{s} = 13$ TeV. 5 2018.
 Not cited.
- [56] ALICE Collaboration.
 Femtoscopy of pp collisions at $\sqrt{s} = 0.9$ and 7 TeV at the LHC with two-pion Bose-Einstein correlations.
Phys. Rev. D, 84:112004, 2011. doi: 10.1103/PhysRevD.84.112004.
 Not cited.
- [57] ALICE Collaboration.
 Two-pion femtoscopy in p-Pb collisions at $\sqrt{s_{NN}} = 5.02$ TeV.
Phys. Rev. C, 91:034906, 2015. doi: 10.1103/PhysRevC.91.034906.
 Cited on page 34.

- [58] Jeremy W. Holt, Norbert Kaiser, and Wolfram Weise.
Nuclear chiral dynamics and thermodynamics.
Prog. Part. Nucl. Phys., 73:35–83, 2013. doi: 10.1016/j.ppnp.2013.08.001.
Cited on pages 34 and 35.
- [59] Yuki Kamiya, Tetsuo Hyodo, Kenji Morita, Akira Ohnishi, and Wolfram Weise.
 $K^- p$ Correlation Function from High-Energy Nuclear Collisions and Chiral SU(3) Dynamics.
Phys. Rev. Lett., 124(13):132501, 2020. doi: 10.1103/PhysRevLett.124.132501.
Cited on pages 43, 44, 150, 151, and 165.
- [60] A.R. Bodmer, Q.N. Usmani, and J. Carlson.
Binding energies of hypernuclei and three-body ANN forces.
Phys. Rev. C, 29:684–687, 1984. doi: 10.1103/PhysRevC.29.684.
Cited on pages 47, 159, and 164.
- [61] Andreas Mathis.
First Measurement of the Proton– Σ^0 Interaction via the Femtoscopy Method.
PhD thesis, Technical University of Munich, 2020.
Cited on pages 49, 53, 54, and 57.
- [62] Bernhard Hohlweger.
First observation of the p – Ξ^- interaction via two-particle correlations.
PhD thesis, Technical University of Munich, 2020.
Cited on pages 49, 53, 54, 102, and 133.
- [63] Georges Aad et al.
Observation of a new particle in the search for the Standard Model Higgs boson with the ATLAS detector at the LHC.
Phys. Lett. B, 716:1–29, 2012. doi: 10.1016/j.physletb.2012.08.020.
Cited on page 53.
- [64] John Ellis.
Searching for supersymmetry and its avatars.
Phil. Trans. Roy. Soc. Lond. A, 377(2161):20190069, 2019. doi: 10.1098/rsta.2019.0069.
Cited on page 53.
- [65] ALICE Collaboration.
The ALICE experiment at the CERN LHC.
JINST, 3:S08002, 2008. doi: 10.1088/1748-0221/3/08/S08002.
Cited on page 54.
- [66] ALICE Collaboration.
ALICE: Physics performance report, volume I.
J. Phys. G, 30:1517–1763, 2004. doi: 10.1088/0954-3899/30/11/001.
Not cited.
- [67] ALICE Collaboration.
ALICE: Physics performance report, volume II.
J. Phys. G, 32:1295–2040, 2006. doi: 10.1088/0954-3899/32/10/001.
Not cited.

- [68] ALICE Collaboration.
Performance of the ALICE Experiment at the CERN LHC.
Int. J. Mod. Phys. A, 29:1430044, 2014. doi: 10.1142/S0217751X14300440.
 Cited on pages 54 and 55.
- [69] ALICE Collaboration.
ALICE Figure repository.
Accessed 4th December 2020.
 Cited on page 55.
- [70] J. Alme et al.
The ALICE TPC, a large 3-dimensional tracking device with fast readout for ultra-high multiplicity events.
Nucl. Instrum. Meth. A, 622:316–367, 2010. doi: 10.1016/j.nima.2010.04.042.
 Cited on page 57.
- [71] ALICE Collaboration.
Real-time data processing in the ALICE High Level Trigger at the LHC.
Comput. Phys. Commun., 242:25–48, 2019. doi: 10.1016/j.cpc.2019.04.011.
 Cited on page 57.
- [72] Torbjorn Sjostrand, Stephen Mrenna, and Peter Z. Skands.
PYTHIA 6.4 Physics and Manual.
JHEP, 05:026, 2006. doi: 10.1088/1126-6708/2006/05/026.
 Cited on pages 62 and 106.
- [73] R. Brun, R. Hagelberg, M. Hansroul, and J.C. Lassalle. **Geant: Simulation Program for Particle Physics Experiments. User Guide and Reference Manual.** 7 1978.
 Cited on page 62.
- [74] Ivan Vorobyev.
Low-mass dielectron production in proton–proton collisions at $\sqrt{s}=13$ TeV with ALICE.
PhD thesis, Technical University of Munich, 2018.
 Cited on page 62.
- [75] Volodymyr Vovchenko and Horst Stoecker.
Thermal-FIST: A package for heavy-ion collisions and hadronic equation of state.
Comput. Phys. Commun., 244:295–310, 2019. doi: 10.1016/j.cpc.2019.06.024.
 Cited on pages 71, 123, and 144.
- [76] J. Adamczewski-Musch et al.
 Σ^0 production in proton nucleus collisions near threshold.
Phys. Lett. B, 781:735–740, 2018. doi: 10.1016/j.physletb.2018.02.043.
 Cited on page 71.
- [77] ALICE Collaboration.
 Σ^0 and $\bar{\Sigma}^0$ Baryon Production in pp Collisions at \sqrt{s} TeV from the Analysis of 2010 Pass-4 ALICE Data.
ALICE preliminary results, 2017.
 Cited on pages 71, 123, and 144.

- [78] Evan Frodermann, Ulrich Heinz, and Michael Annan Lisa.
Fitted HBT radii versus space-time variances in flow-dominated models.
Phys. Rev. C, 73:044908, 2006. doi: 10.1103/PhysRevC.73.044908.
Cited on page 84.
- [79] CMS Collaboration.
Observation of Long-Range Near-Side Angular Correlations in Proton-Proton Collisions at the LHC.
JHEP, 09:091, 2010. doi: 10.1007/JHEP09(2010)091.
Cited on page 85.
- [80] ALICE Collaboration.
Insight into particle production mechanisms via angular correlations of identified particles in pp collisions at $\sqrt{s} = 7$ TeV.
Eur. Phys. J. C, 77(8):569, 2017. doi: 10.1140/epjc/s10052-017-5129-6. [Erratum: *Eur.Phys.J.C* 79, 998 (2019)].
Cited on pages 84, 86, and 87.
- [81] Kevin Dusling, Wei Li, and Björn Schenke.
Novel collective phenomena in high-energy proton–proton and proton–nucleus collisions.
Int. J. Mod. Phys. E, 25(01):1630002, 2016. doi: 10.1142/S0218301316300022.
Cited on page 85.
- [82] James L. Nagle and William A. Zajc.
Small System Collectivity in Relativistic Hadronic and Nuclear Collisions.
Ann. Rev. Nucl. Part. Sci., 68:211–235, 2018. doi: 10.1146/annurev-nucl-101916-123209.
Cited on page 85.
- [83] Torbjörn Sjöstrand.
Collective Effects: the viewpoint of HEP MC codes.
Nucl. Phys. A, 982:43–49, 2019. doi: 10.1016/j.nuclphysa.2018.11.010.
Cited on page 85.
- [84] Klaus Werner, Fu-Ming Liu, and Tanguy Pierog.
Parton ladder splitting and the rapidity dependence of transverse momentum spectra in deuteron-gold collisions at RHIC.
Phys. Rev. C, 74:044902, 2006. doi: 10.1103/PhysRevC.74.044902.
Cited on pages 85 and 106.
- [85] T. Pierog, Iu. Karpenko, J.M. Katzy, E. Yatsenko, and K. Werner.
EPOS LHC: Test of collective hadronization with data measured at the CERN Large Hadron Collider.
Phys. Rev. C, 92(3):034906, 2015. doi: 10.1103/PhysRevC.92.034906.
Cited on pages 85 and 106.
- [86] Yuuka Kanakubo, Yasuki Tachibana, and Tetsufumi Hirano.
Unified description of hadron yield ratios from dynamical core-corona initialization.
Phys. Rev. C, 101(2):024912, 2020. doi: 10.1103/PhysRevC.101.024912.
Cited on page 85.

- [87] Zi-wei Lin and C.M. Ko.
Partonic effects on the elliptic flow at RHIC.
Phys. Rev. C, 65:034904, 2002. doi: 10.1103/PhysRevC.65.034904.
 Cited on page 86.
- [88] Zi-Wei Lin, Che Ming Ko, Bao-An Li, Bin Zhang, and Subrata Pal.
A Multi-phase transport model for relativistic heavy ion collisions.
Phys. Rev. C, 72:064901, 2005. doi: 10.1103/PhysRevC.72.064901.
 Cited on pages 86 and 128.
- [89] Xin-Nian Wang and Miklos Gyulassy.
HJING: A Monte Carlo model for multiple jet production in p p, p A and A A collisions.
Phys. Rev. D, 44:3501–3516, 1991. doi: 10.1103/PhysRevD.44.3501.
 Cited on page 86.
- [90] Bao-An Li and Che Ming Ko.
Formation of superdense hadronic matter in high-energy heavy ion collisions.
Phys. Rev. C, 52:2037–2063, 1995. doi: 10.1103/PhysRevC.52.2037.
 Cited on page 86.
- [91] Feng-Tao Wang and Jun Xu.
Hadronization using the Wigner function approach for a multiphase transport model.
Phys. Rev. C, 100(6):064909, 2019. doi: 10.1103/PhysRevC.100.064909.
 Cited on page 87.
- [92] Liu-Yao Zhang, Jin-Hui Chen, Zi-Wei Lin, Yu-Gang Ma, and Song Zhang.
Two-particle angular correlations in $p p$ and p -Pb collisions at energies available at the CERN Large Hadron Collider from a multiphase transport model.
Phys. Rev. C, 98(3):034912, 2018. doi: 10.1103/PhysRevC.98.034912.
 Cited on pages 87 and 88.
- [93] Tianhao Shao, Jinhui Chen, Che Ming Ko, and Zi-Wei Lin.
Enhanced production of strange baryons in high-energy nuclear collisions from a multiphase transport model.
Phys. Rev. C, 102(1):014906, 2020. doi: 10.1103/PhysRevC.102.014906.
 Cited on page 87.
- [94] Liu-Yao Zhang, Jin-Hui Chen, Zi-Wei Lin, Yu-Gang Ma, and Song Zhang.
Two-particle angular correlations in heavy ion collisions from a multiphase transport model.
Phys. Rev. C, 99(5):054904, 2019. doi: 10.1103/PhysRevC.99.054904.
 Cited on page 87.
- [95] Mikolaj Chojnacki, Adam Kisiel, Wojciech Florkowski, and Wojciech Brotniowski.
THERMINATOR 2: THERMal heavy IoN generATOR 2.
Comput. Phys. Commun., 183:746–773, 2012. doi: 10.1016/j.cpc.2011.11.018.
 Cited on page 89.
- [96] T.J. Humanic.
Extracting the hadronization timescale in $\sqrt{s} = 7$ TeV proton-proton collisions from pion and kaon femtoscopy.

- J. Phys. G*, 41:075105, 2014. doi: 10.1088/0954-3899/41/7/075105.
Cited on page 90.
- [97] ALICE Collaboration.
Based on ALICE preliminary figure ALI-PREL-342616.
<https://alice-figure.web.cern.ch/>, 2020.
Cited on page 92.
- [98] Adam Kisiel, Wojciech Florkowski, and Wojciech Broniowski.
Femtoscopy in hydro-inspired models with resonances.
Phys. Rev. C, 73:064902, 2006. doi: 10.1103/PhysRevC.73.064902.
Cited on page 102.
- [99] Yu.M. Sinyukov, V.M. Shapoval, and V.Yu. Naboka.
On m_T dependence of femtoscopy scales for meson and baryon pairs.
Nucl. Phys. A, 946:227–239, 2016. doi: 10.1016/j.nuclphysa.2015.11.014.
Cited on page 102.
- [100] Adam Kisiel, Mateusz Gałażyn, and Piotr Bożek.
Pion, kaon, and proton femtoscopy in Pb–Pb collisions at $\sqrt{s_{\text{NN}}}=2.76$ TeV modeled in (3+1)D hydrodynamics.
Phys. Rev. C, 90(6):064914, 2014. doi: 10.1103/PhysRevC.90.064914.
Cited on page 102.
- [101] V.M. Shapoval, P. Braun-Munzinger, Iu.A. Karpenko, and Yu.M. Sinyukov.
Femtoscopy correlations of kaons in Pb+Pb collisions at LHC within hydrokinetic model.
Nucl. Phys. A, 929:1–8, 2014. doi: 10.1016/j.nuclphysa.2014.05.003.
Cited on page 102.
- [102] Henk Polinder, Johann Haidenbauer, and Ulf-G. Meissner.
Hyperon-nucleon interactions: A Chiral effective field theory approach.
Nucl. Phys. A, 779:244–266, 2006. doi: 10.1016/j.nuclphysa.2006.09.006.
Cited on pages 103, 110, 123, and 131.
- [103] T. Csorgo, S. Hegyi, and W. A. Zajc.
Bose-Einstein correlations for Levy stable source distributions.
Eur. Phys. J. C, 36:67–78, 2004. doi: 10.1140/epjc/s2004-01870-9.
Cited on page 104.
- [104] Tamas Csorgo.
Correlation Probes of a QCD Critical Point.
Pos, HIGH-PTLHC08:027, 2008. doi: 10.22323/1.076.0027.
Cited on page 104.
- [105] P.A. Zyla et al.
Review of Particle Physics.
PTEP, 2020(8):083C01, 2020. doi: 10.1093/ptep/ptaa104.
Cited on page 106.
- [106] ALICE Collaboration.
Based on ALICE preliminary figure ALI-PREL-350846.
<https://alice-figure.web.cern.ch/>, 2020.
Cited on page 115.

- [107] Robert L. Jaffe. **Perhaps a Stable Dihyperon.** *Phys. Rev. Lett.*, 38:195–198, 1977. doi: 10.1103/PhysRevLett.38.195. [Erratum: *Phys. Rev. Lett.* 38, 617 (1977)].
Cited on page 117.
- [108] Tsutomu Sakai, Kiyotaka Shimizu, and Koichi Yazaki. **H dibaryon.** *Prog. Theor. Phys. Suppl.*, 137:121–145, 2000. doi: 10.1143/PTPS.137.121.
Cited on page 117.
- [109] KEK-PS E224 Collaboration. **Enhanced Lambda Lambda production near threshold in the C-12(K-,K+) reaction.** *Phys. Lett. B*, 444:267–272, 1998. doi: 10.1016/S0370-2693(98)01416-6.
Cited on pages 117 and 118.
- [110] C.J. Yoon et al. **Search for the H-dibaryon resonance in C-12 (K-, K+ Lambda Lambda X).** *Phys. Rev. C*, 75:022201, 2007. doi: 10.1103/PhysRevC.75.022201.
Cited on pages 117 and 118.
- [111] N. Metropolis, R. Bivins, M. Storm, Anthony Turkevich, J.M. Miller, and G. Friedlander. **Monte Carlo Calculations on Intranuclear Cascades. I. Low-Energy Studies.** *Phys. Rev.*, 110(1):185, 1958. doi: 10.1103/PhysRev.110.185.
Cited on page 118.
- [112] KEK-PS E373 Collaboration. **Double- Λ hypernuclei observed in a hybrid emulsion experiment.** *Phys. Rev. C*, 88(1):014003, 2013. doi: 10.1103/PhysRevC.88.014003.
Cited on page 117.
- [113] I.N. Filikhin and A. Gal. **Faddeev-Yakubovsky calculations for light lambda lambda hypernuclei.** *Nucl. Phys. A*, 707:491–509, 2002. doi: 10.1016/S0375-9474(02)01008-4.
Cited on page 118.
- [114] E. Hiyama, M. Kamimura, T. Motoba, T. Yamada, and Y. Yamamoto. **Four-body cluster structure of A = 7 -10 double Lambda hypernuclei.** *Phys. Rev. C*, 66:024007, 2002. doi: 10.1103/PhysRevC.66.024007.
Cited on page 118.
- [115] T. Ueda, K. Tominaga, M. Yamaguchi, N. Kijima, D. Okamoto, K. Miyagawa, and T. Yamada. **ΛN and $\Lambda\Lambda$ interactions in an OBE model and hypernuclei.** *Prog. Theor. Phys.*, 99:891–896, 1998. doi: 10.1143/PTP.99.891.
Cited on page 119.
- [116] M. Danysz et al. **The identification of a double hyperfragment.** *Nucl. Phys.*, 49:121–132, 1963. doi: 10.1016/0029-5582(63)90080-4.
Cited on page 119.

- [117] Y. Fujiwara, M. Kohno, C. Nakamoto, and Y. Suzuki.
Interactions between octet baryons in the SU(6) quark model.
Phys. Rev. C, 64:054001, 2001. doi: 10.1103/PhysRevC.64.054001.
Cited on page 120.
- [118] Y. Fujiwara, Y. Suzuki, and C. Nakamoto.
Baryon-baryon interactions in the SU(6) quark model and their applications to light nuclear systems.
Prog. Part. Nucl. Phys., 58:439–520, 2007. doi: 10.1016/j.ppnp.2006.08.001.
Cited on pages 120 and 170.
- [119] Thomas A. Rijken, M.M. Nagels, and Yasuo Yamamoto.
Baryon-baryon interactions: Nijmegen extended-soft-core models.
Prog. Theor. Phys. Suppl., 185:14–71, 2010. doi: 10.1143/PTPS.185.14.
Cited on page 120.
- [120] M.M. Nagels, T.A. Rijken, and J.J. de Swart.
Baryon Baryon Scattering in a One Boson Exchange Potential Approach. 2. Hyperon-Nucleon Scattering.
Phys. Rev. D, 15:2547, 1977. doi: 10.1103/PhysRevD.15.2547.
Cited on page 120.
- [121] M.M. Nagels, T.A. Rijken, and J.J. de Swart.
Baryon Baryon Scattering in a One Boson Exchange Potential Approach. 3. A Nucleon-Nucleon and Hyperon - Nucleon Analysis Including Contributions of a Nonet of Scalar Mesons.
Phys. Rev. D, 20:1633, 1979. doi: 10.1103/PhysRevD.20.1633.
Not cited.
- [122] T.A. Rijken, V.G.J. Stoks, and Y. Yamamoto.
Soft core hyperon - nucleon potentials.
Phys. Rev. C, 59:21–40, 1999. doi: 10.1103/PhysRevC.59.21.
Cited on page 120.
- [123] Kenji Sasaki et al.
 $\Lambda\Lambda$ and $N\Xi$ interactions from Lattice QCD near the physical point.
Nucl. Phys. A, 121737, 12 2019. doi: 10.1016/j.nuclphysa.2020.121737.
Cited on pages 120, 128, 164, 165, and 197.
- [124] J. Haidenbauer.
Coupled-channel effects in hadron–hadron correlation functions.
Nucl. Phys. A, 981:1–16, 2019. doi: 10.1016/j.nuclphysa.2018.10.090.
Cited on page 120.
- [125] Kenji Sasaki et al.
Baryon interactions from lattice QCD with physical masses – $S = -2$ sector –.
PoS, LATTICE2016:116, 2017. doi: 10.22323/1.256.0116.
Cited on pages 123 and 164.
- [126] A. Stavinskiy, K. Mikhailov, B. Erazmus, and R. Lednický.
Residual correlations between decay products of π^0 π^0 and p Σ^0 systems. 4 2007.
Cited on page 123.

- [127] ALICE Collaboration.
ΛK femtoscopy in Pb-Pb collisions at $\sqrt{s_{\text{NN}}} = 2.76 \text{ TeV}$. 5 2020.
 Cited on page 134.
- [128] M. Bazzi et al.
A New Measurement of Kaonic Hydrogen X-rays.
Phys. Lett. B, 704:113–117, 2011. doi: 10.1016/j.physletb.2011.09.011.
 Cited on page 149.
- [129] Takashi Inoue.
Strange Nuclear Physics from QCD on Lattice.
AIP Conf. Proc., 2130(1):020002, 2019. doi: 10.1063/1.5118370.
 Cited on page 151.
- [130] HAL QCD Collaboration.
 $N\Omega$ dibaryon from lattice QCD near the physical point.
Phys. Lett. B, 792:284–289, 2019. doi: 10.1016/j.physletb.2019.03.050.
 Cited on pages 151, 152, and 165.
- [131] Takayasu Sekihara, Yuki Kamiya, and Tetsuo Hyodo.
 $N\Omega$ interaction: meson exchanges, inelastic channels, and quasibound state.
Phys. Rev. C, 98(1):015205, 2018. doi: 10.1103/PhysRevC.98.015205.
 Cited on pages 151, 152, and 165.
- [132] Kfir Blum and Masahiro Takimoto.
Nuclear coalescence from correlation functions.
Phys. Rev. C, 99(4):044913, 2019. doi: 10.1103/PhysRevC.99.044913.
 Cited on page 153.
- [133] J. Haidenbauer.
Exploring the Λ -deuteron interaction via correlations in heavy-ion collisions.
Phys. Rev. C, 102(3):034001, 2020. doi: 10.1103/PhysRevC.102.034001.
 Cited on page 153.
- [134] Yu. Sinyukov, R. Lednický, S.V. Akkelin, J. Pluta, and B. Erazmus.
Coulomb corrections for interferometry analysis of expanding hadron systems.
Phys. Lett. B, 432:248–257, 1998. doi: 10.1016/S0370-2693(98)00653-4.
 Cited on page 159.
- [135] M.G. Bowler.
Coulomb corrections to Bose-Einstein correlations have been greatly exaggerated.
Phys. Lett. B, 270:69–74, 1991. doi: 10.1016/0370-2693(91)91541-3.
 Not cited.
- [136] Radosław Maj and Stanisław Mrowczynski.
Coulomb Effects in Femtoscopy.
Phys. Rev. C, 80:034907, 2009. doi: 10.1103/PhysRevC.80.034907.
 Cited on page 159.
- [137] STAR Collaboration.
Proton - lambda correlations in central Au+Au collisions at $S(\text{NN})^{}(1/2) = 200\text{-GeV}$.**

- Phys. Rev. C*, 74:064906, 2006. doi: 10.1103/PhysRevC.74.064906.
Cited on page 161.
- [138] Jr. Reid, Roderick V.
Local phenomenological nucleon-nucleon potentials.
Annals Phys., 50:411–448, 1968. doi: 10.1016/0003-4916(68)90126-7.
Cited on page 164.
- [139] K. Sasaki and T. Miyamoto (HAL QCD Collaboration).
Private communications based on [123].
Cited on page 164.
- [140] Kenji Morita, Akira Ohnishi, Faisal Etminan, and Tetsuo Hatsuda.
Probing multistrange dibaryons with proton-omega correlations in high-energy heavy ion collisions.
Phys. Rev. C, 94(3):031901, 2016. doi: 10.1103/PhysRevC.94.031901.
[Erratum: *Phys. Rev. C* 100, 069902 (2019)].
Cited on page 165.
- [141] STAR Collaboration.
The Proton- Ω correlation function in Au+Au collisions at $\sqrt{s_{NN}}=200$ GeV.
Phys. Lett. B, 790:490–497, 2019. doi: 10.1016/j.physletb.2019.01.055.
Cited on page 165.
- [142] Kenta Miyahara and Tetsuo Hyodo.
Structure of $\Lambda(1405)$ and construction of $\bar{K}N$ local potential based on chiral SU(3) dynamics.
Phys. Rev. C, 93(1):015201, 2016. doi: 10.1103/PhysRevC.93.015201.
Cited on page 165.